Corrected,

Heat transfer by forced convection in beds of granular adsorbent material for solid sorption heat pumps.

Roger Thorpe B.Eng.

Submitted for the degree of PhD at the University of Warwick

Department of Engineering

September 1996

Summary

A novel adsorption cycle in which enhanced heat transfer between the adsorbent and external heat sinks and sources is achieved by forced convection of refrigerant gas through the adsorbent bed is presented This cycle is further developed by the use of inert beds to store the heat of desorption and sensible heat between phases. The performance and utility of such a cycle will depend on the heat transfer coefficients and pressure drops that result when the refrigerant gas is circulated through the beds

The heat transfer and pressure drop characteristics of a bed of granular active carbon were investigated using argon, carbon dioxide and ammonia. Equipment was designed and built to pass a stream of gas through a bed at a controlled rate, pressure and temperature. The pressure drop characteristic was found to conform to Ergun equation and the constants for the application of that relation to a commonly available granular active carbon established.

A mathematical model based on a finite difference technique was created and used to predict the progress of a temperature front in the bed and derive the heat transfer characteristics from experimental data. Heat transfer coefficients measured with argon and ammonia appeared inconsistent with each other and after investigations of the data and comparison with established correlations were made it was concluded that carbon during the argon experiments had been contaminated. The heat transfer results with ammonia and carbon were compared with a modified version of the Colburn analogy between heat transfer and pressure loss. A correlation between the Nusselt number and Reynolds number for design purposes was established.

CONTENTS

Acknowledgements

I wish to thank my supervisor Dr R.E.Critoph for his guidance, assistance and good humour. I am also grateful to the technical staff especially John Matteri for his practical help.

This study was carried out with the financial support of British Gas and the Engineering and Physical Science Research Council.

....and ta Chris!

Roger Thorpe

Chapter 1. Introduction

Thermally driven heat pumps and refrigerators

Thermally driven heat pumps offer some advantages over the conventional vapour compression refrigeration technology. Their principal attraction is a better use of primary fuel since the heat rejected by the work producing stage is available for heating at the point of use unlike an electrically driven cycle where this energy is rejected at the power station. A gas burning machine with a COP (Coefficient of Performance, in this case the ratio of heat output to the heat input) of 1.6 would use almost half as much fuel as a conventional gas boiler with a typical efficiency of 0.85 and provide a significant energy saving. As a refrigerator or air conditioner, adsorption machines should be able to approach and exceed the efficiency of the more conventional energy chain using electricity generation. The possibility of using waste or solar heat to drive such cycles is also very attractive.

Thermally driven heat pumps include engine driven devices, liquid absorption, solid adsorption and chemical cycles. Solid sorption (adsorption) may offer the possibility of higher COP than liquid sorption (absorption) since higher generating temperatures may be used. A disadvantage of adsorption systems, however is that the advantages of flow processes, specifically counterflow heat and mass transfer, steady state and continuous operation are not easily available. The development of systems that use thermal waves as described on page 6 should bring a process that is similar to counterflow heat exchange to adsorption and that is the context of this thesis.

Adsorption

The role of the adsorbent bed in an adsorption heat pump is the same as the compressor of a conventional heat pump, it must take the gas at low pressure from the evaporator and deliver it to the condenser at high pressure.

The essential characteristic of adsorption exploited in this type of machine is that a gas can be held on the surface of a solid adsorbent in a dense phase that resembles (but is not) a liquid and may be driven off by raising the temperature of the solid. This happens on an atomic scale, and on porous materials with a large surface area the molar concentration of adsorbate may be quite high. Typically active carbon may adsorb mass concentrations of ammonia up to 25%, 1litre of carbon granules weighing $^1/_2$kg at 30 °C and10 Bar can hold as much ammonia as a vessel of 16 litres with no carbon at the same conditions. The concentration of adsorbate in the adsorbent is a function of temperature and pressure; the closer the temperature and pressure at the adsorbent-gas interface is to saturation then the higher will be the concentration. In many cases the concentration can be represented by a simple function of the ratio of the absolute temperature (T) to the saturation temperature (T_{sat}). An expression that has been used successfully of this type is a modification of the Dubinin-Radushkevich equation:

$$x = x_0 \exp[-K(\frac{T}{T_{sat}} - 1)^n]$$

Where x_0, K, and n are constants derived by experiment and both T and T_{sat} are absolute temperatures.

Desirable characteristics of an adsorbent -adsorbate pair are:

- The adsorbate should have qualities of a good refrigerant such as, a high latent heat, chemical stability, a moderate saturation pressure at the operating temperature range, low toxicity and be environmentally benign.

- The adsorbent should have good physical and chemical stability, high conductivity and low heat capacity.
- The pair should show large concentration changes over the pressure and temperature range of operation.

An adsorption solar refrigerator.

One of the simplest adsorption devices is a basic solar refrigerator and the description of its operation may be useful to the reader who is unfamiliar with this cycle. A diagram of this type of machine is shown in figure (1.1). In this application the carbon bed is connected directly to the condenser and through that to a receiver and a flooded evaporator. The evaporator is surrounded by a water/ice bath in order to give the thermal storage required since cooling is intermittent.

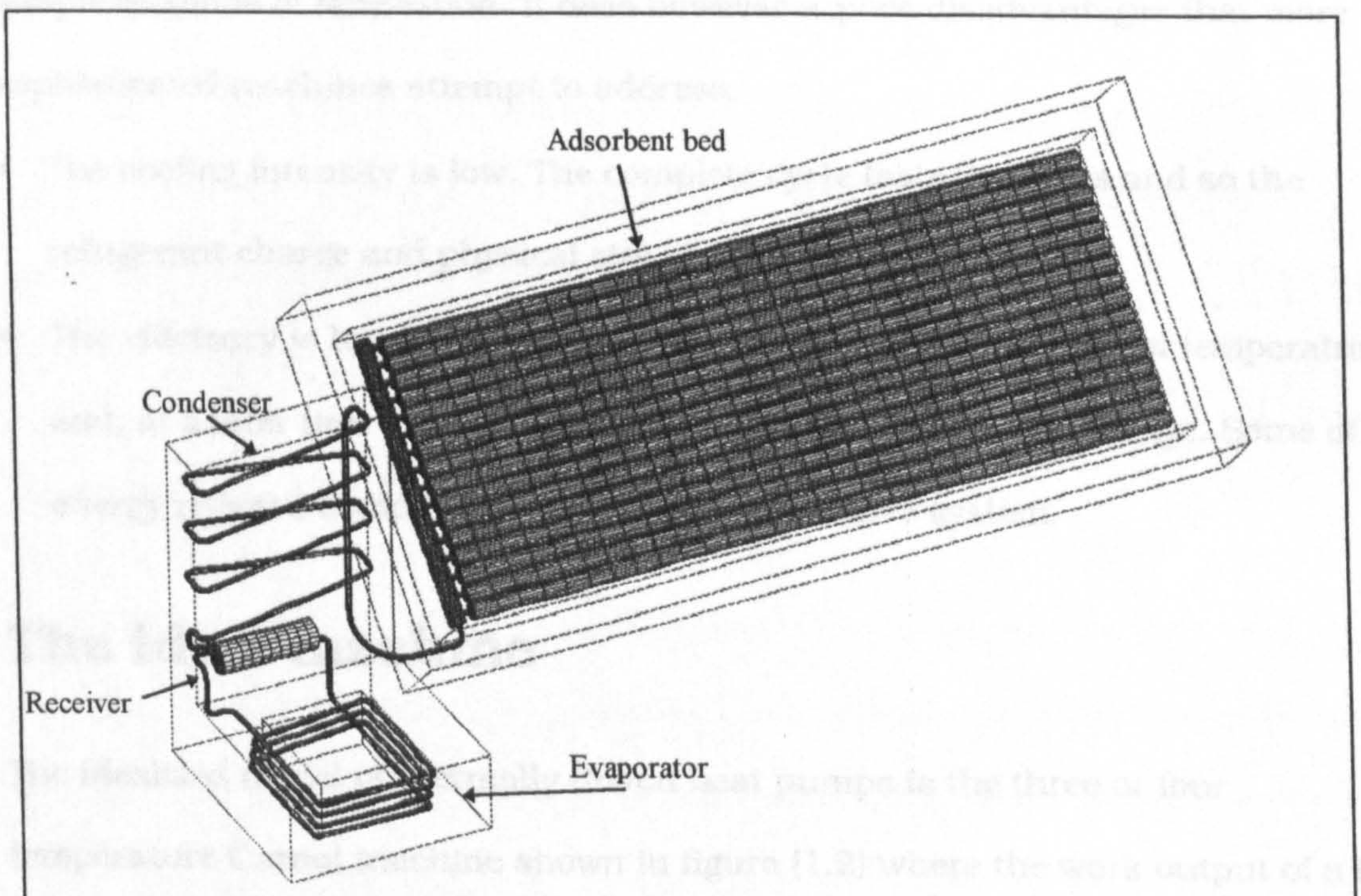

Figure 1.1 A solar refrigerator.

In the morning the bed of the refrigerator starts at the evaporating pressure and low temperature. As the sun heats the adsorbent so some small amount of ammonia is desorbed. Since the evaporator is flooded with liquid the desorbed gas will not condense and the pressure increases. When the pressure has reached the

saturation pressure of the condenser then the gas condenses there and collects in the receiver below. Thus the some of ammonia is driven out of the bed, the proportion desorbed being determined by the ratio of temperature of the bed and that of the condenser at the end of the heating phase.

In the evening the bed of adsorbent is allowed to cool towards the ambient temperature. As it does so it adsorbs more refrigerant, decreasing the pressure of the system until the liquid in the evaporator boils, first in the receiver, cooling its contents until they reach the temperature of the evaporator. and then later in the evaporator itself performing the useful cooling. The system is now ready for the next day's cycle.

The cycle so described has the advantage of simplicity and is very suitable for its purpose, the creation of a small, high value cold space with no moving parts and simple methods of fabrication. It does however expose disadvantages that more sophisticated machines attempt to address.

- The cooling intensity is low. The complete cycle lasts 24 hours and so the refrigerant charge and physical size of the machine is large.
- The efficiency is low. Heat is rejected by the bed across a range of temperatures and, at a later time accepted across a higher but overlapping range. Some of the energy rejected could be recycled by a regenerative system.

The ideal machine

The idealised model of thermally driven heat pumps is the three or four temperature Carnot machine shown in figure (1.2) where the work output of a heat engine drives a reversed heat engine. The three temperature machine is the special case where two heat rejection temperatures are identical. The Carnot COP of a

three temperature device is given by the combination of the two cycles thus:

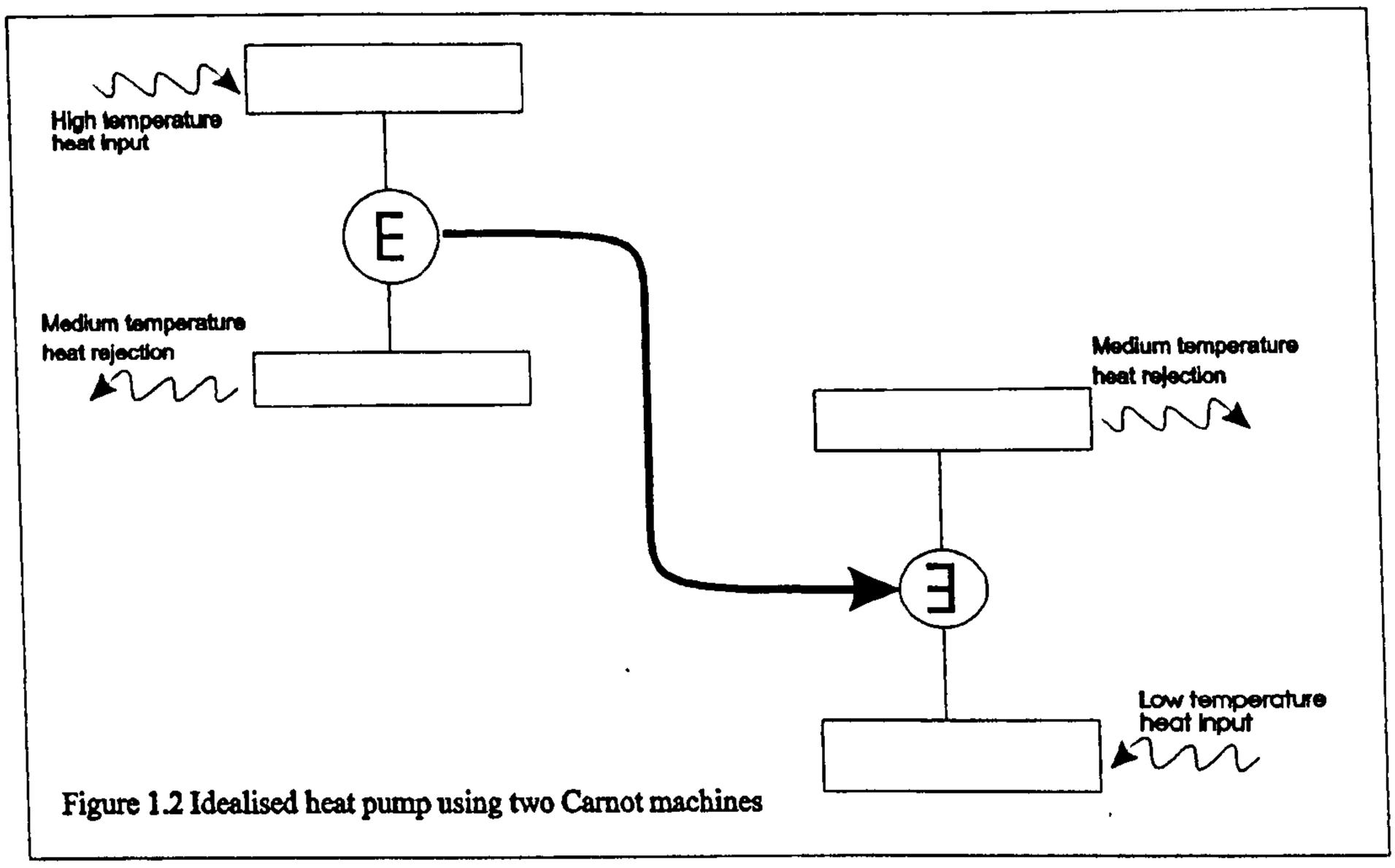

Figure 1.2 Idealised heat pump using two Carnot machines

$$COP_{H(carnot)} = \frac{T_m}{T_h} + \frac{T_h - T_m}{T_h}\frac{T_m}{T_m - T_l}, \qquad COP_{c(carnot)} = \frac{T_h - T_m}{T_h}\frac{T_l}{T_m - T_l}.$$

Real machines, of course cannot achieve these levels due to irreversibilities in the system and the fact that the transfer of heat into and out of the machine is distributed over a range of temperatures rather than the isothermal processes of the Carnot model.

Regeneration

As has been mentioned earlier, the efficiency of an adsorption heat pump may be significantly increased by the regeneration of the heat rejected by the bed during cooling. This may be achieved by the use of multiple beds or by thermal waves.

Multiple beds

In a simple two bed system the enthalpy of adsorption rejected by the bed being cooled is passed to that being heated by a heat transfer fluid until the temperatures of the two beds are nearly equal. This limitation is similar to that of a co-current heat exchanger. A better utilisation of the available energy can be realised if a

greater number of beds are employed with a network of valves allowing the heat transfer connection between beds to be switched so that the operation is similar to counterflow heat exchange between two streams of beds. Meunier[1] has shown the following relationship between number of beds and COP_c for the Zeolite-Water pair cooling at 0°C, condensing at 40 °C, rejecting heat at 50 °C, and using a heat source at 350°C.

Number of beds	COP_c
1	0.425
2	0.648
4	1.008
6	1.293
∞	1.852

Thermal waves

One of the principal inconveniences caused by the use of solid as opposed to liquid sorbents is the fact that they cannot easily be pumped around a system in the same way that a fluid can. This restriction means that the cycle must be a batch rather than steady state process and that direct counterflow heat exchangers cannot be used. Recent developments have lead to the use of so called thermal waves or temperature fronts in order to realise a process that is analogous to the counterflow heat exchanger.

If a fixed bed of material is heated by a fluid flowing slowly and uniformly along its length then a temperature front will propagate and move downstream in both the bed and the fluid. The bed and fluid at the exit of the bed being heated will be relatively cool, and this fluid may be used to cool another bed. The exit stream from the bed being cooled will be hot, and this fluid may be used to heat the first bed. When the beds have each been heated or cooled sufficiently then the flow of the heat transfer fluid may be reversed and the cycle started again with the bed that was being heated now being cooled and *vice versa*. With perfect heat transfer, constant heat capacities and no axial conduction and non-adsorbent beds this

process could carry on *ad infinitum* however in any real process a heater and cooler must be installed to maintain the temperature difference that would otherwise decay until both beds are uniformly lukewarm.

The thermal behaviour of adsorbent beds heated and cooled in this way as implemented in a heat pump cycle is more complex than that of simple non-adsorbent beds these are discussed in chapters 3 and 7 . Thermal waves are used by Shelton, Wepfer and Miles [2] in the Wave air concept and this is shown schematically in figure (1.3).

In order to maintain a reasonably steep thermal wave a high rate of heat transfer must be achieved with a relatively slow moving fluid. The factor that determines the decay of the wavefront ignoring conduction effects is the Number of Transfer Units (*NTU*) which may be expressed as

$$NTU = \frac{\alpha a l}{\dot{m} c_p}$$

where

a= Surface area per unit volume of heat exchanger (m^2/m^3)

α= Heat transfer coefficient (W/m^2K)

l =length of bed(m)

$\dot{m}$= Mass flow per unit cross section area of heat exchanger (kg/m^2s)

c_p= Heat capacity(J/kg K)

$\frac{a\,l}{\dot{m}}$ may be replaced by the total area divided by the actual flow through the exchanger.

In a packed bed the value a used as the area available for heat transfer may be subject to some ambiguity. The area of simple shapes may be easily calculated, but for irregular materials some approximation must be used. In chapter 5 a characteristic length and area dimension are calculated by assuming that the

particles are spherical. Although these are not the true values they allow some compatibility with the work of others.

It is shown in chapter 3 that *NTU* values of 20 or more must be achieved to give the effectiveness of 0.9 that Critoph [3] suggests is needed to achieve an adequate performance high . Although this may be done by conventional means, using a slowly moving heat transfer fluid and extended surfaces, the poor conductivity of the adsorbent and the high surface area needed require such machines to have a high metal content. The sensible heat of the heat exchangers must be carried and regenerated in the cycle and this reduces efficiency. Such devices also require sophisticated manufacturing techniques. An approach to the thermal wave cycle that attempts to solve these problems is the use of forced convection of the adsorbate itself.

Cycles using forced convection

Critoph [4] has proposed that a granular adsorbent bed may be heated and cooled by forced convection of the adsorbate through the bed. In this technique the adsorbent gas itself is working as the heat transfer fluid, passing sensible heat from

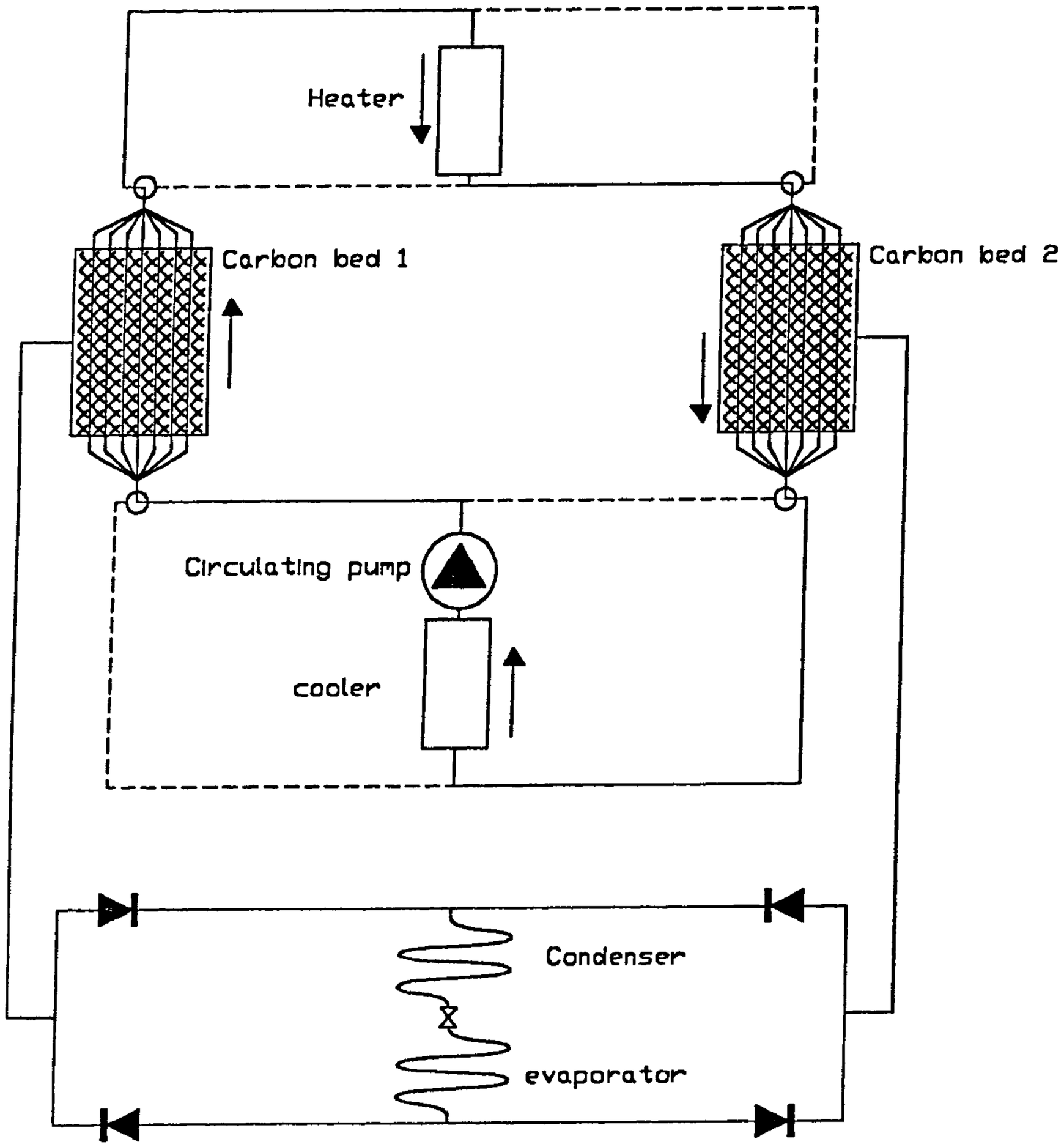

Figure 1.3 A scematic diagram of a solid sorption heat pump using a heat transfer fluid and themal waves.

Bed 1 is being cooled and adsorbing refrigerant from the evaporator. The heat rejected from bed 1 is used to heat bed 2 which is desorbing refrigerant to the condenser.

heat exchangers in the circuit to the adsorbent. This approach exploits the large surface area that is available for heat transfer in packed beds and the low bed conductivity to allow the generation of a thermal wave with a bed of simple construction. It is not possible to use the exit gas from one bed to cool or heat another directly since the beds are at different pressures but it is possible to use a gas to gas heat exchanger to create a regenerative machine. A circuit of this type is shown in figure (1.4). This arrangement uses two reversible pumps and four three-way valves to swap the beds between the heating and cooling circuit at the end of each cycle. A disadvantage of this system is that the gas to gas heat exchanger is an expensive and large component. Such a heat exchanger would have to stand frequent changes of pressure.

Critoph and Thorpe [5] have proposed a system that uses beds of an inert material to store the heat rejected by the bed during the cooling and supply it during the heating phase . A schematic diagram of one configuration for such a cycle is shown in figure (1.5). Although the resulting machine appears complex its construction and operation should be simple. It is possible to simplify this machine, even further as shown in figure(1.6). Although the number of heat exchangers is doubled the total heat transfer area need not be significantly increased since each now has two gas passes per cycle instead of one. If discontinuous cooling is acceptable then the machine may be simplified even further by the use of only one inert and one active bed.

The performance of heat pumps using thermal waves by forced convection will be a function of :

- The operating temperatures.
- The adsorption properties of the adsorbent and adsorbate pair.
- The thermodynamic properties of the refrigerant.
- The heat transfer properties of the adsorbent bed.
- The heat transfer properties of the inert bed.

- The properties of the heat exchangers.
- Thermal losses in the system.
- Parasitic power consumption in gas circulating pumps.
- Operational regime; the length of the heating and cooling period and rate of gas flow.

These systems cannot be evaluated by any steady state technique since all components experience varying conditions during the cycle. The strong couplings between components and nonlinear behaviour of some require that in order to arrive at a reasonable set of design choices sophisticated computer simulations must be carried out.

The purpose of this study is to assess the forced convective heat transfer in the beds, understand the thermal and mechanical behaviour of such beds and establish design tools to enable development of heat pumps using forced convection of the adsorbate.

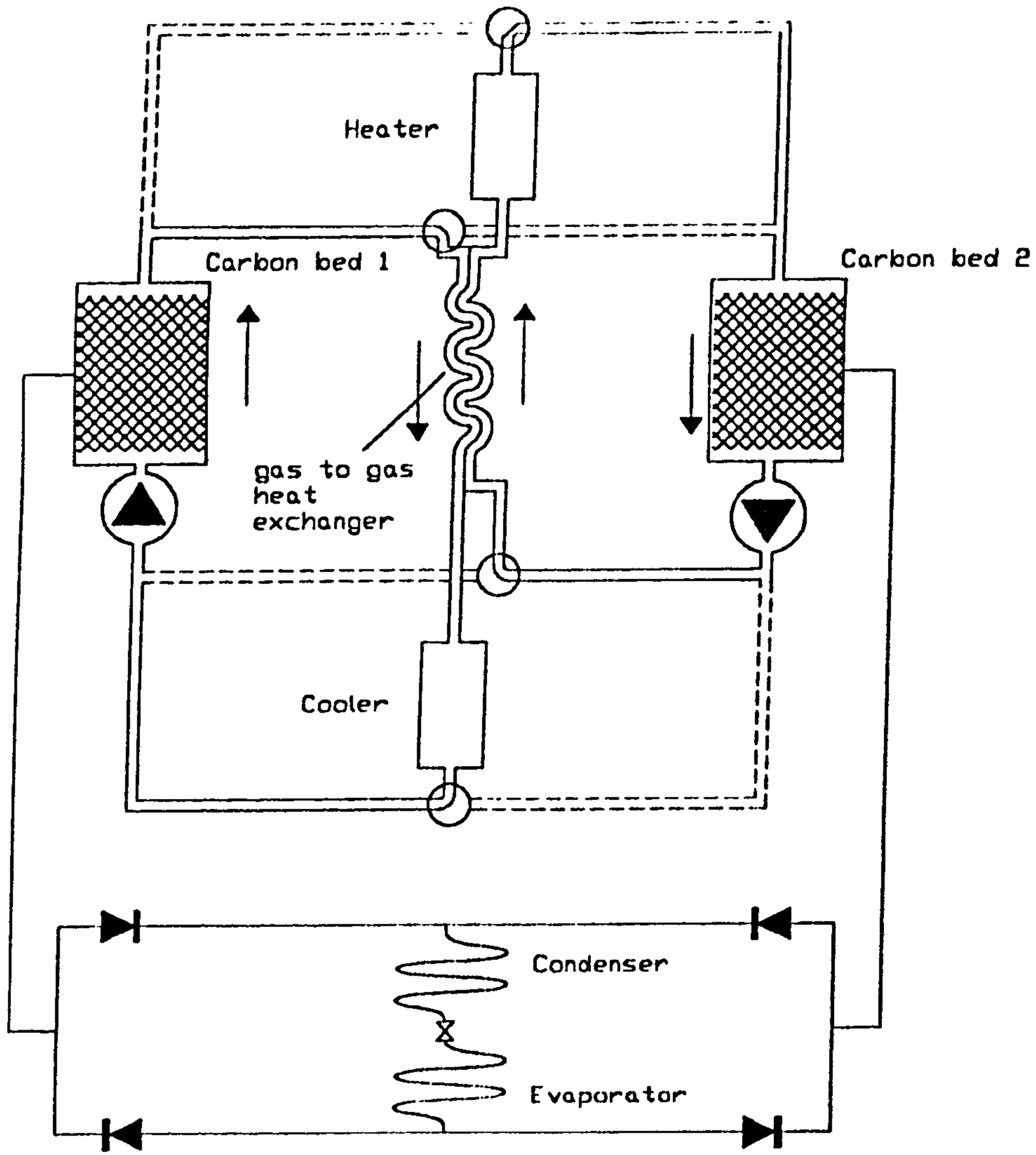

Figure 1.4 A scematic diagram of a solid sorption heat pump using forced convection of the sorbate and thermal waves.
Heat rejected from bed 1 is passed to bed 2 through The central gas to gas heat exchanger.

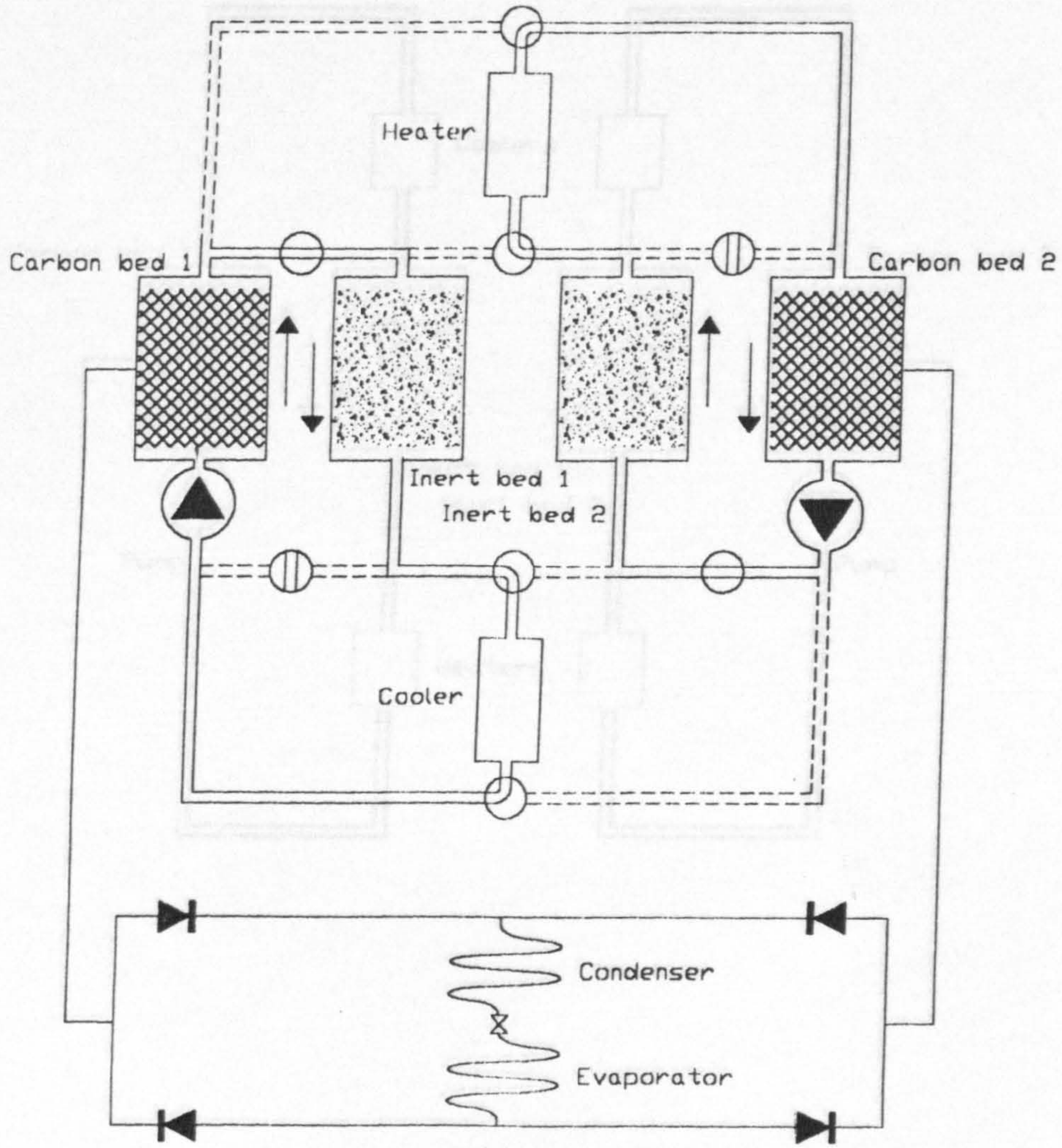

Figure 1.5 A schematic diagram of a solid sorption heat pump using forced convection of the sorbate and inert beds

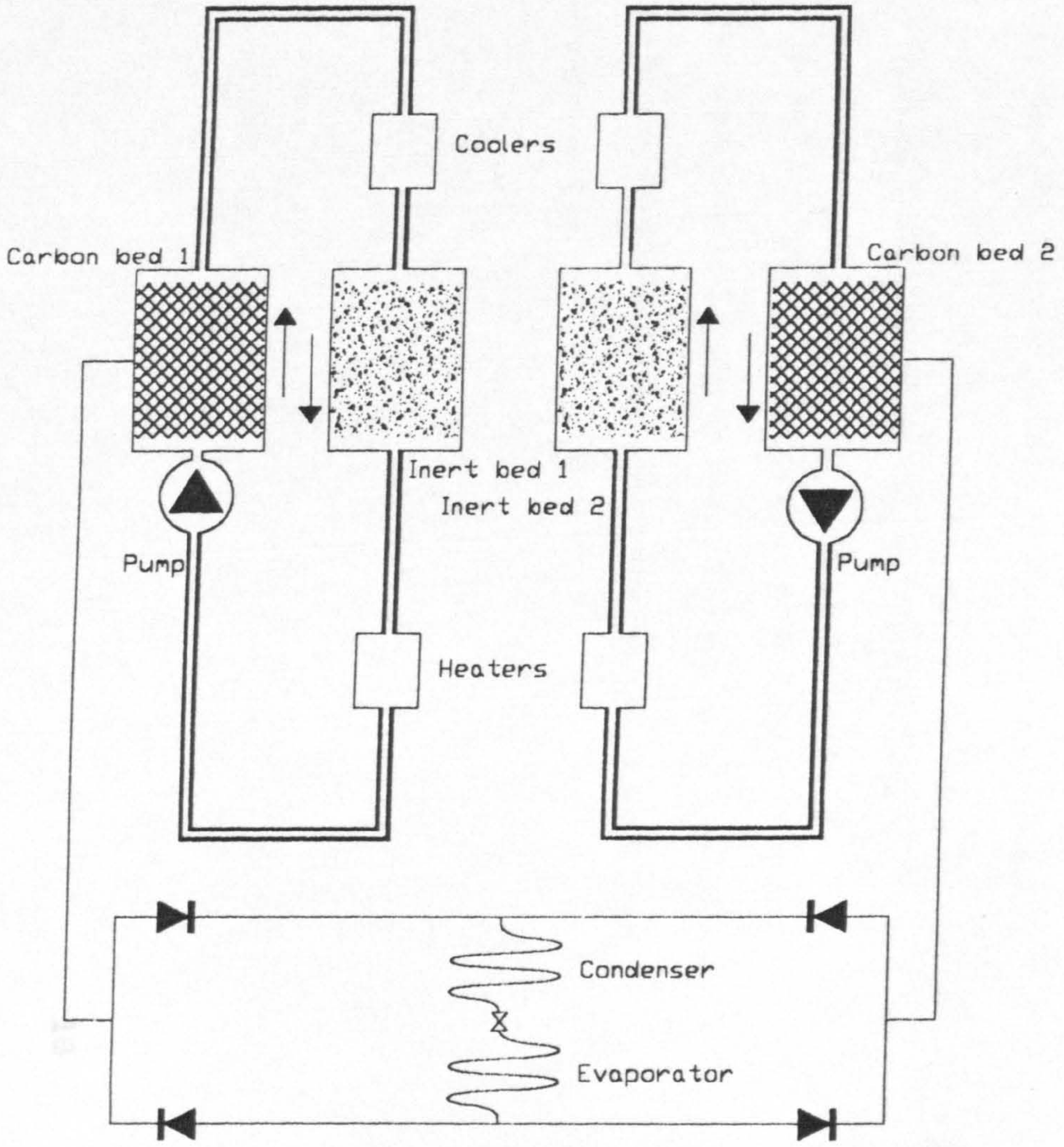

Figure 1.6 A schematic diagram of a solid sorption heat pump using forced convection of the sorbate and inert beds

This is a simplified version of that shown in figure 1.6 and uses continuously operating heates and no valves except check valves.

References

[1] **Meunier F.** Second law analysis of a solid adsorption heat pump operating on reversible cascade cycles *Heat Recovery Systems and CHP* **vol 5** pp133 (1985)

[2] **Shelton S.V. Wepfer W.J. Miles D.J.** Ramp wave analysis of the solid/vapour heat pump. *Journal of Energy Research and Technology* **vol 112**,3 pp69-78 (1990)

[3] **Critoph R.E.**,Performance estimation of convective thermal wave adsorption cycles, *Applied Thermal Engineering* **vol 16,5** pp429,437 (1996)

[4] **Critoph R.E** Forced convection enhancement of adsorption cycles, *Heat Recovery Systems and CHP* **vol 14,4** pp343-350 (1996)

[5] **Critoph R.E., Thorpe R.,** International Patent application *WO 96/09504* (1996)

Chapter 2. Adsorption

Physical description

When a solid is exposed to a gas or liquid there is an interaction between the two materials, the strength and type of this interaction depending on the species involved. This interaction may be a chemical reaction, chemisorption or a physical process, adsorption.

Chemical reactions typically involve an exchange of electrons and the loss of the identity of the original species. Chemisorption is characterised by the formation of surface compounds in stoichiometric ratio and the strong forces due to the interaction of electrons. In adsorption the force involved is the relatively weak van der Waals attraction which is also responsible for condensation. There is, therefore some similarity between adsorption and condensation, for instance the enthalpy of vapourisation is the same order of magnitude as the enthalpy of adsorption and there is usually little evidence of hysterisis in pure adsorption and desorption.

Pressure, temperature and concentration

The most commonly used mathematical relationship used to relate pressure, temperature and concentration is that developed by Dubinin and Radushkevich [1]. This is based upon an understanding of the adsorption process as a filling of micropores and is expressed as

$$V = V_o \exp\left[- D\left(RT \ln \frac{P}{P_{sat}} \right)^n \right] \qquad (2.1)$$

where

V = micropore volume filled by adsorbate.

V_0 = Maximum micropore volume available .

D = Constant.

$n = 2$

T = Absolute temperature (K).

R =Gas constant (J kg^{-1} K^{-1}).

P = Pressure (Pa).

P_{sat}=Saturation pressure at the solid temperature (Pa).

The general form of this equation is derived from theoretical considerations but the constants are usually determined empirically.

Making the assumption that the volume of the adsorbate does not change significantly with pressure or temperature and using the substitution

$$\ln P = A - \frac{C}{T} \quad \text{and} \quad \ln P_{sat} = A - \frac{C}{T_{sat}}$$

where A and C are constants particular to the gas phase, and changes in the adsorbate density are neglected then the Dubinin Radushkevic equation (2.1) may be expressed as

$$x = x_0 \exp\left[- k\left(\frac{T}{T_{sat}} - 1\right)^n \right] \qquad (2.2)$$

where

x_0 = maximum concentration (mass fraction)

x = concentration

k= constant

n=2

In practice n may be given values other than 2 and this is the form of the equation known as the Dubinin-Ashtakov (D-A) equation. The form of this expression gives

some evidence for the link between adsorption and condensation. The value $\frac{T}{T_{sat}}-1$ may be regarded as a dimensionless measure of superheat.

The D-A equation (2.2) has the following properties:

- The maximum rate of change of concentration at constant pressure occurs when

$$\frac{T}{T_{sat}}-1=\left(\frac{kn}{n-1}\right)^{-\frac{1}{n}}$$

- The value of the maximum rate of change of concentration with dimensionless superheat is given by $\frac{dx}{d\tau}=-k\,n\left(\frac{kn}{n-1}\right)^{\frac{n-1}{n}}x_0\exp\left(\frac{n-1}{n}\right)$

- The maximum concentration of adsorbate is x_0 and occurs when $T=T_{sat}$.

- At $\frac{T}{T_{sat}}-1=\infty$, $x=0$.

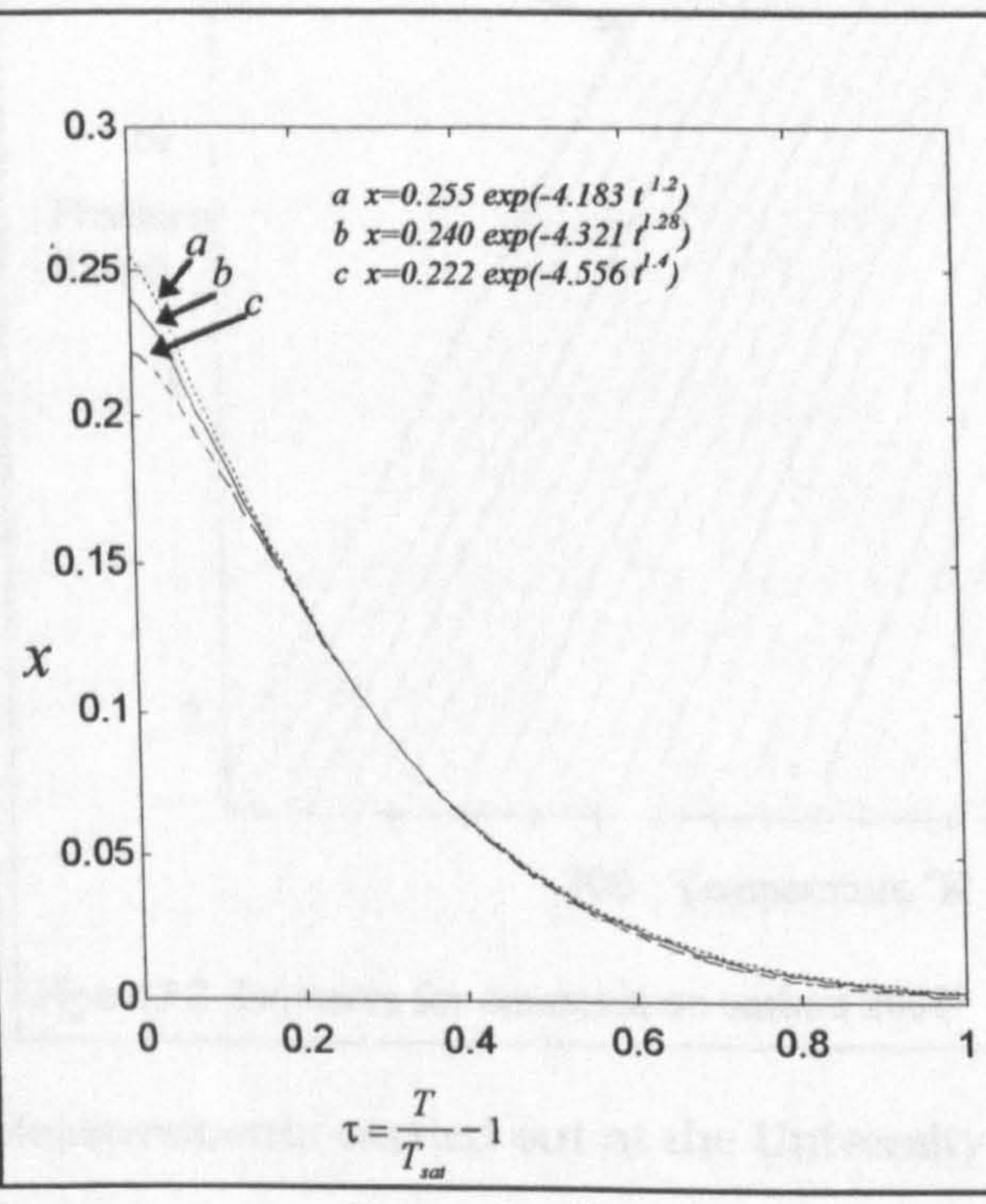

Figure 2.1 .concentration plots for various x_o, k and n selected to give identical concentration and rate of change of concentration at $\tau=0.3$

The factor x_o determines the maximum concentration while k determines the horizontal scale, a low value implying more adsorption at high superheat. It should

be remembered that all these factors work together and that plots using different values of x_0, k and n can produce very similar plots as demonstrated in figure 2.1. The curves of figure 2.1 are typical for ammonia and carbon 208C.

It can be understood from the form of equation (2.2) that a plot of T against T_{sat} or $\frac{1}{T}$ aginst $\frac{1}{T_{sat}}$ for constant concentration, an isostere, will give a straight line.

Since $\ln P \approx A + \frac{C}{T_{sat}}$, then plot of $\ln P$ against $-\frac{1}{T}$ will also give a graph where isosteres are very nearly straight as shown in figure 2.2 which plots the data for ammonia on Sutcliffe-Speakeman 208C carbon.

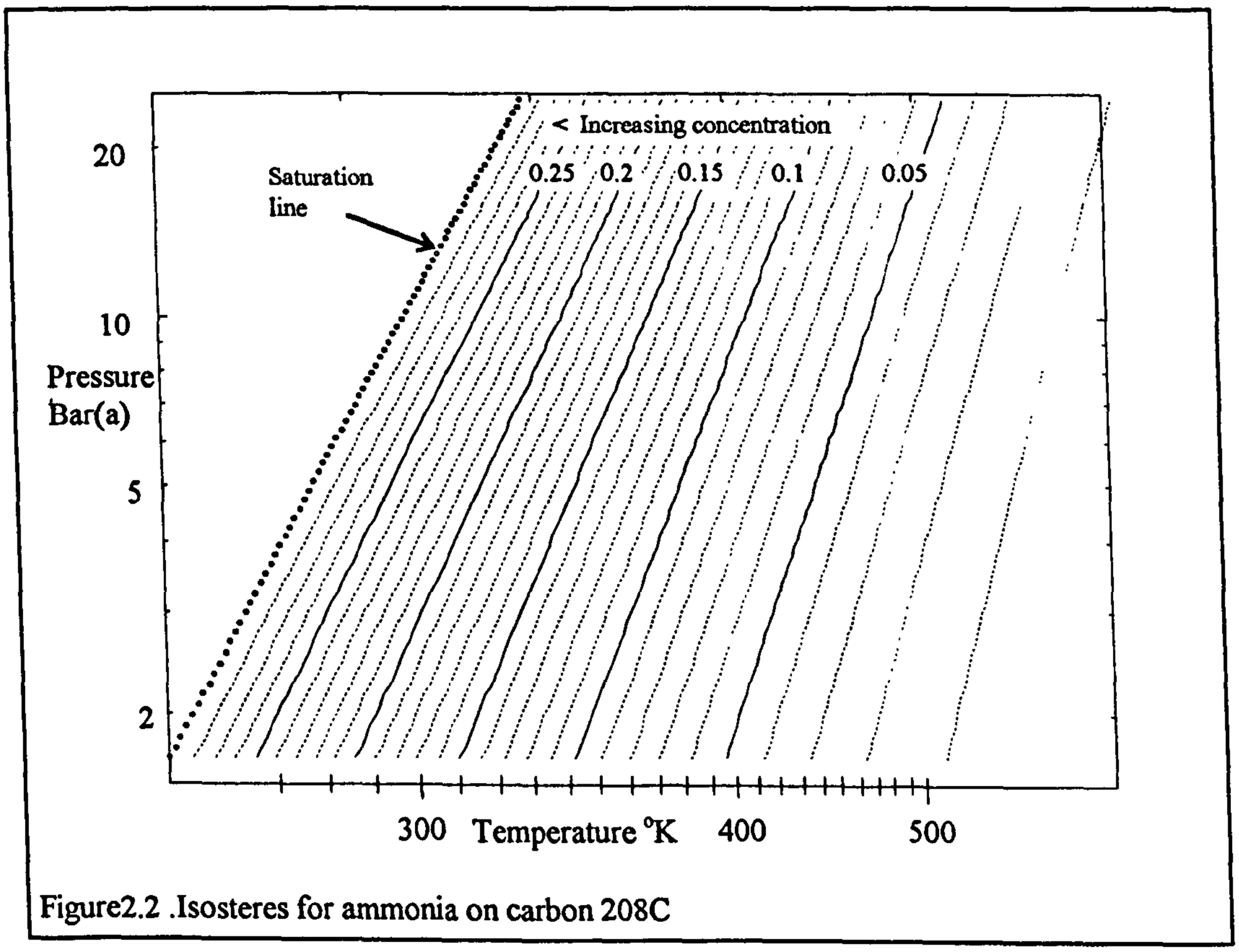

Figure2.2 .Isosteres for ammonia on carbon 208C

Measurements carried out at the University of Warwick by Turner [2] and Critoph [3] have lead to the recommendation of the following values for Sutcliffe-Speakeman 208C carbon and ammonia.

x_0 = 0.2901

k =3.1853

n =1.0957

This expression may be considered valid within the pressure range 1bar < P < 25bar,

and tempeature range 30°C < T < 250°C.

Argon is considered inert and only adsorbable in small amounts. It is used in this study to measure the heat transfer in the absence of strong adsorption.

A short series of experiments gave the following results for the adsorption of argon on 208C.

x_0 = 0.06727

k = 0.0253

n = 5

These figures can only be considered appropriate for pressures up to 16 Bar and to the temperature range 29°C to 90°C. They show a concentration range from approximately zero at atmospheric pressure to 5% at 302K and 8.71 Bar

Enthalpy of adsorption

The enthalpy of adsorption is an important factor in the analysis and performance of a sorption heat pump.

If the adsorbed and gaseous phases of a gas are in equilibrium then the Gibbs free energy of those phases must be equal. The Gibbs free energy is defined as

$$g = h - Ts \tag{2.3}$$

and for a change in temperature and pressure then

$$dg = du + Pdv + vdP - Tds - sdT .$$

From the first and second laws of thermodynamics we know that

$$q = du + Pdv = Tds$$

therefore equation (2.3) becomes

$$d\mathrm{g} = vdP - sdT\,. \qquad (2.4)$$

If both the temperature and pressure of the solid-gas interface change in such a way that the concentration remains constant then the changes in the Gibbs energy of each phase will be identical,

$$d\mathrm{g}_g = d\mathrm{g}_a\,.$$

Therefore

$$v_g dP - s_g dT = v_a dP - s_a dT \qquad (2.5)$$

where the subscripts g and a refer to gas and adsorbed phases respectively.

Rearranging equation (2.5) gives

$$\left.\frac{dP}{dT}\right|_x = \frac{s_g - s_a}{v_g - v_a} \qquad (2.6)$$

The enthalpy of desorption h_{ag} is defined by

$$h_{ag} \equiv h_g - h_a = T\left(s_g - s_a\right)$$

making the assumption that $v_a << v_g$ and making the substitution $v_g = \frac{RT}{P}$ and

rarranging (2.5) gives

$$h_{ag} = \left.\frac{dP}{dT}\right|_x \frac{RT^2}{P}\,. \qquad (2.6)$$

If the concentration is constant then, from the Dubinin-Ashtikov equation, $\frac{T}{T_{sat}}$ is

also constant and so

$$\left.\frac{\partial T_{sat}}{\partial T}\right|_x = \frac{T_{sat}}{T} \quad \text{and therefore}$$

$$\left.\frac{\partial P}{\partial T}\right|_x = \frac{dP}{dT_{sat}}\frac{T_{sat}}{T}\,.$$

substituting this into equation (2.6) gives

$$h_{ag} = \frac{dP}{dT_{sat}} \frac{RTT_{sat}}{P}.$$

where R is defined as the value of $\frac{PV}{T}$ at the temperature and pressure under consideration.

This enables a simple calculation of h_{ag} since $\frac{dP}{dT_{sat}}$ is well known for most gases.

Using a similar approach to find the enthalpy of evaporation h_{fg} yields

$$h_{fg} = \frac{dP}{dT_{sat}} \frac{RT_{sat}^2}{P}. \qquad (2.7)$$

Finally the enthalpy of adsorption may be expressed as a function of h_{fg}, T_{sat} and T in the widely used relation derived from equations (2.6),(2.7)

$$h_{ag} = \frac{T}{T_{sat}} h_{fg}. \qquad (2.8)$$

Making the further assumption that h_{fg} is a constant then equation (2.8) can be rearranged to give

$$\frac{d(\ln P)}{d(1/T_{sat})} = -\frac{h_{fg}}{R} \approx \text{constant}$$

$$\left.\frac{d(\ln P)}{d(1/T)}\right|_x = -\frac{h_{ag}}{R}$$

Hence the gradients of the isosteres on a plot of $\ln P$ against $-\frac{1}{T}$ are proportional to h_{ag}.

References

[1] **Dubinin M.M., Radushkevich L.V.** Equation of the caracteristic curve of activated charcoal. *Doklady Akad Nauk S.S.S.R.* **Vol 55** pp327,398 (1947)

[2] **Turner L.,** Improvement of activated charcoal ammonia adsorption heat pumping/refrigeration cycles. *PhD Thesis. University of Warwick* (1992)

[3] **Critoph R E.,** An evaluation of alternative refrigerant-adsorbate pairs for refrigeration cycles, *Applied Thermal Engineering* , **Vol 16** no 11 pp891-900 (1996)

Chapter 3. Regenerators

Introduction

The implementation of a fixed carbon bed considered in this study has many characteristics that are similar to conventional thermal regenerators, sometimes called periodic flow heat exchangers. Some terms and techniques developed for regenerator analysis are useful aids to the understanding of the operation of the bed. These will be developed in this chapter.

Thermal regenerators have been used for many years in the steelmaking industries and have been the subject of some interest from mathematicians [1,2,3]. A regenerator consists of a stack or bed of solid particles through which a fluid (usually a gas) is passed. Operation is periodic and in the first phase hot gas is circulated through the bed transferring its heat to the solid material. In the second phase the gas to be heated is circulated through the bed and is heated by the solid. During the heating or cooling process a temperature front or `thermal wave' advances through the bed. The steepness of this front will usually decrease as it progresses because of the finite heat transfer coefficient. Regenerators are widely used in the steelmaking industries where they may be referred to as Cowper stoves. In this application they are very large, typically tens of meters in height with a matrix composed of ceramic bricks. At the other end of the size scale regenerators are an important component of the Stirling engine.

Definitions and assumptions of the model

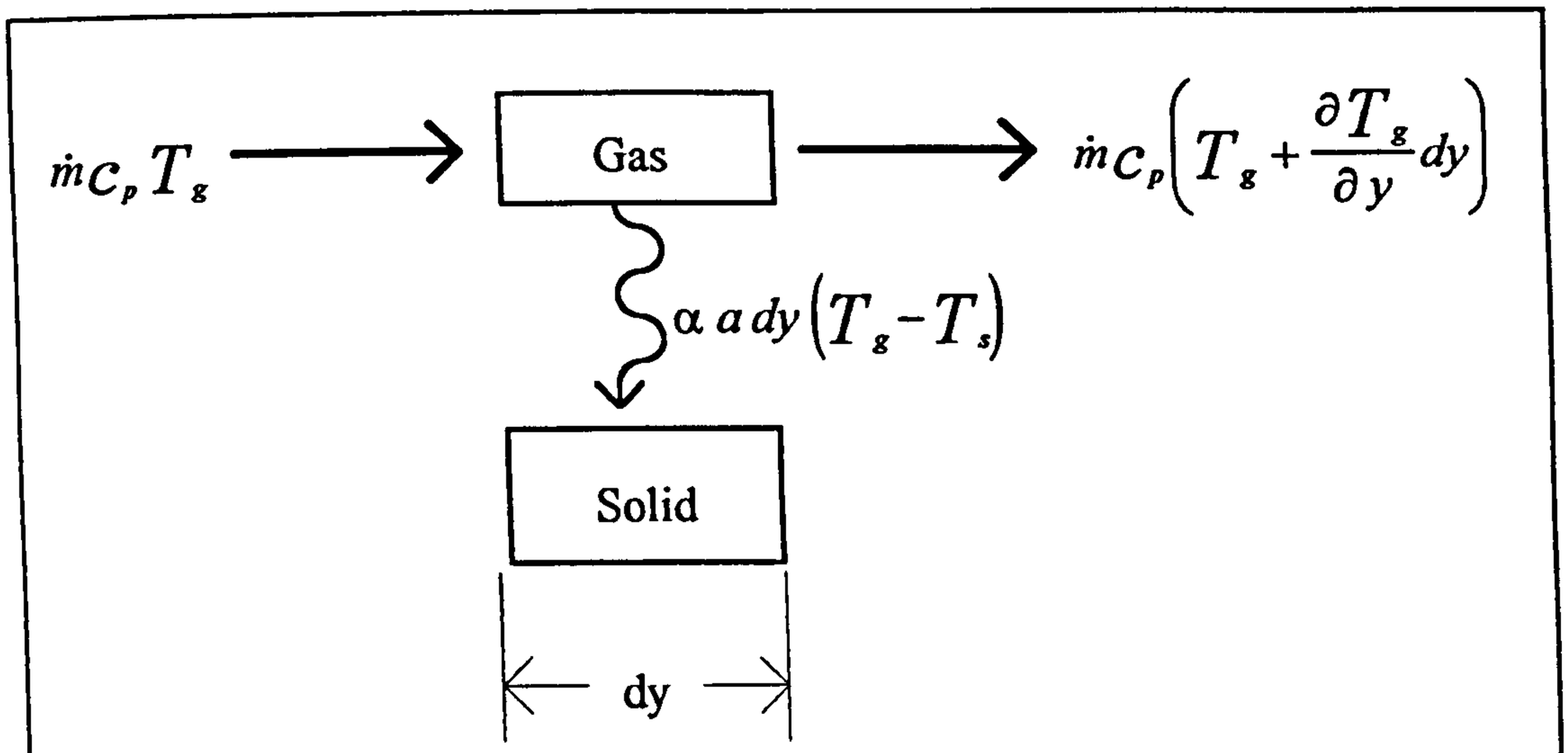

Figure 3.1 Energy flows in a regenerator control volume.

Figure 3.1 shows a control volume for a bed of unit cross section. The bed may take any prismatic shape although that of a cylinder is most common. In this work *axial* will describe the direction parallel to the gross fluid flow and *radial* will describe any direction normal to that. The following nomenclature is used:

a Total surface area of the solid per unit bulk volume. (m^{-1})

c Specific Heat capacity of the matrix. (J/kg.K)

c_p Specific heat capacity of the fluid phase at constant pressure. (J/kg.K)

c_v Specific heat capacity of fluid at constant volume. (J/kg.K)

D_{ax} Axial dispersion coefficient.(m^2/s)

L Length of the bed. (m)

$\dot{m}$ Mass of fluid flowing through a unit cross section of bed per second. ($kg/m^2.s$)

m Bulk density of the matrix. (kg/m^3)

P Period for one blow or half cycle. (s)

T_g, T_s Gas and solid temperatures, respectively (°C or K)

v Fluid velocity in the voids of the bed (m/s)

y Axial position along the bed in the direction of flow (m)

α Heat transfer coefficient (W/m^2K)

ψ Void ratio, [void volume / bulk volume] (Dimensionless)

ρ Density of the fluid phase (kg/m^3)

The analysis of the regenerator is greatly simplified by the use of the following assumptions.

1. The radial conductivity within each particle (intra-grain conductivity) is infinite.

2. The conductivity between grains (inter-particle conductivity) is zero

3. The axial and radial dispersal of the gas flow is zero (plug flow).

4. The matrix is homogeneous and gas flow is constant throughout the bed.

5. There is no conduction of heat to or from the walls of the vessel.

6. The thermal properties of the gas and solid are constant with temperature.

7. The thermal mass of the gas resident in the bed at the start of a cycle can be neglected.

These are the conditions of the model used by Schumann [4] and form the basis of studies by most workers since.

Of these assumptions the first may be justified where the Biot number is small. In this context 'small' means less than 0.1 and the Biot number is defined as:

$Bi = \frac{\alpha r}{\lambda_s}$. where r, is the grain radius and λ_s the solid conductivity. In those cases where the solid material is in the form of a set of parallel walls then r is defined as the semi-thickness of a wall.

The second assumption (of low inter-particle conductivity) is fulfilled by most conditions where the matrix consists of granular material because of the high thermal resistance at the point contact between grains.

The third assumption, that of plug flow, is not strictly valid in most practical applications but may be compensated by the use of a modified heat transfer coefficient as discussed later in this chapter.

The remainder of the points are self evident, although it should be pointed out that the neglect of the gas resident in the regenerator at the start of the cycle and at each reversal is not valid when the period is very short [5], for instance in some Stirling engine applications where the 'flushing ratio' ($\dot{m} P / \psi \rho L$) may be small, sometimes less than unity [6].

Mathematical description

The energy transferred from the solid to the gas $\dot{q}$ at position y, per unit volume of the bed is given by:

$$\dot{q} = \alpha\, a\, \left(T_s - T_g\right)$$

An energy balance on the gas and solid gives

$$\dot{m}\, c_p \frac{\partial T_g}{\partial y} + \psi \rho\, c_v \frac{\partial T_g}{\partial t} \;=\; -\, m\, c \frac{\partial T_s}{\partial t} \;=\; \alpha\, a \left(T_s - T_g\right) \qquad (3.1)$$

where Ψ is the void fraction of the bed. The interstitial velocity of the gas is given by

$v = \dfrac{\dot{m}}{\psi \rho}$, so the energy balance equation may be written

$$\frac{\dot{m}\, c_p}{\alpha\, a}\left(\frac{\partial T_g}{\partial y} + \frac{c_v}{v\, c_p}\frac{\partial T_g}{\partial t}\right) = \frac{-\, m\, c}{\alpha\, a}\frac{\partial T_s}{\partial t} = \left(T_s - T_g\right)$$

Dimensionless parameters

The time and length variables are substituted by dimensionless parameters [1] , η, ξ, chosen so that:

$$\frac{\partial T_s}{\partial \eta} = \left(T_g - T_s\right), \qquad (3.2)$$

$$\frac{\partial T_g}{\partial \xi} = \left(T_s - T_g\right). \qquad (3.3)$$

The energy equation (3.1) may be rewritten as:

$$\left(\frac{\partial T_s}{\partial \eta}\frac{\partial \eta}{\partial t} + \frac{\partial T_s}{\partial \xi}\frac{\partial \xi}{\partial t}\right)\frac{mc}{\alpha a} = \left(T_g - T_s\right),$$

$$\left(\frac{\partial T_g}{\partial \xi}\frac{\partial \xi}{\partial x} + \frac{\partial T_g}{\partial \eta}\frac{\partial \eta}{\partial x}\right)\frac{\dot{m}c_p}{\alpha a} + \left(\frac{\partial T_g}{\partial \xi}\frac{\partial \xi}{\partial t} + \frac{\partial T_g}{\partial \eta}\frac{\partial \eta}{\partial t}\right)\frac{\dot{m}c_v}{\alpha a v} = \left(T_s - T_g\right)$$

to satisfy these conditions then

$$\frac{\partial \xi}{\partial y} = \frac{\alpha a}{\dot{m} c_p}, \qquad \frac{\partial \xi}{\partial t} = 0, \qquad \frac{\partial \eta}{\partial t} = \frac{\alpha a}{mc}, \qquad \text{and } \frac{\dot{m} c_p}{\alpha a}\frac{\partial \eta}{\partial y} + \frac{\dot{m} c_v}{\alpha a v}\frac{\partial \eta}{\partial t} = 0$$

so

$$\frac{\partial \eta}{\partial y} = -\frac{\alpha a}{mc}\frac{c_v}{c_p v}$$

hence

$$\xi = \frac{\alpha a y}{\dot{m} c_p}, \tag{3.4}$$

$$\eta = \frac{\alpha a}{mc}\left(t - \frac{c_v}{c_p}\frac{y}{v}\right) \tag{3.5}$$

The quantity η represents dimensionless time and ξ represents dimensionless distance. In practice it is convenient to neglect $\frac{y}{v}$ in the expression for η. In effect this quantity represents the time taken for the slug of gas to reach the point y along the bed from the entrance and is normally much smaller than the cycle time. Thus

$$\eta \approx \frac{\alpha a t}{mc}.$$

The temperatures may be made dimensionless, where the inlet temperature in the hot and cold periods (T_{hot}, T_{cold}) are constant, by using:

$$\theta = \frac{T - T_{cold}}{T_{hot} - T_{cold}}$$

The values of θ_s and θ_g thus have values that lie in the range 0 to 1 where the inlet temperature in the hot period is 1 and that in the cold period is 0.

In wholly nondimensional terms the governing partial differential equations are:

$$\frac{\partial \theta_s}{\partial \eta} = (\theta_g - \theta_s) \tag{3.6}$$

$$\frac{\partial \theta_g}{\partial \xi} = (\theta_s - \theta_g) \tag{3.7}$$

The principle of dimensional similarity may be applied to regenerators if the effects of nonlinearity can be neglected and when mass flow, heat transfer coefficients and heat capacities are constant, or nearly so with time and temperature. In this case the dimensionless length of the bed is given by

$$\Lambda = \frac{\alpha\, a\, L}{\dot{m}\, Cp} \tag{3.8}$$

This parameter is a very useful measure of merit in the design of conventional regenerators and even nonlinear devices such as the carbon beds that are the object of this study. It can be seen that it is identical to the NTU value used in conventional heat exchangers.

The dimensionless period of the bed is

$$\Pi = \frac{\alpha\, aP}{m\, c} \tag{3.9}$$

where P is the total time for one part of the cycle, the hot blow or the cold blow in seconds.

It should be noted that Kays and London [7] use a value of NTU that gives similarity to the counterflow heat exchanger when Π/Λ is very short.

He defines NTU as:

$$NTU = \left(\frac{1}{\left(\frac{\dot{m} c_p}{\alpha a L}\right)_{hot} + \left(\frac{\dot{m} c_p}{\alpha a L}\right)_{cold}} \right).$$

If Λ is the same in the hot as the cold period then this value of NTU = $\Lambda/2$.

In the balanced regenerator the two periods are identical but where they are different then the cold period is identified by a prime (e.g. Π') . Where the flowrates in the hot and cold periods are not the same then Λ will also have a different value and be identified by a prime.

Finite grain conductivity

The effect of a finite intra-grain conductivity may be allowed for by the use of a modified heat transfer coefficient as developed by Hausen [1]. This is similar to the use of a "lumped parameter" approach.

Consider the temperature profile in a spherical grain of thermal conductivity λ_s and radius R connected to an environment of constantly increasing temperature T_∞ through a heat transfer coefficient at its surface of α.

after some time the temperature gradient in the grain has become constant and the grain is increasing in temperature at the same rate as the environment. At this stage the heat flux into the grain is given by

$$\frac{\dot{Q}}{4\pi R^2} = \left(T_\infty - T_{surf}\right)\alpha$$

where T_{surf} is the temperature at the surface.

The flow of heat through a spherical grain is radial and through the surface of a concentric sperical volume within the grain of radius r the heat flux per unit area is given by

$$\dot{q}(r) = \dot{Q}\frac{r}{4\pi R^3}$$

and the temperature gradient at r by

$$\frac{dT_s}{dr} = -Q\frac{r}{4\pi R^3 \lambda_s}.$$

this can be integrated with the boundary condition that $T=T_{surf}$ at $r=R$ to give an expression for the temperature at r

$$T = T_{surf} + \frac{\dot{Q}}{8\pi R\lambda_s} - \frac{\dot{Q}r^2}{8\pi R^3\lambda_s}$$

This in turn gives the volumetric average temperature

$$\overline{T} = \frac{1}{4/3\,\pi R^3}\int_{r=0}^{r=R} 4\pi r^2 T\,dr \quad = \quad T_{surf} - \frac{\dot{Q}}{20\pi\lambda_s}$$

so the heat flux into the grain is given by

$$\frac{\dot{Q}}{4\pi R^2} = \left(T_{surf} - \overline{T}\right)\frac{5\lambda_s}{R}$$

finally this yields an expression giving the heat flux in terms of the average grain temperature and the free stream gas temperature with a modified heat transfer coefficient

$$\frac{\dot{Q}}{4\pi R^2} = \left(T_\infty - \overline{T}\right)\alpha'$$

where

$$\frac{1}{\alpha'} = \frac{1}{\alpha} + \frac{R}{5\lambda_s} \qquad (3.10)$$

$$\text{or} \quad \alpha' = \frac{\alpha}{1 + \frac{Bi}{5}}$$

Although this modified heat transfer coefficient has been calculated assuming a constant temperature rise with time it has provided a good match to models that

include intra-particle conduction explicitly. Handley and Heggs [8] recommend that for transient experiments then the times for the temperature at the outlet to reach Θ_s =0.2 and 0.8 vary by less than around 1% if the dimensionless quantity

$$\frac{a\lambda_s L}{\dot{m} c_p d} \geq 60 .$$

Numerical solutions to the Schumann model

The partial differential equations that describe the regenerator do not lend themselves to a simple analytical solution but may be solved readily by numerical methods. Modern computers have made this process much more easy in the past twenty years.

The solid and gas temperatures are functions of space and time $\theta=\theta(\xi,\eta)$.

The boundary conditions for the regenerator for the first blow (assuming that this is hot) are simply

$\theta_g(0,\eta)=1$ (inlet gas temperature =1)

$\theta_s(\xi,0)=0$ (Initial solid temperature=0)

For most applications it is the condition of dynamic equilibrium that is reached after many cycles that is of interest and for the case where $\Pi = \Pi'$, that is to say the balanced regenerator, then the boundary conditions may be taken as

$\theta_g(0,\eta)=1$

$\theta_s(\xi,0) = 1-\theta_s(\Lambda-\xi,\Pi)$

since in the balanced regenerator the temperature distribution at the end of the hot period is that at the beginning of the cold period and symmetry dictates that this be identical with that at the beginning of the hot period reversed in space and inverted in the temperature dimension.

There are two classes of solution method, 'closed' and 'open'. In the closed methods the conditions of dynamic equilibrium are reached directly [12] but the methods become complex and are not easily applied to the nonlinear case. Open methods cycle the model to reach the equilibrium state. Although this method uses more computing time it has the advantage of simplicity and may be more easily incorporated in the simulation of more complex systems where mass flow and heat capacity are not constant as are the object of this study. In most cases ten cycles will bring the model close to equilibrium although where Π/Λ is small then more will be needed.

The Willmott method

Willmott devised a finite difference scheme which has proved to be adaptable and robust [13]

A grid of space and time (r, s) is created as shown in figure 2.2 . The partial differential equations are solved using the trapezium rule. The temperatures are calculated by integrating along the bed in the direction of the gas flow for each time step in turn. The governing finite difference equations are :

$$\theta_s(r,s) = \theta_s(r,s-1) + \frac{A}{2}\left(\theta_g(r,s) - \theta_s(r,s) + \theta_g(r,s-1) - \theta_s(r,s-1)\right) \qquad (3.11)$$

$$\theta_g(r,s) = \theta_g(r-1,s) + \frac{B}{2}\left(\theta_s(r,s) - \theta_g(r,s) + \theta_s(r-1,s) - \theta_g(r-1,s)\right) \qquad (3.12)$$

where

$$B = \Delta\xi \quad = \frac{\alpha\, a}{\dot{m}\, Cp}\Delta y \qquad (3.13)$$

$$A = \Delta\eta \quad = \frac{\alpha\, a}{m\, c}\Delta t \tag{3.14}$$

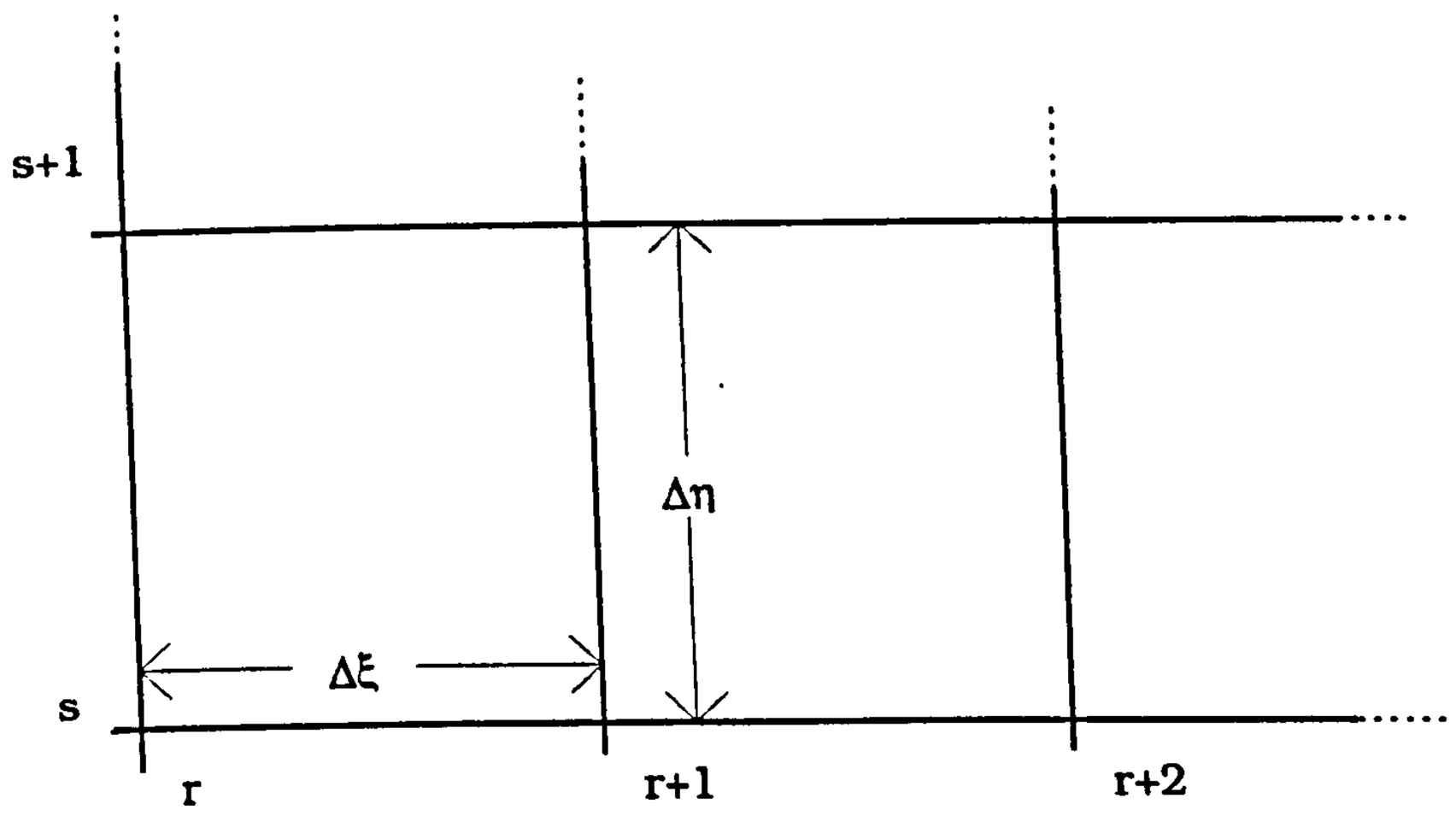

Figure 3.2 The finite difference grid

The solid temperatures at time s=1 are the known or supposed initial conditions.

The gas temperatures are calculated from the known inlet temperature by:

$$\theta_g(r,1) = \frac{2-B}{2+B}\theta_g(r-1,1) \;+\; \frac{B}{2+B}\theta_s(r,1) \;+\; \frac{B}{2+B}\theta_s(r-1,1) \tag{3.15}$$

The solid inlet temperature at the next timestep is found from:

$$\theta_s(1,s) = \frac{2-A}{2+A}\theta_s(1,s-1) \;+\; \frac{A}{2+A}\theta_g(1,s) \;+\; \frac{A}{2+A}\theta_g(1,s-1) \tag{3.16}$$

Thereafter, for each new timestep the temperatures of the solid are calculated moving stepwise along the bed from

$$\theta_s(r,s) = \frac{\left(\frac{2-A}{2+A}\theta_s(r,s-1) \;+\; \frac{A}{2+A}\theta_g(r,s-1) \;+\; \frac{A}{2+A}\frac{B}{2+B}\theta_s(r-1,s) \;+\; \frac{A}{2+A}\frac{2-B}{2+B}\theta_g(r-1,s)\right)}{1-\frac{AB}{(2+A)(2+B)}} \tag{3.17}$$

once the solid temperature at the new time and position are known then the simpler expression

$$\theta_g(r,s)=\frac{2-B}{2+B}\theta_g(r-1,s) + \frac{B}{2+B}\theta_s(r,s) + \frac{B}{2+B}\theta_s(r-1,s) \qquad (3.18)$$

may be used to calculate the new gas temperature.

Accuracy of the Willmott method

In order to assess the accuracy of this method simulations have been carried out for the single blow case for a small range of lengths and mesh step sizes. The temperature distribution of the solid at the time $\Pi=\Lambda$ was compared with the results of a simulation using a step size of $\Delta\xi=\Delta\eta=0.05$. The error was defined as simply the maximum deviation of the temperature. The results show that the error for any one simulation varies in space and time. For a given time the position of the maximum error appears to be associated with the maximum absolute value of $\frac{\partial^2\theta}{\partial\xi^2}$. figure 3.3 shows the variation of the error with mesh size. For the range $0<\Delta\xi<3$,where $\Delta\xi\approx\Delta\eta$ the error increases in proportion to $(\Delta\xi)^2$. As the length of the bed is increased so the error decreases approximately linearly.

For the conditions:

$0<\Delta\xi<3, \qquad 5<\Pi<50, \qquad 5<\Lambda<50$

then error $\approx \frac{0.04}{\Lambda}(\Delta\xi)^2$.

for most cases then to achieve an accuracy of 0.1% then a step size of $\Delta\xi\approx\Delta\eta\approx0.5$ will be adequate. In the past this requirement has meant that simulations took up a large amount of computer memory and were slow. A great deal of effort was put into techniques that reduced the load on the computer at the expense of more complex programming using variable mesh sizes and methods that accelerated the approach to equilibrium. With the speed and memory available in modern computers this is no longer so important .

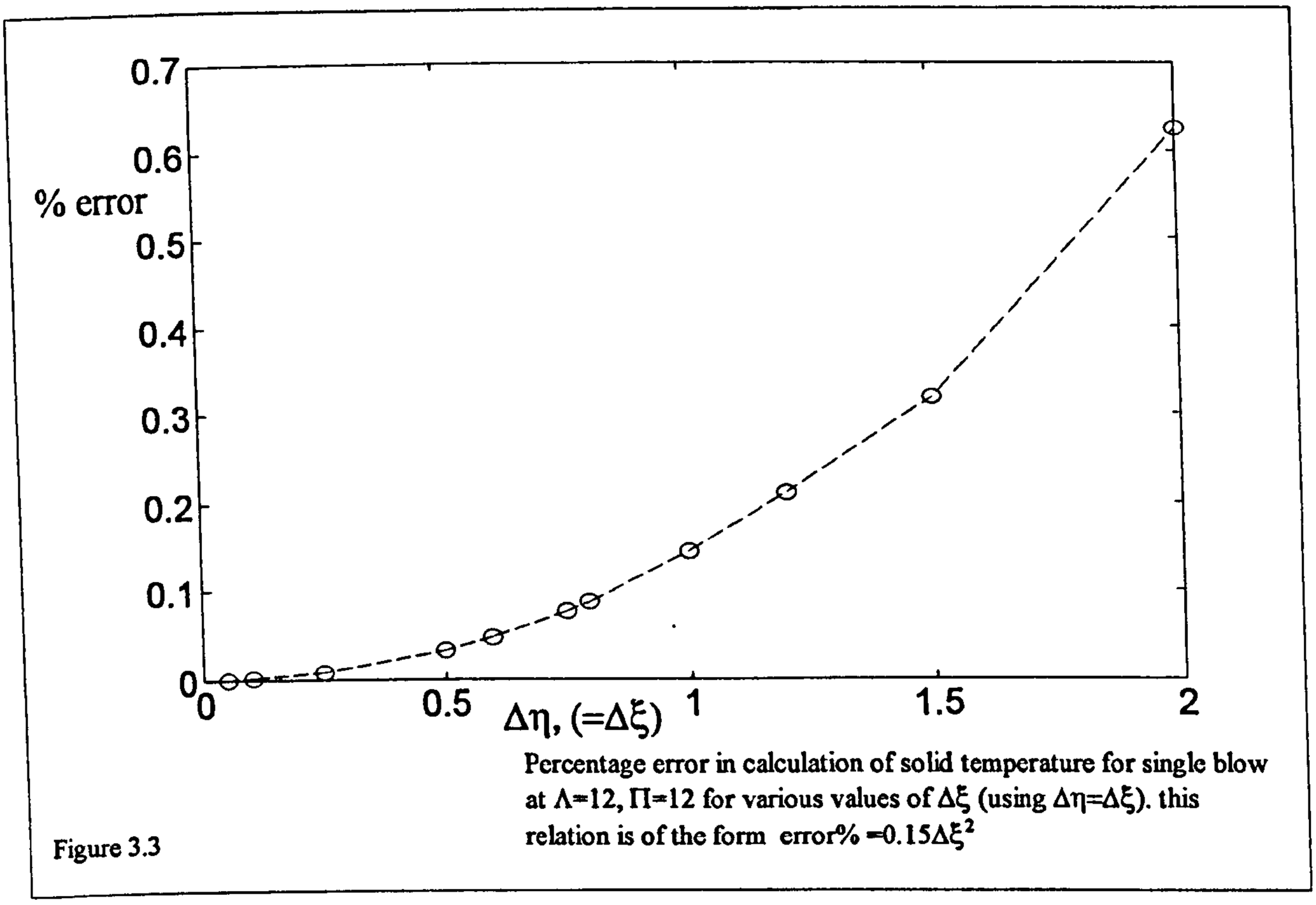

Percentage error in calculation of solid temperature for single blow at Λ=12, Π=12 for various values of $\Delta\xi$ (using $\Delta\eta$=$\Delta\xi$). this relation is of the form error% =$0.15\Delta\xi^2$

Figure 3.3

Thermal behaviour of simple regenerators

Internal temperature variations

The calculation method outlined above has been used to give a plot of the solid temperatures in a regenerator of dimensionless length 10 during the first hot blow and are shown in figure 3.4.

Figure 3.5 shows how the maximum rate of change of temperature decays as the temperature front travels down the bed.

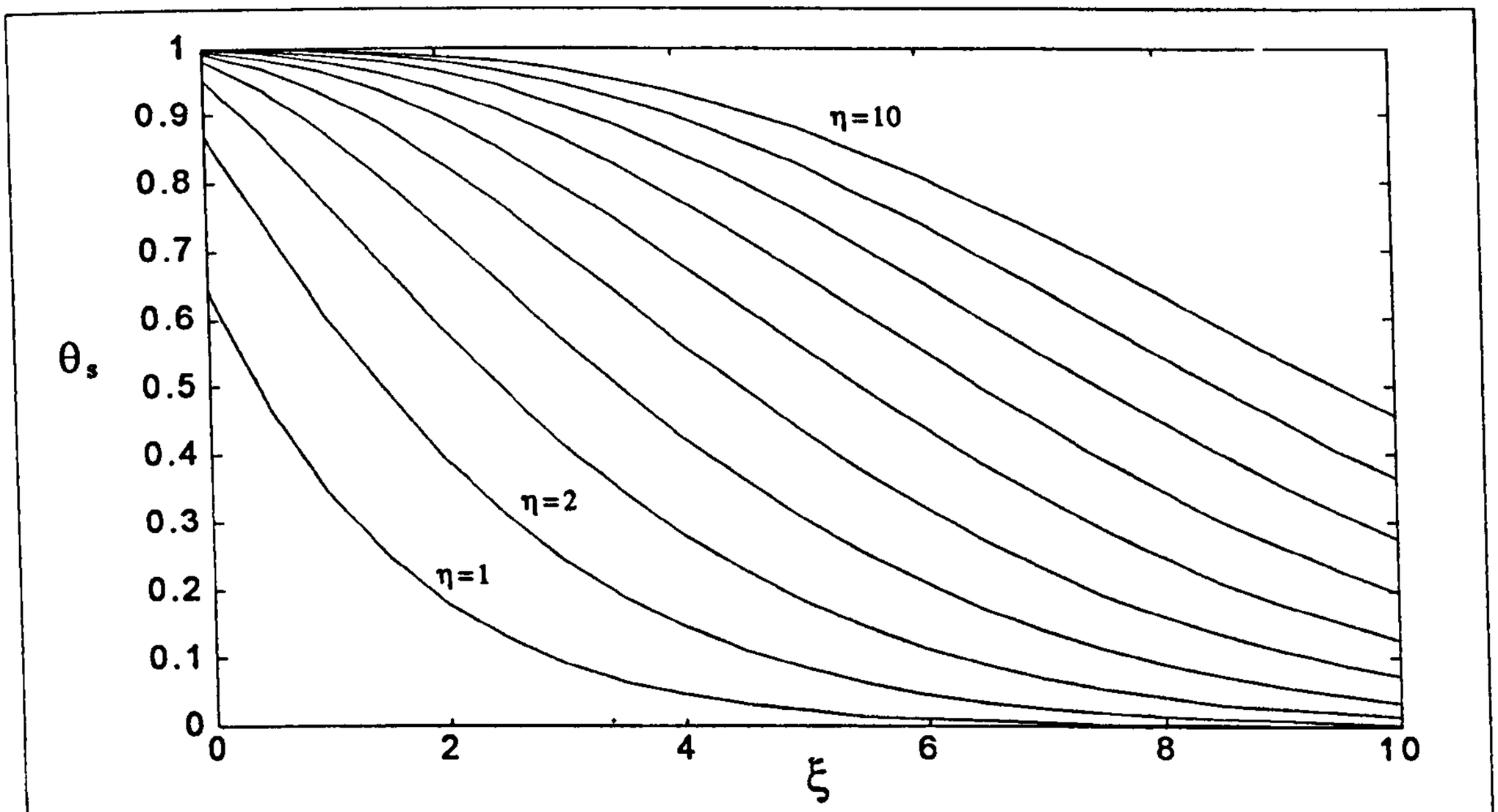

figure 3.4 Solid temperatures during the first blow from η=1 to 10

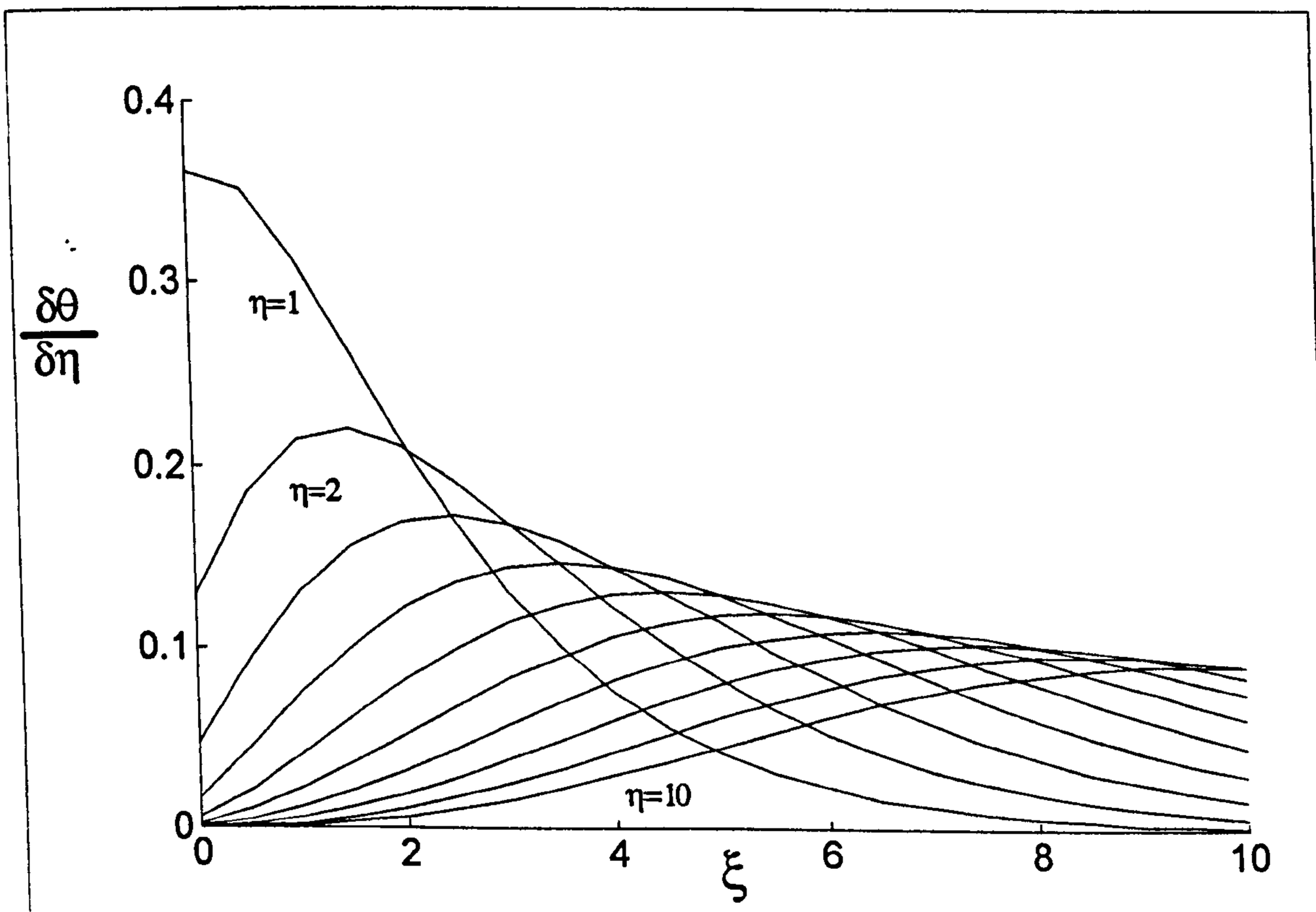

figure 3.5 Solid temperature rates of change for first blow at times η =1 to 10.

Internal temperatures of the regenerator at equilibrium.

The temperatures at dynamic equilibrium are of most interest, and are represented in 3.6 which shows the temperature profiles of a bed after 10 complete cycles. It is clear from this that no part of the bed goes through the whole temperature range and the temperatures experienced by the hot end of the bed can be very different from those of the cold end. The temperature swing is related to the amount of energy stored in each cycle, and so to Π/Λ. Figure 3.6 shows a regenerator with $\Pi/\Lambda=0.667$, figure 3.7 shows the variation of outlet gas temperature during the cold period of the same regenerator.

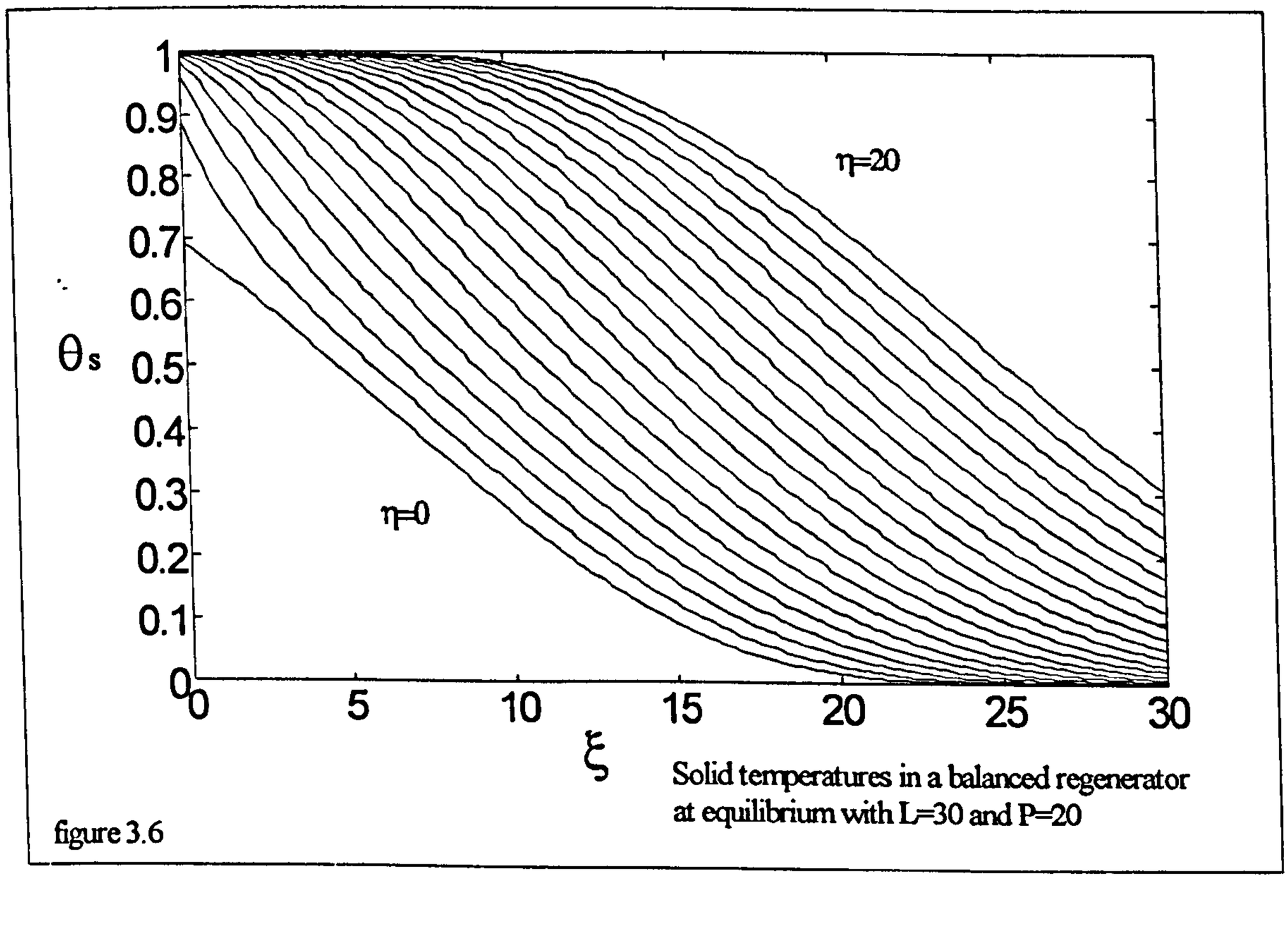

Solid temperatures in a balanced regenerator at equilibrium with L=30 and P=20

figure 3.6

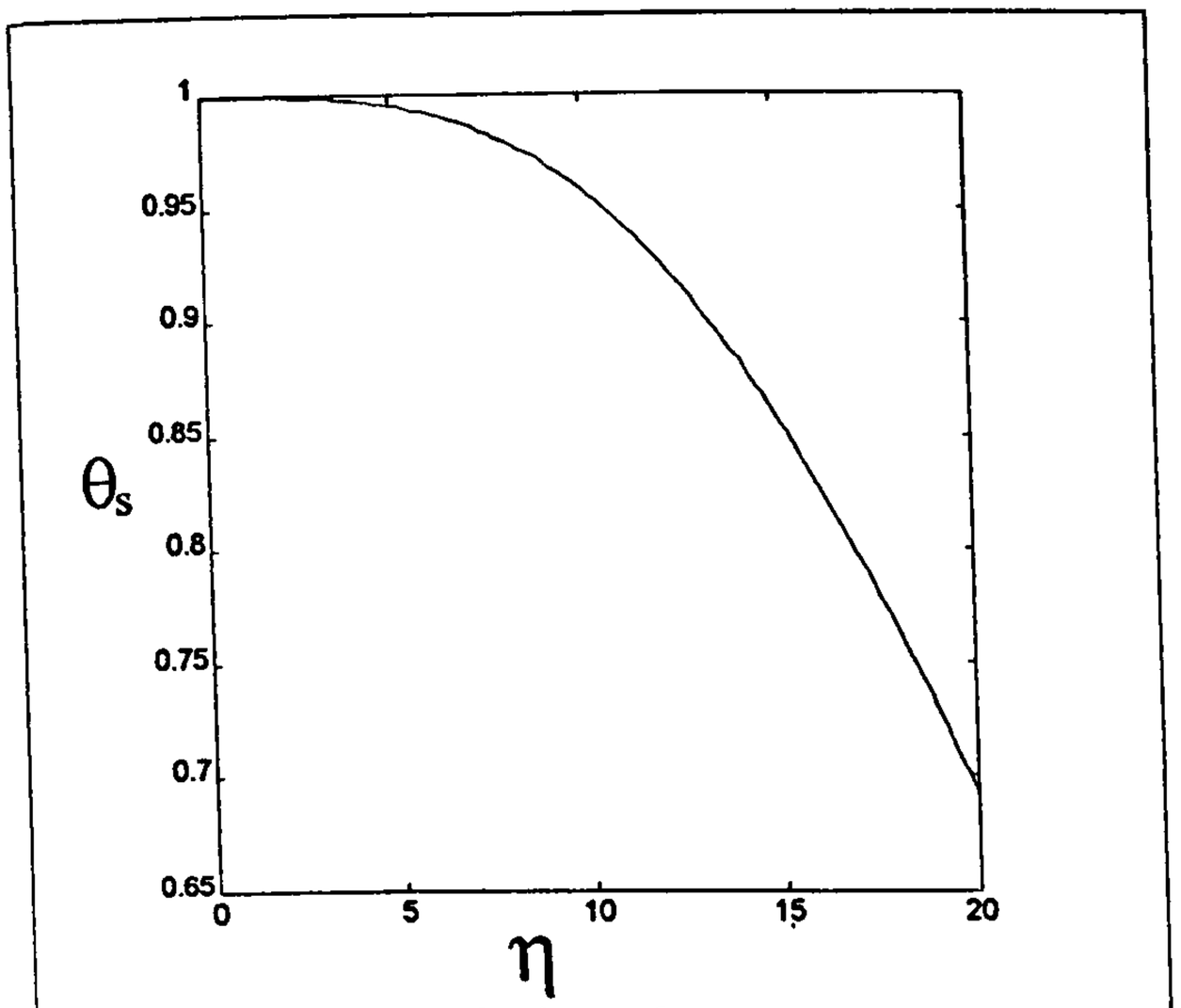

Temperature of exit gas from a regenerator at equilibrium during the cold blow Π=20 Λ=30

figure 3.7

Effectiveness of the regenerator

The effectiveness of the regenerator is defined as the amount of energy transferred from the hot stream to the cold stream divided by the ideal energy transfer. The variation of effectiveness with Π/Λ and Λ is shown in figure 3.8. In the limit as Π/Λ tends to zero so the effectiveness of a regenerator is the same as that for a counterflow heat exchanger with NTU = $\Lambda/2$. For very short periods, however the carryover of the gas volume in the pore space between gas streams becomes more significant.

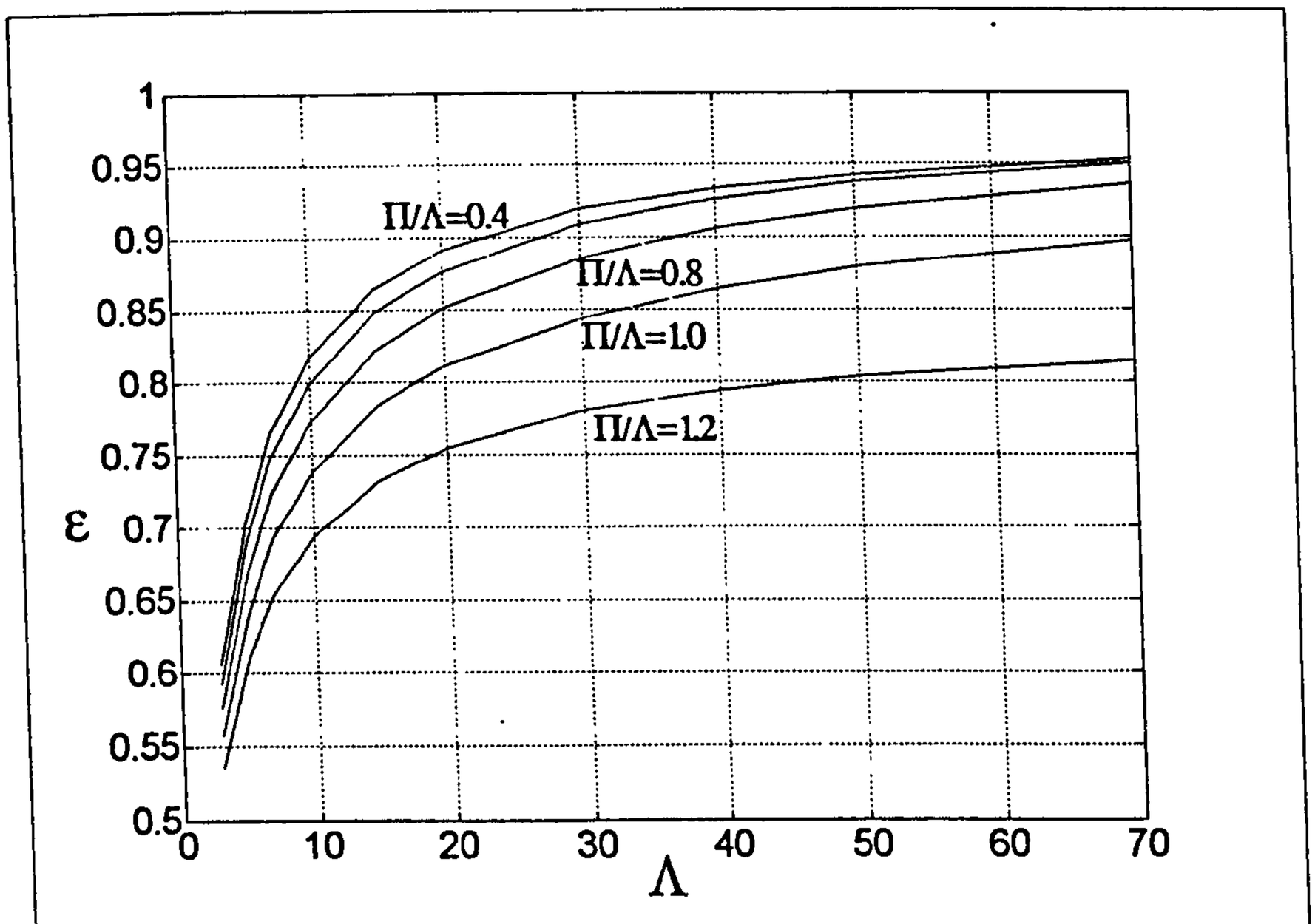

Effectiveness of a balanced regenerator.

figure 3.8

Regenerator geometry

The characteristics of a regenerator are determined by its geometry, mass flow and operation. The effect of changing parameters for a given duty and dimensionless length on the pressure loss can be given a broad description as follows

- Diameter: As the diameter of a bed is reduced, so for a given total mass flow the velocities will increase with the inverse square of the diameter. The heat transfer coefficient may be taken as proportional to the 0.8^{th} power of velocity and so $\Lambda \propto D^{0.4}$ .If the total volume is kept constant as the diameter is reduced so the length increases meaning that $\Lambda \propto D^{-1.6}$. Pressure loss may be assumed to be proportional to the product of the square of the velocity and the length so for a constant total volume then $\Delta P \propto D^{-4}$.
- Grain size: Since $Nu \propto \mathrm{Re}^{0.8}$ then $\alpha \propto d^{-0.2}$. The specific surface area is inversely proportional to grain size and so $\Lambda \propto d^{-1.2}$. Pressure loss may be taken as inversely proportional to grain size.

For a target value of Λ the choice of bed diameter, length and grain size will be determined by the permitted mass and pressure drop, pressure considerations favouring short, wide beds while heat transfer is favoured by longer,narrow designs.

References

[1] **Hausen, H.** Heat transfer in counterflow parallel flow and cross flow ,*Mcgraw-Hill*,(1983)

[2] **Nusselt,W.** Die theorie des winderhitzers, *Zeitschrift des vereins Deutscher Ingenieure* **Vol71** pp 85-91 (1927)

[3] **Nahavandi, A.H.** A solution to the periodic flow regenerative heat exchanger problem, *Applied Scientific research* ,**Vol 10** pp 335-348 (1961)

[4] **Schumann, T.E.W.** Heat transfer: liquid flowing through a porous prism, *Journal of the Franklin Institute*, **Vol 208** pp 405-416 (1929)

[5] **Willmott,A.J.** ,Hinchcliffe, C. The Effect of gas heat storage upon the performance of the thermal regenerator, *International Journal of Heat and mass Transfer*, **Vol 19** pp 821-826 (1976)

[6] **Organ, A.J.** Solution of the classic thermal regenerator problem, *Proceedings of the Institute of Mechanical Engineers* **Vol 208** pp187-197 (1994)

[7] **Kays, W.M. London, A.L.** Compact heat exchangers *Mcgraw-Hill* (1984)

[8] **Handley D., Heggs P.J.,** The effect of thermal conductivity of the packing material on transient heat transfer in a fixed bed *International Journal of Heat and Mass Transfer* **vol 12** pp549-570 (1969)

[9] **Kaviany, M.** Principles of heat transfer in porous media, *Springer verlag* (1995)

[10] **Wakao,N. Kaguei, S.** Heat and mass transfer in packed beds, *Gordon and Breach science* (1982)

[11] **Bradshaw, A. V. Johnson, A. McLachlan, N. H. Chui, Y-T.** Heat transfer between air and nitrogen and beds of non reacting solids, *Transactions of the Institution of Chemical Engineers* **vol 48** pp T77-T84 (1970)

[12] **Hill, A.** Stable closed methods of thermal regenerator simulations, *Phd Thesis University of York* (1988)

[13] **Willmott A. J.** Simulation of thermal a thermal regenerator under conditions of variable mass flow. *International journal of heat and mass transfer* vol 11 pp1105-1116 (1968)

Chapter 4. Experimental equipment

In order to investigate the pressure drop and heat transfer characteristics in beds of granular active carbon with forced convection of gas an experimental rig was designed and built. The rig was designed to deliver gas at a controlled rate and temperature into the bed with the possibility of reversing the flow. Temperature, pressure and mass flow were to be measured, controlled and recorded by computer. A schematic diagram is shown in Figure 4.1. The major components were an electrically powered heater, a circulating pump, a cooler and the bed of carbon. In addition there was a water cooled condenser/evaporator which was intended to regulate the pressure, simulating a complete refrigeration cycle.

Circulating pump

The requirement was for a circulating pump which was compatible with ammonia, could circulate gas at 3 l/s against a pressure drop in the bed and ancillary components estimated as 1 bar, could withstand internal pressures of 25 bar, was oil free and could be speed controlled. A rotary vane pump would have been preferred since they can be obtained oil-free with graphite vanes. However, the crankcase would have to be reinforced and a shaft seal capable of resisting 25 bar fitted. Anticipating that this might involve a large time delay and certification difficulties, a different option was used. An open compressor designed for conventional ammonia refrigeration was utilised. This had the advantages of sufficient crankcase strength for the line pressure and shaft seals designed to prevent ammonia leakage. However, the volume flow from a reciprocating pump is less steady than that of a rotary vane pump and the system is not oil free. It was

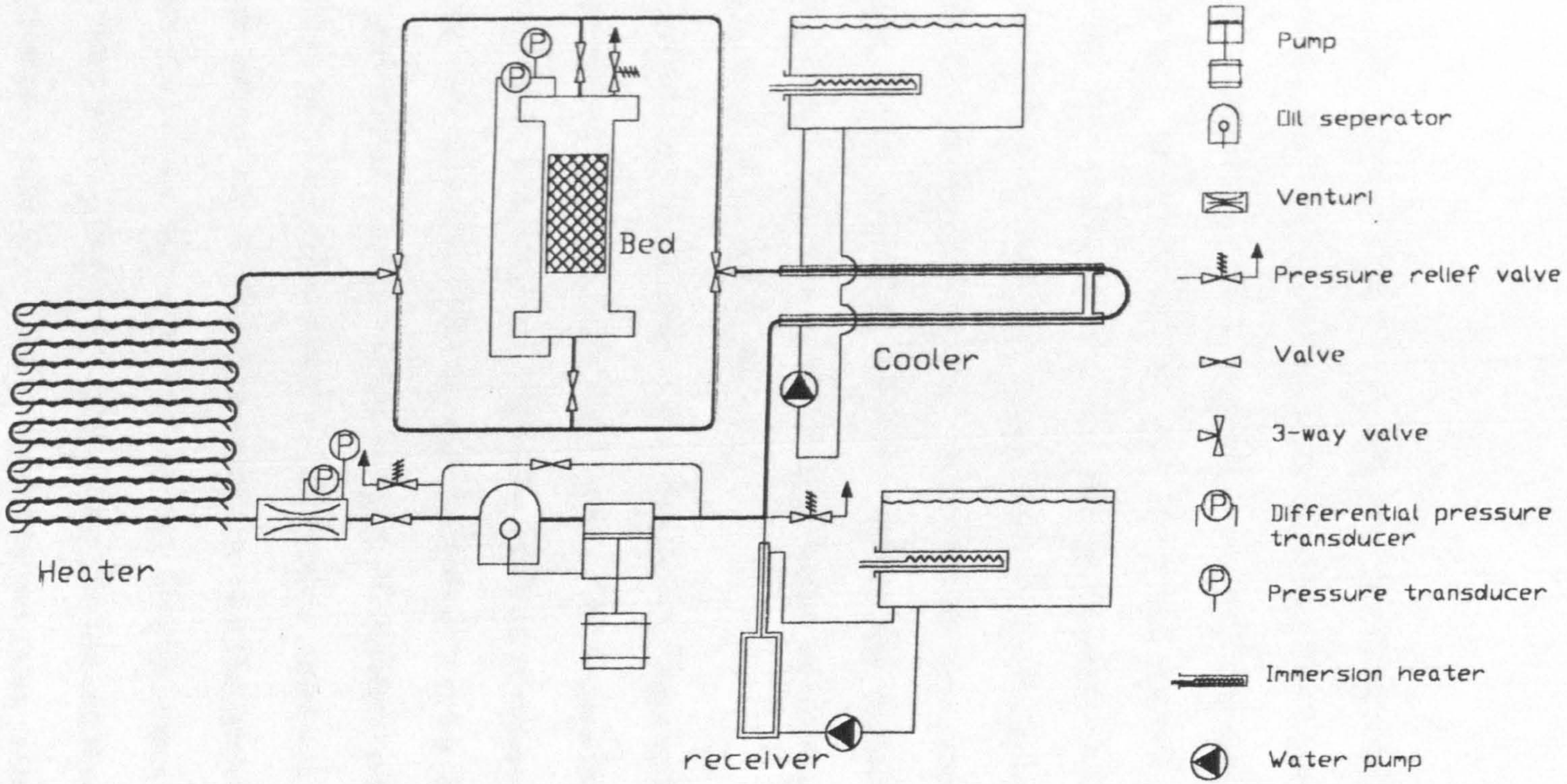

Figure 4.1 Schematic diagram of the forced convection test apparatus

anticipated that an oil separator would be sufficient to prevent any oil carryover to the carbon bed and that the system had a suitable combination of dead volume and pressure drop to damp out volume flow oscillations in the bed. The compressor was driven through a veebelt by a DC permanent magnet motor controlled by a solid state power supply. The speed of this motor could be regulated by either a potentiometer on the control panel or by the computer.

Heaters

Many options for possible electric heater configurations were considered. Cartridge heaters in a concentric tube design would have been suitable but for the high cost; £2000. A large number would have been needed to avoid high temperature areas that might possibly cause dissociation of the ammonia. It was originally intended to heat the ammonia to 300°C. Ideally the exit gas temperature was to have been closely held to a constant value, despite fluctuations in the temperature of the gas leaving the bed. The final solution decided on was to oversize the cooler to regulate the temperature of gas entering the heater and to utilise a large thermal mass in the heater. The alternative option of a thermally light heater with fast response invited potential control and stability difficulties.

Twelve heaters, each rated at one kilowatt were constructed using coils of stainless steel wire, each wound over an electrically insulating sleeve of glass fibre on a 1.8 metre length of one half inch diameter stainless steel tube, and connected in series. Six of these heaters were connected through manual switches to the 240v ac power supply and the remaining six were connected to a pair of thyristor controllers that could be regulated by either a potentiometer on the control panel or a 0-10v output from the computer. Relays and interlocks were used so that the heaters could not be operated unless the circulating pump was running. Thermal fuses manufactured to open at 280°C were fitted to disconnect power from the heaters through a relay should this temperature be exceeded. Each heating element was protected by a

conventional fuse and the whole electrical system was protected by a residual current sensing circuit breaker (RCD).

Cooler

A simple tube in tube heat exchanger utilising 1/2" 316 Stainless Steel within 22mm copper water tubing was constructed using a combination of Swagelok and modified plumbing compression fittings. Simple heat transfer correlations were used to size the heat exchanger for a flow rate of 0.016 kg/s ammonia at 300°C exiting at 40°C. The exchanger was 6m long in two sections. A standard central heating circulator pumped water from a 160 litre water tank through the heat exchanger and back to the tank. The water volume was sufficient so that the water temperature did not rise by more than 1°C per minute during a test run. An electric immersion heater within the tank was used to preheat the cooling water to the chosen temperature and the tank was left uninsulated.

Condenser / Receiver / Evaporator Assembly

Initial plans included running tests that would simulate a cycle in a heat pump application and others where the pressure was regulated by a condenser/evaporator unit held at a constant temperature. A small unit was designed and built as shown in figure 4.2. The temperature of this unit was controlled by a similar water tank and pump to that used in the gas cooler. It was designed to be easy and cheap to manufacture and modify and included a capacitance probe to measure the level of liquid ammonia within. It was connected as a branch from the main loop.

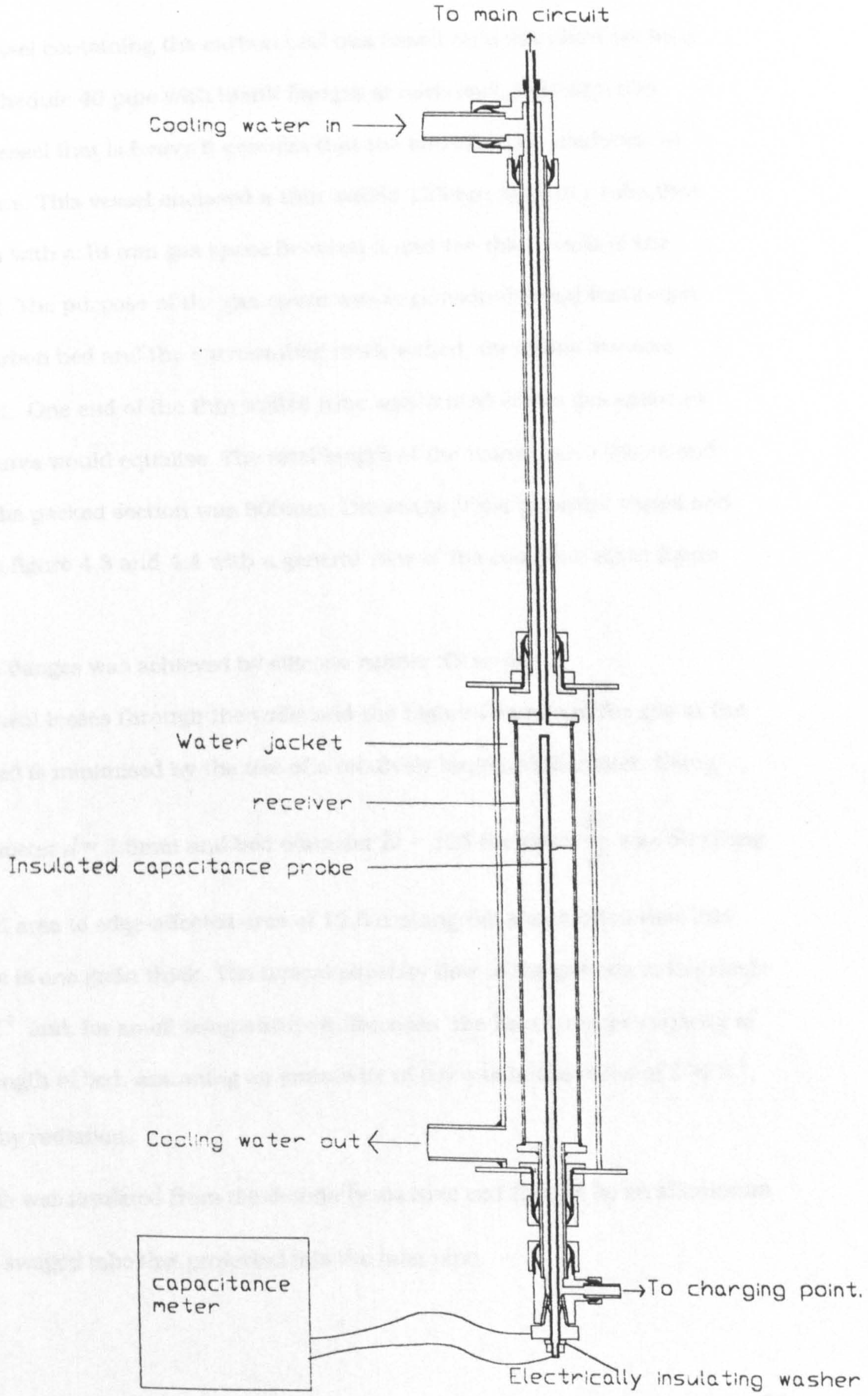

Figure 4 2 Receiver assembly

Pressure Vessel and Carbon Bed

The pressure vessel containing the carbon bed was based on a standard six inch nominal bore schedule 40 pipe with blank flanges at each end. Although this design gives a vessel that is heavy it ensures that the construction conforms to safety regulations. This vessel enclosed a thin walled 125mm diameter tube that held the carbon with a 13 mm gas space between it and the thick walls of the pressure vessel. The purpose of the gas space was to provide thermal insulation between the carbon bed and the surrounding thick walled, thermally massive pressure vessel. One end of the thin walled tube was vented to the gas space so that the pressures would equalise. The total length of the vessel was 1 metre and the length of the packed section was 500mm. Drawings of the pressure vessel and bed is given in figure 4.3 and 4.4 with a general view of the complete rig in figure 4.5.

Sealing of the flanges was achieved by silicone rubber 'O' rings.

The effect of heat losses through the walls and the higher flowrate of the gas at the edge of the bed is minimised by the use of a relatively large bed diameter. Using grains of diameter $d = 2.5$mm and bed diameter $D = 125$ the ratio $\frac{D}{d}$ was 50 giving a ratio of bed area to edge-affected area of 12.5 making the assumption that this affected zone is one grain thick. The typical capacity flow of the gas lies in the range 25 - 80 W K^{-1} and, for small temperature differences the heat transfer capacity of a 250mm length of bed, assuming an emissivity of 0.6 was in the order of 2 W K^{-1}, principally by radiation.

The gas path was insulated from the thermally massive end flanges by an aluminium plate and a swaged tube that projected into the inlet pipe.

Figure 4.3

Bed entrance or exit section (each are identical)

1 Carbon bed
2 Baffle
3 Thin walled tube
4 Baffle support (1 of 4)
5 1/2" Compression fitting
6 1/4" Compression fitting
7, 8, 9 'O' rings
10 Aluminium plate
11 Fine stainless steel gauze
12 1/4" Tube
13 Bed locating gauze
14 gauze carrier

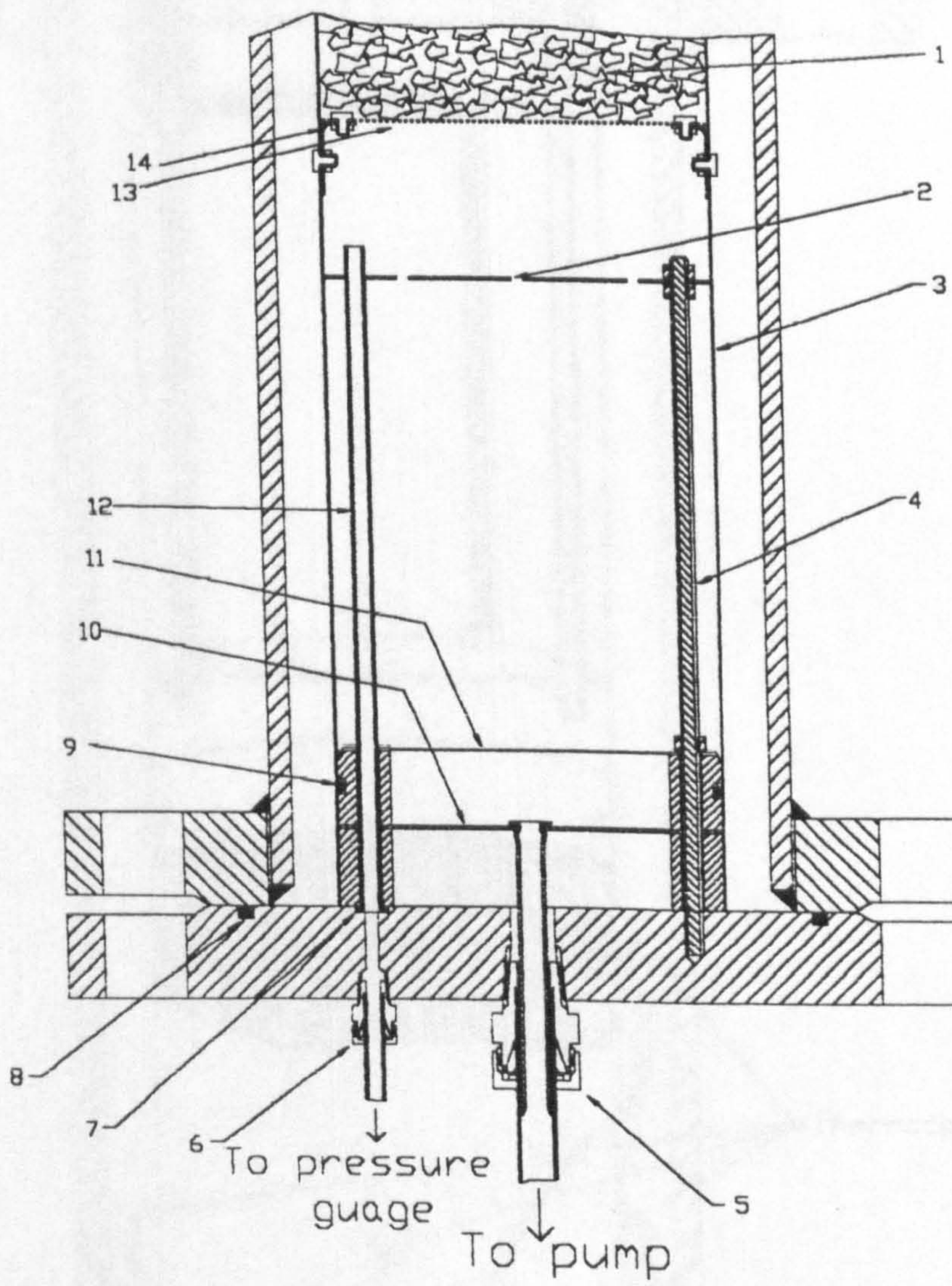

Figure 4.4 Cut-away view of the bed and pressure vessel.

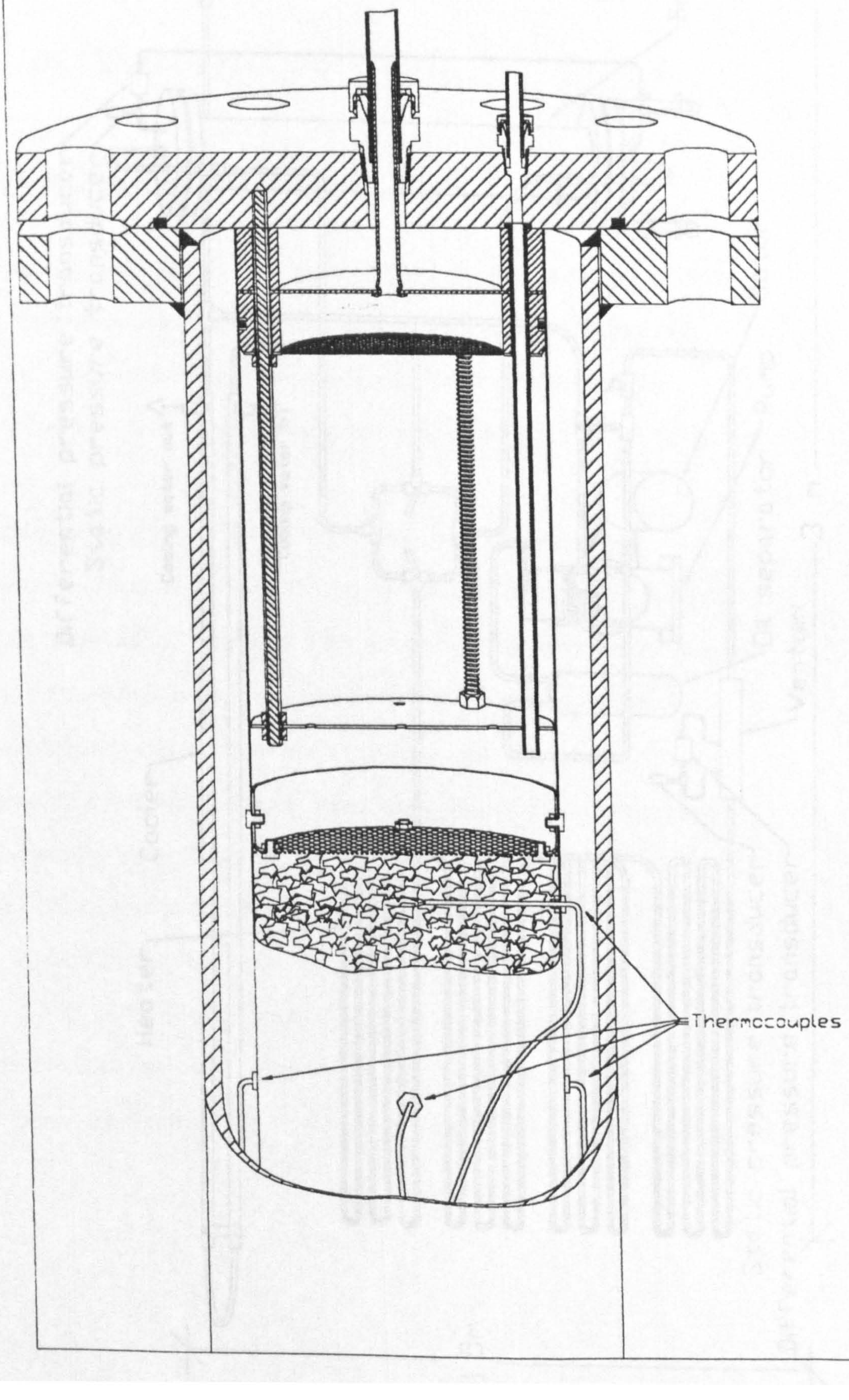

Figure 4.5 Simplified general view of the apparatus

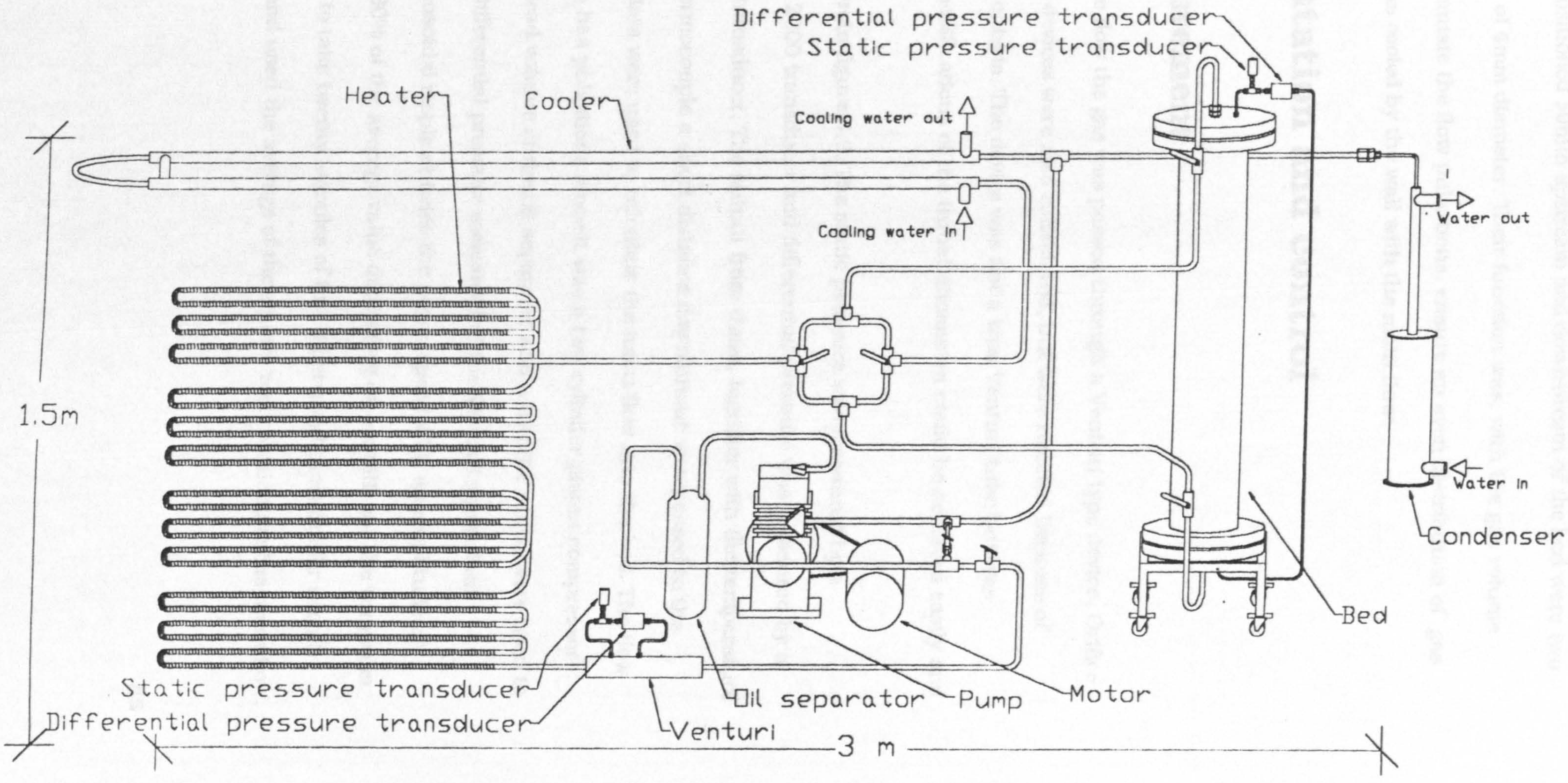

The carbon bed was fixed in position between two wire gauze panels in the central part of the vessel. Positioned 50mm upstream and downstream of the bed were two baffles with 5 holes of 4mm diameter. Their function was, with the gas volume behind them to attenuate the flow pulsations, ensure an even distribution of gas flow and mix the gas cooled by the wall with the main flow.

Instrumentation and control

Flow measurement

In order to measure flow the gas was passed through a Venturi type device. Orifice plates and turbine devices were also considered, but were rejected because of accuracy and cost criteria. The device was not a true Venturi tube but was designed so that modifications of the throat dimension could be achieved easily and cheaply.

The device is shown in figure 4.6. The static pressure was measured by a Transinstruments 2000 transducer and differential pressure was measured by a Druck PDCR 135 transducer. The output from these, together with the temperature measured by a thermocouple a short distance downstream was passed to the controller. These data were used to calculate the mass flow into the bed. The flow through the pump has pulsations since it was a two cylinder piston compressor and, despite the dead volume of the oil separator and a throttle which were used to reduce them the differential pressure measured at the Venturi showed an approximately sinusoidal ripple at twice the pump speed with an amplitude of between 5% and 30% of the average value depending on conditions. The computer was programmed to take twenty samples of this differential pressure for each 3 second timestep and used the average of the square root to calculate the mass flow.

Figure 4.6 Engineering drawings of the venturi tube

All parts constructed from 316 stainless steel.
Dimensions in millimetersexcept threads as indicated

Centre section. 1 off

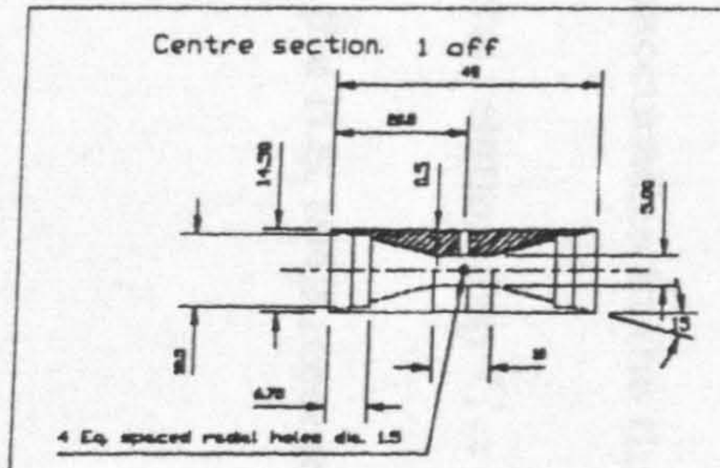

Venturi body
1 off

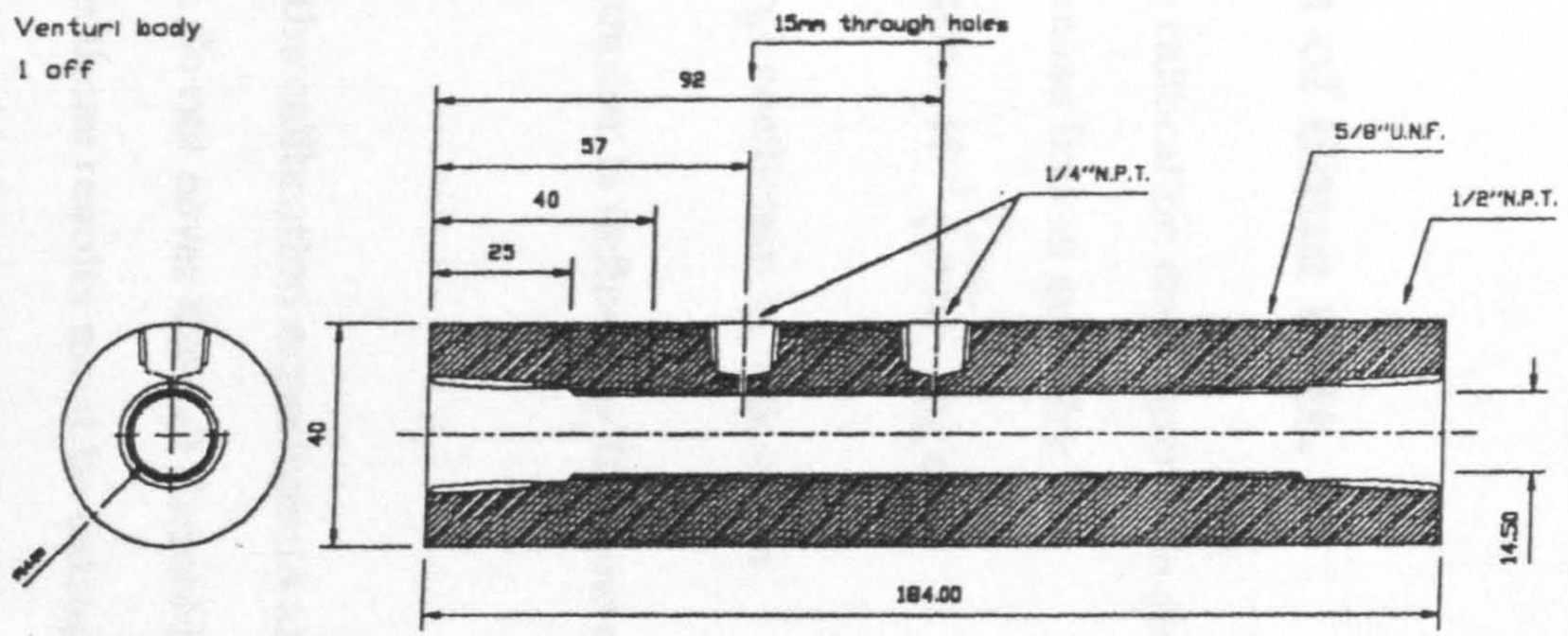

Compression fitting, supplied with stepped through hole.
Please bore through body to 1/2"

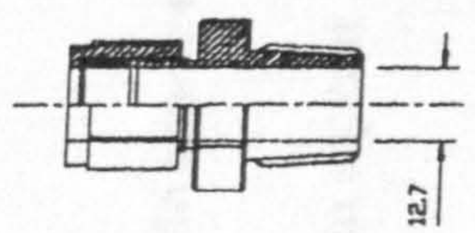

Entrance section. 1 off.

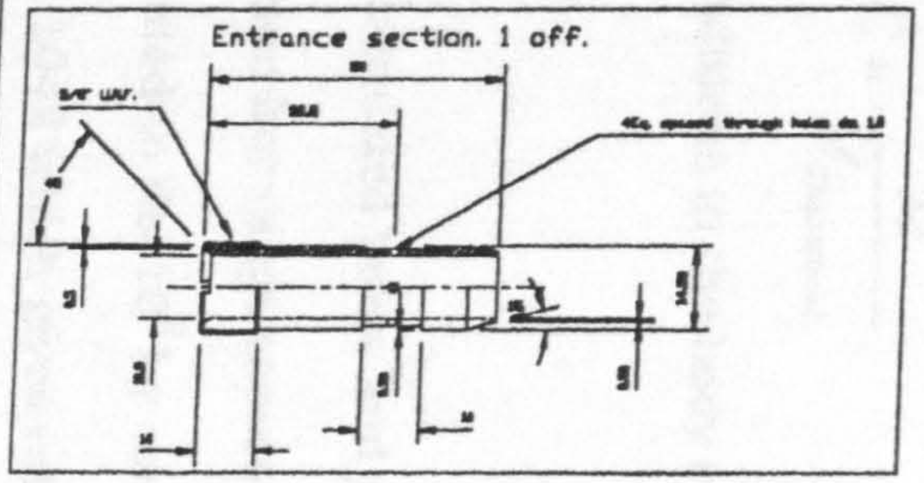

General assembly

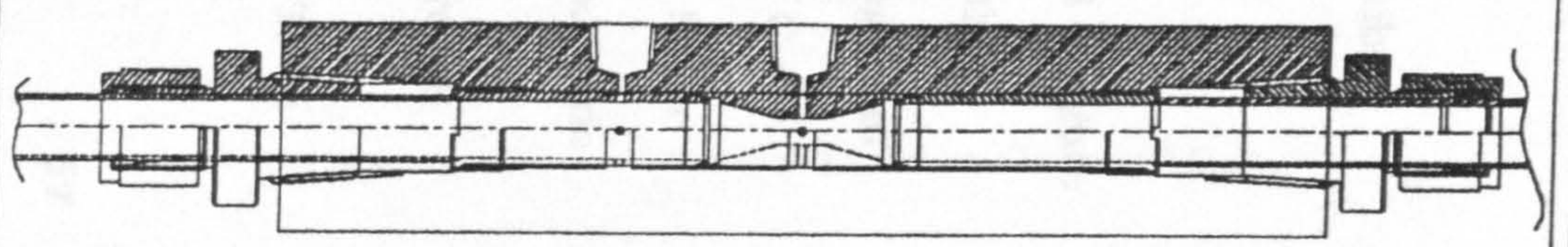

Exit section 1 off

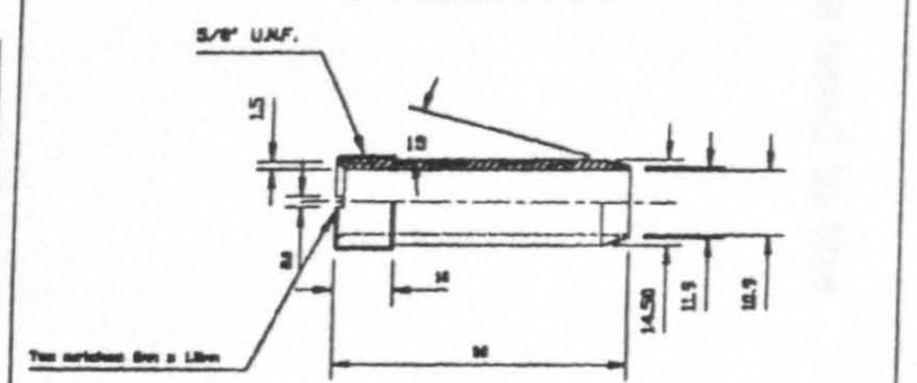

The Venturi was used in two configurations, initially with a throat diameter of 5mm and later with a throat diameter of 6mm. In the case of the 5mm throat the unit was calibrated with water. The water was allowed to flow through the unit for a measured time period into a container and then weighed. In the case of the 6mm throat the Venturi was calibrated using air from the laboratory compressed air supply and the flow measured using rotameters. In both cases the differential pressure was measured by the same Druck PDCR 135 transducer as used in the experiments.

Calibration of 6mm unit.

The data for the calibration experiments is given below.

The theoretical mass flow is given by:

$$\dot{M}_{Theoretical} = 2.8404 \times 10^{-5} \sqrt{\rho \, \Delta P} \ \ (\mathrm{kg\ s^{-1}})$$

and the discharge coefficient is defined as $C = \dfrac{\dot{M}}{\dot{M}_{Theoretical}}$.

The Reynolds number is defined by the flow conditions in the body of the tube,

$$\mathrm{Re}_D = \frac{4}{\pi} \frac{\dot{M}}{\mu D}$$

The results of the calibration experiments are tabulated below and plotted in figure 4.7 , these data do not cover the full Reynolds number range expected for the machine and so these results must be extrapolated to Re=10^5 by comparing them with the trend of table B.1 of British Standard 1042 which gives values of C for Re_D from 40000 to 150000. These values are extrapolated and scaled by a factor that compensates for inaccuracies in the throat measurement. This method leads to the conclusion that the relationship $C = 1.1 - \dfrac{54}{\mathrm{Re}_D^{0.66}}$ may be used. Figure 4.8 shows the results with the B.S.1042 recommendations scaled up by 1.1. Some

doubt must be expressed in the validity of this extrapolation but given the constraints of time and equipment it may be accepted with an accuracy of 5%.

Mass flow kg/s	Δp Pa	Theoretical mass flow kg/s	Discharge coefficient $C = \frac{\dot{m}}{\dot{m}_{theoretical}}$	Re_D
0.0519	3521	0.0532	0.9738	4663
0.08397	8967	0.08506	0.9872	7460
0.09746	12194	0.09918	0.9823	8690
0.12381	19432	0.12521	1.0113	11040
0.16492	31612	0.15970	1.0326	14700
0.2263	60298	0.22056	1.0260	20180

medium: water @10°C, $\rho = 1000$ kg/m^3, $\mu = 0.00131$ Pa.s

Dimensions: $d = 5$mm, $D = 10.9$mm

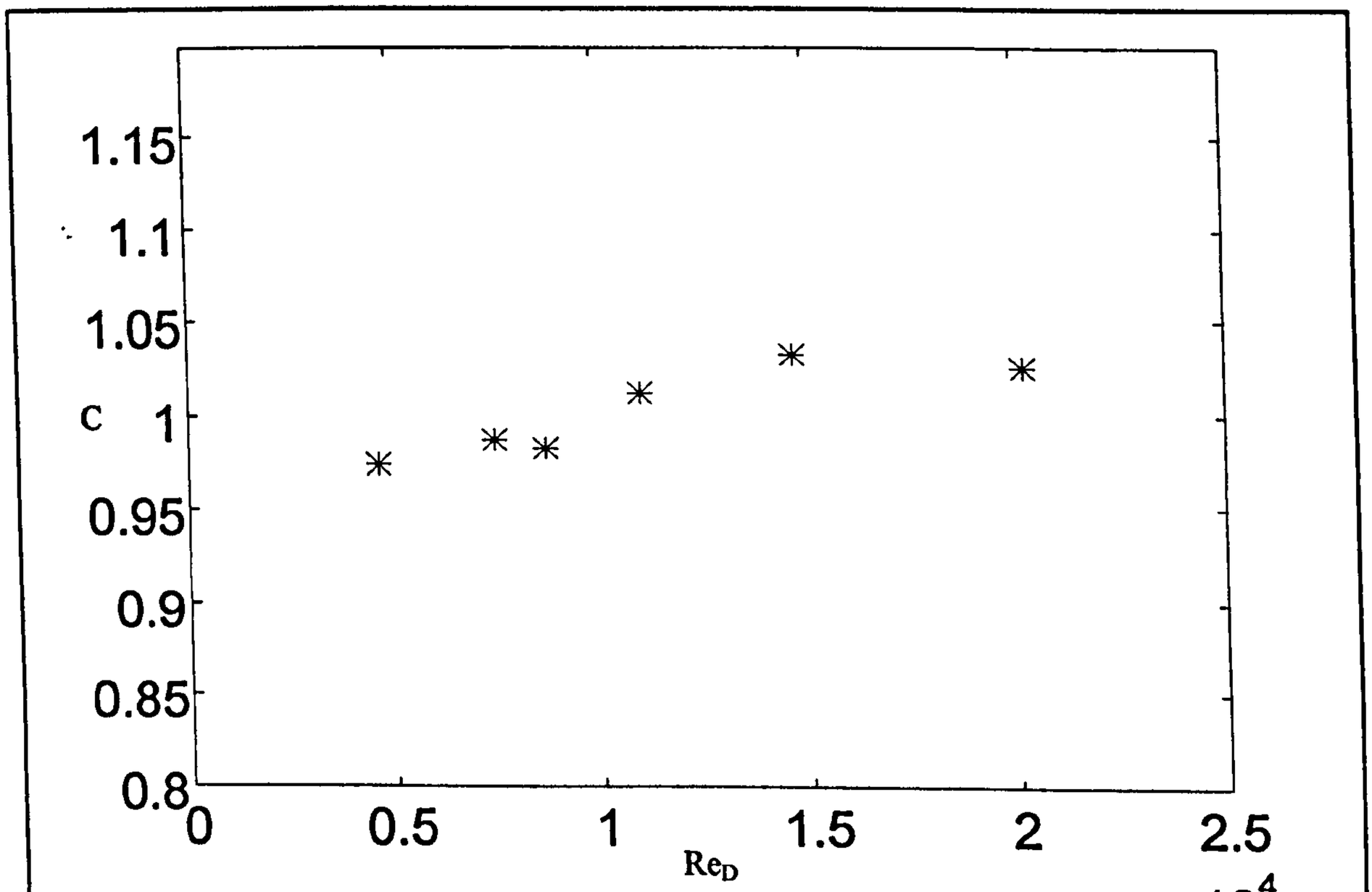

Figure 4.7 Discharge coefficient for 5mm venturi against Re_D

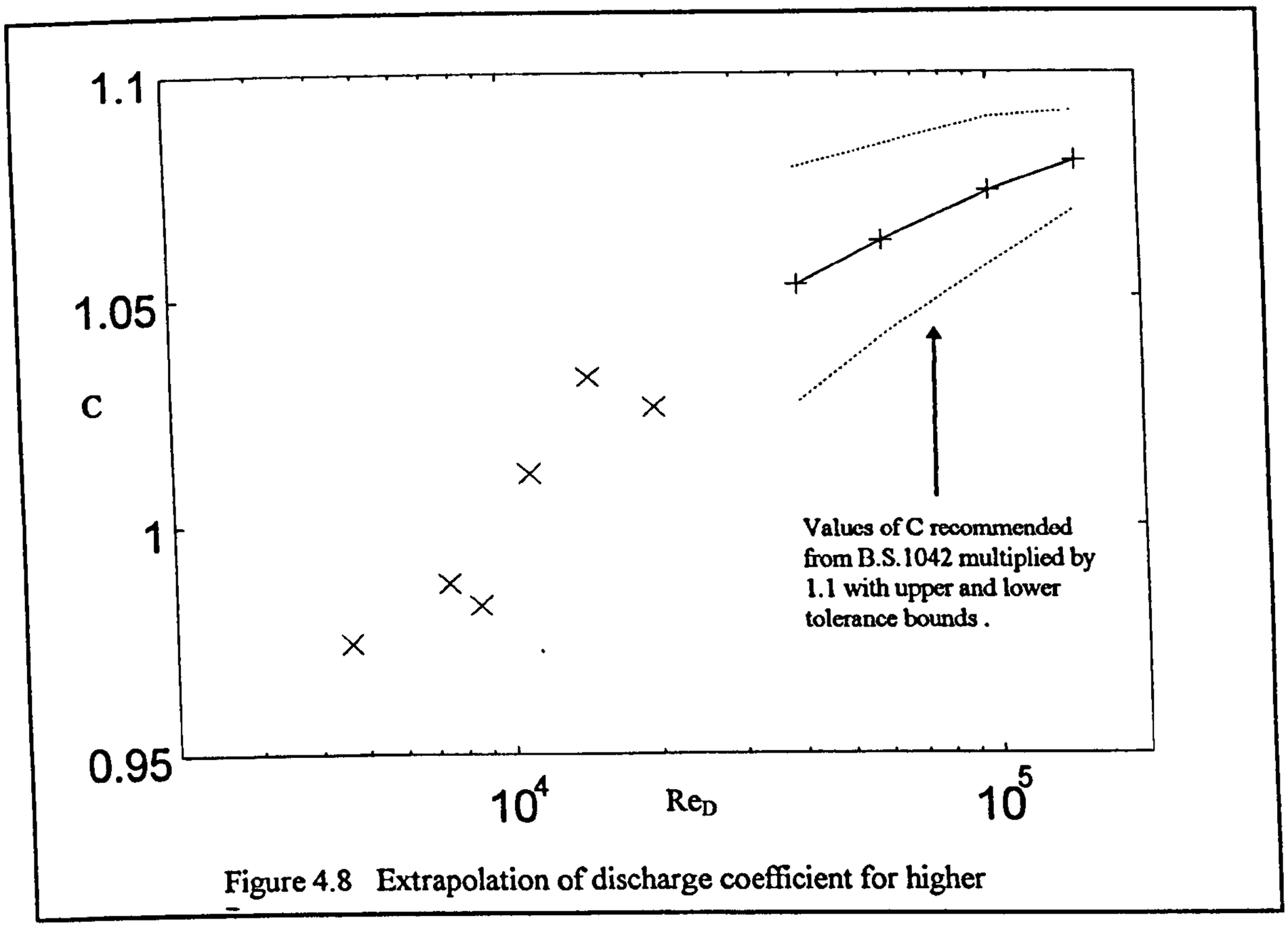

Figure 4.8 Extrapolation of discharge coefficient for higher

6mm Venturi

Two rotameters were used to measure the airflow through the Venturi covering the ranges 2-20 l/min and 10-100 l/min

$$\dot{M}_{Theoretical} = 4.068 \times 10^{-5} \sqrt{\rho \Delta P} \quad (\text{kg s}^{-1}) \qquad C = \frac{\dot{M}}{\dot{M}_{Theoretical}}$$

The tables and plots below show the results from these tests. The outlying data points represent measurements made near the limits of the range for each rotameter and are assumed to show the inaccuracies of this region.

Using a similar approach to extrapolate the applicability of this calibration as for the 5mm Venturi it was found that a value of C given by $C = 1.12 - \frac{56}{Re_D^{0.66}}$ should give an accuracy of 3%.

Static Pressure Bar(a)	Gas density kg/m^3	Δp Pa	Theoretical volume flow $x10^{-3}\ m^3/s$	Measured Volume flow $x10^{-3}\ m^3/s$	Discharge coefficient $C = \frac{\dot{m}}{\dot{m}_{theoretical}}$	Re_D

Rotameter range 10-100 l/min

1.17	1.407	1234	1.205	1.283	1.065	11780
1.168	1.405	1090	1.133	1.2	1.059	11002
1.166	1.403	998	1.085	1.125	1.037	10300
1.165	1.402	937	1.051	1.095	1.042	10018
1.163	1.399	815	0.9819	1.033	1.052	9430
1.16	1.396	694	0.9070	0.933	1.029	8499
1.15	1.384	586	0.8371	0.866	1.035	7821
1.156	1.391	382	0.6741	0.708	1.050	6427
1.155	1.390	316	0.6134	0.633	1.032	5742
1.153	1.387	210	0.5006	0.533	1.065	4842
1.153	1.387	221	0.5135	0.54	1.052	4888
1.152	1.386	118	0.3754	0.433	1.153	3916

Rotameter range 2-20 l/min

1.115	1.342	54	0.2580	0.2563	0.993	2245
1.149	1.382	33	0.1988	0.1967	0.989	1774
1.149	1.382	15	0.1340	0.13	0.970	1172
1.148	1.381	14	0.1295	0.126	0.973	1136
1.15	1.384	14	0.1295	0.123	0.950	1111
1.15	1.384	10	0.1093	0.0966	0.884	862
1.15	1.384	10	0.1093	0.0983	0.899	888

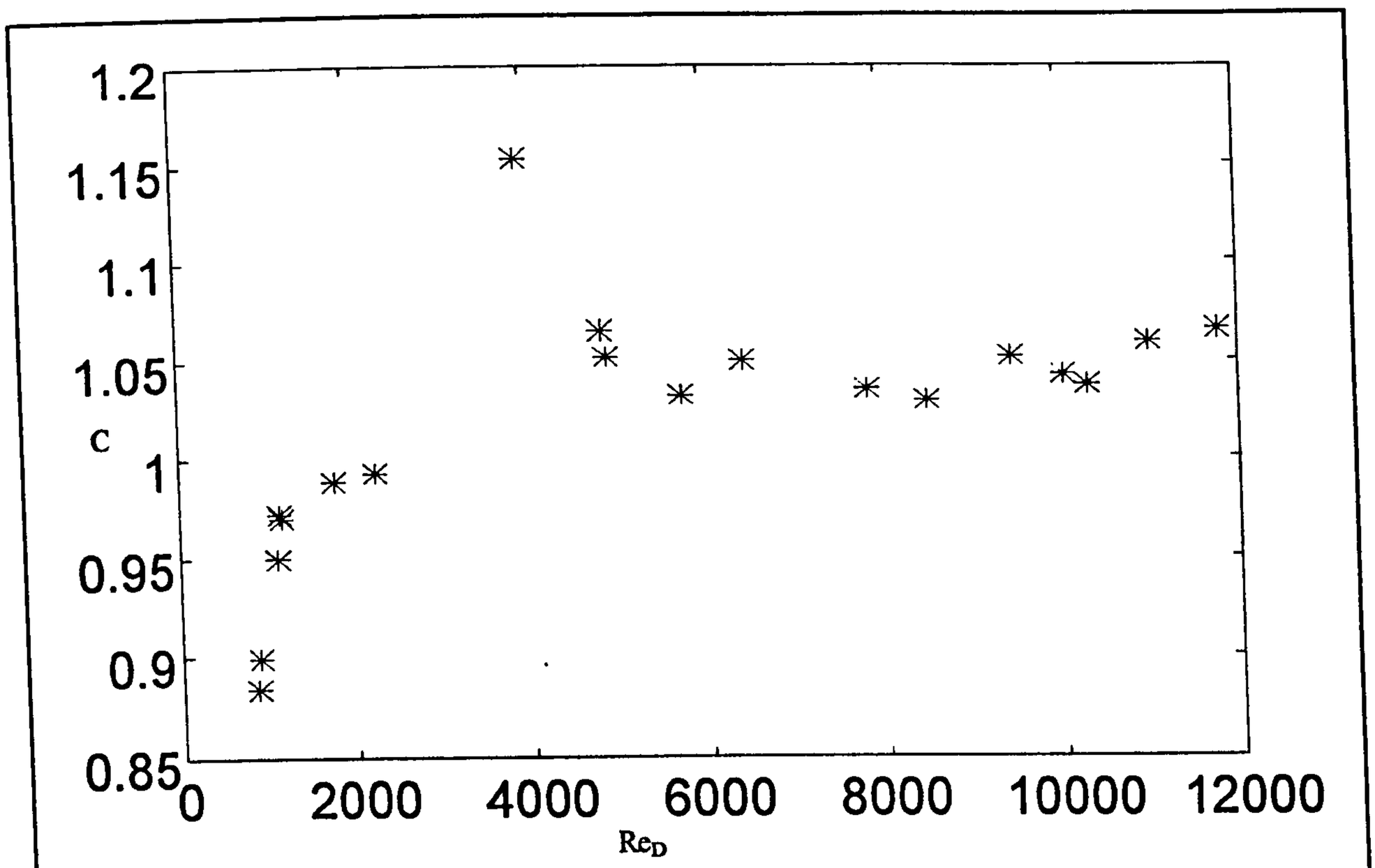

Figure 4.7 Experimental discharge coefficient for 6mm venturi

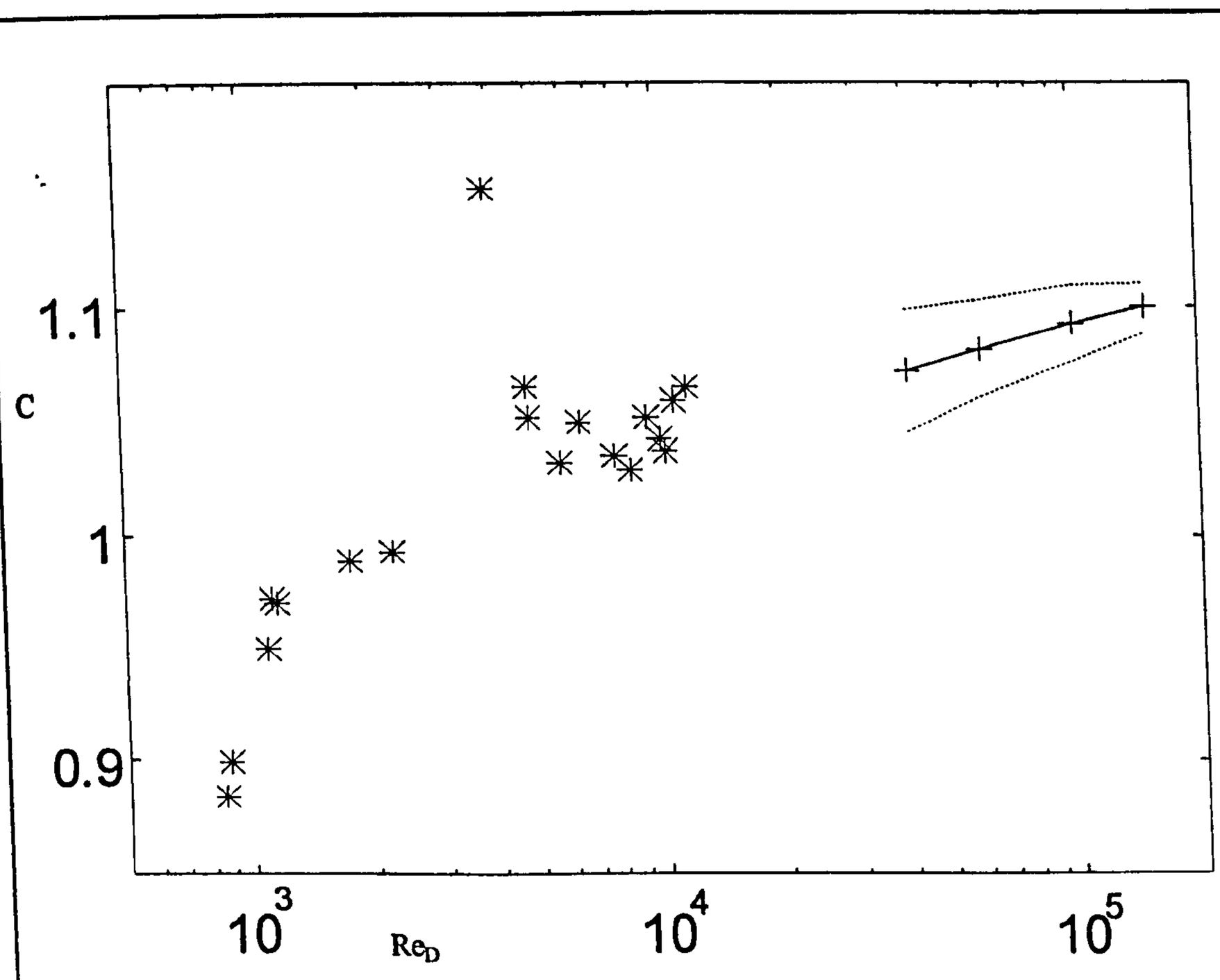

Figure 4.8 Experimental discharge coefficientsfor 6mm venturi with scaled B.S.1042 suggested values

Pressures

Line pressures were measured with Transinstruments 2000 series transducers and differential pressures by Druck PDCR135 transducers. After some weeks of tests with ammonia the Druck units became damaged by the gas. Ammonia had softened the epoxy resin that is used to bind the sensing elements to the diaphragm. Since it was not practical or economic to replace them they were protected by flooding the diaphragm chambers with oil. This solution stopped the offset drift that had been seen and the slope of the calibration remained unchanged within the accuracy of some simple tests. However it must be assumed that their accuracy was compromised during the ammonia tests which were carried out after those with argon.

Temperatures

Measurement of the temperatures in the bed was given careful consideration. It was not possible to measure directly the gas and solid temperature at the same time, but it was realised that an accurate history of either the gas or solid temperature alone would give enough information to calculate the heat transfer coefficient. Since carbon is a good conductor of electricity it was possible to use thermocouples in an arrangement where the junction was made through the carbon. The temperature measured in the experiments is therefore that of the carbon surface at the contact points. To make this 'intrinsic' type of thermocouple a number of steel sheathed, exposed junction units with 25mm of exposed 'K' type thermocouple wires at the junction end were puchased from T.C. limited. The junction was removed and the wires bent so that they were at a constant distance from the axis and in a plane normal to that axis. These devices have a higher resistance than conventional thermocouples, typically from 50Ω to 100Ω in the worst case at the top of the bed where contact pressure was low. Since the data acquisition hardware has an input

impedance of 1MΩ the effect was considered to be negligible in normal circumstances. On some occasions however, with severe oil contamination of the carbon the impedance increased to a much higher level giving rise to evidently faulty readings. The occasions where this had taken place were clearly identifiable and the results from those tests discarded.

Liquid level

Several options were considered to measure the amount of liquid in the receiver, amongst them were floats with magnetic sensors, differential pressure transducers with oil-filled lines and electrical resistance measurement. Ultrasonic techniques have been used in this laboratory with success but the output from this method requires interpretation and is not directly suitable for datalogging. The cheapest and simplest techniques are those using the electrical properties of capacitance or resistance. The electrical resistivity of ammonia is high and strongly affected by the presence of dissolved ions which would raise problems in calibration. Capacitance was therefore selected, a decision reinforced by its use in industry. A commercially available probe was purchased and calibrated. The mass of ammonia was measured by weighing the vessel and its contents. the calibration curve is shown in figure 4.10 on page 62. This curve shows the effect of the geometry of the bottom of the receiver. This calibration may be compared with a theoretical analysis neglecting end effects.

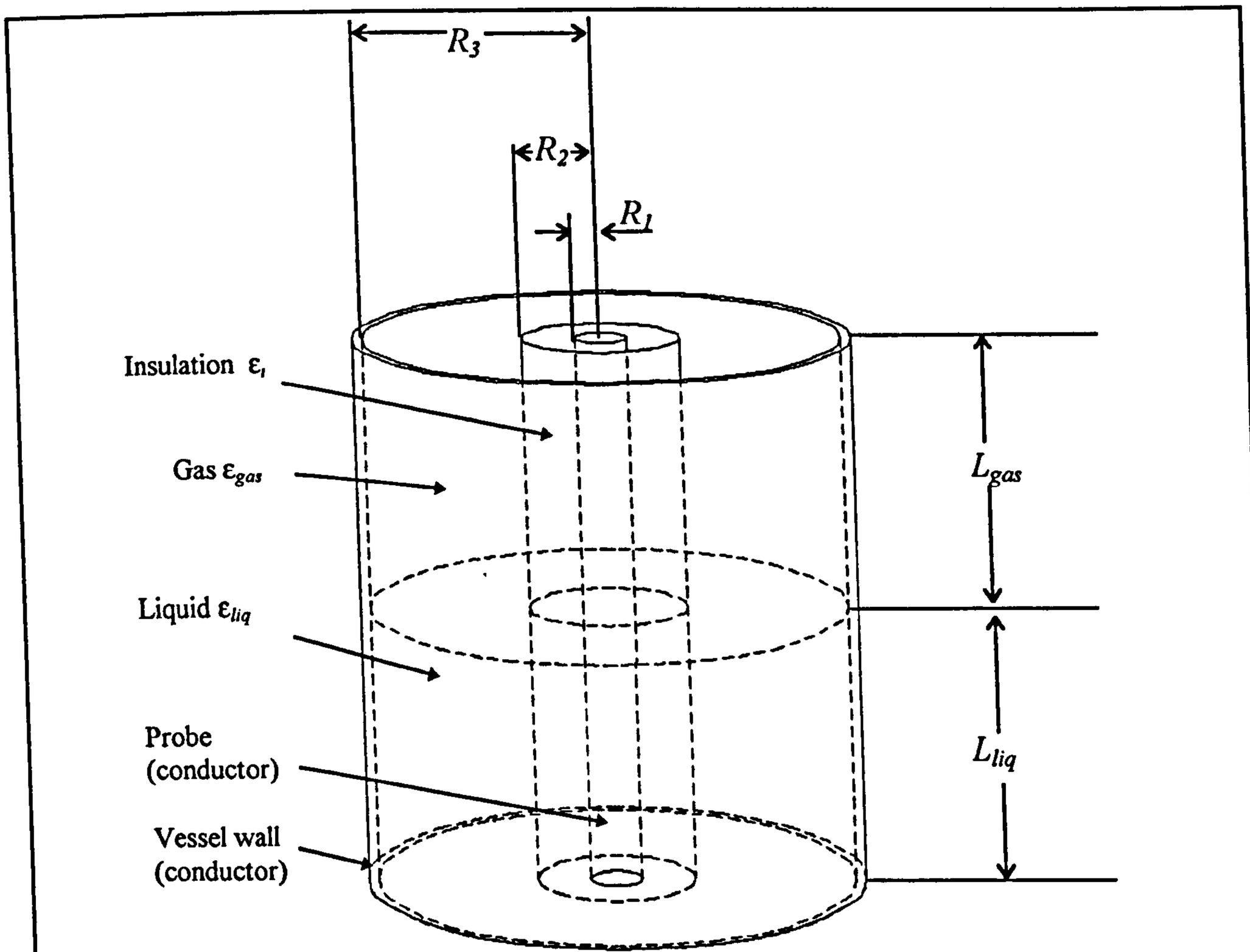

Figure 4.9 Idealised capacitance probe

The capacitance of the probe in figure 4.11 would be given by

$$C = \frac{L_{liq}}{\frac{1}{E_I} + \frac{1}{E_{liq}}} + \frac{L_{gas}}{\frac{1}{E_I} + \frac{1}{E_{gas}}}$$

where E_x is the capacitance per unit length of an annulus of the insulating material or electrolyte given by

$$E_I = \frac{2\pi e_0 \varepsilon_I}{\ln\left(\frac{r_2}{r_1}\right)} \quad E_{gas} = \frac{2\pi e_0 \varepsilon_{gas}}{\ln\left(\frac{r_3}{r_2}\right)} \quad E_{liq} = \frac{2\pi e_0 \varepsilon_{liq}}{\ln\left(\frac{r_3}{r_2}\right)}$$

r_3 = Vessel inner radius

r_2 = Insulation outer radius

r_1 = probe radius

ε = Relative permittivity

e_0 =Permittivity of free space = 8.854 x10^{-12} F m^{-1}

L = total length of the probe = 0.381 m

l = depth of ammonia

The capacitance per unit length of the probe insulation E_I was measured by wrapping the probe tightly with metal foil and measuring the capacitance between the probe and the foil directly. This gave E_I = 516.5 pF m^{-1}

The theoretical capacitance per unit length of the gas space, using ε=1.006 for the gas is 50 pF m^{-1}.

The theoretical capacitance per unit length for the liquid E_{liq} is 907 pF m^{-1} at 12°C using ε=18.1 at 12°C

When these values are substituted in the expression above for C then:

$C=17.4 + 283\,l$. where l is given in metres and C in pico Farads.

Converting to capacitance per unit mass then this becomes

$C=17.4 + 432\,M$ where M is given in kg and C in pico Farads.

This compares very well with the results of the calibration experiments which give $C=126 + 428\,M$ as shown in figure 4.12. The difference in the offset is due to the geometry of the lower part of the receiver.

The density and relative permitivity of the liquid ammonia vary with temperature but their effects largely cancel each other and the calibration changes by less than 1% for temperatures between 0°C and 40°C . The variation of relative permittivity with temperature is shown in figure 4.11 and a plot of the calibration slope against temperature is shown in figure 4.12. The experimentally derived calibration may

therefore be assumed accurate for that range of temperatures. It should however be noted that this capacitance is low and that its measurement at these level will be affected by stray capacitance from instrumentation cables (typically 150pF m^{-1}) and in some cases polarity of the circuit.

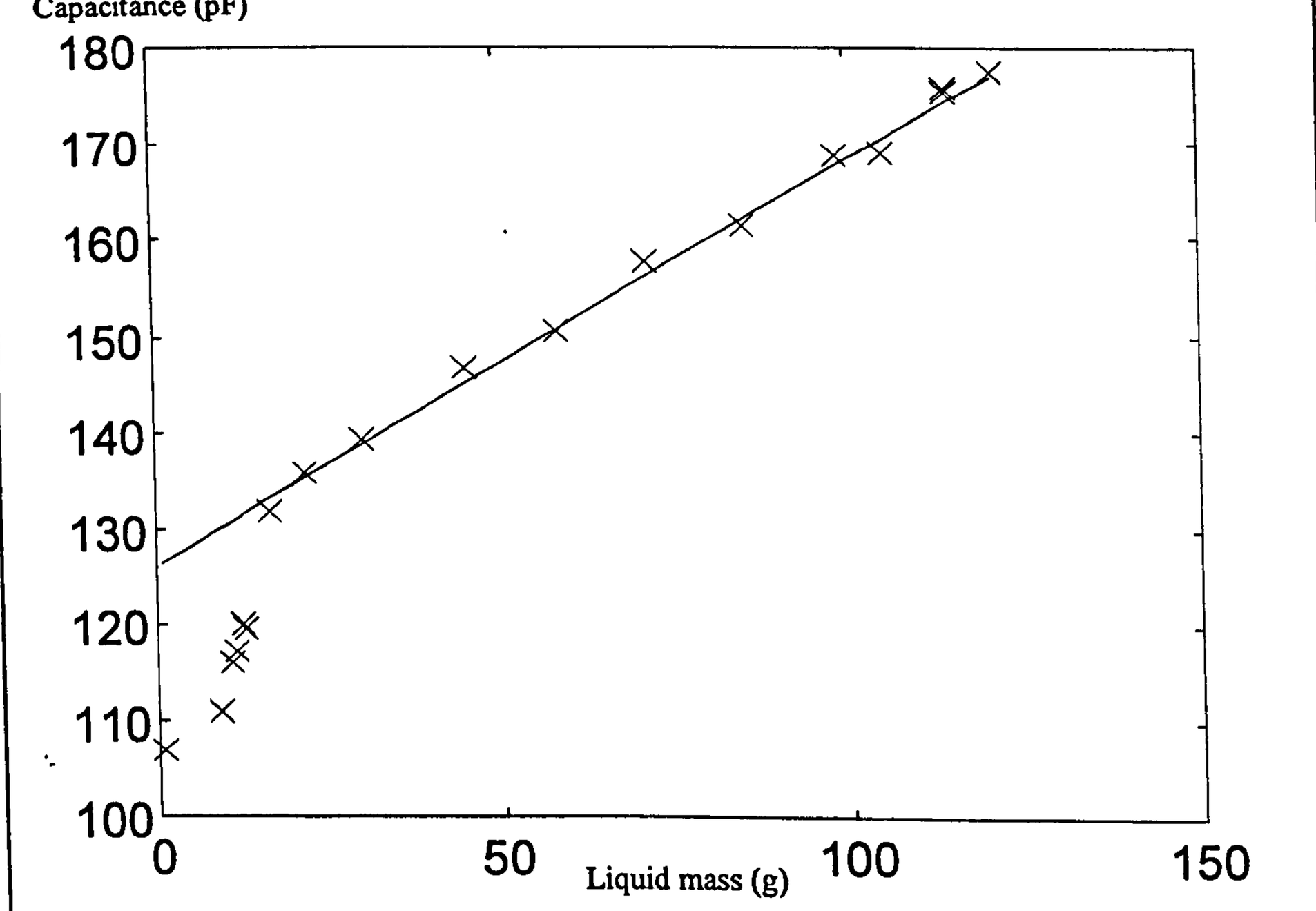

Figure 4.10 Calibration of the capacitance

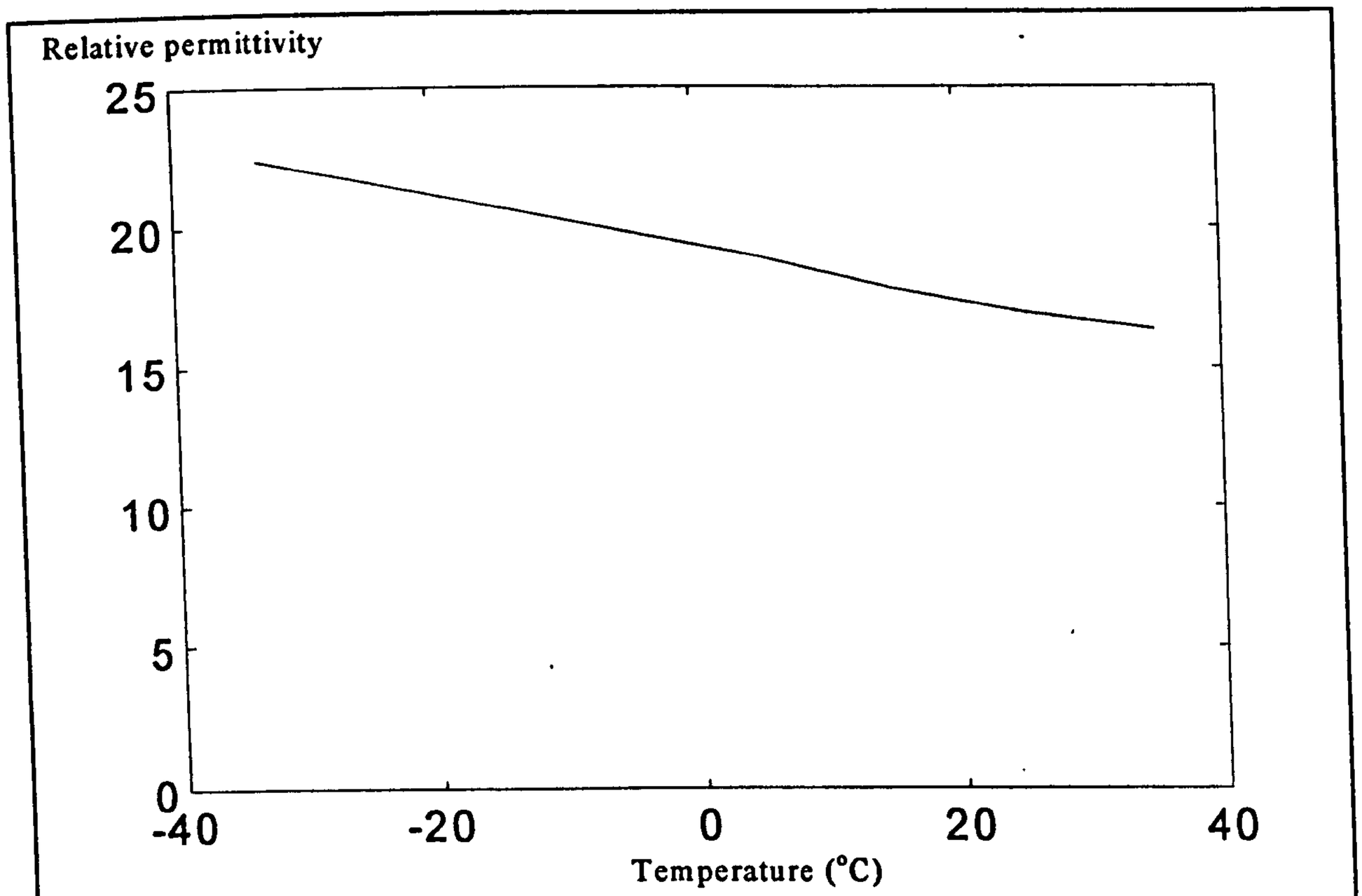

Figure 4.11 Effect of temperature on relative permittivity of ammonia liquid

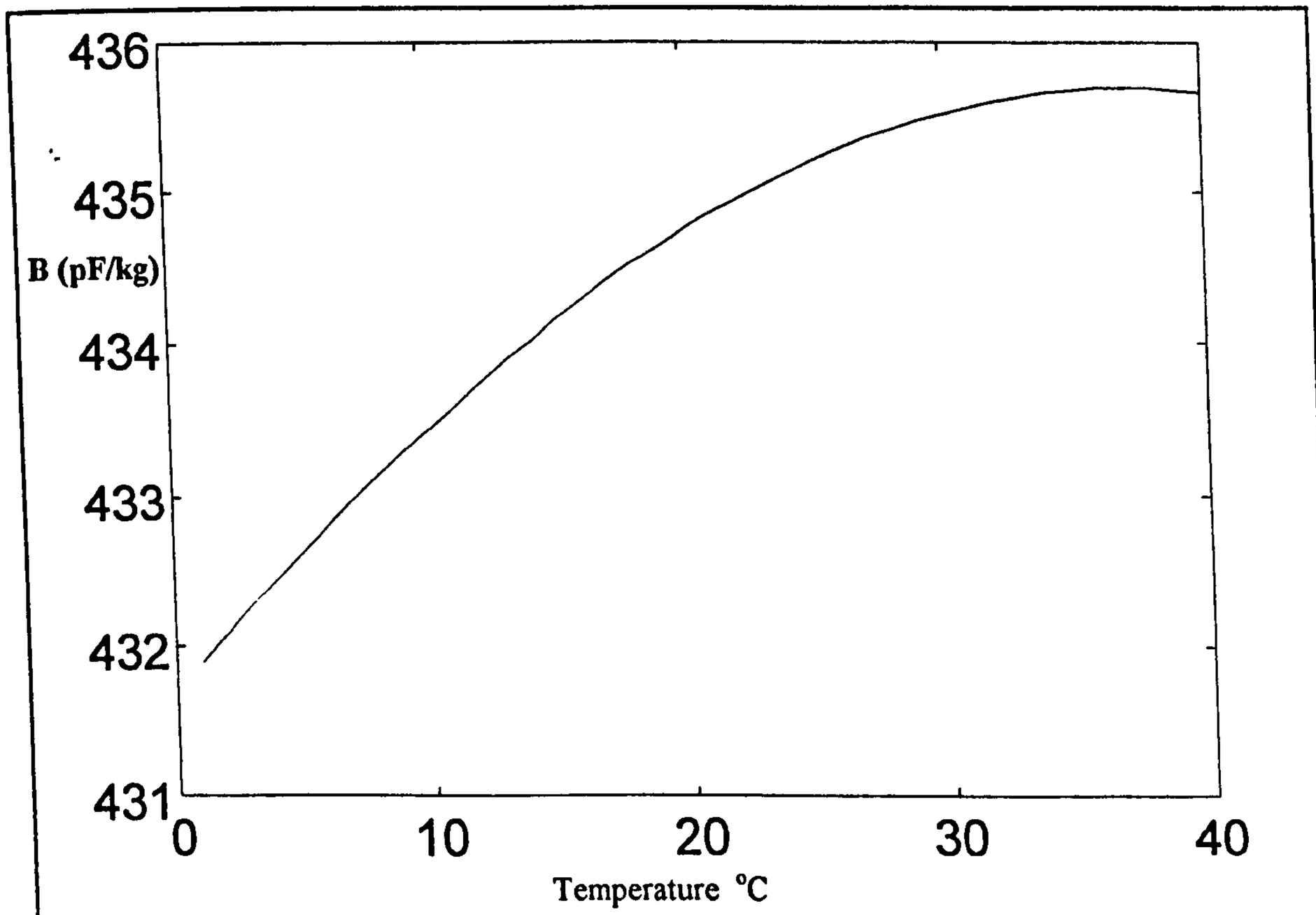

Figure 4.12 Constant B in capacitance probe calibration as a function of temperature.

Computer datalogging and control package

Logging and control of the rig was made to an I.B.M. copmatible personal computer through an Omega OM700 data acquisition and control unit. This device was programmed using a form of BASIC to monitor 12 thermocouples using its own cold junction compensation, 2 differential pressure transducers and 2 line pressures. The mass flow was calculated from the differential and static pressures at the venturi and the result used to control the motor speed in order to maintain a constant mass flow. Heater control was made by computer during some experiments, in particular those experiments where the inlet temperature was varied sinusoidally.

Chapter 5. Results of pressure loss tests

Introduction

The pressure loss through the granular carbon bed has been matched to parameters of length, flow, gas density, gas viscosity, bed voidage and grain radius by the Ergun equation [1]. Three gases, carbon dioxide, argon and ammonia were used to establish a friction factor as a function of the Reynolds number.

Nomenclature

c constant from the Ergun equation related to viscous pressure loss

d Grain diameter

D Bed diameter

Dh Hydraulic diameter (m)

f Friction factor

m Constant from the Ergun equation related to inertial pressure loss.

$\dot{m}$ Mass flow per unit cross section of the bed (kg/m^2 s)

Re_{Dh} Reynolds number based on hydraulic diameter and interstitial velocity

u Gas velocity over free area [$u = \dot{m} / \rho$] (m/s)

u_{int} mean interstitial gas velocity [$u_{int} = u / \psi$] (m/s)

$\frac{\Delta P}{L}$ Pressure loss per unit length of the bed (Pa/m)

μ Gas viscosity(Pa.s)

ρ Gas density(kg/m^3)

ψ Void ratio defined as the volume of the void / total volume

subscripts:

$_c$ Properties related to the core of the bed.

$_e$ Properties related to the edge of the bed.

The Ergun equation

The most commonly used correlation for flow in granular media is that developed by Sabri Ergun which may be represented as

$$\frac{\Delta P}{L} = c\frac{(1-\psi)^2}{\psi^3}\frac{\mu u}{d^2} + m\frac{(1-\psi)}{\psi^3}\frac{\rho u^2}{d} \qquad (5.1)$$

where u is the free stream velocity and d is the grain diameter. In his paper Ergun recommends c=150, m=1.75 although later workers have found that these values vary according to the size, shape and packing arrangement of the bed [2].

Using the interstitial velocity of the gas and the hydraulic diameter defined by

$$u_{\text{int}} = \frac{u}{\psi} \quad \text{and} \quad Dh = \frac{4\psi d}{6(1-\psi)}$$

then this becomes

$$\frac{\Delta P}{L} = \frac{4}{9}c\frac{\mu u_{\text{int}}}{Dh^2} + \frac{2}{3}m\frac{\rho u_{\text{int}}^2}{Dh}.$$

This in turn may be expressed as a relationship between a Darcey type friction factor and the Reynolds number using the hydraulic diameter and interstitial velocity since

$$f \equiv 2\frac{\Delta P}{L}\frac{Dh}{\rho u_{\text{int}}^2}$$

then

$$f = \frac{8}{9}\frac{c}{\text{Re}_{Dh}} + \frac{4}{3}m. \qquad (5.2)$$

This linear relationship allows a simple treatment of pressure loss data to find the values of m and c for a particular medium.

Method

Argon, carbon dioxide and ammonia were passed through the bed of carbon granules with the equipment described in chapter 4 to give a range of density, viscosity and mass flow. The flow rates and pressure differences were corrected for the effect of flow maldistribution at the interface of the bed and the container walls.

Characteristic dimensions of the carbon bed

In order to make an analysis of the behavior of the bed it is necessary to have estimates of the void ratio, specific surface area and grain diameter. The range of grain sizes is narrow but each grain is irregular and so the characteristic dimensions were evaluated as follows.

In order to estimate the void ratio of the packed bed a sample of known volume was saturated with water, the sample drained and the mass of water needed to refill the voids between grains measured. This suggested a ratio of voids to bulk volume of

$\psi = 0.374$

Although this method may not be as accurate as the three digit number given implies it does give repeatable results and allows comparison of similar materials. The bulk density of the carbon bed was measured. The average grain mass was calculated by weighing a known number of grains. This enables a calculation of the number of grains per unit volume and, with the void ratio the average volume of each grain. The characteristic diameter was then calculated on the assumption that the grain was spherical giving d=2.5mm. The specific surface area was then calculated with the same assumptions leading to $a = {}^{6(1-\psi)}/_{d}$ m^2m^{-3}.

Although this analysis uses the clearly fictitious assumption that the grains are spherical it does allow some consistency with other work.

Correction for flow maldistribution

The local values of void ratio and hydraulic radius are different near the flat surface of the vessel walls from those in the core of the bed where grains can pack more closely through interlocking. These different flow conditions allow a higher mass flow and local fluid velocity for a given pressure gradient in this region. The actual flow measured is therefore not evenly distributed over the bed cross section and in order to give a better estimate of the flow in the body of the bed this maldistribution must be accounted for.

An estimate of the flow conditions at the region of the wall may be made by consideration of the single layer of grains in contact with the wall. Assuming that the zone influenced by the presence of the wall extends to a thickness of one grain radius then the local void ratio ψ and hydraulic diameter Dh may be estimated.

For three cotangent spheres on a plane surface ψ =0.395, four spheres in a square arrangement give ψ=0.476. The mean, ψ_e =0.435 is taken to be a reasonable estimate of the true value. The hydraulic diameter may be calculated from

$Dh_e = \frac{4\psi d}{6(1-\psi)}$ giving a value of Dh_e=1.28mm. The values in the core of the bed are

ψ_c=0.374, Dh_c=0.996mm.

The Ergun equation (5.1) uses a value m that is referred to as the inertia tortuosity factor. It may be assumed that this factor is proportional to the changes in direction of the fluid per unit length of the bed then it is possible to make an estimate of the local value of m from the fit given by the uncorrected data. The

number of spheres within a volume is proportional to $1-\psi$ and thus an estimate of the ratio of m in the wall region to that in the core may be made.

Using the subscript $_c$ and $_e$ to represent core and edge conditions respectively some manipulation of the Ergun equations for each condition gives

$$\rho\frac{\Delta P}{L} = A_c\dot{m}_c + B_c\dot{m}_c^2 = A_eK\dot{m}_c + B_eK^2\dot{m}_c^2 \qquad (5.3)$$

where

$$A_c = c\frac{(1-\psi_c)^2\mu}{\psi_c^3 d^2}, \quad B_c = m\frac{(1-\psi_c)}{\psi_c^3 d}, \quad A_e = c\frac{(1-\psi_e)^2\mu}{\psi_e^3 d^2}, \quad B_e = m\frac{(1-\psi_e)^2}{(1-\psi_c)\psi_e^3 d}$$

and

$$K = \frac{\dot{m}_e}{\dot{m}_c}$$

equation 5.3 gives an equation that is quadratic in K and can be solved by

$$K = \sqrt{\frac{p^2}{4}+q} - \frac{p}{2}$$

where

$$p = \frac{2}{3}\frac{c}{m}\frac{1}{\mathrm{Re}_{Dh}}$$

$$q = \frac{(1-\psi_c)^2}{(1-\psi_e)^2}\frac{\psi_e^3}{\psi_c^3}\left(\frac{2}{3}\frac{c}{m}\frac{1}{\mathrm{Re}_{Dh}}+1\right)$$

It is possible to use the same method without the explicit link that is made between void ratio and hydraulic diameter that has been used here. The effect of Dh is strongest at low Reynolds numbers, and for the purposes of this study the variation of K with credible values of Dh_e is not considered significant.

A plot of $\frac{\dot{m}_e}{\dot{m}_c}$ against Re_{Dh} is shown in figure 5.1

The corrected mass flow is therefore given by

$$\dot{m}_c = \frac{\overline{\dot{m}}}{1+2(k-1)\frac{d}{D}}$$

Where $\overline{\dot{m}}$ is the total mass flow divided by the whole cross section area, d is the grain diameter and D is the bed diameter.

Since the value of $\frac{d}{D}$ is 0.02 for the equipment then the effect is not great and the approximations made in the derivation of K may be justified for this analysis.

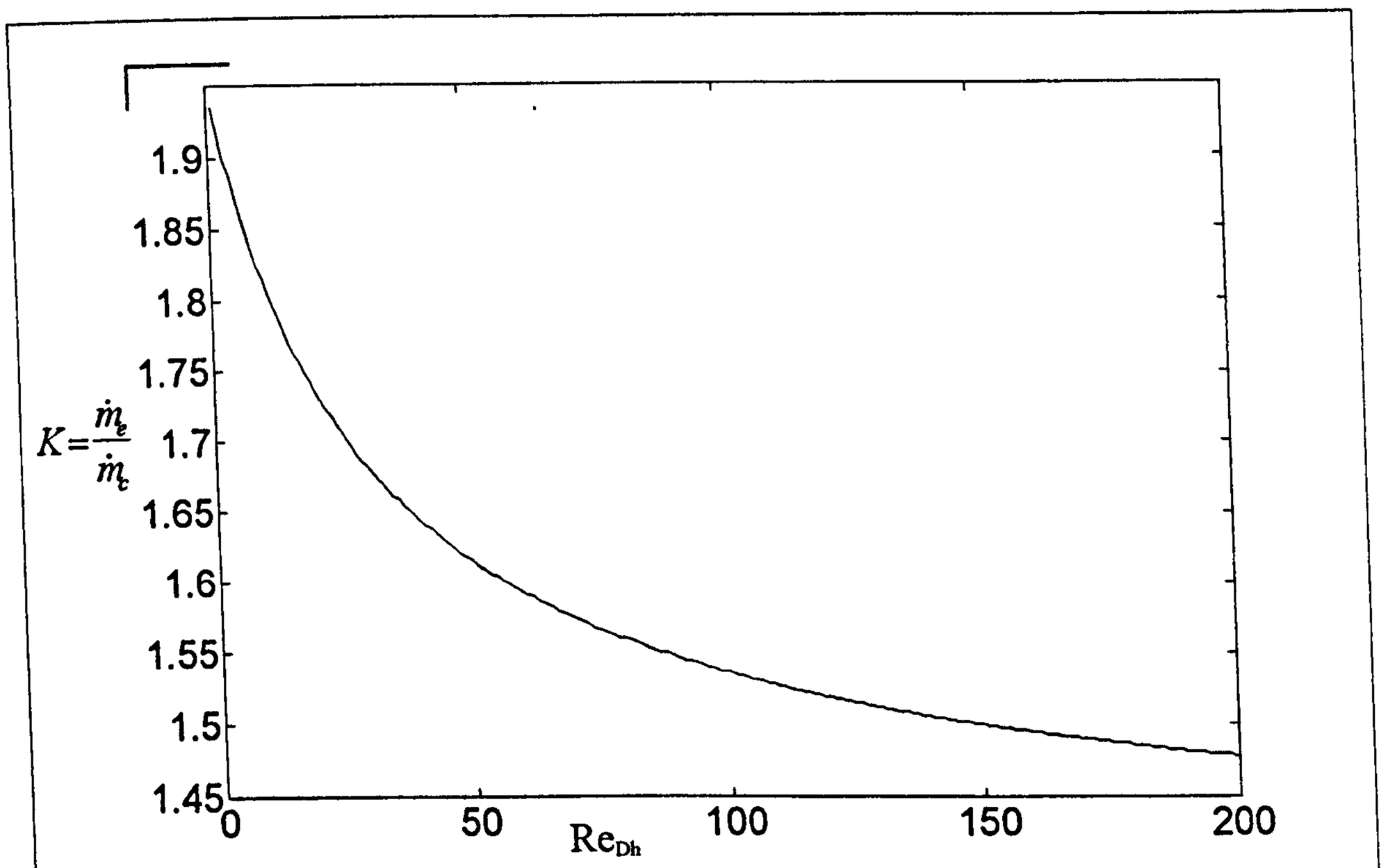

Figure 5.1: Ratio of edge to core flowrates as a function of reynolds number.

Correction for entrance and exit losses

The pressure loss due to the entry of the fluid into the bed may be estimated from the empirical relationship given by Kays and London [3]

$$C_{entry} = 0.42(1-\psi)$$

and for exit by

$$C_{exit} = (1-\psi)^2$$

where

$$\Delta P = C\frac{1}{2}\rho u_{\text{int}}^2$$

These relationships are based on sharp entrance and exit profiles, hence figures calculated in this way give an upper bound to the loss. For the range of conditions examined here the entry and exit losses are negligibly small, typically less than one Pascal compared with the total pressure loss which lies in the range 200-1700 Pa.

Estimates of gas properties.

The density of ammonia is well documented in reference [4]. These values have been fitted to a polynomial in temperature and pressure and this is used to calculate the density for the experiments. Neither carbon dioxide or argon deviate appreciably from ideal behavior over the conditions used. The gas constant of carbon dioxide is taken as 208 $Jkg^{-1}K^{-1}$and for carbon dioxide as 297 $Jkg^{-1}K^{-1}$ The viscosities of argon and carbon dioxide are taken to be those documented at atmospheric pressure [5] as a function of temperature alone since the real pressures used are far from their saturation conditions. The viscosity of ammonia is a function of both temperature and pressure. Reference [4] lists the values for both saturation pressure and atmospheric pressure over a range of temperatures. The viscosity used in this work is calculated from these values by interpolation between the saturation and low pressure data assuming that at a fixed temperature it varies linearly with density.

Comments upon the results

The corrected data are shown in figure 5.2 as the friction factor f plotted against the inverse of the Reynolds number. The data for argon and carbon dioxide provide a good fit to the Ergun equation with m=2.14 and c=316. The regression coefficient is 0.9922. Figure 5.3 shows the ratio of measured to predicted mass flow plotted against Reynolds number.

It is clear that there is much more uncertainty over the data for ammonia. This may be accounted for by experimental difficulties that were encountered with the equipment and in particular the softening of the epoxy resin binding the sensing strain gauge to the sensing membrane in the differential pressure transducers. It may be observed that if the mass flow figures for the experiments with ammonia are reduced by 5% then the results lie symmetrically about the data points for the other two gases and give a reasonable visual fit however this cannot be justified on other than subjective grounds.

Figure 5.4 compares the deduced values of m and c in with the results of studies by Handley and Heggs[2]. It is clear that the results for different shapes and sizes fall over a wide range. It may be assumed that a similar variation, particularly of m with grain size will apply to those used in this study, and in the range of mass flows that are of interest in heat pump applications it is the inertia pressure loss that dominates. Therefore, although the Ergun equation with the values of m and c given above may be used with confidence for a range of fluids and flowrates some caution must be used in its extrapolation to different grain sizes. For an 'order of magnitude' estimate of the pressure loss it may be useful to consider that from the form of equation 5.1 that there will be approximately $2m\frac{(1-\psi)}{\psi^3 d} \approx 4\text{x}10^4$ velocity heads lost per metre length of the bed for Reynolds numbers above 200.

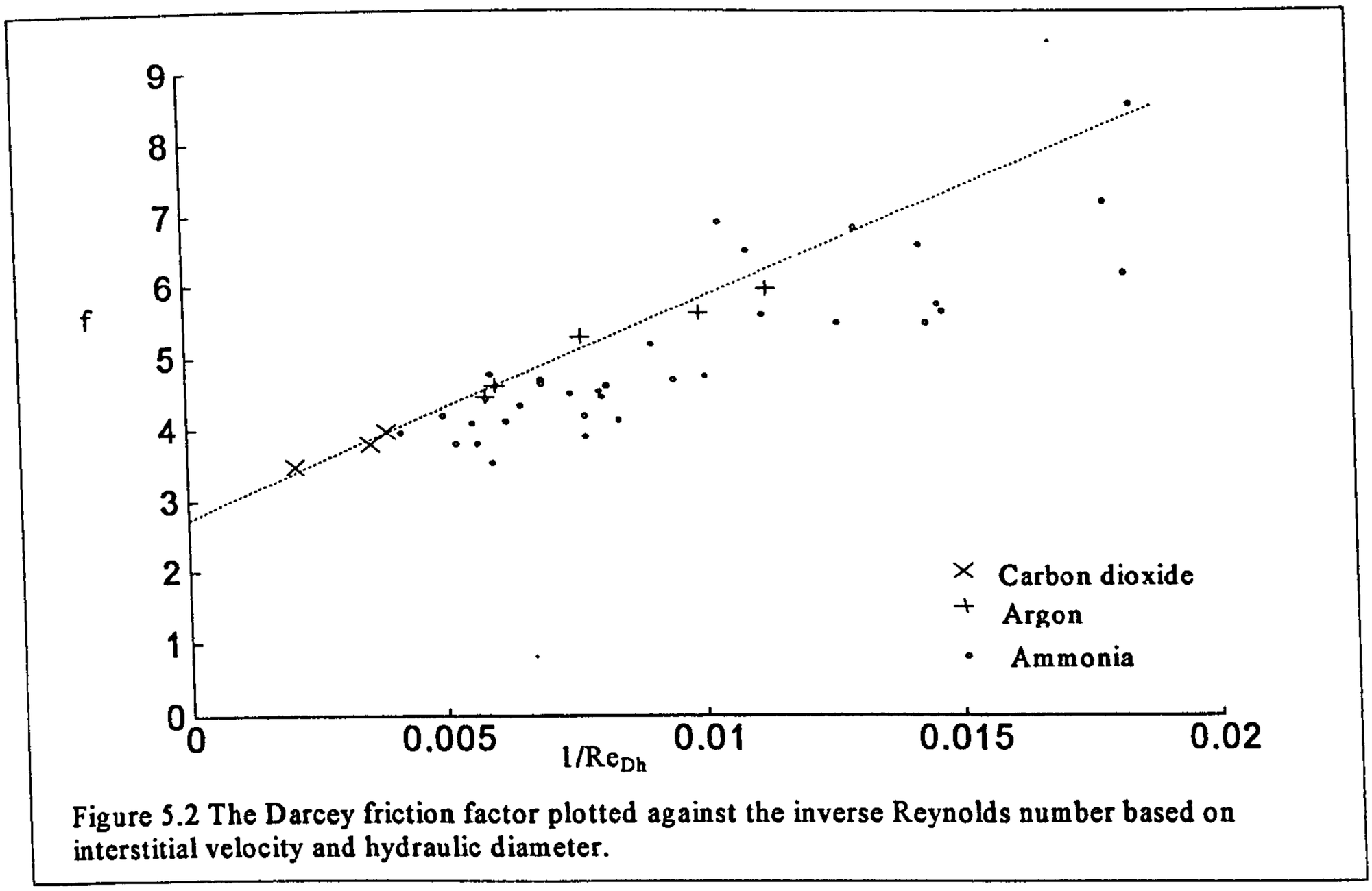

Figure 5.2 The Darcey friction factor plotted against the inverse Reynolds number based on interstitial velocity and hydraulic diameter.

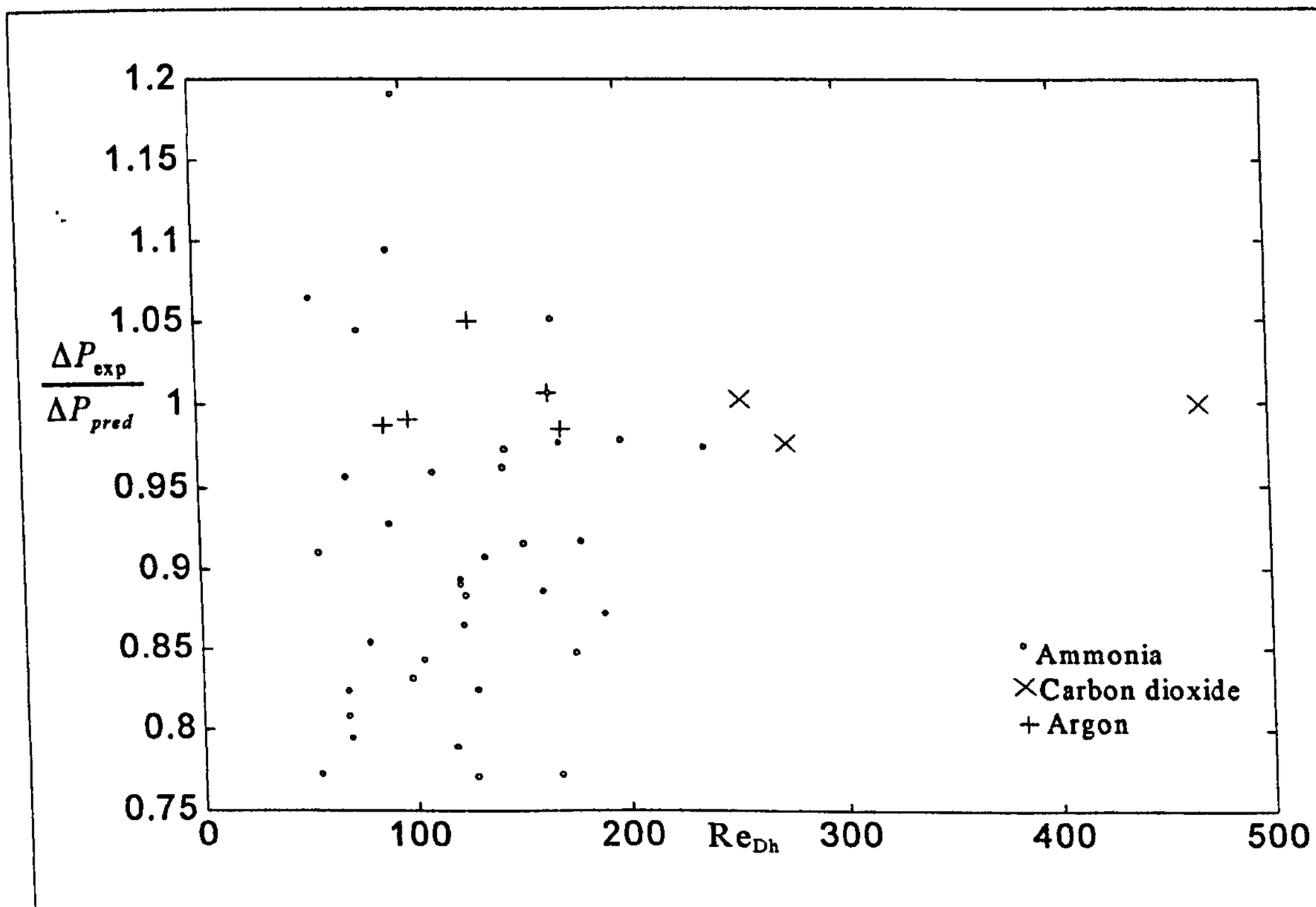

Figure 5.3 A comparison of experimental and predicted pressure losses

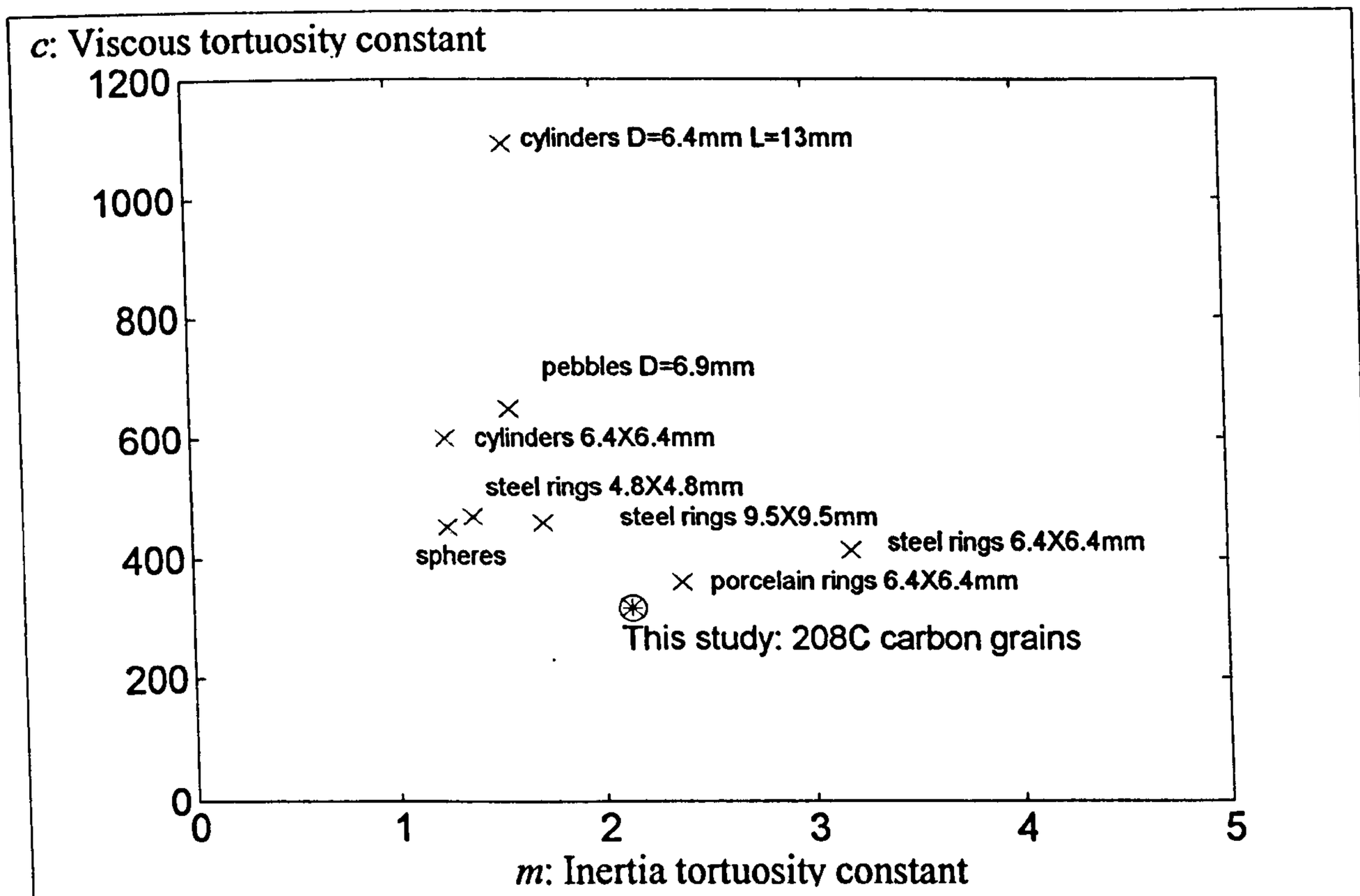

figure 5.4 Comparison of values of *m* and c for a variety of randomly packed shapes. Adapted from Handley and Heggs,*Momentum and heat transfer mechanisms in regularly shaped packings*,Trans. Inst.Chem.Eng.V46.,1968.

Pressure loss data: ammonia
Bed length: 598mm
Venturi used: 6mm dia

Mass flow $kg/m^2.s$	Pressure loss Pa	Gas density kg/m^3	Gas Viscosity Pa.s
0.418144	694.	2.11341	.00001113
0.538014	633.	3.33802	.00001194
0.451855	687.	2.45551	.00001133
0.545466	800.	3.02400	.00001177
0.546905	803.	3.03696	.00001179
0.482475	802.	2.66170	.00001152
0.754763	705.	5.01988	.00001188
0.747673	900.	4.16658	.00001125
0.745275	959.	4.89796	.00001171
0.732891	1056.	3.97218	.00001139
0.730830	951.	4.57470	.00001168
0.619027	994.	3.19737	.00001135
0.614934	1074.	2.89056	.00001130
0.555908	707.	3.01559	.00001143
0.359145	310.	4.03362	.00001198
0.790187	1169.	3.84690	.00001165
0.856707	1196.	4.11646	.00001189
1.120724	1724.	5.09283	.00001248
0.549532	742.	3.00282	.00001126
0.303219	641.	1.72556	.00001039
0.296202	312.	2.72220	.00001120

0.298276	359.	2.87639	.00001122
0.938578	1367.	4.77599	.00001247
0.672452	1047.	3.29173	.00001162
0.938578	1367.	4.77599	.00001247
0.231242	321.	2.10474	.00001085
0.235160	297.	2.80848	.00001138
0.238791	216.	2.87279	.00001145
0.299208	291.	3.06635	.00001156
0.299991	310.	2.93643	.00001151
0.394000	669.	2.66401	.00001135
0.420764	709.	3.04133	.00001154
0.389952	502.	2.98944	.00001154
0.550588	734.	3.25012	.00001178
0.548087	808.	2.98132	.00001164
0.609645	817.	3.62827	.00001203
0.733012	1095.	3.55366	.00001206

□

Pressure loss data: argon
Bed length:490mm
Venturi used: 5mm dia

Mass flow $kg/m^2.s$	Pressure loss Pa	Gas density kg/m^3	Gas Viscosity Pa.s
0.7408	551	10,33	0.0000221
1.08436	1062	10,20	0.0000221
1.383	1515	10.11	0.0000221
0.8267	672	9.945	0.0000218
1.4082	1569	9.78	0.0000218

Pressure loss data: carbon dioxide
Bed length:490mm
Venturi used: 5mmdia

Mass flow $kg/m^2.s$	Pressure loss Pa	Gas density kg/m^3	Gas Viscosity Pa.s
1.4585	646	22.83	0.0000151
2.6413	1868	22.60	0.0000149
1.555	718	22.29	0.0000149

References for chapter 5

[1] **Ergun, S.** Fluid flow through packed columns. *Chemical Engineering Progress* ,vol 48 pp89-94 (1952)

[2] **Handley, D. Heggs, P.J.** Momentum and heat transfer mechanisms in regular shaped packings.

Transactions of the Institution of Chemical Engineers, Vol 46 ppT251-T263

[3] **Kays, W.M., London, A.L.** Compact Heat Exchangers *McGraw -Hill* (1984)

[4] Thermodynamic and physical properties of ammonia. *International Institute of Refrigeration.* Paris.

(1981)

[5] Physical property data tables published in *Hemisphere Handbook for Heat Exchanger Design.*

Hemisphere, Washington

Chapter 6 Heat transfer experiments and results

Introduction

A rapid change of inlet temperature was applied to the bed using the equipment described in chapter 4 and the temperatures at the downstream stations recorded. A computer programme was then used to match the response of the bed to that of a mathematical model. This process was carried out using ammonia and argon.

Analysis programme

A top level flowchart of the programme used to find the effective heat transfer coefficient is shown in figure 6.1 At its core is a finite difference model of the bed using the trapezium method proposed by Willmott and described in chapter 3 with some modifications for the effects of adsorption. The flowrates, pressures and inlet temperatures are used to derive a theoretical exit temperature profile for some point downstream in the bed. These theoretical profiles are compared with the experimental data and the heat transfer coefficient adjusted until the best match is made. The program was written in Fortran 90 and takes some five minutes to run for each data set on a Sun sparc 5 workstation.

The analysis program uses the Schumann model [1] and therefore makes all the assumptions of that model that follow:

- There is no axial conduction within the gas or solid phases
- The finite conductivity of the solid and the effect of axial mixing in the gas may be accounted for by the use of a modified heat transfer coefficient.

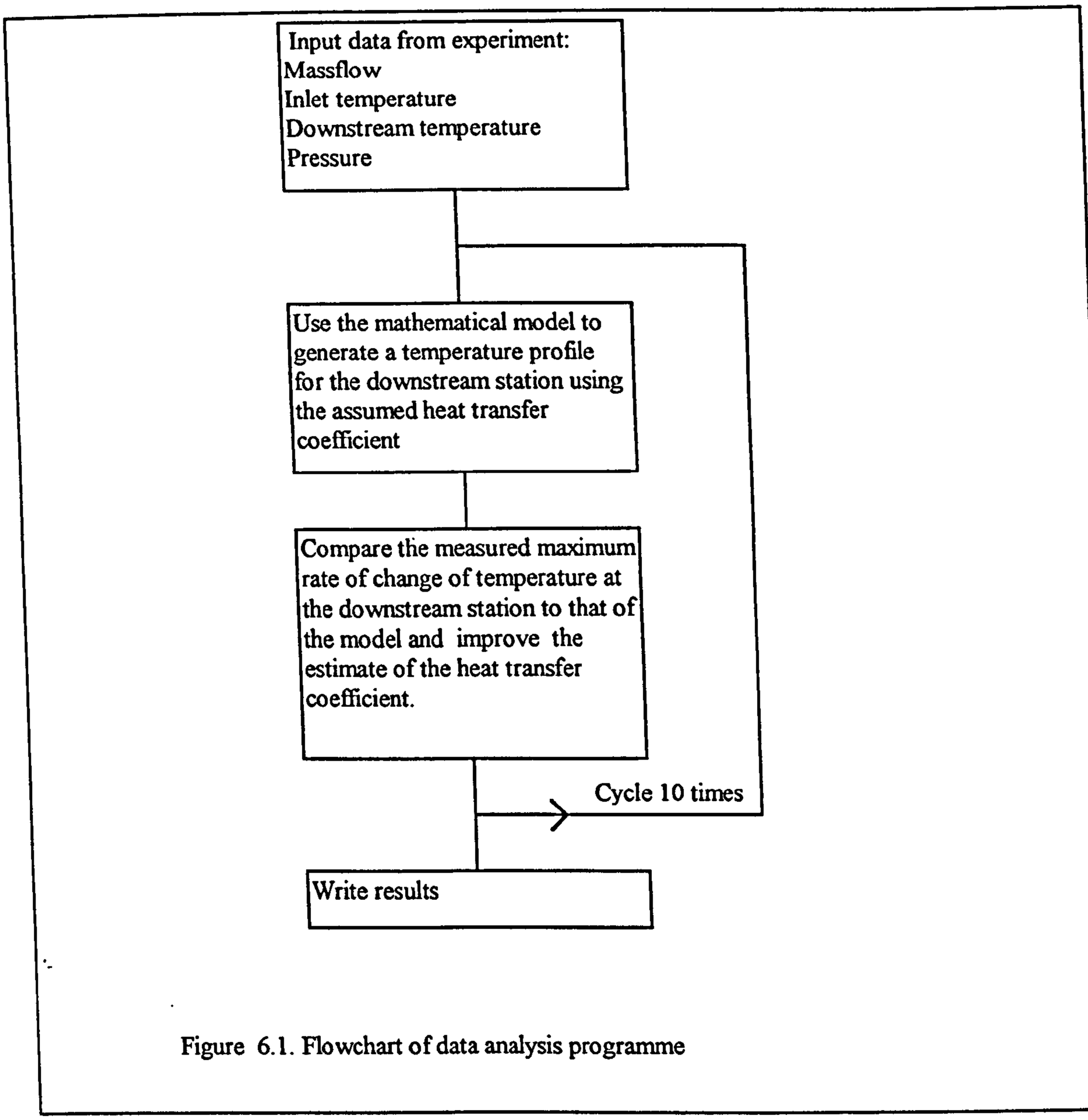

Figure 6.1. Flowchart of data analysis programme

- There is no radial conduction through the bed to the pressure vessel walls.
- The mass flow is constant over the whole cross-section of the bed.

Application of the finite difference model

Since the data is recorded at three second intervals it is expanded by linear interpolation to give the shorter timesteps, typically less than one second, required by the model for accuracy and stability. It is assumed that the temperature measured by the thermocouples is the solid temperature, and so the model differs

from the conventional regenerator model in that the inlet gas temperatures must be calculated from the rate of change of the solid temperature at the inlet using

$$T_g = \frac{m c_{eff}}{\alpha a} \frac{\partial T_s}{\partial t} + T_s$$

where c_{eff} is the effective heat capacity of the solid.

The effective heat capacity of the bed is a function of the enthalpy of desorption of ammonia and the heat capacity of the carbon with the adsorbed phase of ammonia.

$$c_{eff} = c_s + x c_a - h_{ag} \frac{\partial x}{\partial T}$$

where

c_s = Heat capacity of carbon (J/kg K)

c_a = Heat capacity of the adsorbed phase (J/kg K)

x = Concentration of adsorbate (kg/kg)

h_{ag} = Enthalpy of desorption (J/kg)

When the pressure is not constant then the effect of the change in concentration caused by the change in saturation temperature and consequent heating or cooling of the solid should be taken into account.

So

$$\left(T_g - T_s\right)\frac{\alpha a}{m} + h_{ag}\left(\frac{\partial x}{\partial T_s}\frac{\partial T_s}{\partial t} + \frac{\partial x}{\partial T_{sat}}\frac{\partial T_{sat}}{\partial t}\right) = \left(c_s + x c_a\right)\frac{\partial T_s}{\partial t}$$

Which may be rearranged as

$$\frac{\partial T_s}{\partial t} = \frac{\left(T_g - T_s\right)\alpha a}{m\left(c_a + x c_s - h_{ag}\dfrac{\partial x}{\partial T_s}\right)} + \frac{h_{ag}\dfrac{\partial x}{\partial T_{sat}}\dfrac{\partial T_{sat}}{\partial t}}{c_a + x c_s - h_{ag}\dfrac{\partial x}{\partial T_s}}. \qquad (6.1)$$

In the right hand side of equation 6.1 there are clearly two parts, a temperature change due to convective heat transfer and a temperature change driven by the change in saturation temperature.

The finite difference equation (3.17) now becomes

$$T_s(r,s)=\frac{\left(\frac{2-A}{2+A}T_s(r,s-1)\ +\ \frac{A}{2+A}T_g(r,s-1)\ +\ \frac{A}{2+A}\frac{B}{2+B}T_g(r,s-1)\ +\ \frac{A}{2+A}\frac{2-B}{2+B}T_g(r-1,s)+\frac{2}{2+A}C\right)}{1-\frac{AB}{(2+A)(2+B)}}$$

and equation (3.18) becomes

$$T_g(r,s)=\frac{2-B}{2+B}T_g(r-1,s)\ +\ \frac{B}{2+B}T_s(r,s)\ +\ \frac{B}{2+B}T_s(r-1,s)$$

where

$$A=\frac{\alpha a\,\Delta t}{m\left(c_s+x\,c_a-h_{ag}\frac{\partial x}{\partial T_s}\right)}$$

$$B=\frac{\alpha a\Delta y}{\dot{m}c_p}$$

$$C=\frac{h_{ag}\frac{\partial x}{\partial T_{sat}}\Delta T_{sat}}{c_s+x\,c_a-h_{ag}\frac{\partial x}{\partial T_s}}$$

The Dubinin - Ashtakov equation is taken to represent the adsorption characteristic of the carbon.

$$x=x_o\exp\left(-k\left(\frac{T}{T_{sat}}-1\right)^n\right)$$

where x_o, k and n are constants measured by experiment and both T and T_{sat} are expressed as absolute temperature and x is the concentration in mass of adsorbate per mass of adsorbent.

The partial differentials of x with temperature and saturation temperature are therefore

$$\frac{\partial x}{\partial T_{sat}} = \frac{x\,k\,n\,T\left(\frac{T}{T_{sat}}-1\right)^{n-1}}{T_{sat}^2}$$

$$\frac{\partial x}{\partial T} = -\frac{x\,k\,n\left(\frac{T}{T_{sat}}-1\right)^{n-1}}{T_{sat}}$$

Implicit in this calculation method is the assumption that $\frac{\partial x}{\partial T}$ and $\frac{\partial x}{\partial T_{sat}}$ are contsant through each time step.

Matching of the model to the results

When the programme has generated a theoretical temperature history for the downstream station in the bed this is differentiated with respect to time and passed through a smoothing process and compared with the differentiated and smoothed temperature history obtained by experiment. The programme produces a new estimate of the effective Nusselt number by comparing the maximum value of $\frac{\partial T_s}{\partial t}$ using

$$Nu_{new} = \left[\left(2\frac{\frac{\partial T}{\partial t}\text{ experiment}}{\frac{\partial T}{\partial t}\text{ model}}\right)-1\right]Nu_{old}.$$

This method usually produces a convergence to within 1% by seven cycles. During the simulation the inlet mass flow is calculated from the data returned by the venturi tube but is corrected by a factor optimised by the program to ensure that the time for the wave to reach the exit of the bed is the same as that in the experiment. This correction factor is recorded by the program and varies from 0.86 to 0.94. This will be discussed further in chapter 7.

At each step along the bed the mass flow for the next step is adjusted to account for the gas that has been put into or taken out of the stream by the carbon.

The Reynolds number and Nusselt number during each run are not truly constant in either time or space. There are small variations of mass flow during each run and both viscosity and conductivity of the gas are functions of temperature and, less strongly of pressure. In the model the value of Reynolds and Nusselt number returned are based on the average conditions. Inside the program, however the local value of Reynolds number is calculated for the particular position and time. The local Nusselt number is derived from the average value of Nusselt number on the assumption that $Nu \propto \mathrm{Re}$. The local heat transfer coefficient is then calculated using the gas conductivity for those particular conditions. The use of a small temperature step and constant mass flow makes this technique valid within the overall accuracy of the experiment.

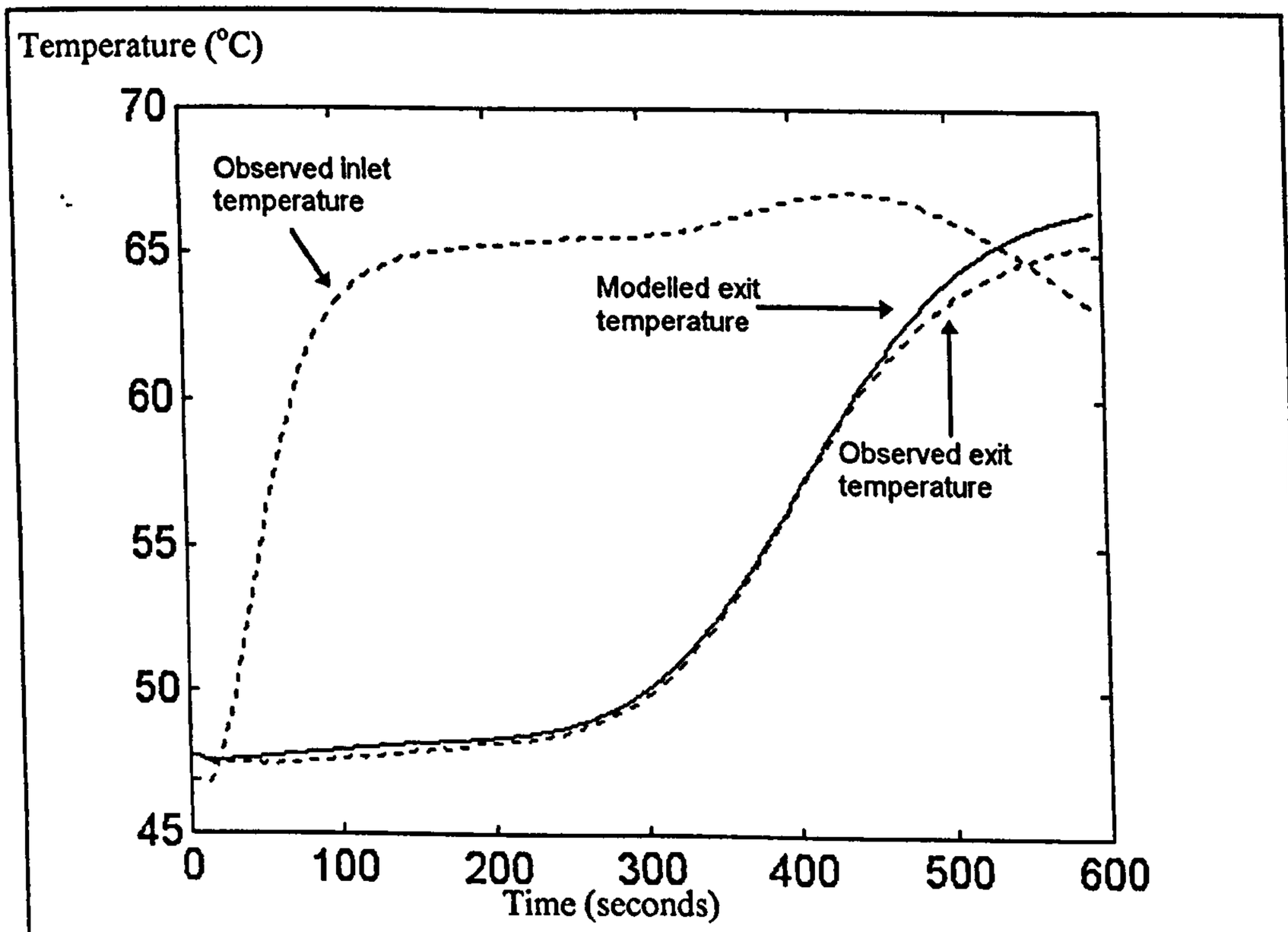

Figure 6.2 an example plot comparing the observed and modelled temperature histories of a typical experiment.

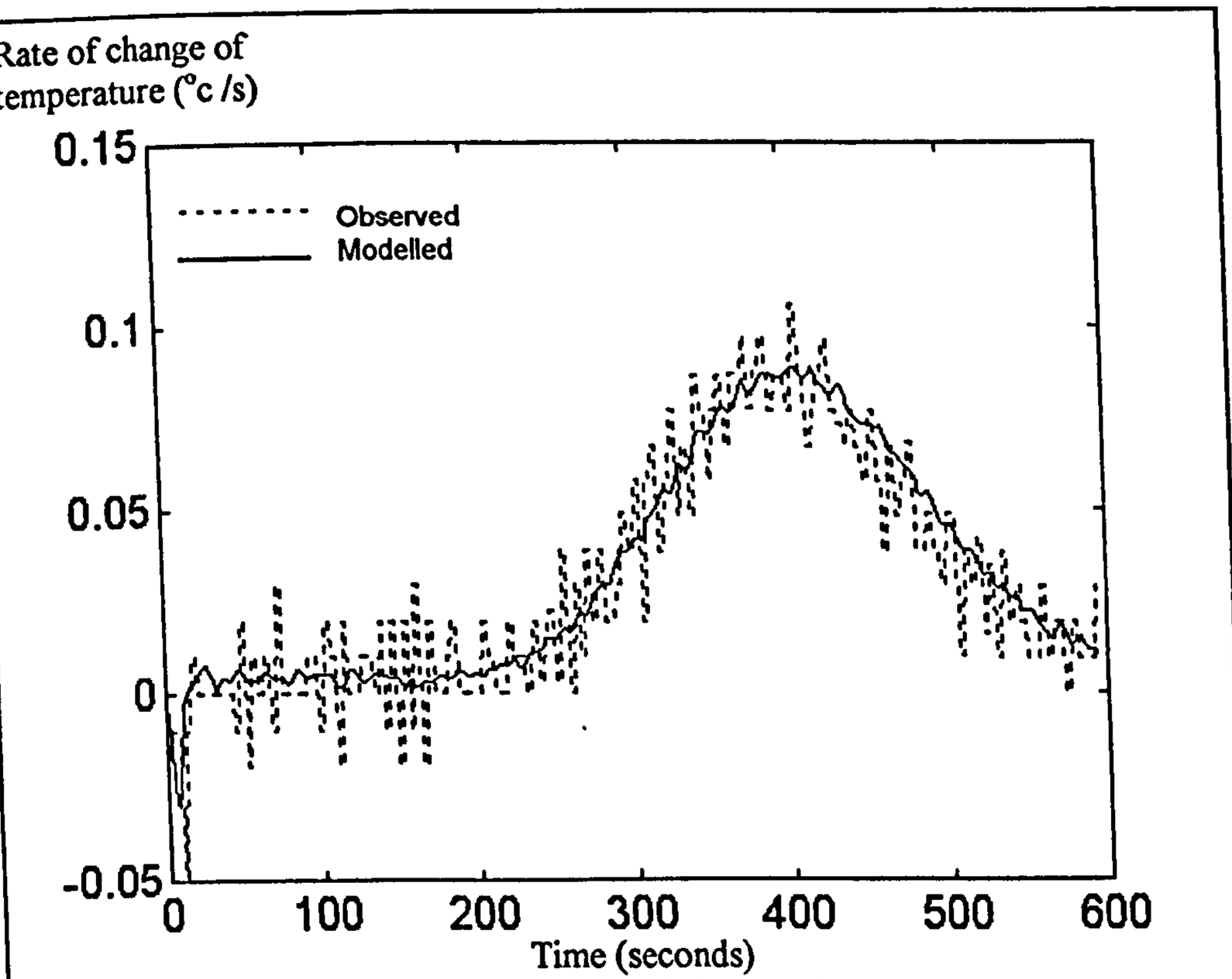

Figure 6. 3 Observed and modelled rates of change of temperature for the same experiment as figure 6.

Thermophysical properties of ammonia used in the simulations

Saturation temperature

The relationship between pressure and temperature at saturation can be approximated by:

$$T_{sat}=2766.1/(11.5774-\ln(P)) \qquad (6.2)$$

where T_{sat} is expressed in K and pressure in bar(a). This provides an accuracy of +0.25°K ,-0.5 K for the range 2bar < T_{sat} < 25 bar and +0.25 K-0.15 Kor the range 0.5bar < T_{sat} < 60bar

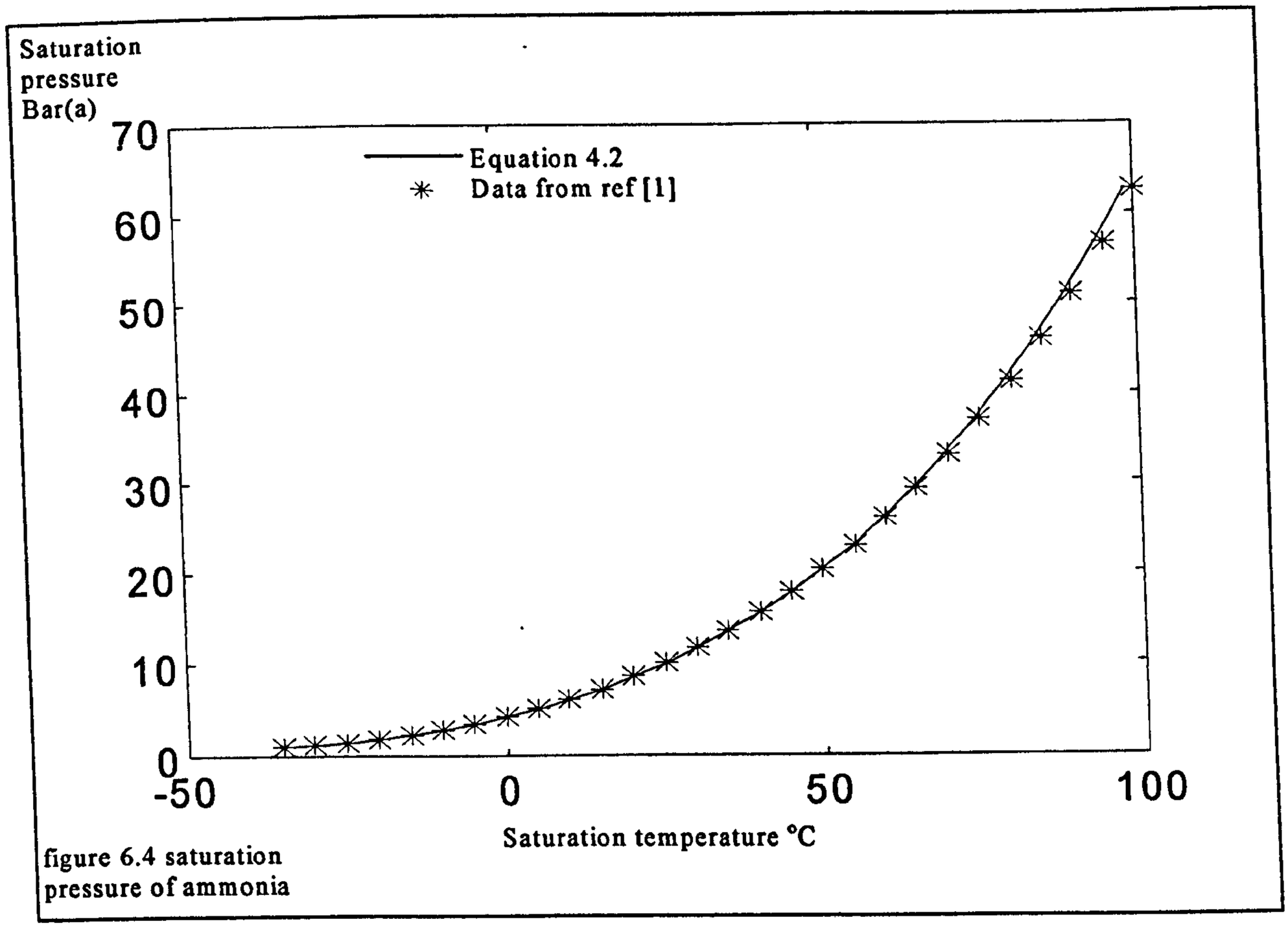

figure 6.4 saturation pressure of ammonia

Density

The density of the gas is calculated from an algorithm that returns an approximate value for R from the temperature and superheat. This algorithm gives an accuracy of + or - 1.5 % over the range of $0 < T_{sup} < 100^{\circ}C$, $-40 < T_{sat} < 60^{\circ}C$.

$$R=448.77 - 1.0763\,T_{sat} + (1.430 + 0.02715\,T_{sat})\,T_{sup}^{0.67} \ldots\ldots$$

$$\ldots + (0.0975 + 0.001352\,T_{sat})\,T_{sup} \ldots\ldots$$

$$- (758.65\times10^{-6} + 1.97\times10^{-6}\,T_{sat})\,T_{sup}^{2} \qquad (6.3)$$

Where T_{sat} and T_{sup} are in °C.

Heat capacity of the gas

The specific heat capacity at constant pressure is found from an algorithm that uses the superheat (T_{sup}) and the saturation temperature in °C to return a value in

kJ/kg K to an accuracy of + or - 1.5% within the range of $0 < T_{sup} < 100°C$, $-40 < T_{sat} < 60°C$.

$$c_p = 1.962 + 0.00168\,T_{sup} + 0.00099\,T_{sat} - 4.5754 \times 10^{-6}\,T_{sat}^2 + \ldots\ldots$$

$$\ldots.(0.0049714\,T_{sat}^2 + 0.55846\,T_{sat} + 27.048)/(T_{sup} + 40) \qquad (6.4)$$

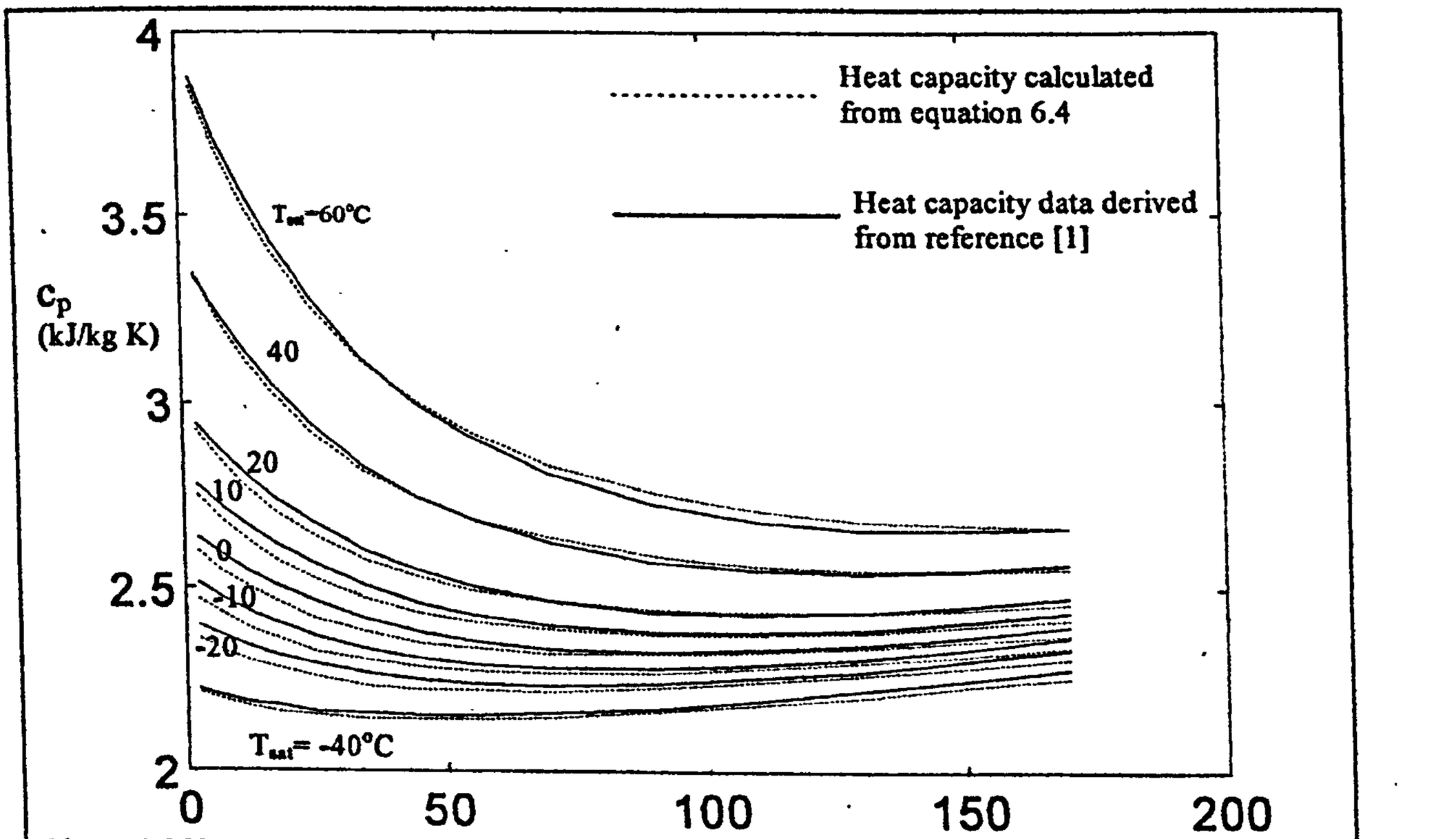

Figure 6.5 Heat capacity of ammonia gas

Heat capacity of the adsorbed phase

The heat capacity of the adsorbed phase on the carbon is not known, but the value used by most workers is that of the adsorbed phase and that is the value used in this work.

The heat capacity of the liquid is plotted in figure 6.6 from data given in [1] with the algorithm used in the model,

$c_a = 4.633 - (0.0002302T) + (0.000136T^2)$ where T is given in °C and c_a in kJ/kg K.

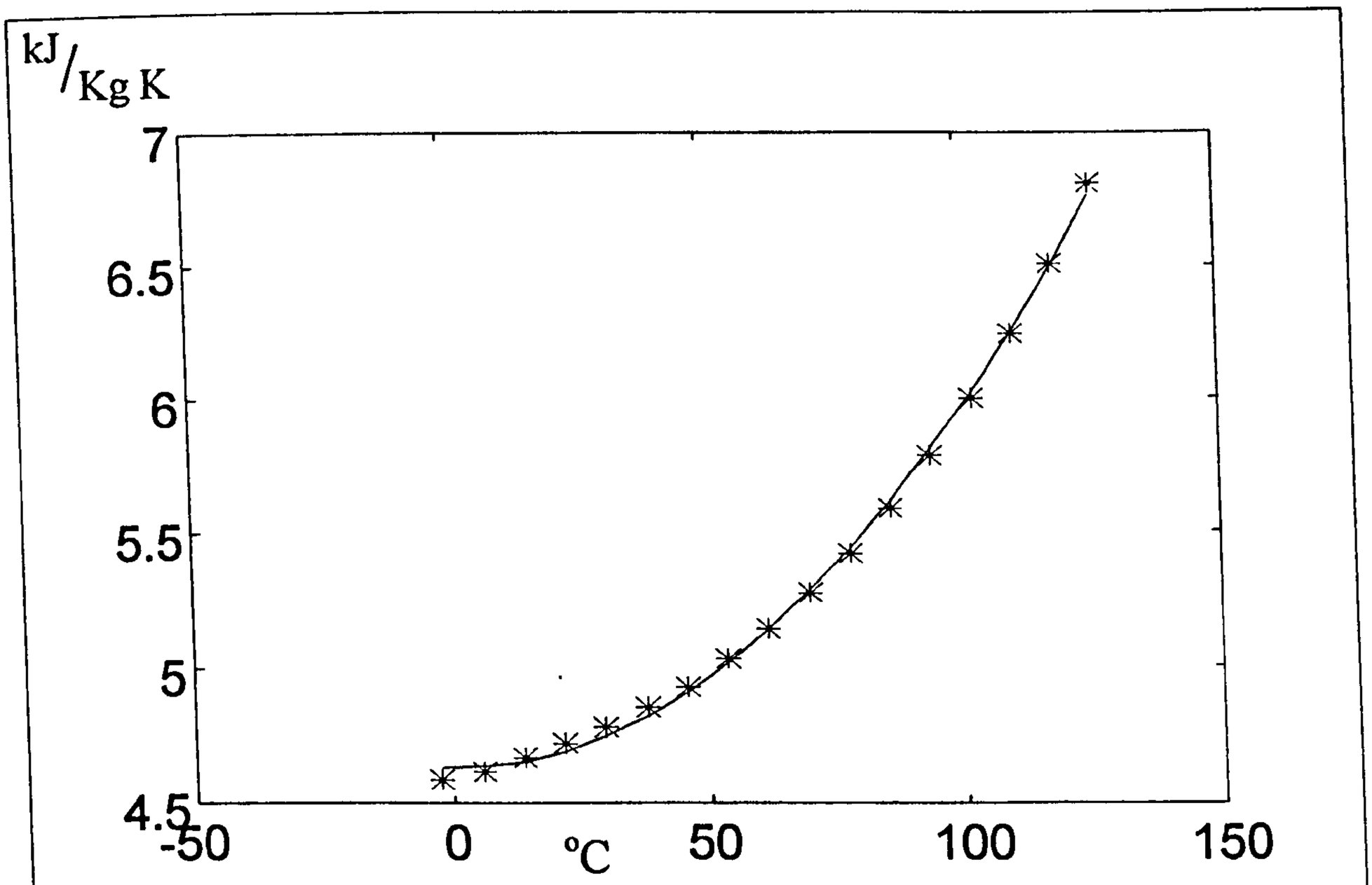

Figure 6.6 Heat capacity of the adsorbed phase of ammonia.

Viscosity

The viscosity of ammonia gas is calculated in the programme as a function of temperature and density. Algorithms are used to find the viscosity at saturation pressure and at 1bar for the temperature of the gas. The value of viscosity at the given pressure is then calculated by linear interpolation with density between saturation and 1bar.

For atmospheric pressure:

$$\mu \approx (0.9268 + 0.0036T) \times 10^{-5} \quad \text{(Pa.s)} \tag{6.5}$$

and at saturation:

$$\mu \approx \left(1.0353 + 0.0041T + 10^{-3.339+0.0226T}\right) \times 10^{-5} \quad \text{(Pa.s)} \tag{6.6}$$

where T is given in centigrade.

The values of viscosity at low pressure and saturation pressure are documented in reference [1] and [2], these data are shown plotted with those algorithms used in the simulation in figure

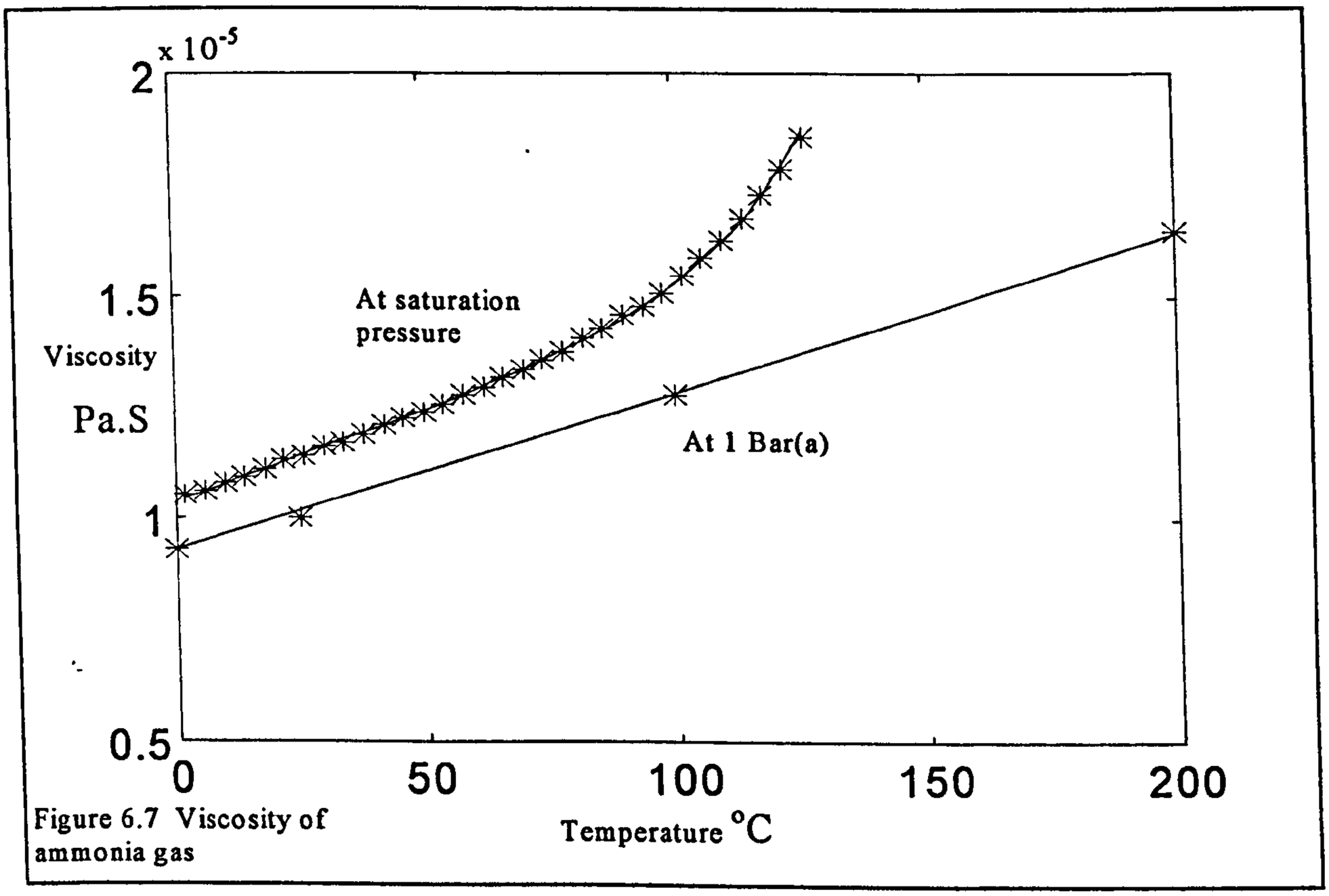

Figure 6.7 Viscosity of ammonia gas

Thermal conductivity

The thermal conductivity of ammonia gas used in the simulation is calculated in a similar way to the viscosity. The values at saturation and at low pressure are each approximated by functions of temperature. The value at the given pressure and temperature is then calculated by linear interpolation with density.

At atmospheric pressure:

$$\lambda \approx (21.616 + 0.112T) \times 10^{-3} \tag{6.7}$$

for saturation conditions :

$$\lambda \approx \left(23.87 + 0.0298 * T + 0.0037 * T^2\right) \times 10^{-3} \tag{6.8}$$

Where the temperature is given in centigrade.

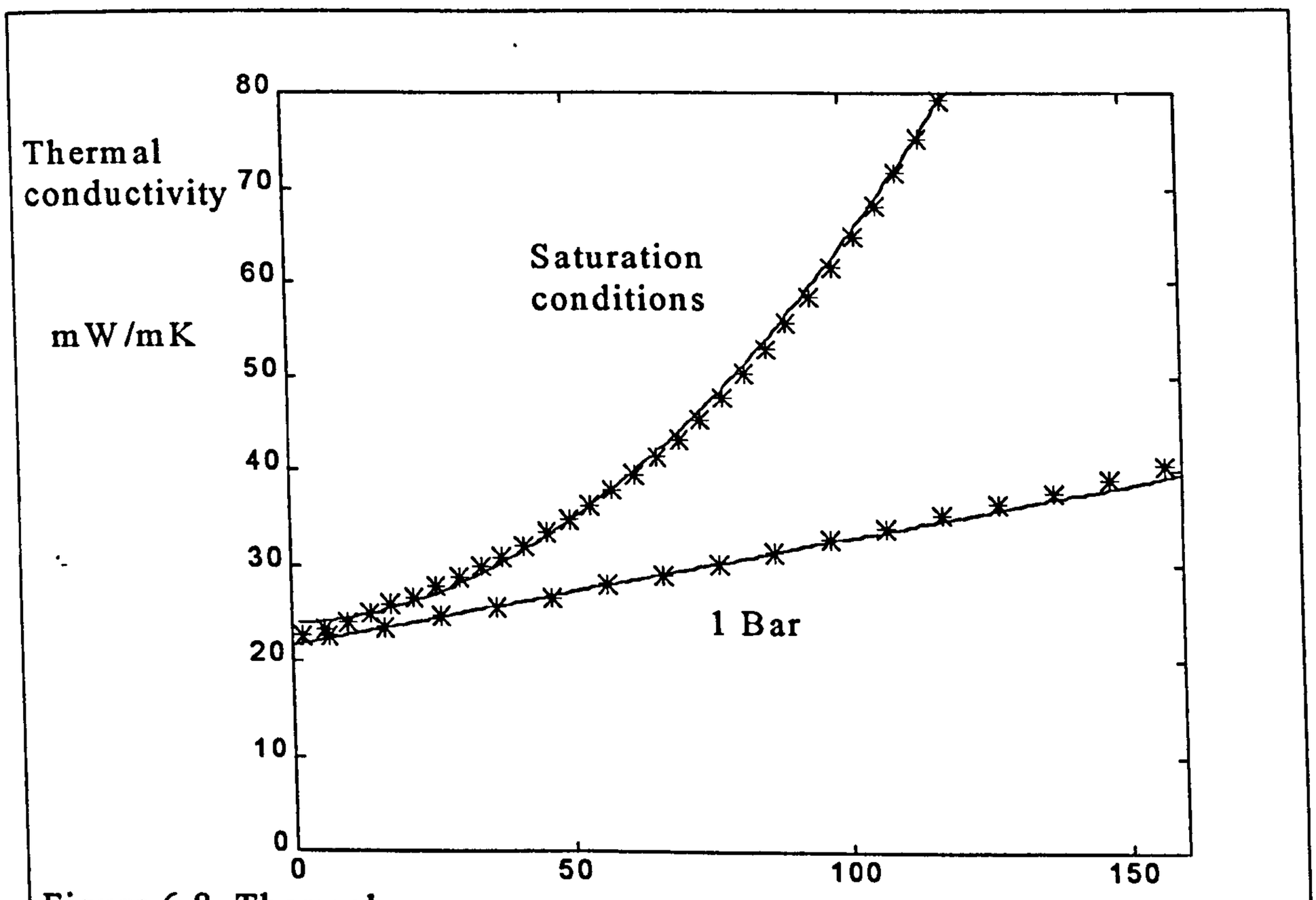

Figure 6.8 Thermal conductivity of ammonia gas

Thermophysical properties of argon used in the simulations

Saturation temperature

The relationship between pressure and temperature at saturation can be approximated by:

$T_{sat}=792.4/(9.1028-\ln(P))$

Where T_{sat} is given in K and pressure in bar(a)

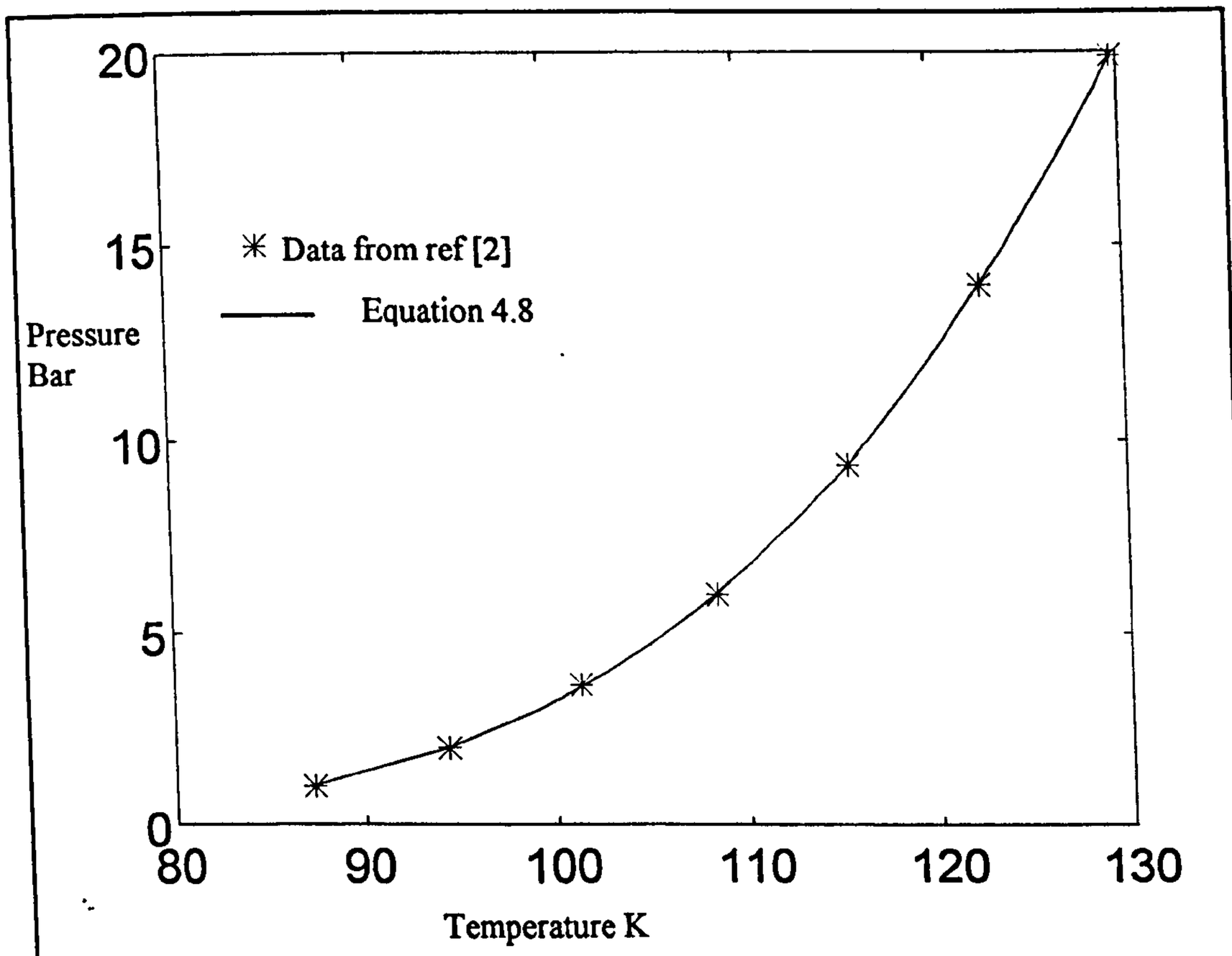

Fig 6.9 Saturation temperature and pressure of argon

Density of the gas

Over the temperature and pressure range used it is assumed that argon obeys the equation

$$\rho = \frac{P}{RT}$$

where R=208 J $kg^{-1}K^{-1}$ given in K, P in Pa ρ in kg/m^3.

Heat capacity of the gas

For the range of pressures and temperatures used the specifc heat capacity of argon gas is taken as c_p=0.519 kJ/kg K

Heat capacity of the adsorbed phase

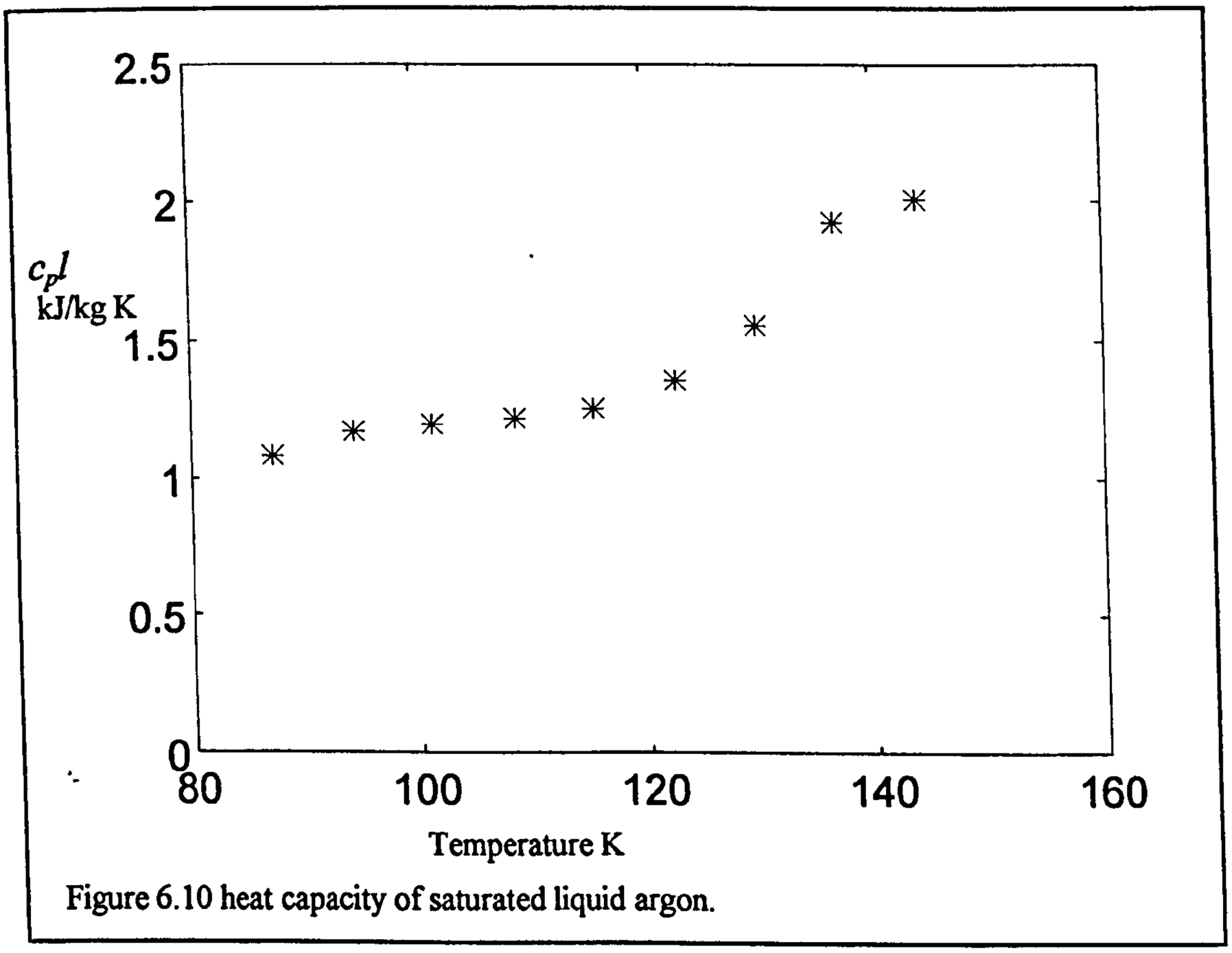

Figure 6.10 heat capacity of saturated liquid argon.

The specific heat capacity of liquid argon shows a sharp increase as it reaches its critical temperature as shown in figure 6.10 which is plotted from data given in reference[2]. It is not easy to make a good estimate of the heat capacity of the adsorbed phase at temperatures above critical, however the effect of the value used on the result of the simulation is small and the value selected, 2.0 kJ/kg K seems credible.

Viscosity

Figure 6.11 shows the viscosity of argon gas at atmospheric pressure taken from data published in [2] and the function μ=(2.11+0.0055 T)x10^{-5} Pa.s where T is

given in °C. The increase of viscosity with pressure is small rising only some 1.5% over 20 bar [3] and is neglected.

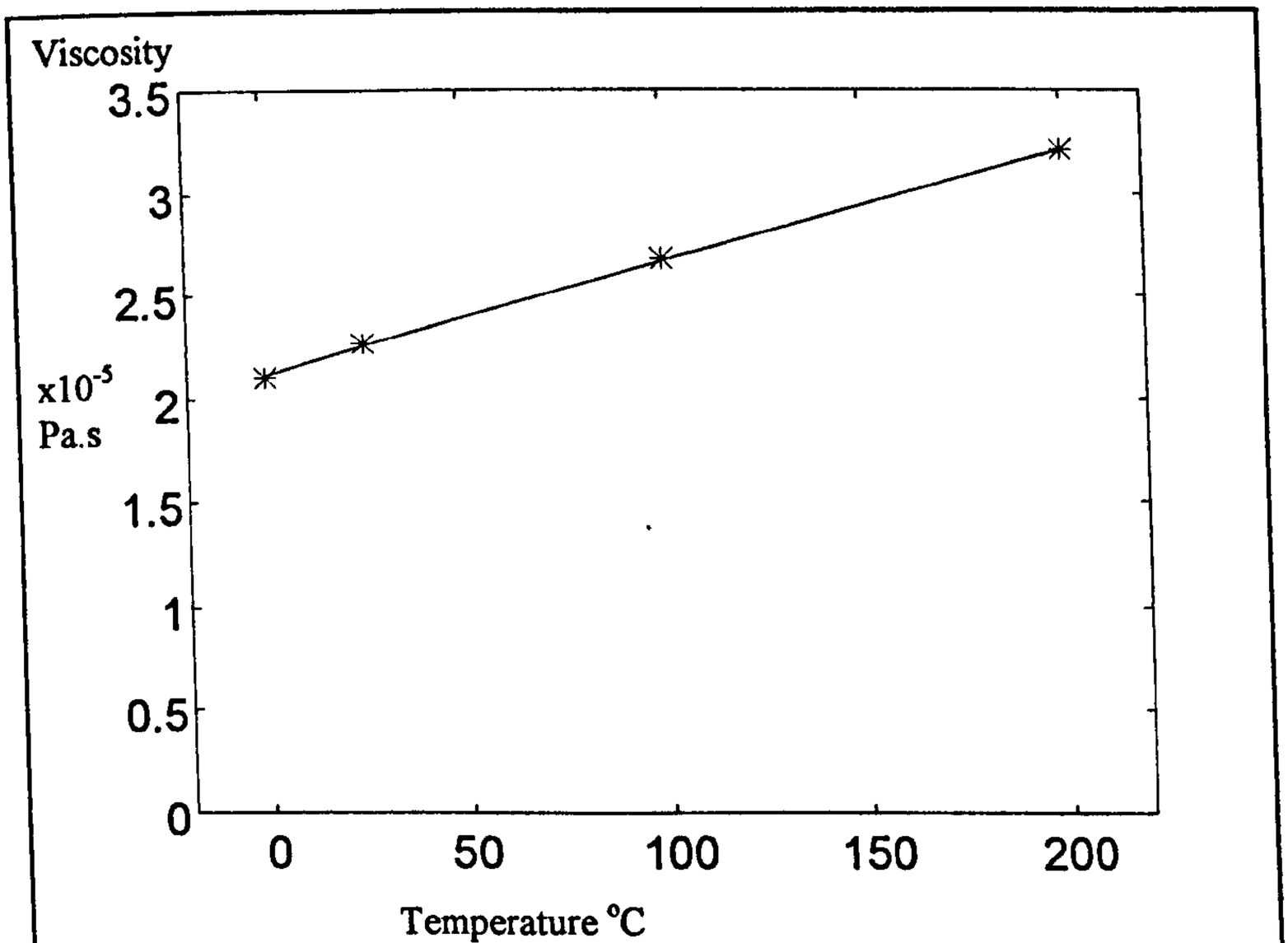

Figure 6.11 Viscosity of argon gas at atmospheric pressure

Thermal conductivity

Figure 6.12 shows the Thermal conductivity of argon gas at atmospheric pressure plotted against temperature compared with the equation $\lambda = 0.0164 + 4.8 \times 10^{-5} T$ (W m^{-1} K^{-1}) where T is given in °C . Data published in [3] suggests that the increase in conductivity with pressure is of the order 0.18% for each bar above atmospheric pressure.

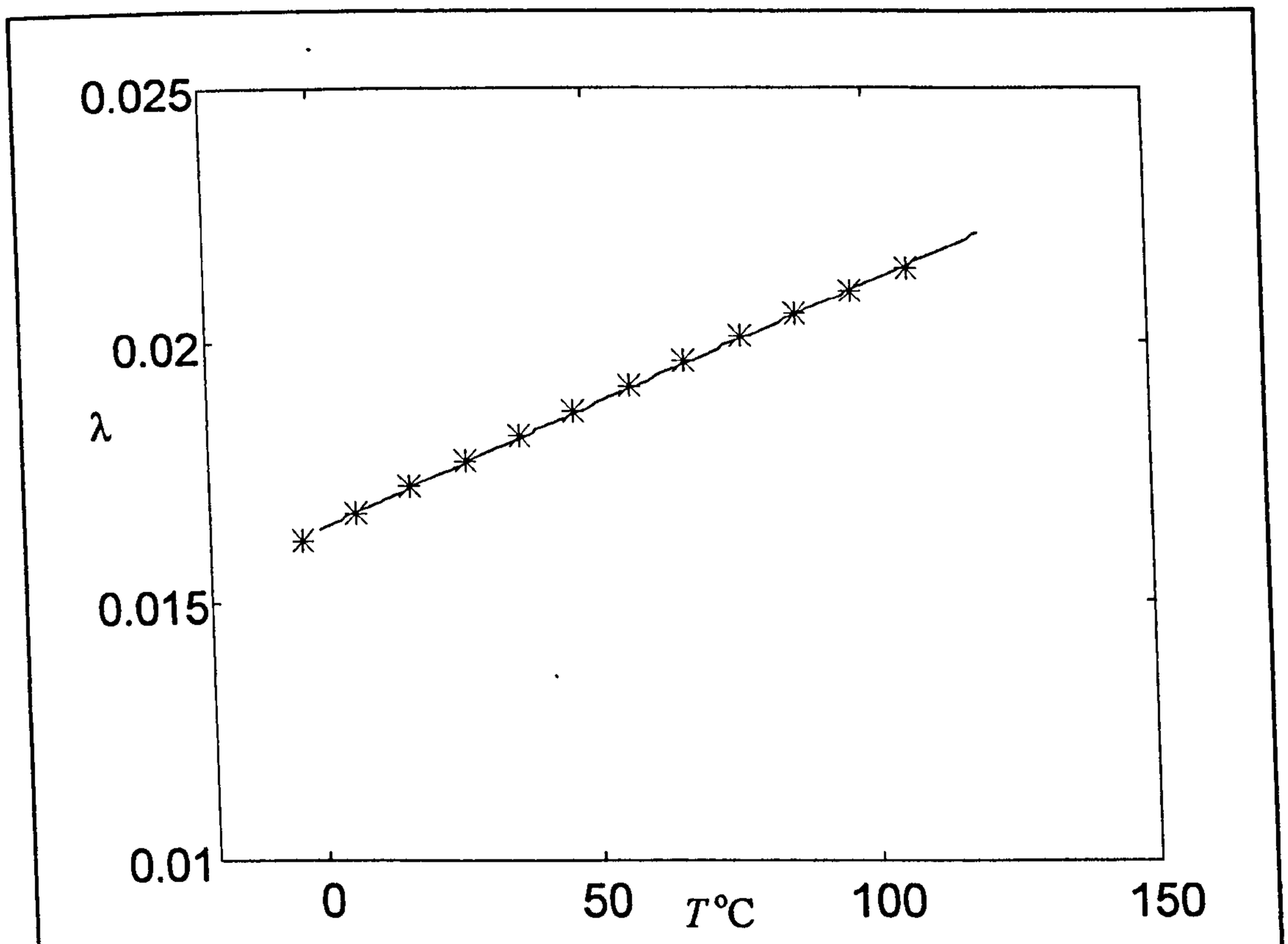

Figure 6.12 Thermal conductivity of argon

Results of experiments with ammonia and argon

Figure 6.13 shows the effective Nusselt numbers for the experiments with ammonia and argon plotted against Reynolds number . Figure 6.14 shows a similar plot of the Nusselt number of the film resistance derived from the effective Nusselt number with corrections for the effects of axial dispersion, axial conductivity and intra-particle conduction as described in chapter 3.

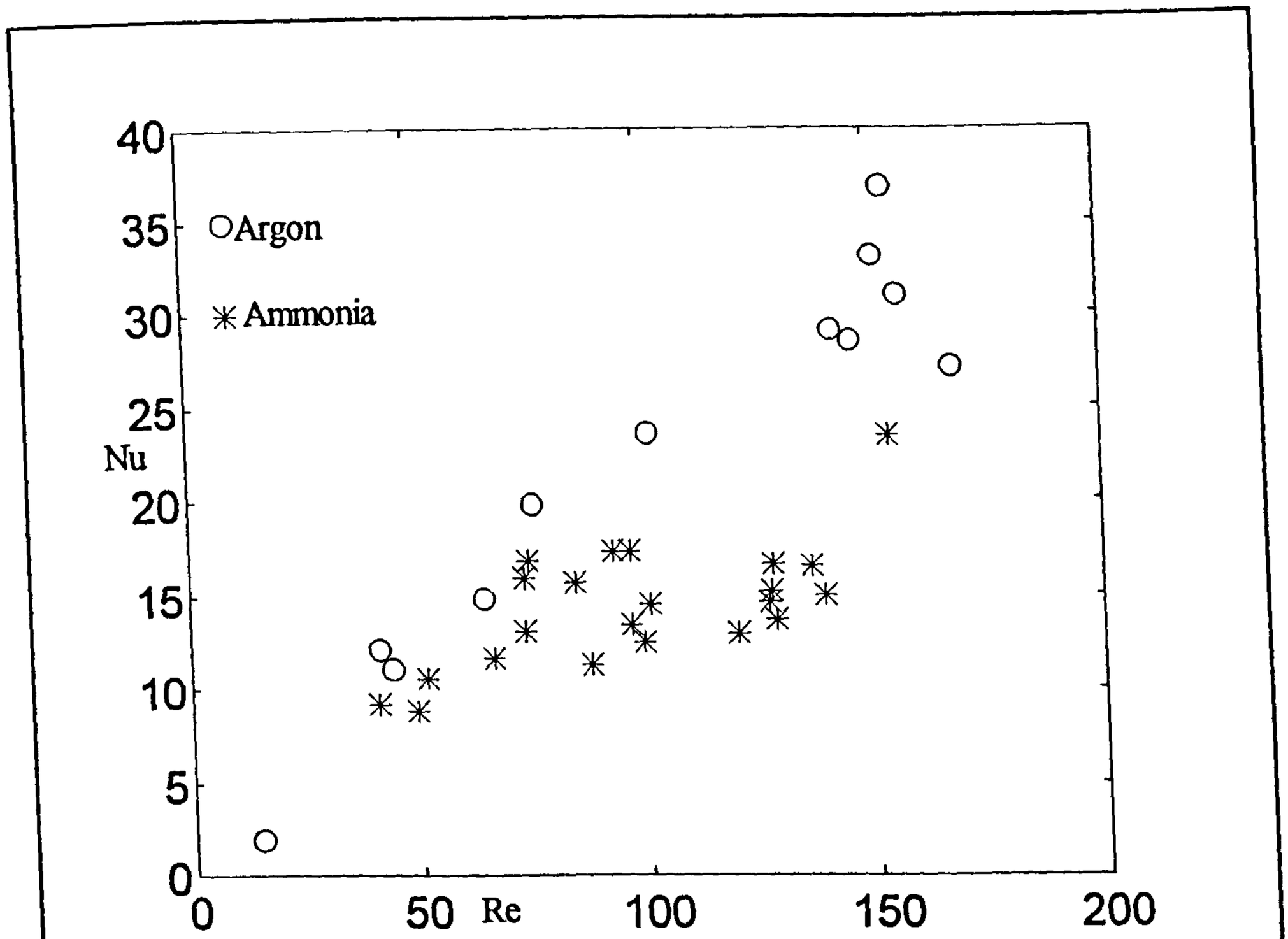

Figure 6.13 Nusselt number plotted against Reynolds number.

Table 6.1 Results from tests with Argon

Run	Re	Pr	Nu
4	153.4400	0.6218	36.8810
5	76.1640	0.6302	19.7130
6	44.6820	0.6269	11.0010
7	146.3260	0.6233	28.5210
8	151.1220	0.6123	33.1100
11	41.5370	0.6653	12.0760
12	141.8460	0.6174	29.0710
14	156.1830	0.6190	30.9450
15	101.7710	0.6227	23.5770
16	64.8570	0.6204	14.8280
17	167.8700	0.6150	27.0600
21	14.6380	0.6749	1.8780

Table 6.2 Results from tests with Ammonia			
Run	**Re**	**Pr**	**Nu**
50a	99.9800	0.9280	12.4380
70m	73.6960	0.9082	15.8700
70n	73.6100	0.9151	13.1110
90o	97.1350	0.9167	17.3470
60c	136.4330	0.9474	16.5140
60a	127.2020	0.9661	14.6220
60b	128.0590	0.9483	16.5460
60d	120.2510	0.9516	12.9090
60e	127.6670	0.9482	15.1590
60f	128.5960	0.9467	13.6370
50b	93.0520	0.9161	17.3150
45a	88.2750	0.9165	11.2790
30a	49.5710	0.9268	8.7720
130a	139.3910	0.9387	14.9770
90a	84.8410	0.9240	15.6090
50c	51.9330	0.9207	10.5910
40b	41.4830	0.9260	9.1760
90m	100.9700	0.9118	14.5070
70b	74.5800	0.9158	16.8820
60g	66.9010	0.9222	11.6150
140a	153.7030	0.9278	23.4450
90n	97.1810	0.9089	13.4600

References

[1] Thermodynamic and physical properties of ammonia. *International Institute of Refrigeration.* Paris. (1981)

[2] Physical property data tables published in Hemisphere Handbook for Heat Exchanger Design. Hemisphere, Washington

[3] Reid R.C., Prausnitz J. M., Sherwood T.K.,*The Properties of Gases and Liquids* Mcgraw Hill (1977)

Chapter 7 Analysis of the results from the heat transfer experiments

Components of the overall heat transfer coefficient

There are a number of heat transfer processes occurring in a fixed bed subject to forced convection. They are;

- Convective heat transfer to the surface of the solid from the gas.
- Intra-grain conduction.
- Axial and radial conduction through the bed.
- Convective dispersion caused by variations in the flow velocity and direction due to the distribution of channel sizes and orientation

It is possible to transform the effects of intra-particle conduction, axial conduction and axial dispersal into a modified heat transfer coefficient. It is useful, in this context to define a dimensionless resistance that is the inverse of the Nusselt number

$$\Re_{eff} = \frac{\lambda_g}{\alpha_{eff} d} \qquad (7.1)$$

where

d = grain diameter.

α_{eff}= effective heat transfer coefficient

λ_g = Thermal conductivity of the gas

It is then possible to evaluate the resistance components $\Re_{ax}$ for axial conduction, $\Re_{ipc}$ intra-grain conduction and a film resistance $\Re_{film}$ such that

$\Re_{eff}=\Re_{film}+\Re_{ipc}+\Re_{ax}$

In chapter 3 it was demonstrated that the effect of finite intra-grain conductivity may be included in the Schumann model by the use of a modified heat transfer coefficient from equation 3.10,

$$\frac{1}{\alpha'}=\frac{1}{\alpha}+\frac{d}{10\lambda_s}. \tag{3.10}$$

therefore

$$\Re_{ipc}=\frac{\lambda_g}{10\lambda_s} \tag{7.2}$$

Convective dispersion acts as an effective conductivity in the gas phase. This may be added to the stagnant bed conductivity to give a total axial conductivity λ_{ax}.

If the bed is assumed to be radially isothermal then the partial differential equations (3.1) describing the energy flows, including axial conductivity become

$$\dot{m}c_p\frac{\partial T_g}{\partial y}+\psi\rho c_v\frac{\partial T_g}{\partial t}=\lambda_{gax}\frac{\partial^2 T_g}{\partial y^2}+\alpha a\left(T_s-T_g\right) \tag{7.3}$$

$$mc\frac{\partial T_s}{\partial t}=\lambda_{sax}\frac{\partial^2 T_s}{\partial y^2}+\alpha a\left(T_g-T_s\right) \tag{7.4}$$

λ_{gax} = Axial conductivity in the gas phase

λ_{sax} = Axial conductivity in the solid phase

Bradshaw *et al.* [2] used Laplace transforms to develop a modified heat transfer coefficient where the axial conductivities in the gas and solid phase are transformed into a thermal resistance term. This is given by

$$\Re_{ax}=\frac{\lambda_{ax}a}{d\left(\dot{m}c_p\right)^2} \tag{7.5}$$

where λ_{ax} is the sum of the effective axial thermal conductivities due to conduction in the solid and gas phases and convective dispersion.

This expression is valid for experiments where a step change in the inlet temperature used.

The validity of this transformation of the bed conductivity into a resistance term into the range of experiments made in this study has been confirmed by the use of a numerical model that included conduction explicitly. It is assumed that the effect of transferring all the axial conduction into the gas phase equation is negligible.

The partial differential equations then give the following finite difference equations

$$\Delta T_g = \left(\frac{\alpha a}{\dot{m} c_p} \left(T_s - T_g \right) + \frac{\lambda_{ax}}{\dot{m} c_p} \frac{\partial^2 T_g}{\partial y^2} \right) \Delta y \qquad (7.6)$$

$$\Delta T_s = \frac{\alpha a}{mc} \left(T_g - T_s \right) \qquad (7.7)$$

$$\frac{\partial^2 T_g}{\partial y^2} = \frac{\alpha a}{\dot{m} c_p} \left(\frac{\partial T_s}{\partial y} - \frac{\partial T_g}{\partial y} \right) + \frac{\lambda_{ax}}{\dot{m} c_p} \frac{\partial^3 T_g}{\partial y^3}$$

by neglecting the $\frac{\lambda_{ax}}{\dot{m} c_p} \frac{\partial^3 T_g}{\partial y^3}$ term we may use the approximation

$$\frac{\partial^2 T_g}{\partial y^2} \approx \frac{\alpha a}{\dot{m} c_p} \left(T_s(r,s) - T_g(r,s) - T_s(r-1,s) + T_g(r-1,s) \right) \frac{1}{\Delta y} \qquad (7.8)$$

then definine K such that $K = \frac{\alpha a \lambda_{ax}}{\left(\dot{m} c_p \right)^2}$.

The equations to be applied along the boundaries at $r=1$ and at $s=1$ become :

$$T_g(r,1) = \frac{2 - B + 2K}{2 + B + 2K} T_g(r-1,1) + \frac{B + 2K}{2 + B + 2K} T_s(r,1) + \frac{B - 2K}{2 + B + 2K} T_s(r-1,1) \qquad (7.9)$$

$$T_s(1,s) = \frac{2 - A}{2 + A} T_s(1,s-1) + \frac{A}{2 + A} T_g(1,s) + \frac{A}{2 + A} T_g(1,s-1) \qquad (7.10)$$

and the equations for the rest of the bed are:

$$T_s(r,s)=\frac{\left(\frac{2-A}{2+A}T_s(r,s-1)+\frac{A}{2+A}T_g(r,s-1)+\frac{A}{2+A}\frac{B-2K}{2+B+2K}T_s(r-1,s)+\frac{A}{2+A}\frac{2-B+2K}{2+B+2K}T_g(r-1,s)\right)}{1-\frac{A}{(2+A)}\frac{B+2K}{2+B+2K}}$$

(7.11)

$$T_g(r,s)=\frac{2-B+2K}{2+B+2K}T_g(r-1,s) \;+\; \frac{B+2K}{2+B+2K}T_s(r,s) \;+\; \frac{B-2K}{2+B+2K}T_s(r-1,s)$$

(7.12)

Where

$$A=\frac{\alpha a\,\Delta t}{mc_{eff}} \qquad (7.13)$$

c_{eff} is the effective heat capacity of the solid $c_{eff}=c_s+xc_a-h_{ag}\frac{\partial x}{dT_s}$

$$B=\frac{\alpha\, a\,\Delta y}{\dot{m}c_p} \qquad (7.14)$$

as before in chapter 6

Estimate of thermal resistance due to intra-grain conduction

The value of the resistance due to intra-grain conduction given by eq 7.2

($\Re_{ipc}=\frac{\lambda_g}{10\lambda_s}$) is that derived for a spherical grain. Values derived for other shapes such as cylinders and plates give constants in the denominator of 8 and 6 respectively. It may be argued that the surface area per unit volume of irregular grains is closer to that of plates or cylinders and therefore this estimate will give a high estimate of the resistance. It may also, however be argued that the heat transfer coefficient will vary over the area of the grain, with localised zones of high gas velocity and heat transfer. This argument would suggest that the assumption of constant heat flux over a spherical surface will predict a low value of the resistance

term. In the absence of any better data on the shape and the grain-scale temperature distribution and given that the influence of the resistance due to intra-grain conduction is low then it seems reasonable to accept equation [Eq 7.2].

Grain conductivity

The thermal conductivity of the grain λ_s has been shown by Turner[3] to vary little with concentration of adsorbate at moderate concentrations. With ammonia as the adsorbate Turner recommends

$$\text{for } 0 < x < 0.197 \qquad \lambda_s = 0.863$$

$$\text{for } 1.97 < x < 0.259 \qquad \lambda_s = 0.863 + 7.86(x - 0.197) \qquad (7.15)$$

where λ_s is given in W/mK and x as a mass fraction.

Typical values of $\Re_{lpc}$

Although the conductivities of the gases used in the experiments are a function of pressure and temperature there is only a small variation through the range of experiments. The following mean values of $\Re_{lpc}$ may be used:

For experiments with ammonia $\Re_{lpc} \cong 0.0034$. The standard deviation of the values calculated individually is 3.2% of this value.

For experiments with argon $\Re_{lpc} \cong 0.0023$. The standard deviation is 4.3% of this value.

Estimate of thermal resistance due to axial dispersion and conduction

The components of axial conductivity and conduction are calculated separately so that

$\lambda_{ax} = \lambda_{dax} + \lambda_{cax}$, and $\Re_{ax} = \Re_{dax} + \Re_{cax}$

The subscripts *cax* and *dax* refer to the effects of conduction and dispersion respectively.

Conductivity of the stagnant bed

The Thermal conductivity of the stagnant bed is a function of

- The grain thermal conductivity
- The gas thermal conductivity
- The structure of the bed (grain size, contact area, void ratio)
- The conductivity between grains by radiation

Turner [3] made a series of measurements of the thermal conductivity of stagnant beds of granular carbon 208C with a range of gases and under vacuum. She fitted the data to the Zehner-Bauer model [4] which a complex expression to yield the bed conductivity. A simpler expression is given by Hadley [5] and recommended by Kaviany[6]:

$$\frac{\lambda_{bc}}{\lambda_g} = (1-A)\frac{\psi f_0 + \left(\frac{\lambda_s}{\lambda_g}\right)(1-\psi f_0)}{1-\psi(1-f_0)+\left(\frac{\lambda_s}{\lambda_g}\right)\psi(1-f_0)} + \frac{2\left(\frac{\lambda_s}{\lambda_g}\right)^2(1-\psi)+(1+2\psi)\left(\frac{\lambda_s}{\lambda_g}\right)}{(2+\psi)\left(\frac{\lambda_s}{\lambda_g}\right)+1-\psi} \quad (7.16)$$

where λ_{bc} is the stagnant bed conductivity neglecting the effect of radiation and

$A = 10^{-1.084-6.778(\psi-0.298)}$ for $0.298 \le \psi \le 0.58$.

The radiative conductivity may be estimated from an expression given by Kaviany [6] and attributed to Tien and Drolen [7].

$$\lambda_{br} = 4Fd\sigma\overline{T}^3 \quad (7.17)$$

where

σ is the Stefan-Boltzmann constant $\left(4.67\times10^{-8}\,\mathrm{W/m^2K^4}\right)$.

and

$$F = 0.548 Tan^{-1}\left(\frac{\lambda_s}{4d\sigma\overline{T}^3}\right) \qquad (7.18)$$

so $\lambda_{cax} = \lambda_{bc} + \lambda_{br}$

The results from calculations using these models for λ_{cax} correspond to within 15% to the experimental results of Turner for the range of temperatures and pressures used.

For experiments with ammonia the average value of $\frac{\lambda_{cax}}{\lambda_g} = 8.5$ with a standard deviation of 1% of that value.

For experiments with argon the average value of $\frac{\lambda_{cax}}{\lambda_g} = 9.845$ with a standard deviation of 1% of that value.

Convective dispersion

In a packed bed the local velocity will vary in speed and direction due to the distribution of size and orientation of the channels between grains. This variation in flow acts as an effective thermal conductivity by convective transport in both axial and radial directions. The convective dispersal D has units m^2/s and is a function of the packing geometry , gas velocity and gas transport properties. The effective bed conductivity due to dispersion is given by

$$\lambda_d = D\rho c_p \qquad (7.19)$$

where

ρ = Density of the fluid.

c_p = Heat capacity of the fluid.

λ_d = Effective conductivity due to dispersal.

The magnitude of dispersion is not the same in radial and axial directions in isotropic media hence the axial dispersion is given the symbol D_{ax} and the axial conductivity due to dispersal is λ_{ax}.

A Lewis number for the dispersal may be defined as

$$\mathrm{Le} = \frac{\lambda_g}{D\rho C_P} = \frac{\lambda_g}{\lambda_{dax}} \tag{7.20}$$

Wakao and Kaguei [9] suggest that

$$D_{ax} = 0.5\psi u_p d \tag{7.21}$$

where u_p is the gas velocity in the pores.

Using the superficial velocity given by

$$u = \psi u_p$$

then

$$\frac{1}{\mathrm{Le}} = 0.5\,\mathrm{Re}\,\mathrm{Pr} \tag{7.22}$$

hence

$$\lambda_{dax} = 0.5\,\mathrm{Re}\,\mathrm{Pr}\,\lambda_g = \dot{m}c_p\frac{d}{2} \tag{7.23}$$

Typical values of $\Re_{ax}$

The resistance terms for axial dispersion $\Re_{dax}$ and axial conduction $\Re_{cax}$ are given by

$$\Re_{dax} = \frac{\lambda_g \lambda_{dax} a}{d\left(\dot{m}c_p\right)^2} \tag{7.24}$$

$$\Re_{cax} = \frac{\lambda_g \lambda_{cax} a}{d\left(\dot{m}c_p\right)^2} \tag{7.25}$$

substituting $\dot{m}c_p = \mathrm{Re}\,\mathrm{Pr}\frac{\lambda_g}{d}$ and $a = \frac{6(1-\psi)}{d}$ together with the appropriate expressions for λ_{dax} and λ_{cax} gives

$$\Re_{dax} = \frac{3(1-\psi)}{\mathrm{Re}\,\mathrm{Pr}} \text{ for both ammonia and argon} \qquad (7.26)$$

$$\Re_{cax} = 8.5\frac{6(1-\psi)}{(\mathrm{Re}\,\mathrm{Pr})^2} \text{ for ammonia} \qquad (7.27)$$

$$\Re_{cax} = 9.84\frac{6(1-\psi)}{(\mathrm{Re}\,\mathrm{Pr})^2} \text{ for argon} \qquad (7.28)$$

Estimate of the film heat transfer coefficient

The film heat transfer resistance in packed beds is a function of the packing arrangement, the shape of the grains, the flow regime and the transport properties of the gas. Wakao and Kaguei [9] looked at the results of a number of experimenters using a variety of techniques. They recommended the following correlation for packed beds of spheres.

$$Nu=2+1.1Re^{0.6}Pr^{1/3} \qquad (7.29)$$

Laminar flow solutions based on hydraulic diameter for circular ducts with uniform wall temperature give

$$Nu_{Dh}=3.657$$

where the hydraulic diameter is $Dh = \frac{4A}{P}$ where A is the flow cross section area and P is the wetted perimeter therefore

$$Dh = \frac{4\psi d}{6(1-\psi)}$$

This suggests that, with Ψ=0.373 then as Re→0 then Nu→9.22. This result is in conflict with equation [Eq 7.29] which returns Nu=2 at Re=0. It may be argued that the estimate from the laminar solution can be expected to give a high value of Nu since it assumes that the whole area of the grain is available for heat transfer, however this is not sufficient to explain the divergence.

The Reynolds-Colburn analogy

Handley and Heggs [10] showed that if the Reynolds-Colburn [11] analogy between heat transfer and friction as formulated for turbulent flow in straight pipes were to apply to packed beds then

$$\frac{j_h \Psi}{f_v'} = \frac{4}{\mathrm{Re}_{Dh}} = \frac{6(1-\psi)}{\mathrm{Re}} \tag{7.30}$$

where j_h is the Colburn j-factor for heat transfer

$$j_h = \frac{\mathrm{Nu}}{\mathrm{RePr}^{1/3}} \tag{7.31}$$

and f_v' is a viscous friction factor

$$f_v' = \frac{f_v}{36} = \frac{1}{36}\frac{\Delta P}{L}\frac{d^2}{\mu u}\frac{\psi^3}{(1-\psi)^2} \tag{7.32}$$

Handley and Heggs studied a variety of packings and found that $\frac{j_h \Psi}{f_v'}$ was in all cases lower than those valued predicted by the analogy. They did, however find that it was a well behaved function of Reynolds number so that

$$\frac{j_h \Psi}{f_v'} = \frac{c''}{(\mathrm{Re}_{Dh})^{m''}} \tag{7.33}$$

where c'' and m'' are properties of the packing and independent of the gas properties. They further demonstrated that the deviation from the Reynolds Colburn analogy was greatest at high values of the inertia tortuosity constant m

from the Ergun equation and demonstrated that as m increases so c'' decreases. In the absence of any better data on the film heat transfer coefficient it seems reasonable to use the inertia tortuosity constant as a characteristic indicating a similarity of the $\frac{j_h\Psi}{f_v'}$ behaviour between packings.

The factors m, c'' and m'' from the results of Handley and Heggs are :

Packing type		m	c''	m''
Spheres		1.24	1.08	1.15
Cylinders	1/4" x 1/4"	1.25	0.29	1.01
Cylinders	3/16" x 3/16"	1.28	0.83	1.17
Cylinders	1/4" x 1/2"	1.54	0.29	1.01
Rings, porcelain	3/8" x 3/8"	1.72	0.78	1.17
Rings, porcelain	1/4" x 1/4"	2.37	0.77	1.17
Rings, Steel	1/4" x 1/4"	3.15	0.43	1.11

For the carbon bed in this investigation the value of the inertia tortuosity constant determined in chapter 5 was m=2.14 and therefore it is proposed that equation [Eq 7.33] may be used with

$$c'' = 0.77, \qquad m'' = 1.17$$

Substitution of the Ergun equation [Eq 5.1] for Dp in (Eq 7.32) gives

$$f_v' = \frac{c}{36} + \frac{m}{36}\frac{\mathrm{Re}}{(1-\psi)} \tag{7.34}$$

Substitution of this expression into equation 7.33 and rearranging gives

$$j_h = \frac{cc''}{36}\left(\frac{3(1-\psi)}{2}\right)^{m''}\frac{1}{\psi}\frac{1}{\mathrm{Re}^{m''}} + \frac{mc''}{36}\left(\frac{3(1-\psi)}{2}\right)^{m''}\frac{1}{\psi}\mathrm{Re}^{(1-m'')} \tag{7.35}$$

inserting the values determined for the viscous and inertia tortuosity factors found in chapter 5 (m=2.14, c=316) with ψ =0.373, c" =0.77, m"=1.17 into (Eq 7.35) produces

$$j_h = \frac{16.9}{\mathrm{Re}^{1.17}} + \frac{0.182}{\mathrm{Re}^{0.17}} \tag{7.36}$$

and finally from the definition of j_h (Eq 7.31) we arrive at

$$\mathrm{Nu} = \frac{16.9\,\mathrm{Pr}^{1/3}}{\mathrm{Re}^{0.17}} + 0.182\,\mathrm{Re}^{0.83}\,\mathrm{Pr}^{1/3} \qquad (7.37)$$

The lower limit of the Reynolds number regimes investigated by Handley and Heggs was 100. At numbers below 100 the $\mathrm{Re}^{-0.17}$ term in equation (Eq 7.37) begins to have a large effect and in order to avoid this artefact the relation

$$Nu = 7.21\,\mathrm{Pr}^{1/3} + 0.182\,\mathrm{Re}^{0.83}\,\mathrm{Pr}^{1/3} \qquad (7.38)$$

gives the same value for Nu at Re=150 and may be expected to be more reliable at lower Reynolds numbers than (Eq 7.37) however some caution must be expressed since the lower limit of applicability for this relation is not established.

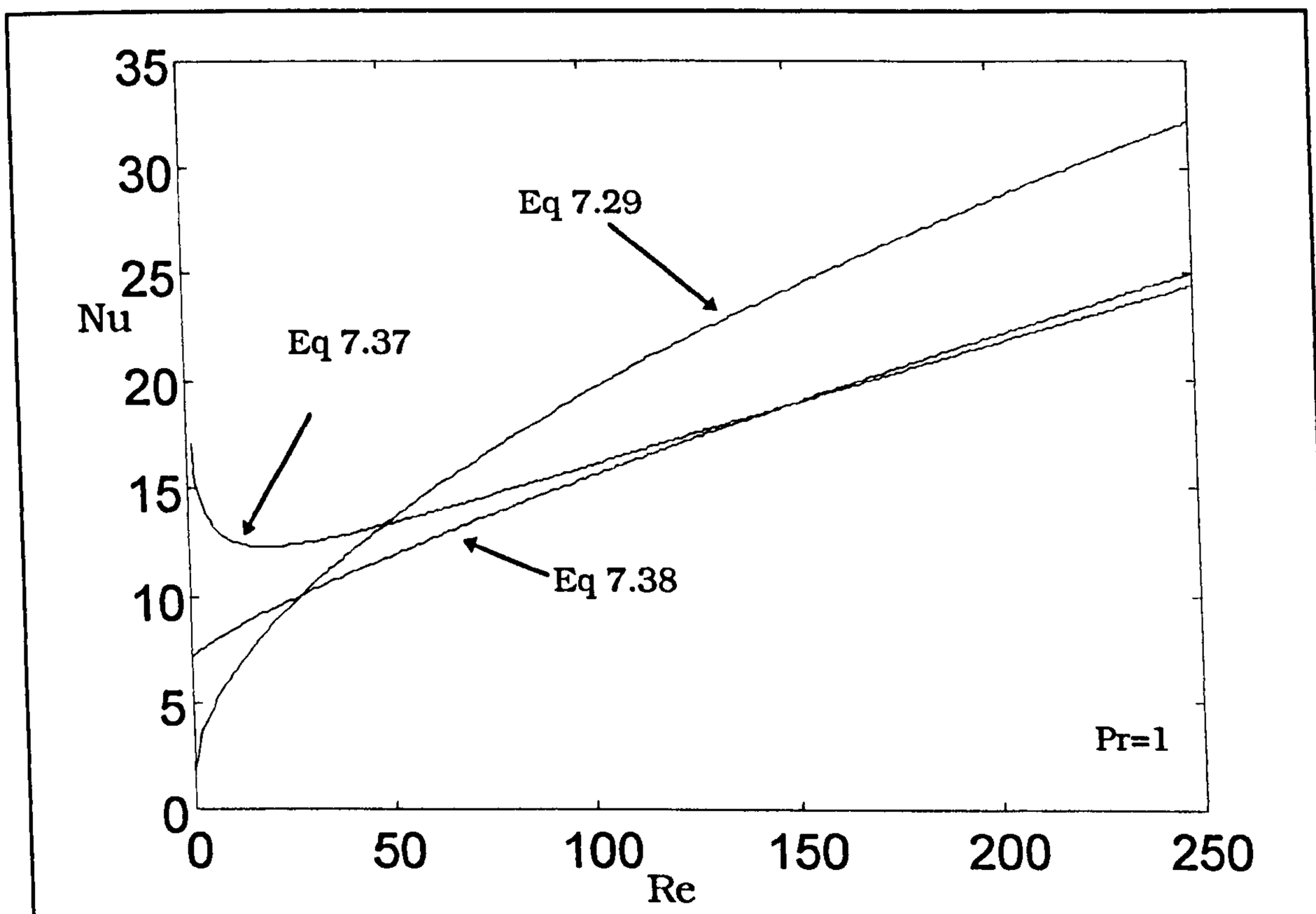

Figure 7.1 Correlations for the film Nusselt number

Relative magnitude of the four resistance components

The values for dimensionless thermal resistances due to intra-grain conduction (Eq 7.2), axial dispersion (Eq 7.26), axial conduction (Eq 7.27) and film resistance (Eq 7.38) are plotted in figure 7.2 where their relative magnitudes can be seen.

For Reynolds numbers below 100 the resistance terms due to axial conduction and dispersal are significant and for those below 50 they are dominant.

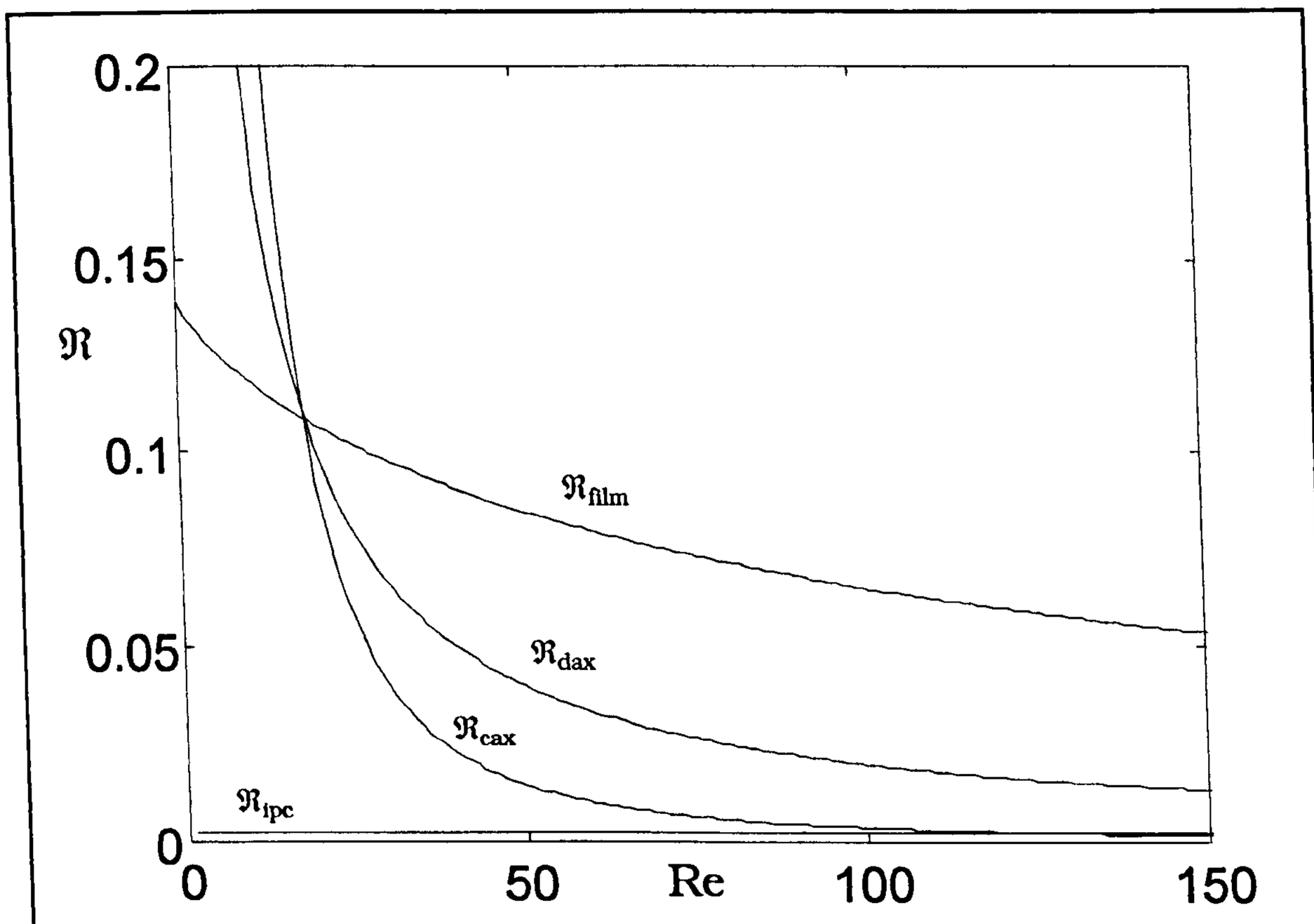

Figure 7.2 Components of the total resistance for the Schumann model

Comparison between the predicted and experimentally observed heat transfer results

Figures 7.3 and 7.4 show the Nusselt number predicted by summing the theoretical resistances due to intra-grain conduction, axial conduction, axial dispersion and film resistance plotted with the results derived from the experiments as described in chapter 6. There is clearly a discrepancy between the results using the different gases and also between the predicted and observed results. In order to investigate this inconsistency the confidence in the predicted valued of the thermal resistance components should be considered. It is possible to have high confidence in the thermal resistance term for axial conduction since it is based on the conductivity of the bed confirmed by the measurements of Turner. The film resistance based on the pressure loss-heat transfer analogy is based on reasonable assumptions but it cannot be considered to be completely reliable, while less confidence can be invested in the predicted dispersion term since it is based on results for beds of spheres. It is therefore useful to compare the results based on theory and experiment with the axial conduction term removed. It can be seen that if the results of the tests with ammonia are valid then the true value of film resistance, that of dispersion or both must be lower than the predictions. The results for argon imply very low film resistance and dispersal.

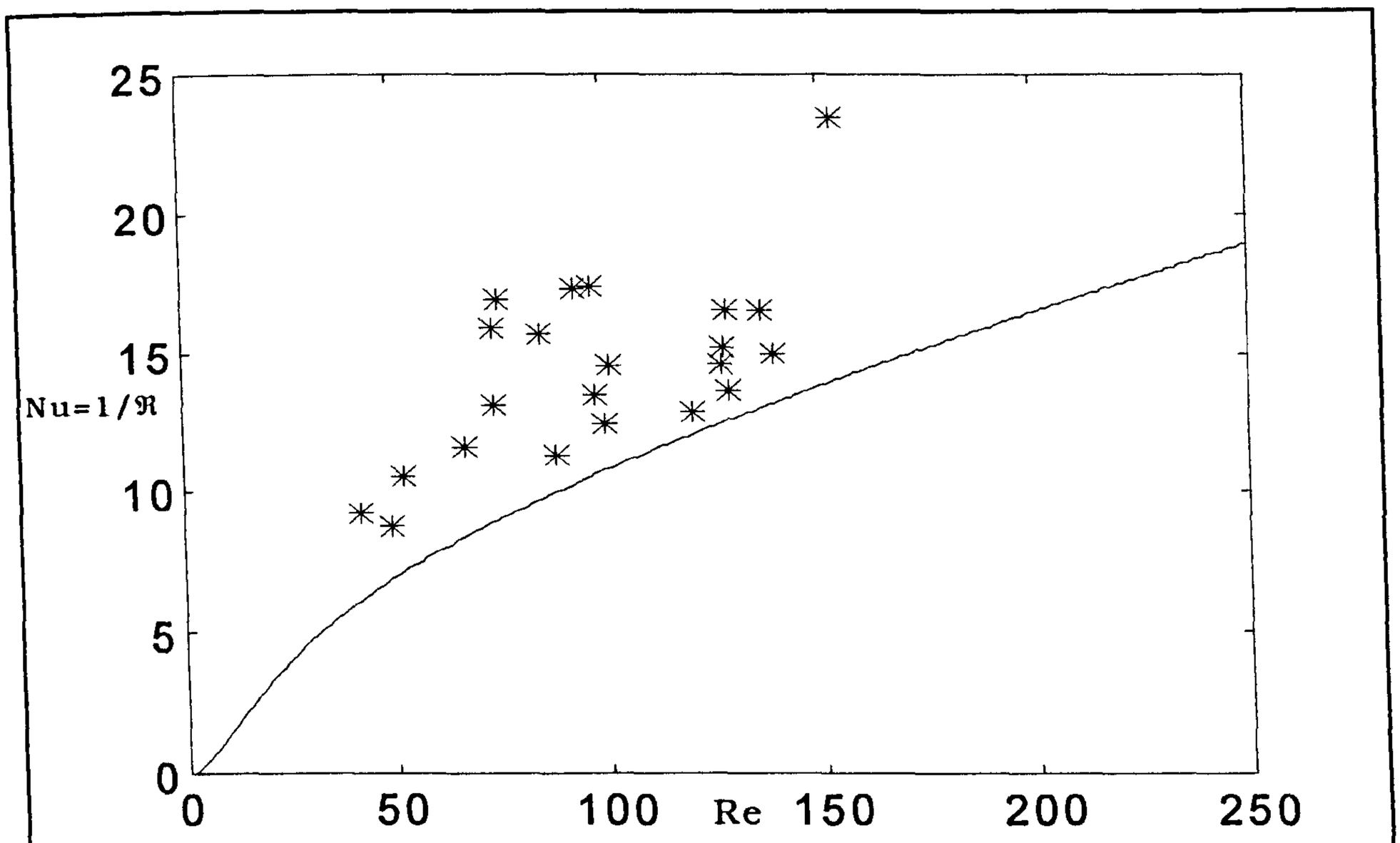

figure 7.3 Predicted and measured Nusselt numbers for ammonia experiments.

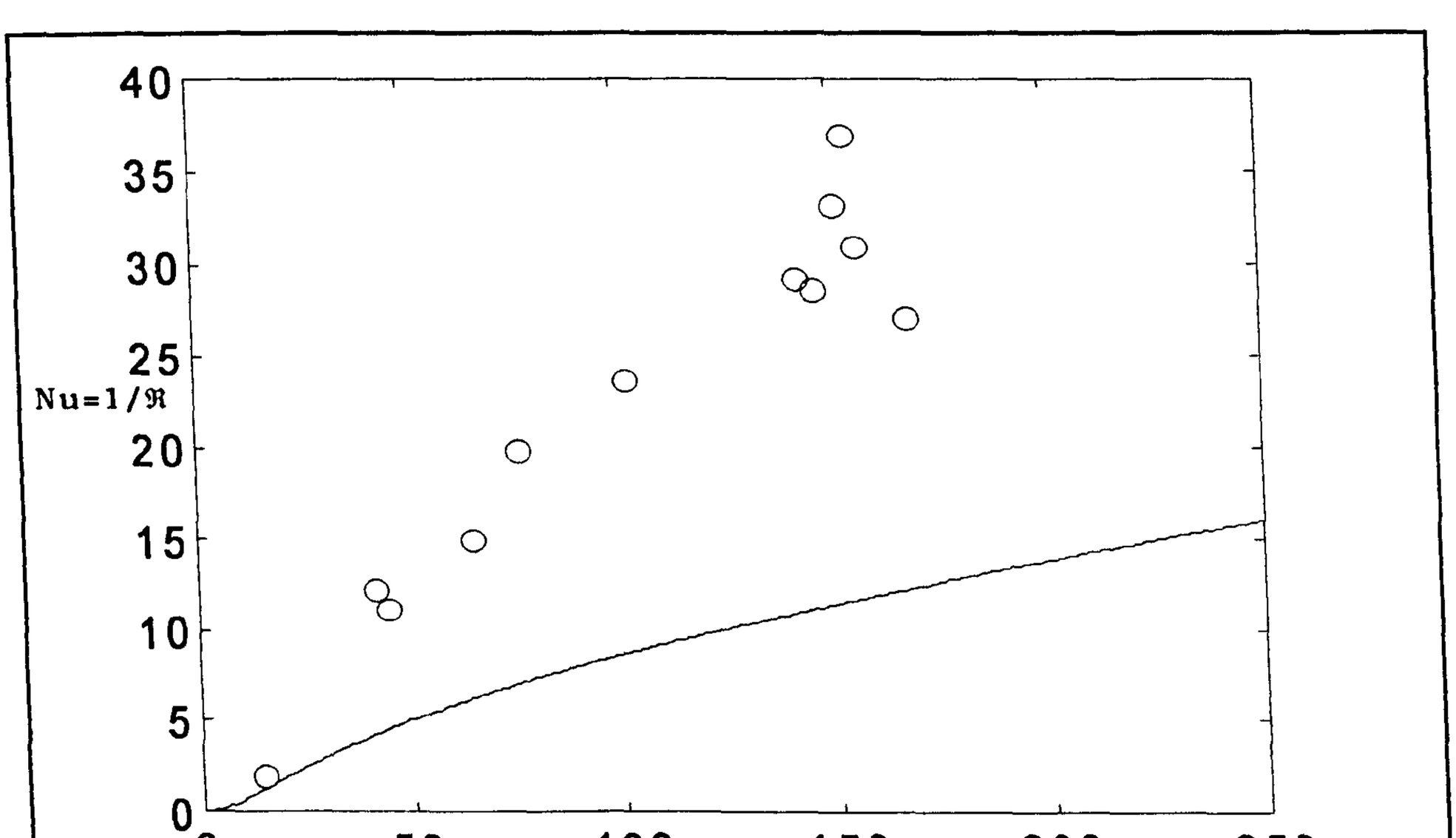

Figure 7.4 Predicted and measured Nusselt numbers for argon experiments

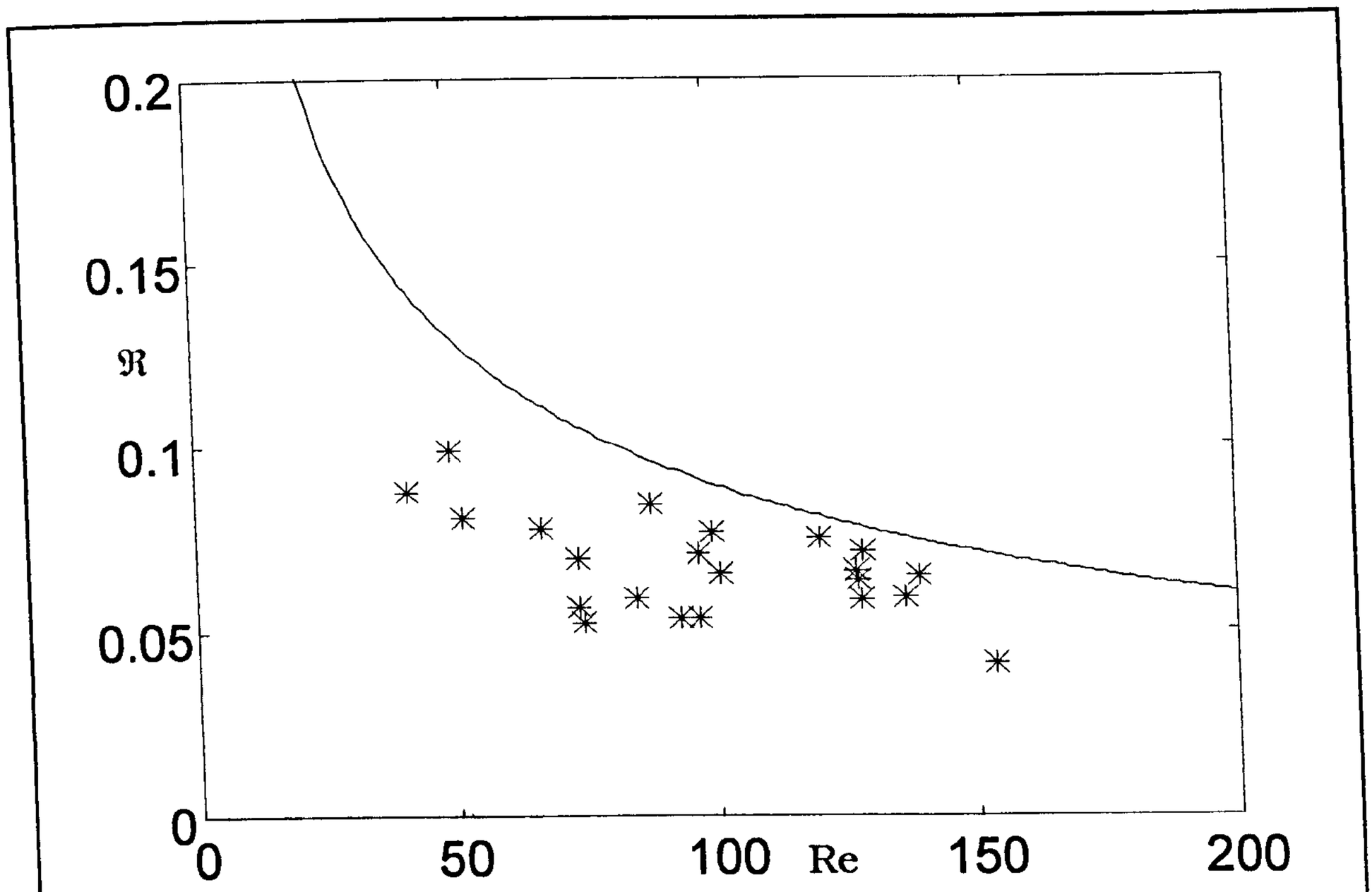

Figure 7.5 Predicted and experimental values of $\Re$-$\Re_{cax}$ for ammonia

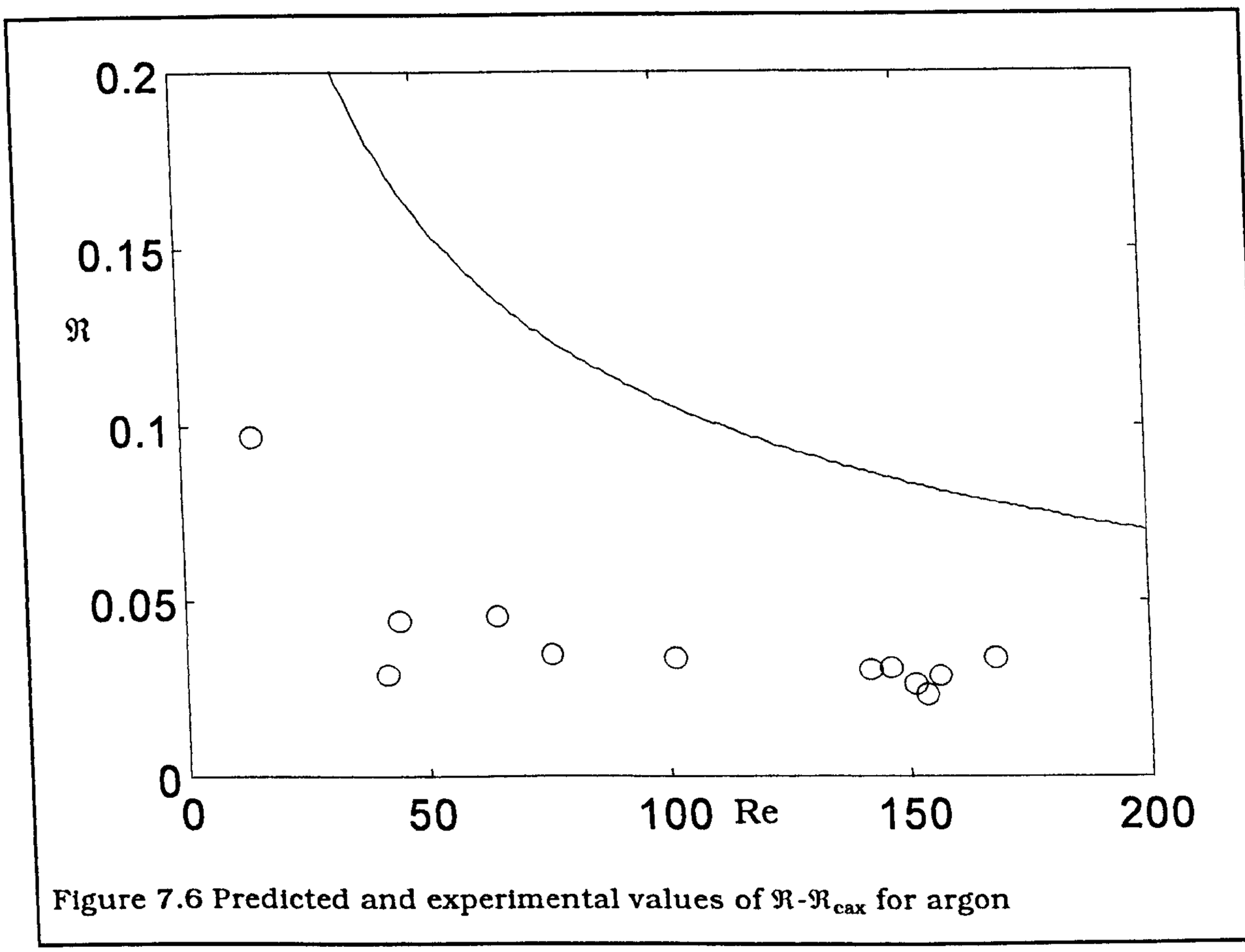

Figure 7.6 Predicted and experimental values of $\Re$-$\Re_{cax}$ for argon

The discrepancy between the results using ammonia and argon suggest that either:

- Some phenomenon connected with adsorption has had an effect on the heat transfer coefficient

or

- A systematic error has occurred in the analysis of the experimental data

or

- A systematic error has occurred in the physical experiment

These three possibilities will be considered separately

Physical phenomena affecting the measured heat transfer coefficient

Transpiration

One cause for the apparent divergence between the results of experiments with ammonia and argon lies in the phenomenon of transpiration. This effect occurs in situations where a gas is ejected from or drawn into the porous surface of a solid. The injection of gas into the boundary layer insulates the solid and reduces the convective heat transfer coefficient. Suction, of course has the opposite effect. Hartnett and Eckert [12] provided solutions to the problem based on flow over a flat plate for fully developed thermal and momentum boundary layers. An accurate estimate of the effect of transpiration through the grain surface of a grain in a packed bed is not easily made, but using some crude assumptions it is possible to make a reasonable 'order of magnitude ' calculation.

Consider a flat plate exposed to flow of gas $\dot{m}_{\infty}$ with a transpiration flow $\dot{m}_{transp}$ as shown in figure 7.7. The boundary layer thickness δ is given by the accepted solution

$$\frac{\delta}{x} = \frac{5}{\sqrt{\mathrm{Re}_x}} \tag{7.39}$$

Where Re_x is the local Reynolds number defined by the distance from the start and the interstitial gas velocity. The velocity profile within this boundary layer is given by the approximate solution from Karman [13].

$$\dot{m}_{local} = \dot{m}_\infty \left(\frac{2y}{\delta} + \frac{y^2}{\delta^2} \right) \tag{7.40}$$

where y is the distance from the wall. Close to the surface this may be approximated by

$$\dot{m}_{local} = \dot{m}_\infty \frac{2y}{\delta} \tag{7.41}$$

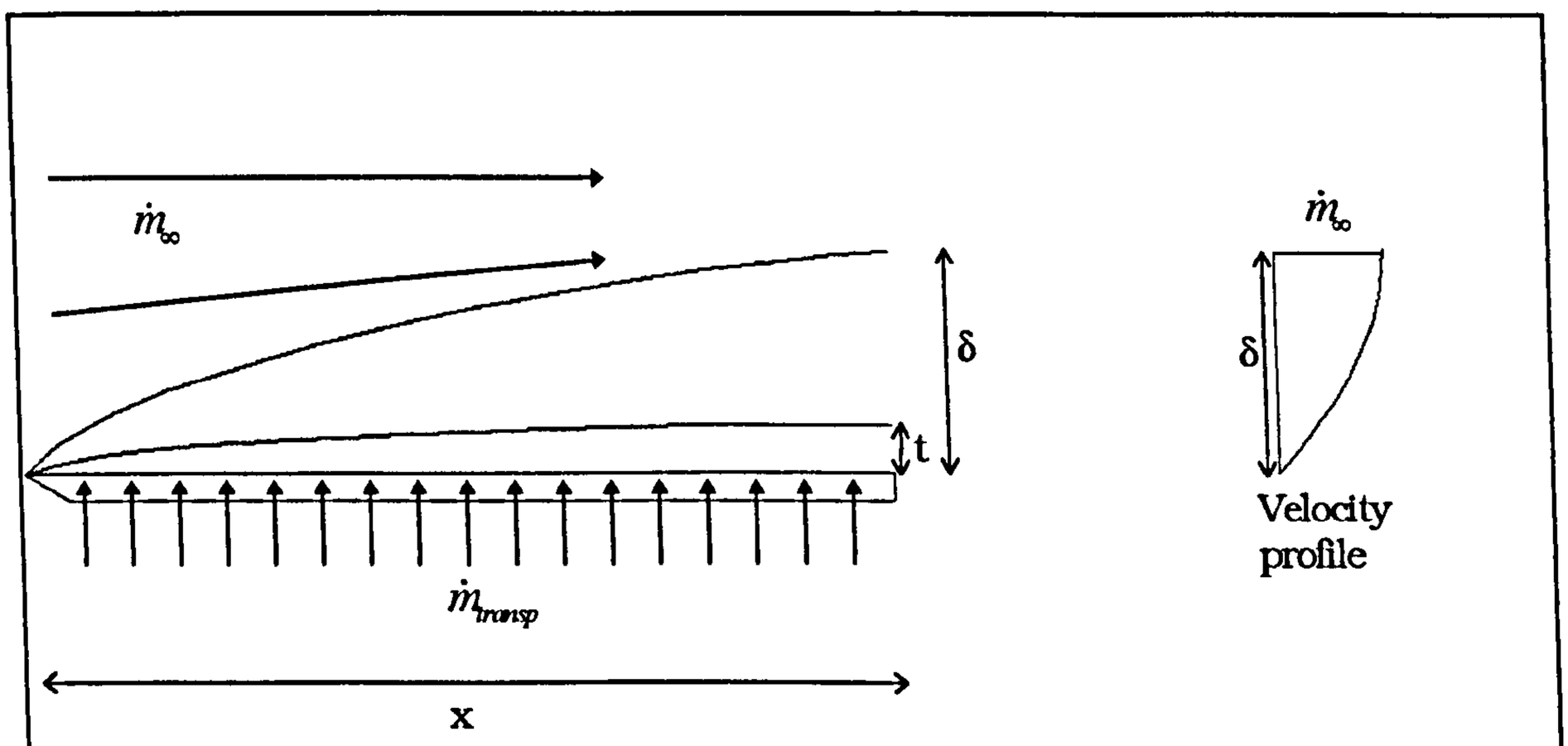

Figure 7.7 A laminar boundary layer with transpiration.

At some distance x along the plate it is possible to define a distance t so that all the gas injected into the boundary layer flows between $y=0$ and $y=t$. Since the transpired mass flow entering this region must be the same as that leaving then

$$x\dot{m}_{transp} = \int_{y=0}^{y=t} \dot{m}_{local} dy \tag{7.42}$$

and so

$$t = \sqrt{5}\sqrt{\frac{\dot{m}_{transp}}{\dot{m}_{\infty}}}\frac{x}{\mathrm{Re}_x^{0.25}} \tag{7.43}$$

and the average thickness $\bar{t}$ along the length x of this transpired layer is

$$\bar{t} = \frac{\sqrt{5}}{1.75}\sqrt{\frac{\dot{m}_{transp}}{\dot{m}_{\infty}}}\frac{x}{\mathrm{Re}_x^{0.25}} \tag{7.44}$$

The dimensionless thermal resistance of this transpired layer, if modelled as an insulating envelope of gas of thickness $\bar{t}$ is given by

$$\Re_{transp} = \frac{\bar{t}}{d} \tag{7.45}$$

Making the assumption that this boundary layer survives for a distance downstream equal to one grain diameter then , replacing the Reynolds number using the local gas velocity by that defined by the superficial velocity and the grain diameter then the thermal resistance becomes

$$\Re_{transp} = \sqrt{\frac{\dot{m}_{transp}}{\dot{m}_{\infty}}}\frac{1.278\psi^{0.25}}{\mathrm{Re}^{0.25}} \tag{7.46}$$

Typical values may be calculated using the maximum rate of change of temperature of 1°C/s which gives a rate of change of concentration of the adsorbate of $2.4 \times 10^{-3}\ s^{-1}$ This represents a rate of transpiration of 8×10^{-4} kg $m^{-2}s^{-1}$. at Re=100 typical interstitial mass flows are 1kg $m^{-2}s^{-1}$. Inserting these values into equation (Eq 7.46) gives $\Re_{transp} \cong 0.0086$ which is around 9% of the total resistance at that Reynolds number. Since the rate of transpiration is not constant throughout the bed it can not be included in the resistance terms directly. figure 7.8 shows the effect of the inclusion of transpiration into the numerical model that is used to derive the overall thermal resistance from the experimental data.

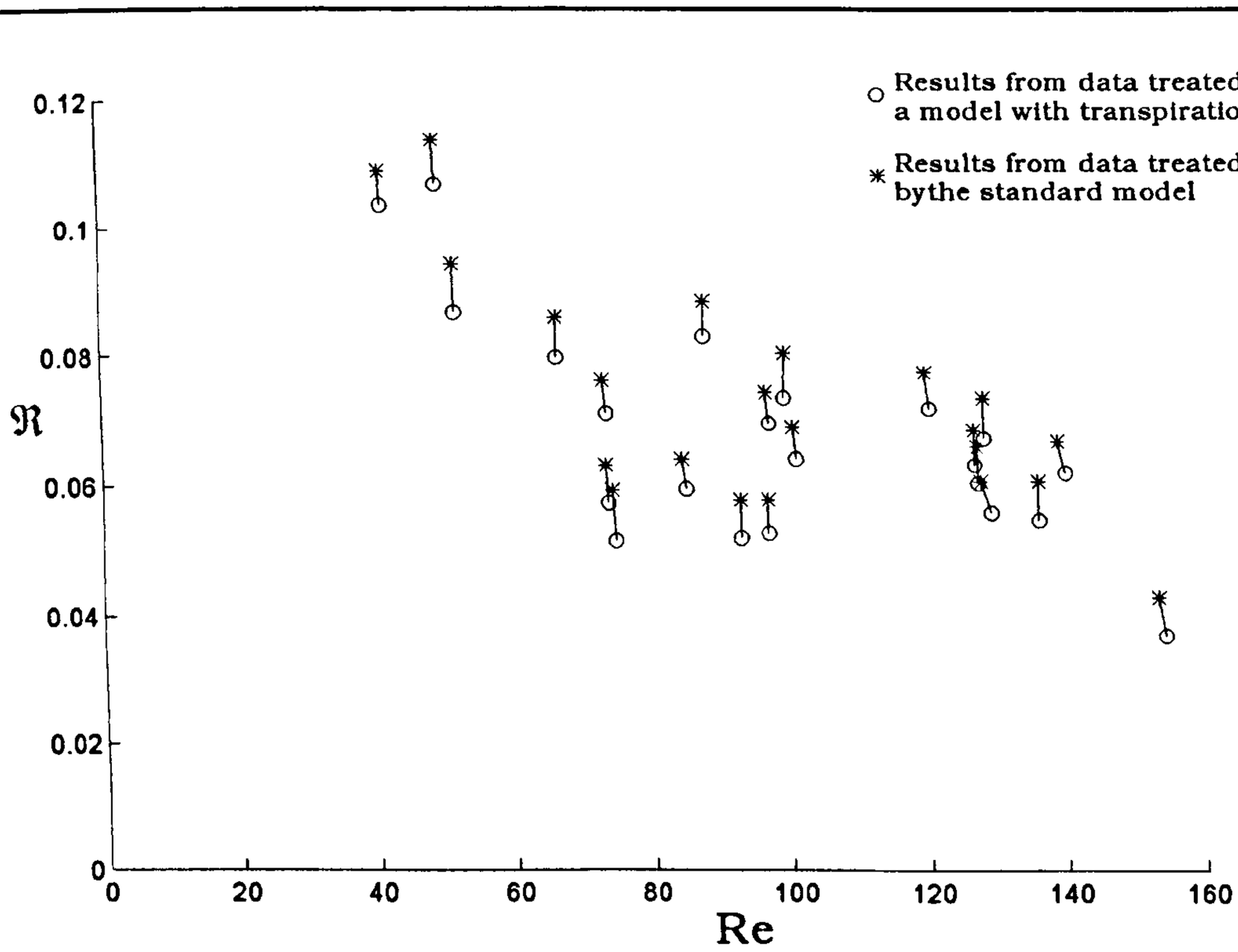

Figure 7.8 Results from the experimental data analysed by a program including transpiration as equation7.46.

Increased grain conductivity due to the presence of adsorbed material

Turner has shown that the grain conductivity of active carbon does increase at high concentrations of adsorbate and that the maximum conductivity may be 50% higher than the conductivity at zero concentration. Using equation 7.15 and 7.27 the maximum credible change in $\Re_{cax}$ at RePr =100 is $\Delta\Re$=0.0016. This has only a negligible effect on the total thermal resistance which is 0.075

Systematic errors in data interpretation

The computer program that interprets the data from the experiments to determine the effective Nusselt number was checked and rewritten several times. Using a

dummy set of input data the program returned the same temperature profiles as those published by Schmidt and Willmott [14] for the single blow regenerator.
The effect of changing the model step size and the computational precision was investigated and showed that step sizes were adequately small.
All algorithms for the thermodynamic and transport properties of the gases were tested and validated against published values.

It is recognised that there may be some uncertainty over the pressure -temperature -concentration relationship for carbon and ammonia. A number of correlations have been used at Warwick from experimental data and all produced similar heat transfer results when used in the programme within a range of 4%. Changing the Individual constants of the Dubinin -Astakhov equation by 10% gave the following deviations in deduced Nu.

$$\frac{\Delta k}{k} = 0.1, \quad \frac{\Delta Nu}{Nu} = 0.025$$

$$\frac{\Delta x_0}{x} = 0.1, \quad \frac{\Delta Nu}{Nu} = 0.084$$

The true value of the heat capacity of the adsorbed phase is not known with any accuracy. Changing the value used by 10% changed the resulting Nu by 1.8%

Systematic errors in the experiments

Radial conduction

The radial temperature distribution was monitored for experiments with argon by the use of three thermocouples at different radial positions for each station in the bed. The bed radius is 62.5mm and the thermocouples were at 10, 37.5 and 52.5mm from the centre. The results from the experiments clearly show the influence of the different conditions at the wall on the outer thermocouple but the

similarity of the traces for the two inner thermocouples gives confidence that the effect in the core of the bed is negligible.

Presence of adsorbed gases in the argon experiments

The good repeatability of the argon results compared with the less consistent data from the ammonia experiments led most investigations to be aimed at finding errors in the ammonia experiments. Examination of the predicted and observed temperature profiles at the downstream part of the bed show an increase in temperature that is not reflected in the simulation. This is seen in some of the plots in the appendix and in figure 7.9. This temperature rise is due to the enthalpy of adsorption of a gas as the pressure or partial pressure increased. The adsorption data for argon on carbon indicates that it is not the readsorption of argon that is likely to be responsible for this phenomenon. Changing the assumed adsorption characteristic within a credible range failed to give the same temperature rise in the simulation as that observed.

It may be assumed that there was an adsorbable gas present during the argon experiments, and there are a number of possible scenarios

- During preparation of the active carbon in the laboratory prior to the loading of the equipment it is normally heated to 200°C under vacuum. Several problems were encountered with the vacuum pump due to condensation of water vapour, reducing the effectiveness of the pump. It is possible, therefore that the carbon was not properly degassed and that some water vapour was present during the experiments.
- It is possible that the charging manifold or hoses contained some water from previous use and that this passed into the experimental apparatus during charging.

- Carbon dioxide may have dissolved in the lubricant of the gas circulating pump.

  This gas may then have been released during the argon tests.

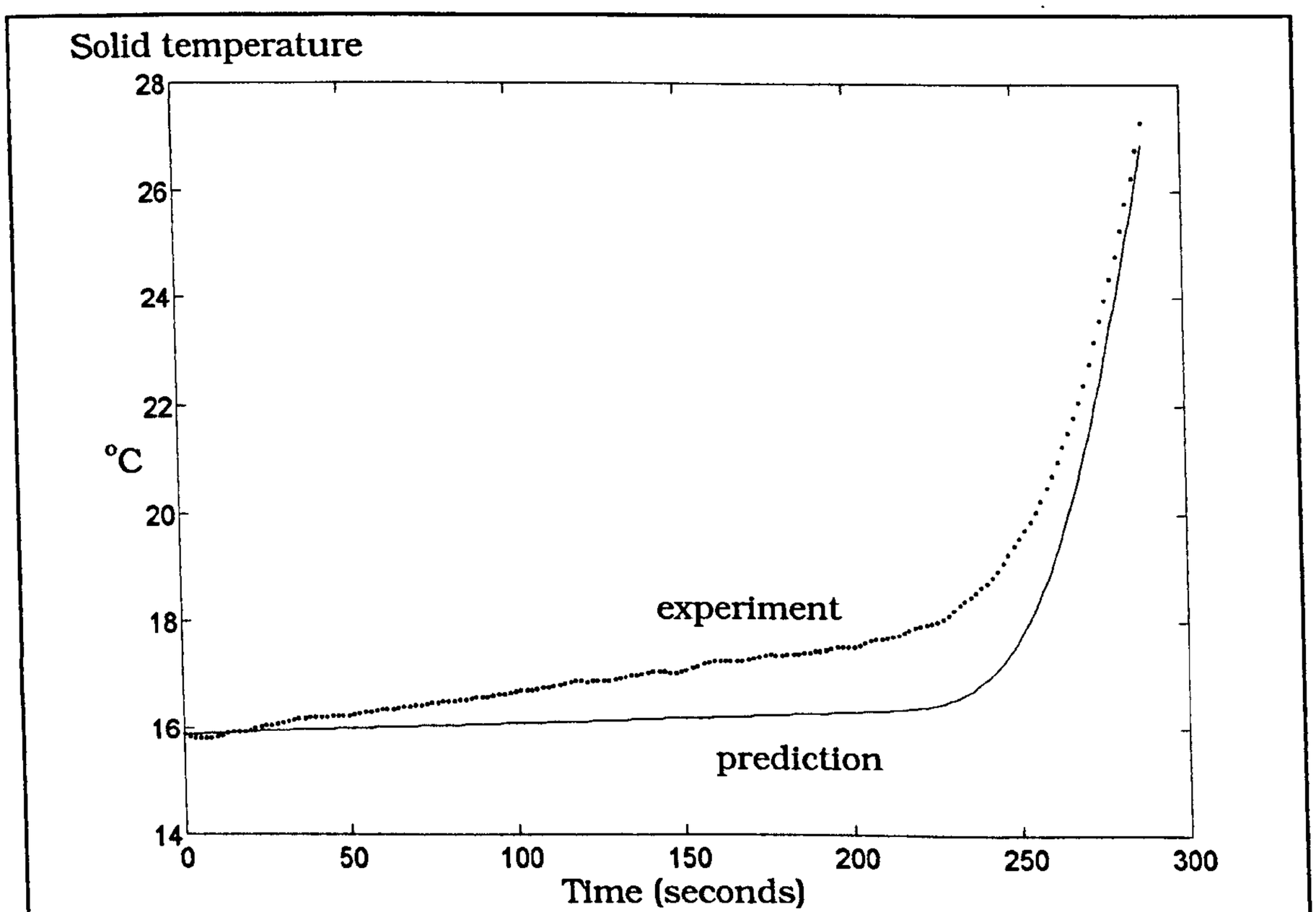

Figure 7.9 Experimental and predicted solid temperatures at the start of run AR5.

The effect of an adsorbed gas on the carbon is to change the effective heat capacity of solid and to make it a function of temperature and partial pressure of the adsorbate. The total effective heat capacity is given by

$$c_{eff} = c_s + xc_a + h_{ag}\frac{\partial x}{\partial T}$$

where

c_s = Heat capacity of the adsorbed phase

h_{ag}=Enthalpy of adsorption

$\frac{\partial x}{\partial T}$ = Rate of change of concentration with temperature

The magnitude of this effect is shown in figure 7.10. where the individual components of c_{eff} can be seen.

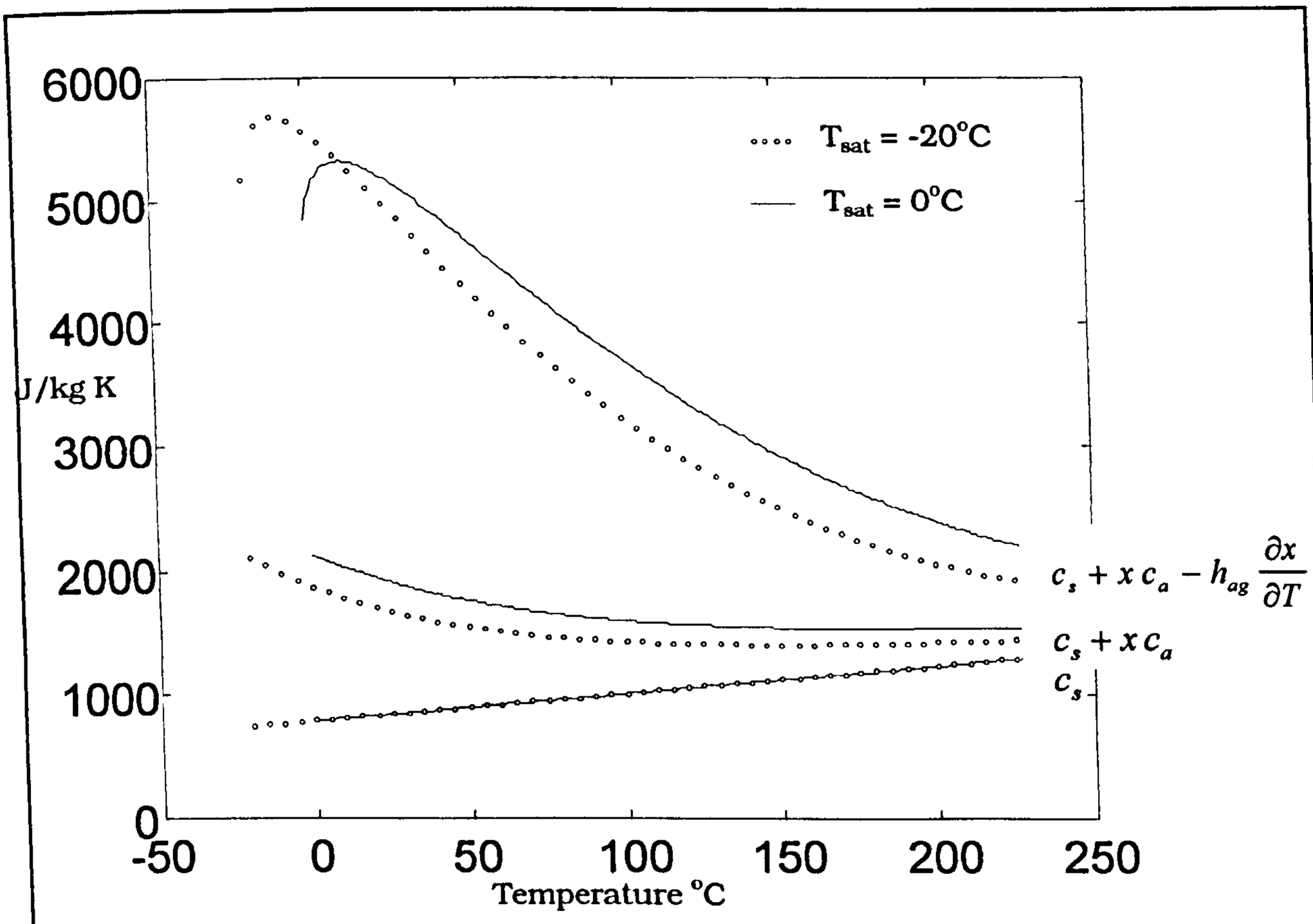

Figure 7.10 Effective heat capacity for cabon 208C with ammonia at two

The variation of heat capacity with temperature has a strong influence on the development of the temperature profile within the bed. This is because the propagation speed of the temperature front is determined by the ratio $\frac{\dot{m}c_p}{mc_{eff}}$. In situations where the effective heat capacity of the solid decreases with temperature the propagation velocity will be higher in the hot part of the wave than the cold part. This has the effect of increasing the steepness of a hot front and decreasing the steepness of a cold one in the absence of any thermal resistance. In real beds, where the thermal resistance is finite the reduction in steepness of a hot front decreases less as it progresses down the bed than it would in a bed with constant thermal properties. For very long beds it is possible for the temperature front to become stable and progress with no change in steepness.

This behaviour is confirmed by the numerical model. Figure 7.11 shows how the maximum rate of change of temperature decays as the temperature front travels down the bed and how this decay is reduced in the two non-linear cases plotted. It is possible to see how the non-linearity leads to an error in the calculation of heat transfer coefficient in figure 7.12. The quantity $\frac{\partial T_s}{\partial \eta}\eta$ where η is the dimensionless time since the start of the blow is equivalent to $\frac{\partial T_s}{\partial t}t$ where t is the time (in any units) since the start of the blow. Since the time that the rate of change of temperature reaches its maximum is relatively insensitive to the heat transfer coefficient then for a wide range of heat transfer coefficients and flow rates $\left(\frac{\partial T_s}{\partial t}\right)_{max} \propto \left(\frac{\partial T_s}{\partial \eta}\right)_{max} \eta$. For a bed of a given physical length L and fluid heat capacity flux per unit cross section $\dot{m}c_p$ the heat transfer characteristic αa is proportional to Λ since $\Lambda \equiv \frac{\alpha a L}{\dot{m} c_p}$. Figure 7.12 shows how the maximum value of $\frac{\partial T_s}{\partial t}$ for a bed with constant heat capacity and dimension less length Λ of 50 is identical to that of $\Lambda = 34$ if the heat capacity at the hot temperature is 20% higher than that at the low temperature. The error in measurement of the heat transfer coefficient caused in this way increases with Λ.

Analysis of the experimental data with some assumed adsorbable gas built into the model confirmed that the possible magnitude of this effect is enough to bring the heat transfer data for argon and ammonia into some agreement . Since the nature and concentration of any contaminant is, however unknown and not constant it is not possible to correct for this effect or give any estimate of its size.

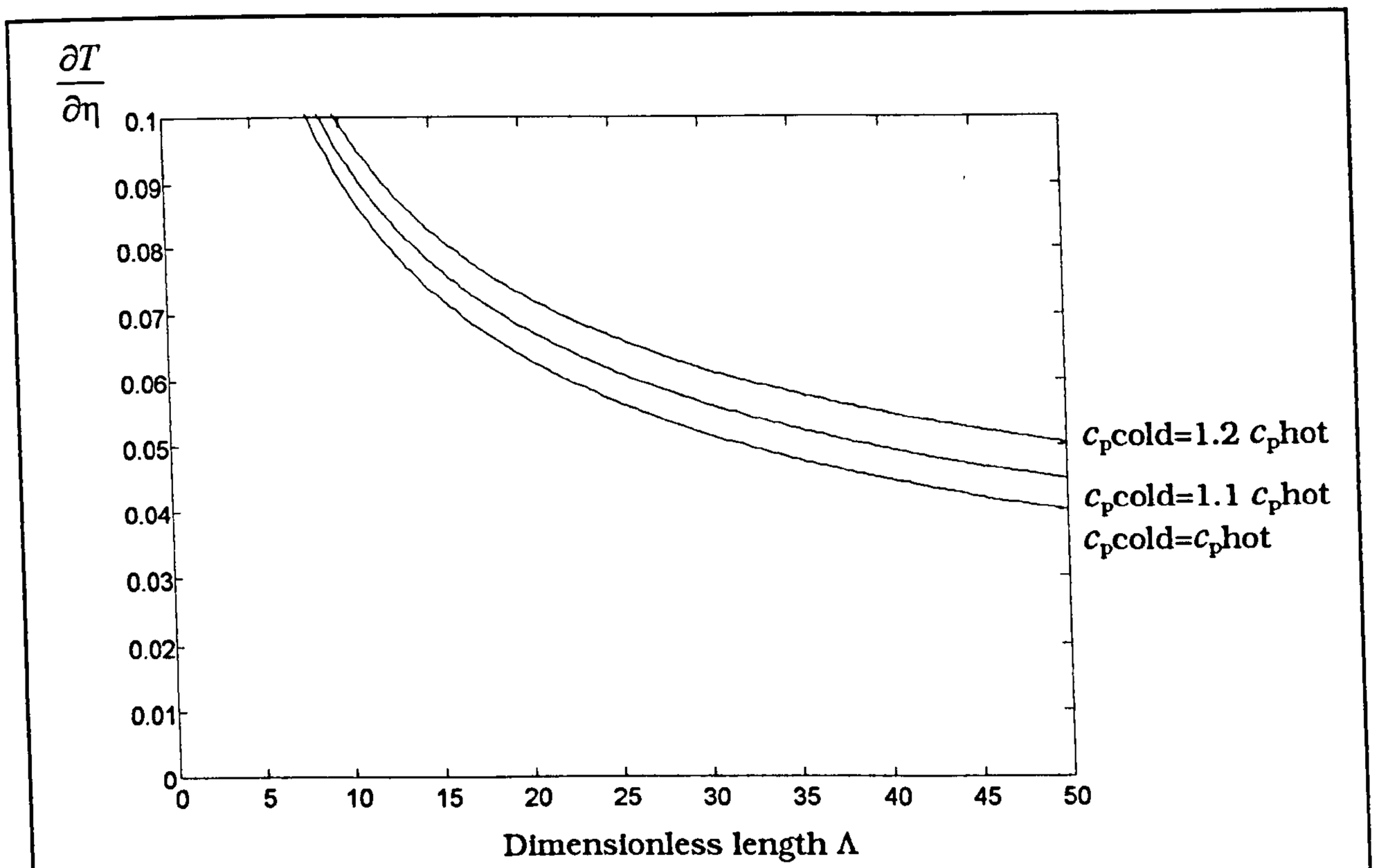

Figure 7.11 Rate of change of temperature with dimensionless time plotted against dimensionless length

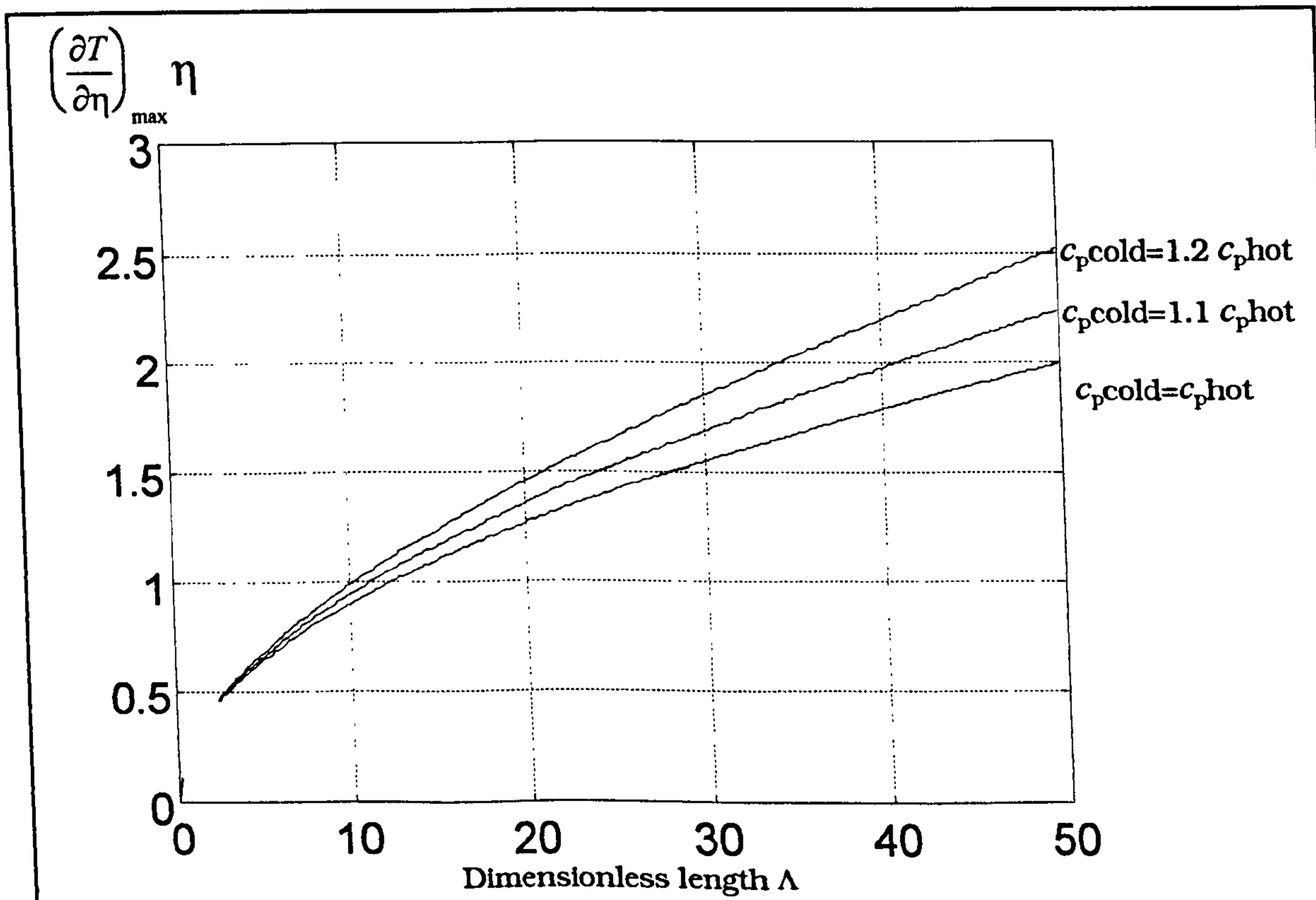

Figure 7.12 Rate of change of temperature with time plotted against dimensionless length for the nonlinear regenerator

Oil contamination of the carbon

During the recharging of the carbon bed it was noticed that significant amounts of oil were being carried into the bed despite the use of an oil separator. On one occasion, while the pressure of ammonia in the system was being reduced severe contamination was caused by foaming of the oil in the separator and the sump of the pump. This is due to the solution of gas by the oil. Once this had been discovered the pipework was cleaned and the carbon replaced. Foaming was reduced by the use of a sump heater and trace heating of the oil separator. Despite these measures some carryover of oil continued. The first effect to be observed caused by the oil although not recognised as such at the time was that the electrical resistance of the intrinsic thermocouples at the top of the bed where contact pressure is lowest increased causing erratic temperature readings. Although this symptom was reduced by heating the bed to beyond 100°C it seems likely that some oil remained. Figure 7.12 shows some evidence of the effect of oil contamination on the temperature profiles. Two features should be noted.

In the first part of the test, up to about 120 seconds from the start, as the pressure increases so the temperature of the downstream station rises due to the adsorption of more ammonia. The predicted rise is greater than the observed rise and this may be attributed to the blockage of pores by an oil film.

At about 250 seconds the temperature gradient falls considerably. This may be attributed to the energy lost from the evaporation of oil from the grain surface.

These features may be used as a diagnostic test for oil contamination and used to eliminate some of the experiments from the analysis. Some selection of experiments took place early in the study and seven experiments that showed clear deviations were eliminated. Care was taken to ensure that this selection took place by observation of the temperature profiles alone without reference to the heat transfer coefficients derived from them in order to retain as much objectivity as possible.

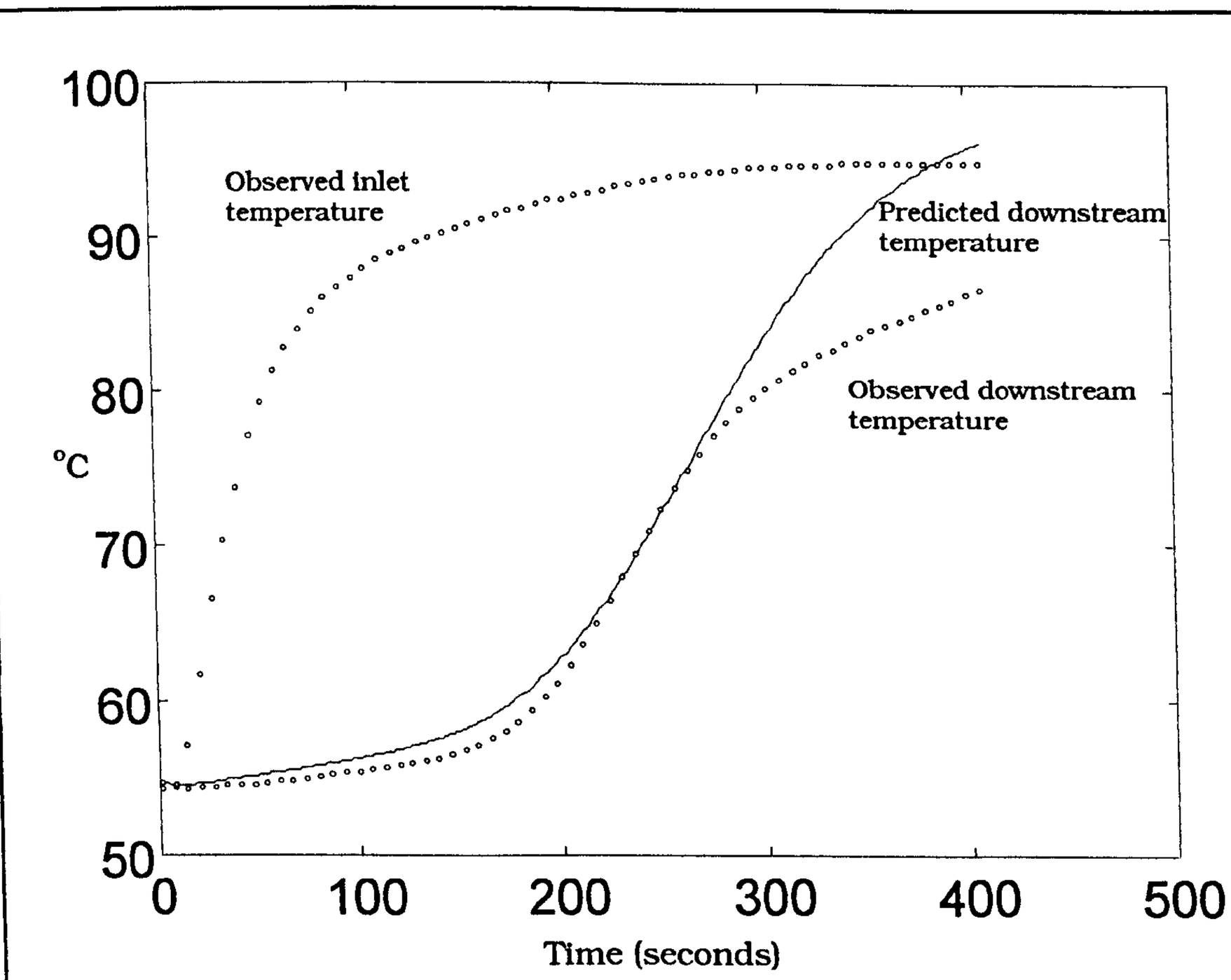

Figure 7.13 Observed and predicted temperature profiles from experiment 100a showing the effects of oil contamination.

Conclusions

None of the effects of axial dispersion, axial conduction, grain conductivity or transpiration can be invoked to account for the deviation between the results from the tests with argon from those with ammonia. Comparison with the predicted heat transfer data show the argon results to be implausible. It is unlikely that there are errors in the model since the models have been examined and rebuilt a number of times. It seems most probable that an adsorbable gas, either carbon dioxide or water is responsible for the high Nusselt numbers returned by the experiments with argon. It is also likely that the oil contamination in varying quantities is responsible for the spread of the data in the results using ammonia.

The values of $\frac{j_h \Psi}{f_v'}$ where jh is defined using the overall Nusselt number are plotted

against Re in figure 7.14. These data fit the relationship

$$\frac{j_h \psi}{f_v'} = \frac{0.37}{\mathrm{Re}_{Dh}^{1.032}}$$

which suggests that a reasonable correlation between Nusselt and Reynolds number is

$$Nu = 8.174\,\mathrm{Pr}^{1/3}\,\mathrm{Re}^{0.032} + 0.088\,\mathrm{Pr}^{1/3}\,\mathrm{Re}^{0.968} \qquad (7.47)$$

this may be linearised to

$$\mathrm{Nu} \approx 7.3701 + 0.0694\,\mathrm{Re} \qquad (7.48)$$

for Pr=0.93.

This relationship is shown in figure 7.15 as a plot of Nu against Re. For the application of regenerators it is the dimensionless length or number of transfer units (NTU) that is of interest and a more useful way to present the heat transfer data is to plot NTU_g against Re where NTU_g is defined by

$$NTU_g = \frac{\alpha a d}{\dot{m} c_p} \qquad (7.49)$$

Its physical interpretation is the dimensionless length of a bed one grain diameter in length.

Substituting

$$a \equiv \frac{6(1-\psi)}{d}$$

then

$$\mathrm{NTU_g} = \frac{6(1-\psi)\alpha}{\dot{m} c_p} = 6(1-\psi)\frac{\mathrm{Nu}}{\mathrm{RePr}}. \qquad (7.50)$$

This relationship is shown in figure 7.16

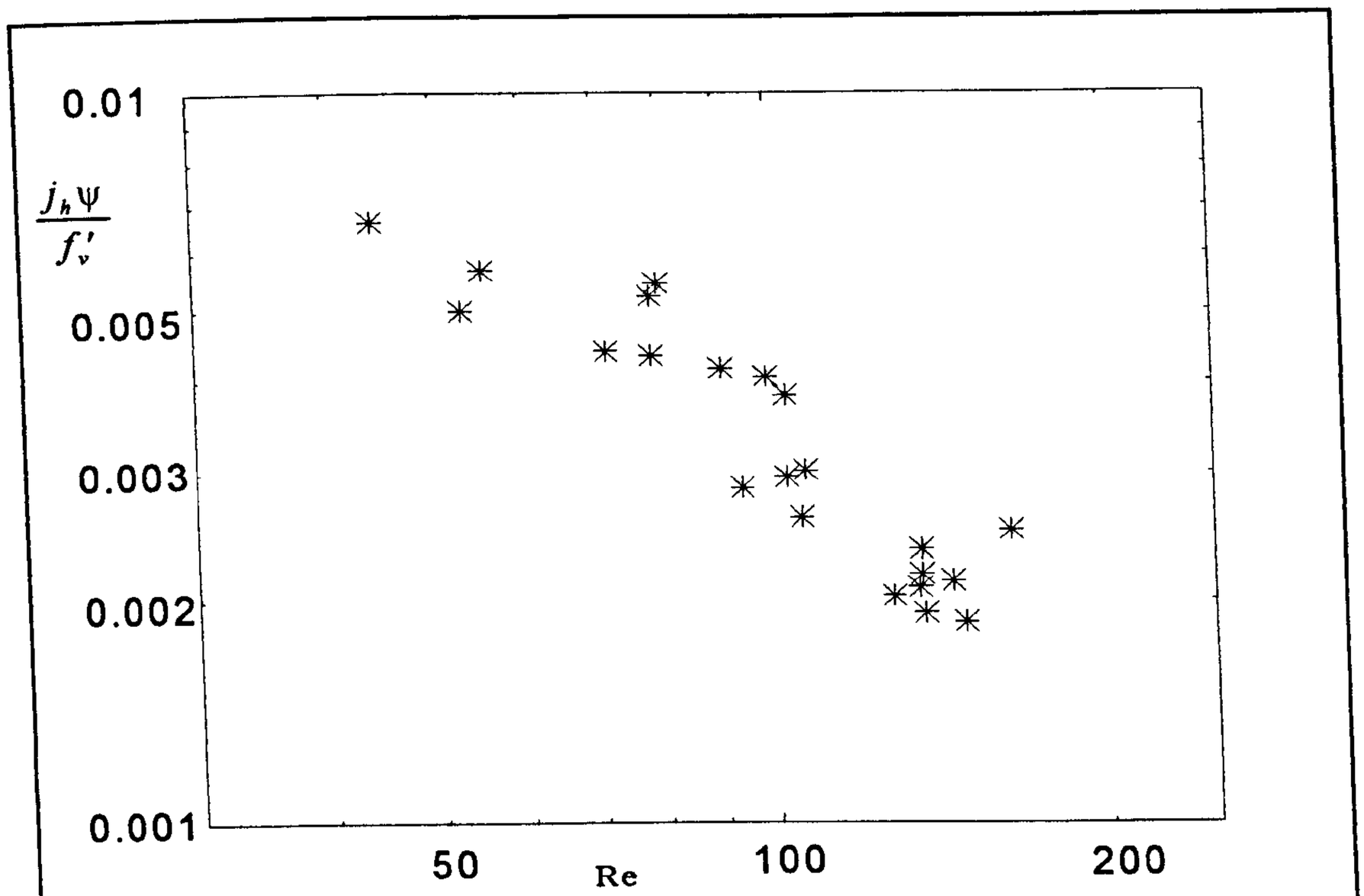

Figure 7.14 A log-log plot of $\frac{j_h \Psi}{f_v'}$ against Re.

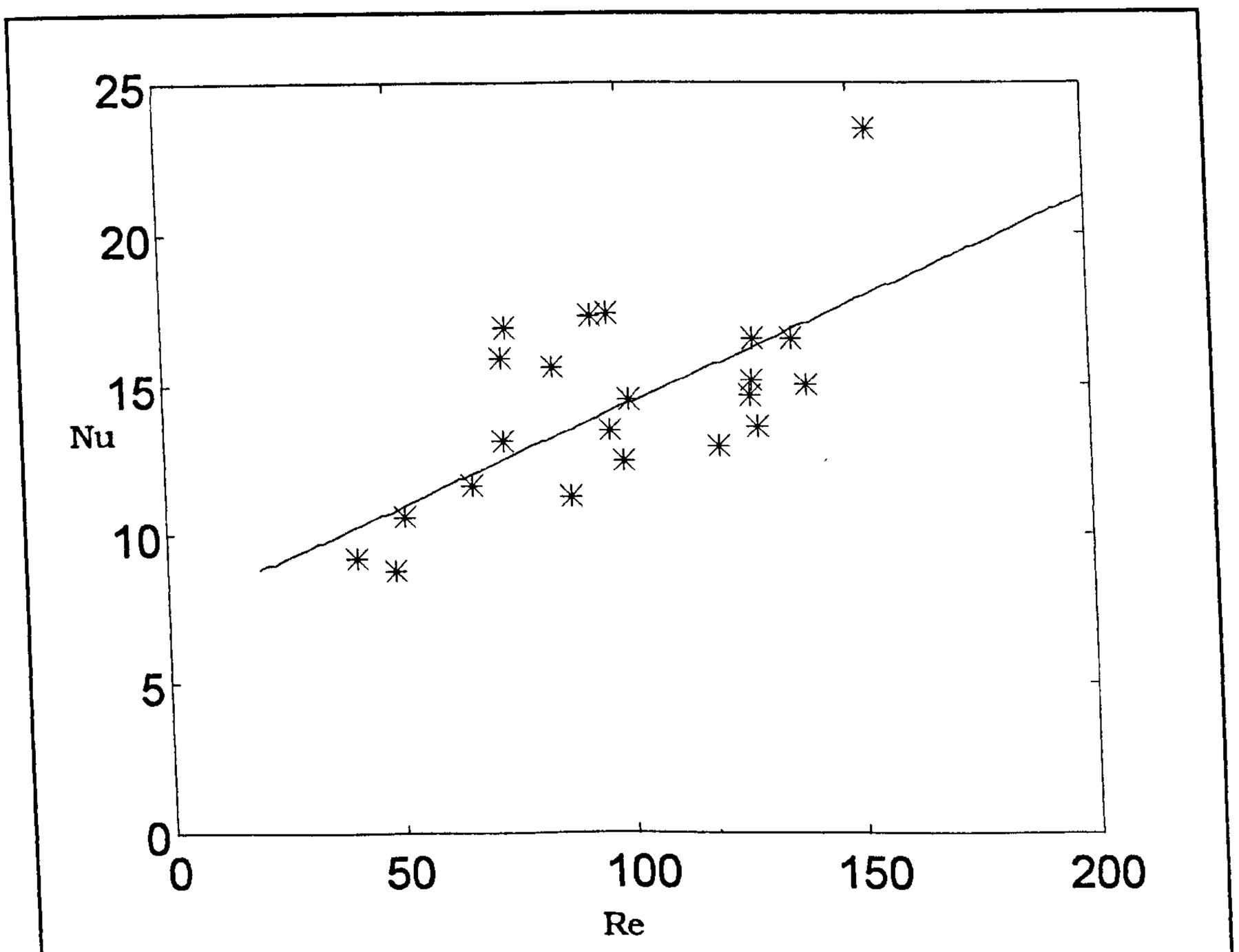

Figure 7.15Ammonia results and the correlation Nu=7.3701+0.0694Re

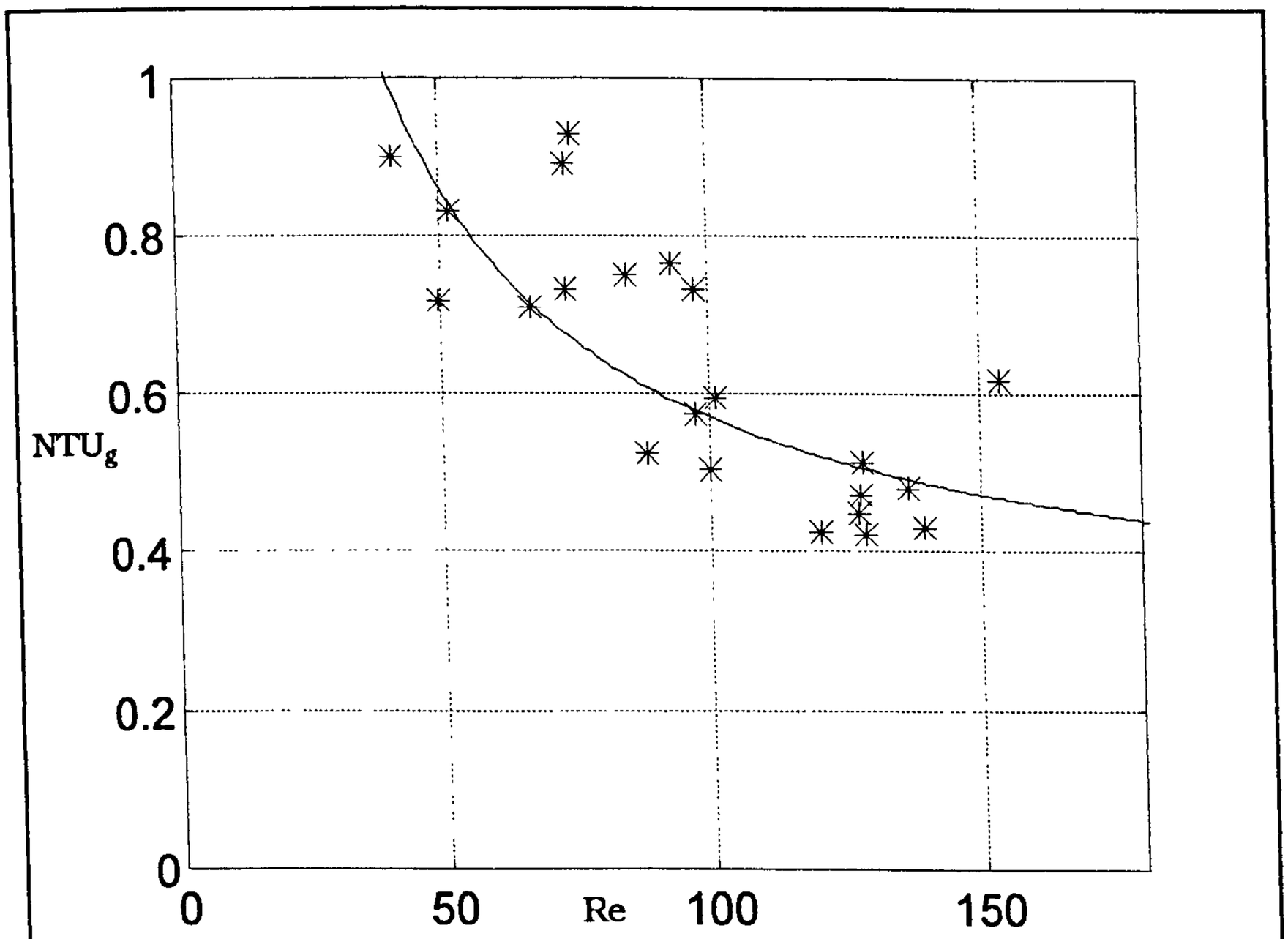

Figure 7.16 NTU_g plotted against Reynolds number for ammonia on carbon 208C

References

[1] **Hausen H.,** Heat transfer in counterflow, parallel flow and crossflow., *McGraw-Hill* (1983)

[2]**Bradshaw A.V., Johnson A., McLachlan N.H., Chui Y-T.,** Heat transfer between air and nitrogen and packed beds of non-reacting solids. *Transactions of the Institute of Chemical Engineers* **Vol 48** ppT77-T84 (1970)

[3] **Turner H.L.,** Improvement of activated charcoal - ammonia adsorption heat pumping/refrigerating cycles - investigation of porosity and heat/mass transfer characteristics, *PhD Thesis University of Warwick* (1992)

[4] **Bauer R.,** Effektive radiale warmleitfahigekeit gasdruchstromter schuttungen mit partikeln unterschiedlerform und grossenverteilung VDI Forschungsh 528

[5] **Hadley G.R.,** Thermal conductivity of packed metal powders, *International journal for heat and mass transfer*, **Vol 29** pp909-920 (1986)

[6] **Kaviany M.,** Principles of heat transfer in porous media, springer (1995)

[7] **Tien C-L., Drolen B.L.,** Thermal radiation in particulate media with dependant and independant scattering, *Annual Review of Numerical Fluid Mechanics and Heat Transfer* Vol 1 p1-32 (1987)

[8] **Gunn D.J.,** Mixing in packed and fluidised beds, *The Chemical Engineer*, **June 1968** ppCE153-172

[9] **Wakao N., Kaguei S.,** Haet and mass transfer in packed beds, *Gordon and Breach science* (1982)

[10] **Handley D., Heggs P.J.,** Momentum and heat transfer in regular shaped packings, *Transactions of the American Institute of Chemical Engineers*, **Vol29** ppT251-T263 (1968)

[11] **Colburn A.P.,** Amethod of correlating forced convection heat transfer data and a comparison with fluid friction, *Transactions of the American Institute of Chemical Engineers* **Vol 29** pp174-210 (1933)

[12] **Hartnett J.P., Eckert E.R.G.,** Mass transfer cooling in a laminar boundary layer with constant fluid properties, *Transactions of the American Society of Mechanical Engineers* **February 1957** pp247-254

[13] **von Karaman** On laminar and turbulent friction, *Z agnew math mech* pp235-236 (1921)

[14] **Schmidt F.W., Weillmott A.J.,** Thermal energy storage and regeneration, *Hemisphere* (1981)

Chapter 8 Closure

A novel adsorption cycle in which enhanced heat transfer between the adsorbent and external heat sinks and sources is achieved by forced convection of refrigerant gas through the adsorbent bed has been presented in Chapter 1. This cycle is further developed by the use of inert beds to store the heat of desorption and sensible heat between phases. The performance and utility of such a cycle will depend on the heat transfer coefficients and pressure drops that result when the refrigerant gas is circulated through the beds. An investigation of the variation of the heat transfer and pressure drop in this situation is the purpose of this work. Chapters 2 and 3 discuss the fundamentals of adsorption and heat transfer in regenerators that must be understood in order to model the processes that will occur in a real heat pump or refrigerator using the convective thermal wave cycle. In order to measure the heat transfer and pressure drop characteristics a test rig which allows the circulation of adsorbed and inert gases through adsorptive beds at controlled temperatures pressures and flowrates was built. This is described in detail in Chapter 4.

The apparatus was used to measure the pressure drops encountered when circulating either argon (inert) carbon dioxide (adsorbed) or ammonia (adsorbed) through the active carbon granular bed. Good agreement with the Ergun equation was obtained. The analysis of heat transfer between the gas and bed is much more complex. Measurements depend on setting up a thermal wave travelling along the bed and altering the heat transfer coefficient in a computer simulation until similar temperature and pressure profiles are obtained.

The heat transfer coefficients measured for argon and for ammonia appear inconsistent with respect to each other. A thorough analysis of all conceivable sources of error revealed that the argon results were probably invalidated due to

the effects of contamination of the carbon with water vapour or retained carbon dioxide. There is some evidence for oil contamination in the experiments with ammonia and this may be responsible for the poor repeatability of those results. However, the ammonia results do appear to be consistent with a heat transfer relationship based on a Reynolds Colburn analogy expressed in equation 7.49. The single blow method remains a valid technique for the measurement of the heat transfer coefficient, however for adsorbent beds the variation of effective heat capacity with temperature has a large effect on the development of the temperature front and unless the model accurately reflects this then errors will occur. An approach to solve this problem is to use small temperature swings, a range of temperature swings and both hot and cold blows.

Transpiration will have some effect on the film heat transfer coefficient and this may be expected to be strongest at the ends of the bed where the rate of change of temperature is highest. It will not be easy to measure the effect of transpiration without accurate information on the thermal properties of the adsorbent-adsorbate pair since its effect is likely to be small.

Bed sizing using the pressure drop and heat transfer relations

The Ergun equation (5.1) is

$$\frac{\Delta P}{L} = c\frac{(1-\psi)^2}{\psi^3}\frac{\mu u}{d^2} + m\frac{(1-\psi)}{\psi^3}\frac{\rho u^2}{d}$$

substituting

$u = \frac{\dot{m}}{\rho}$, c=316, m=2.14, ψ=0.374

gives

$$\frac{\Delta P}{L} = 2370\frac{\mu \dot{m}}{\rho d^2} + 25.6\frac{\dot{m}^2}{\rho d}.$$

The recommended correlation for heat transfer is given by equation 7.48

$$Nu \approx 7.37 + 0.069\,\mathrm{Re}.$$

using this relation, and $a = {6(1-\psi)}/{d}$ the dimensionless length may be expressed by

$$\Lambda = \frac{\alpha a L}{\dot{m} c_p} = \frac{27.7\lambda}{d^2 \dot{m} c_p} + \frac{0.261\lambda}{d\mu c_p}.$$

If the properties of the gas are set then the length of bed required to give a design target value of Λ and the associated pressure drop are both functions of the grain diameter and the gas flow per unit surface area of the bed. The total mass flow $\dot{M}$ is associated with the heat input to the bed.

$$Heat\ in = \dot{M} c_p \left(T_{in} - T_{out}\right)$$

if this is regarded as a fixed parameter then the pressure drop and total bed volume for a given L are functions of grain and bed diameter.

Figures 8.1 to 8.2 show the pressure drop, volume and bed length associated with the following parameters, which are typical for the low pressure phase where pressure drop is most critical.

μ=1.25 Pa S

ρ=2 kg m^{-3}

λ=0.035 W m^{-1} K^{-1}

c_p =2400 J kg^{-1} K^{-1}

$\dot{M}$ =0.05 kg s^{-1} (This gives a heat input to the bed of 24 kW for ΔT=200 K)

It can be seen that the pressure drop is strongly a function of bed diameter as may be expected since this parameter determines the velocity of the gas through the bed. It is only weakly affected by the selection of grain diameter since, although the

pressure drop per metre through the bed is nearly inversely proportional to the grain diameter, the larger specific surface area allows a shorter bed for the same Λ. The grain size has a stronger effect on the total volume of the bed. Smaller grains will favour more compact designs, however a small bed will have a short period and rapid cycling may be undesirable for mechanical reasons. There are losses associated with each cycle due to the work done in compressing the gas in the void volume which is not completely recovered during the expansion phase, this will also limit the short-period, small bed design. The optimisation of grain size requires sophisticated analysis therefore, possibly full cycle simulation.

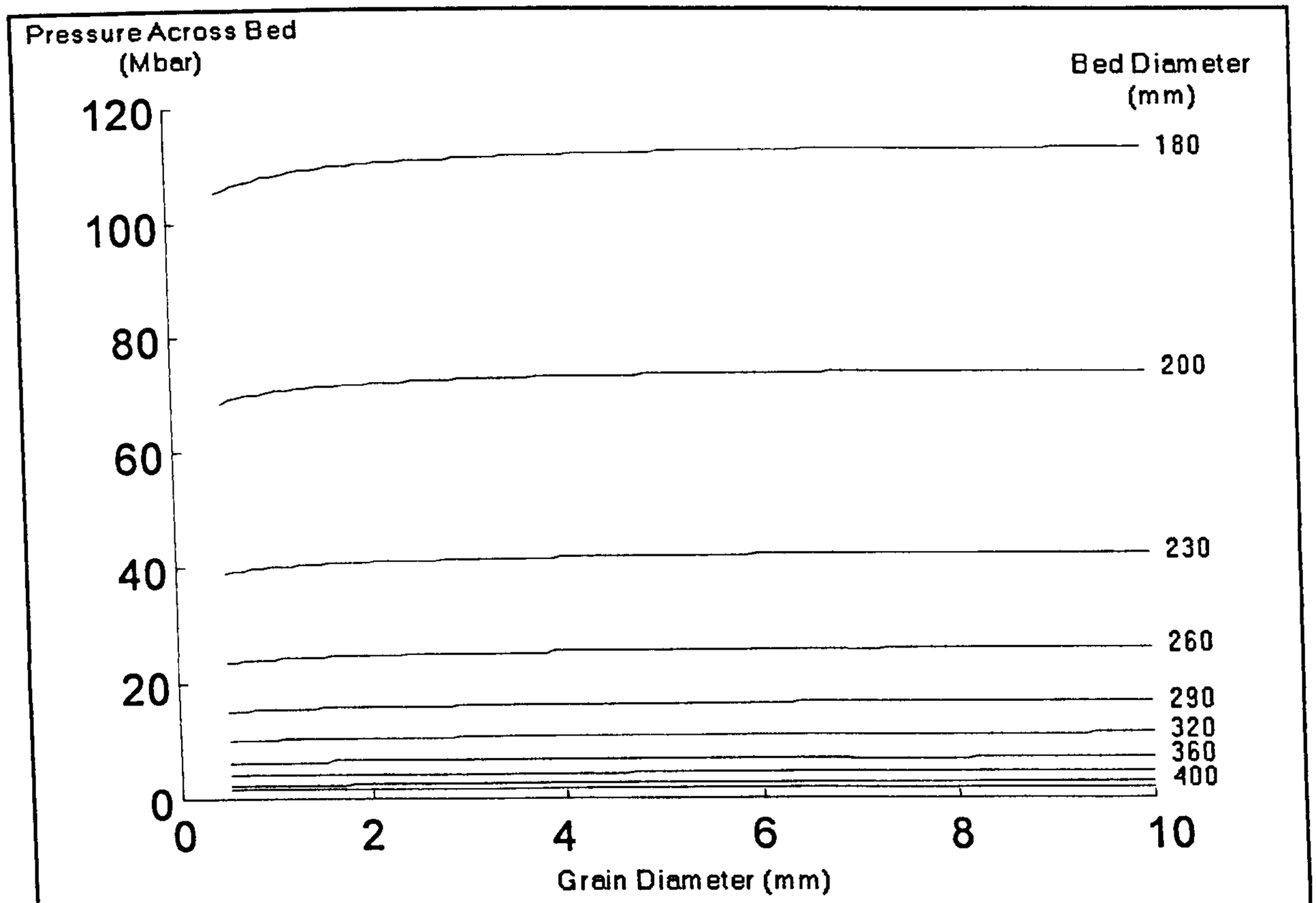

Figure 2.1 Pressure loss across a bed of carbon designed to achieve $\Lambda = 70$ for a mass flow of 0.05 kg/s as a function of grain size for a range of bed diameters.

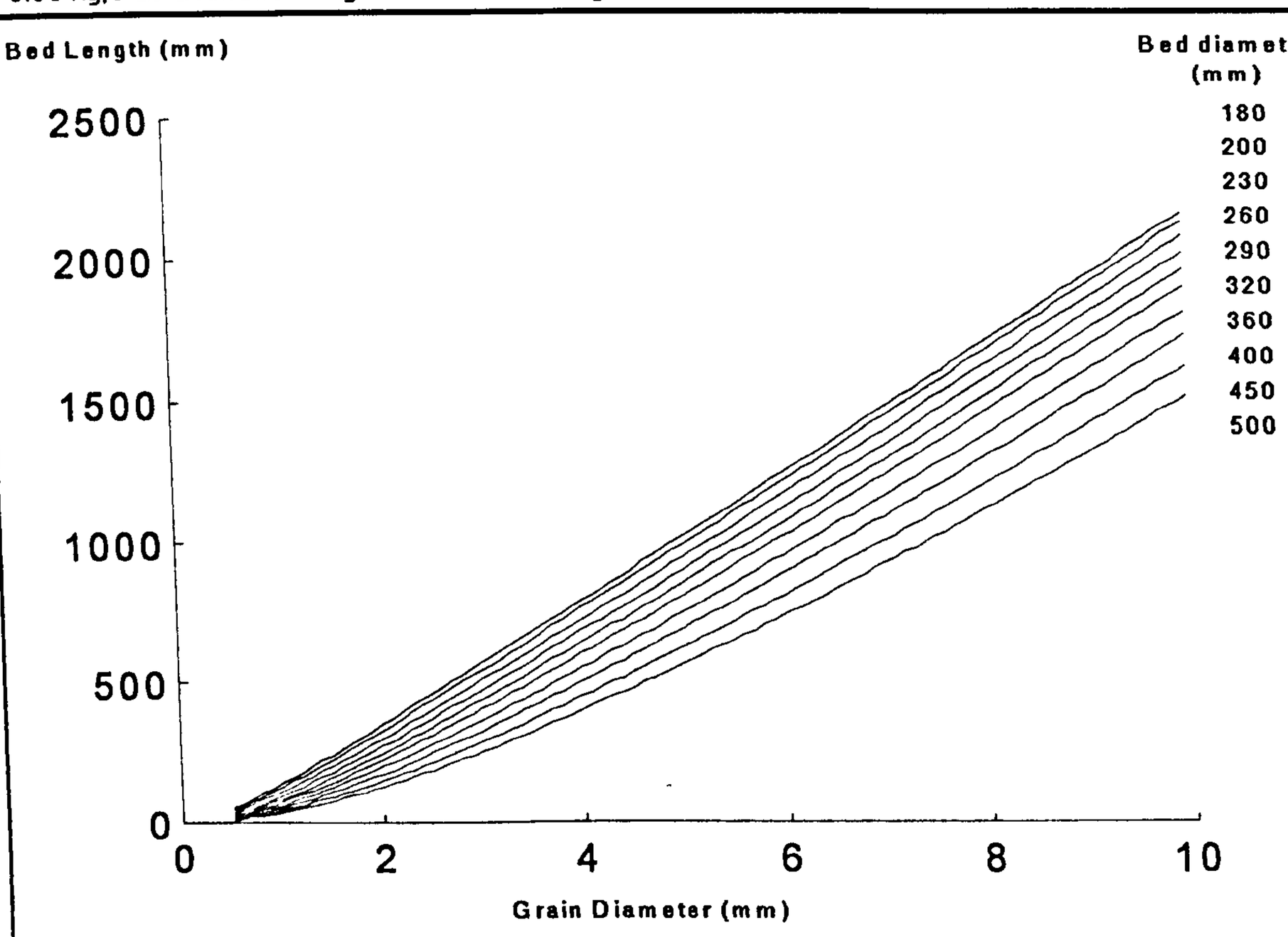

Figure 2.2 Bed length required to achieve $\Lambda = 70$ for a mass flow of 0.05 kg/s as a function of grain size for a range of bed diameters.

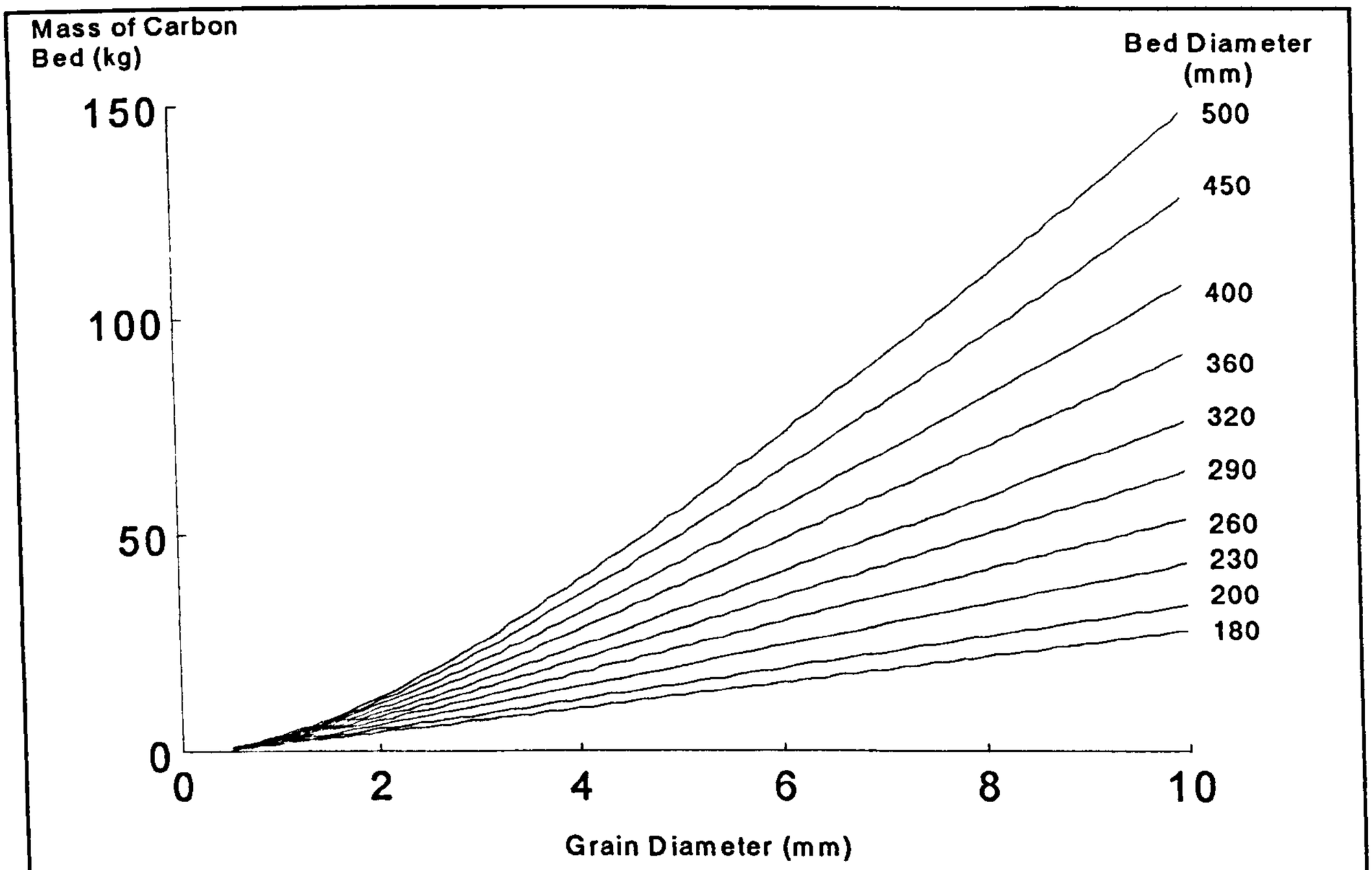

Figure 2.3 Mass of carbon bed required to achieve Λ = 70 for a mass flow of 0.05 kg/s as a function of grain size for a range of bed diameters.

The heat transfer and pressure drop relationships developed in chapter 7 have been used in a separate cycle simulation model [1] , the results of which are presented here to place the heat transfer measurements in context and to confirm the utility of the proposed convective wave cycle. A single example of a cycle simulation is presented below which serves to give an indication of anticipated performance and size:

Evaporating temperature	5°C
Condensing temperature	55°C
Heat source temperature	250°C
Heat sink temperature	55°C
Bed length	300mm
Bed diameter	300mm
COP_{hp}	1.487
Carnot COP	3.073
Power density	647 Watts of heat output per kilogram of carbon
Heating power	13.7kW (for machine with two active beds)
Power required by circulating pumps (each) 2 required	maximum 600W, average 200W.

Although the COP offered by this cycle is high it is still much lower than the Carnot efficiency. The principal cause for this lies not in the heat transfer directly but is in the temperature mismatch in the heating and cooling heat exchangers. This is due to the heating of the cold part of the bed by the readsorption of gas at the beginning of the hot blow as the pressure increases and the cooling of the hot end of the bed during the cold blow as pressure falls. These features may be seen in the temperature profiles of figures 8.1 and 8.2. and more clearly in the gas exit temperature profiles of figure 8.3. This phenomenon is common to all simple thermal wave cycles. It may be that there is some cycle or technique that will circumvent this limitation and some research in this direction would be useful.

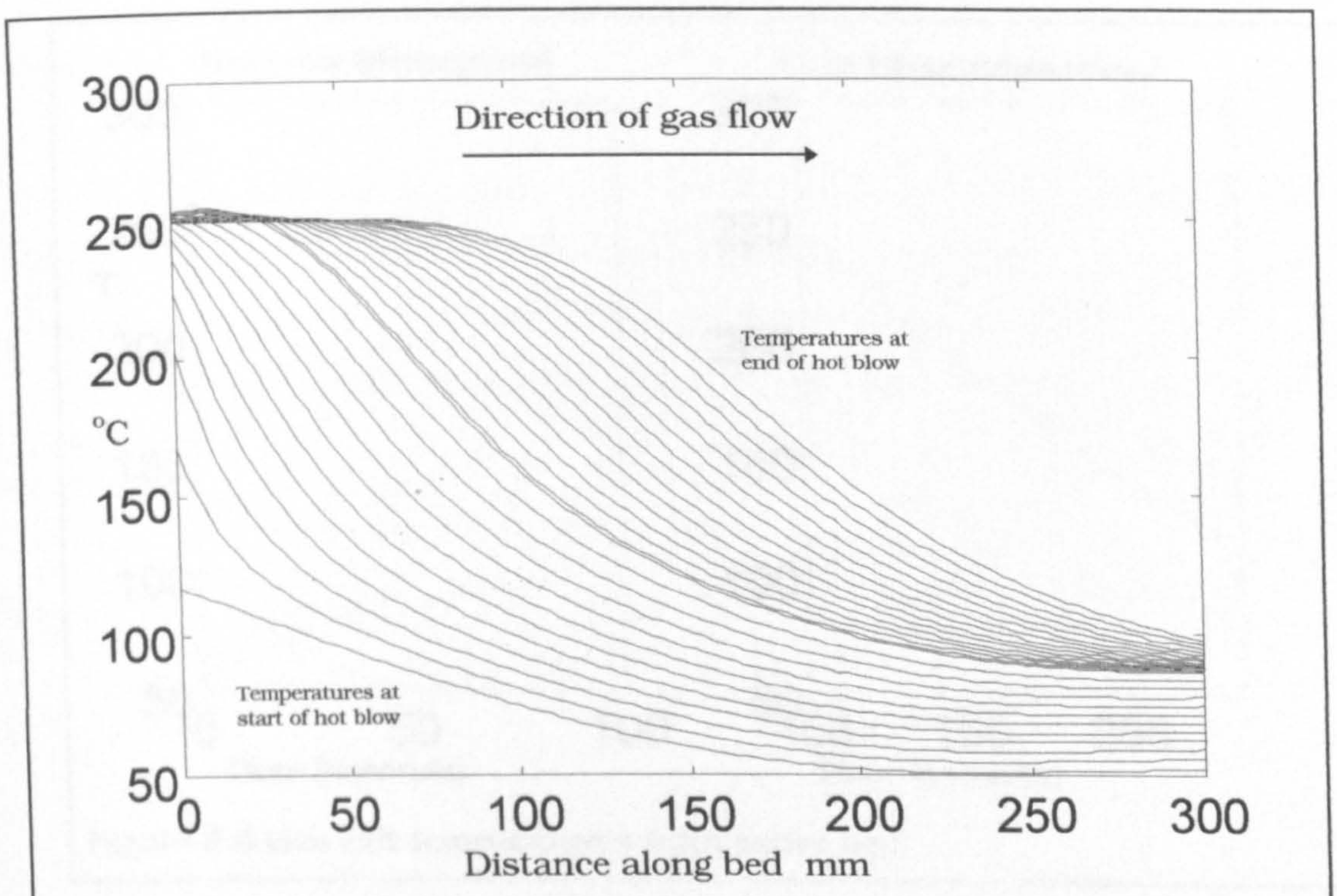

Figure 8.4 Solid temperatures of an active bed during the hot blow

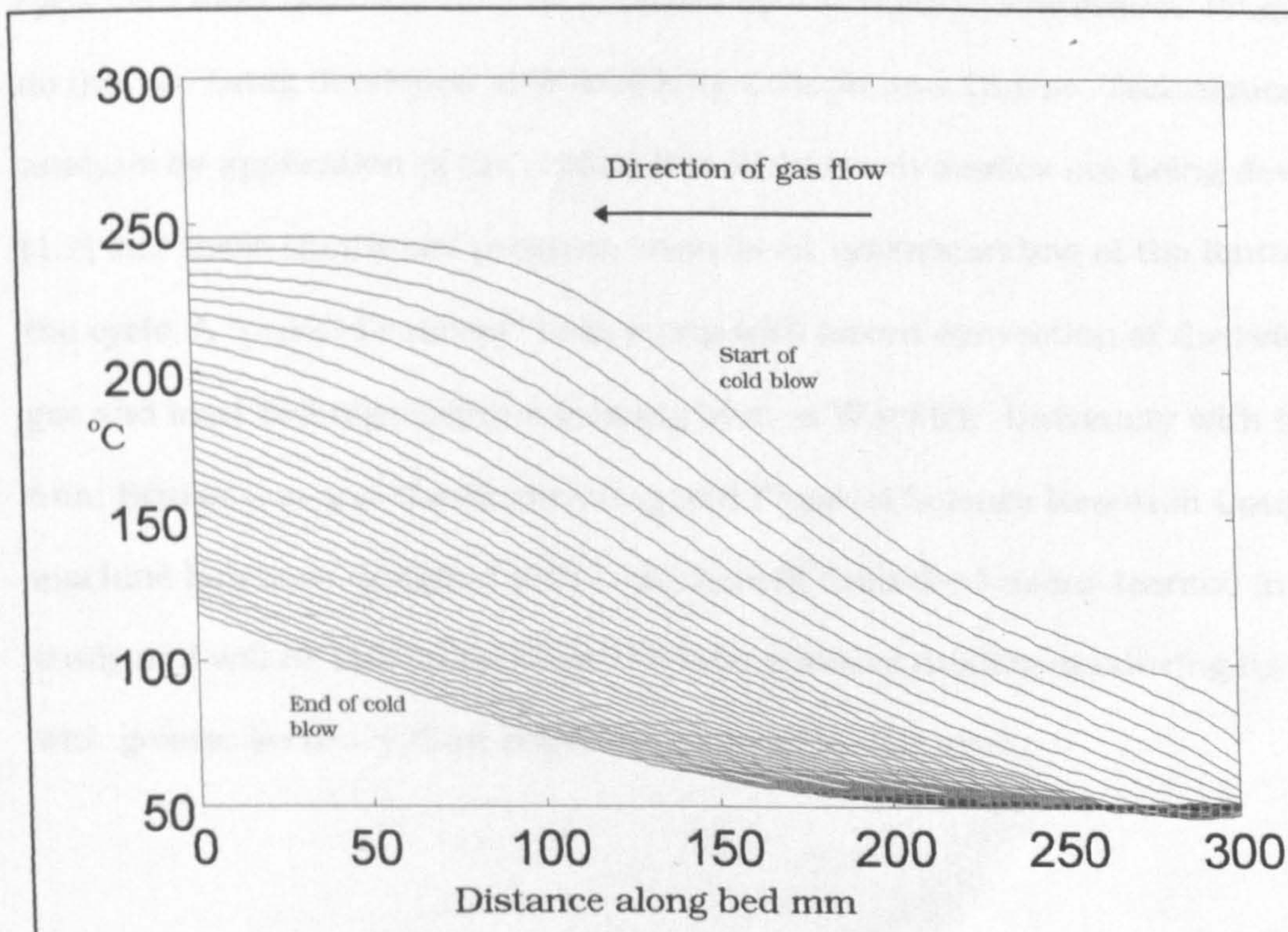

Figure 8.5 Temperatures in the active bed during the cold blow

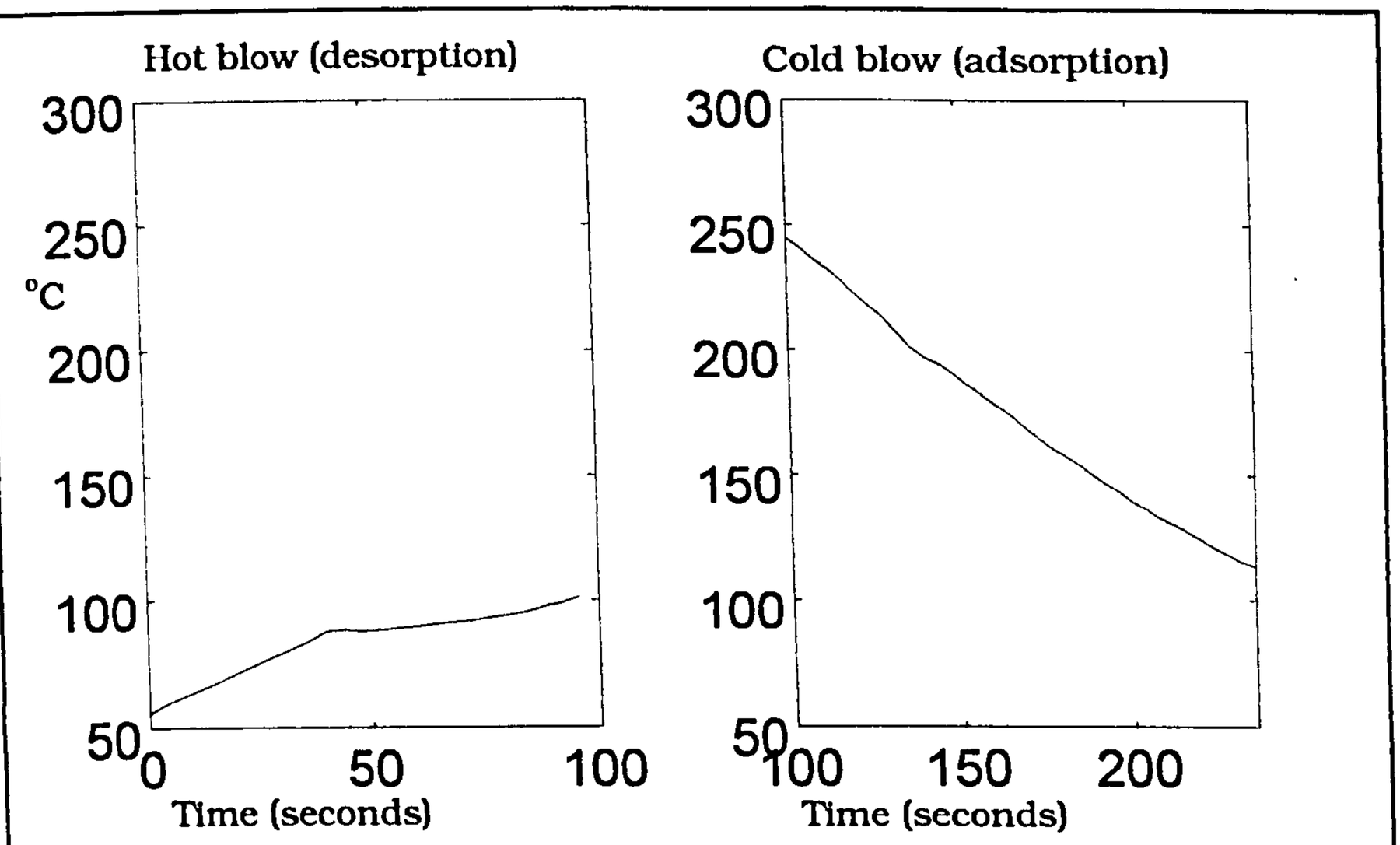

Figure 8.6 Gas exit temperatures from active bed

Optimisation and design of a real heat pump using the convective thermal wave cycle with inert beds can only be achieved by a computer simulation. Programs to do this are being developed at Warwick by Critoph and Thorpe. Techniques of analysis by application of the second law of thermodynamics are being developed [1,2] and these should aid progress towards an understanding of the limitations of the cycle. A "proof of concept" heat pump with forced convection of the refrigerant gas and inert bed regenerators is being built at Warwick University with funding from British Gas and the Engineering and Physical Science Research Council. This machine has been designed with some benefit from the lessons learned in this study and will be able to measure the heat transfer coefficients during its operation with greater accuracy than could be achieved in this work.

References

[1] **Critoph R.E.,** Gas-fired air conditioning using a carbon-ammonia convective thermal wave cycle, *International Ab-sorption Heat Pump Conference* Montreal **September 1996**

[2] **Meunier F., Kaushik S.C., Neveu P., Poyelle F.,** A comparative thermodynamic study of sorption systems: second law analysis, *International Ab-sorption Heat Pump Conference* Montreal **September 1996**

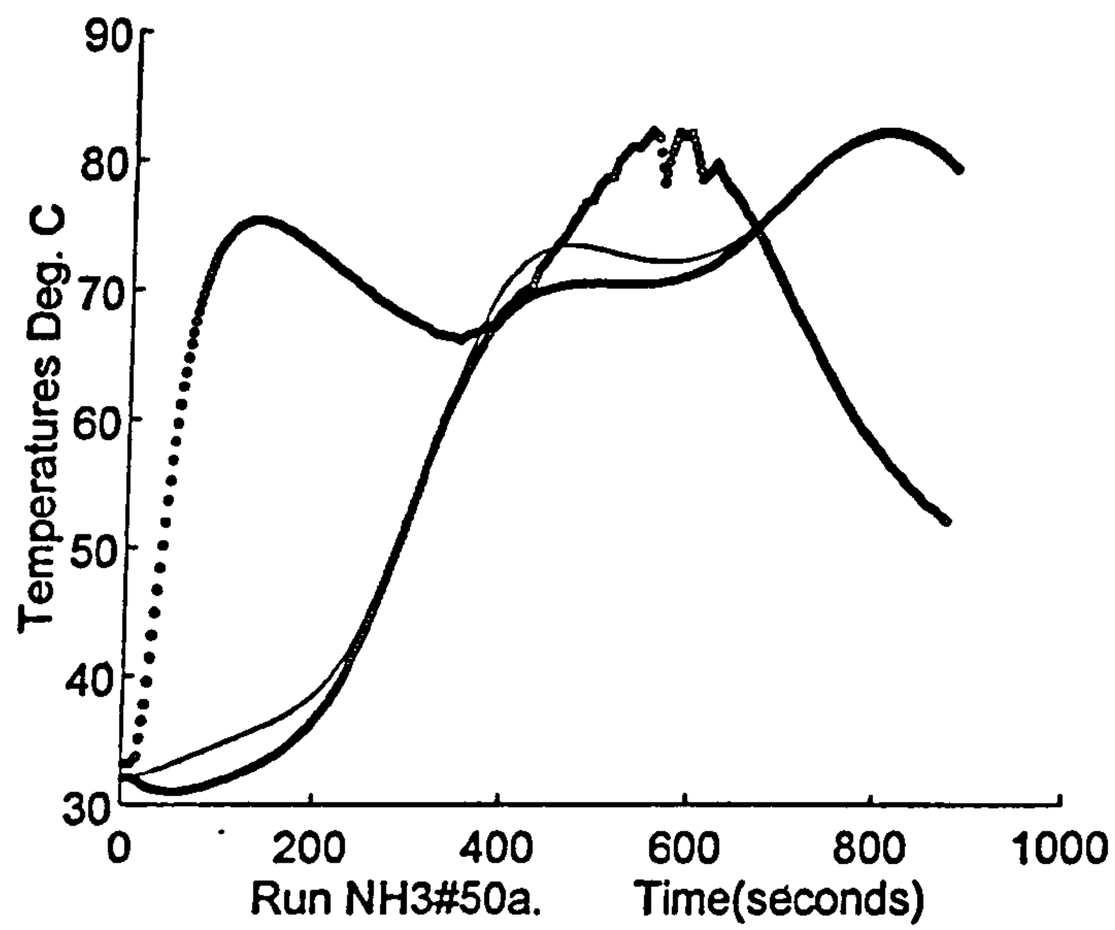
Temperatures Deg. C
90
80
70
60
50
40
30
0
200
400
600
800
1000
Run NH3#50a.
Time(seconds)

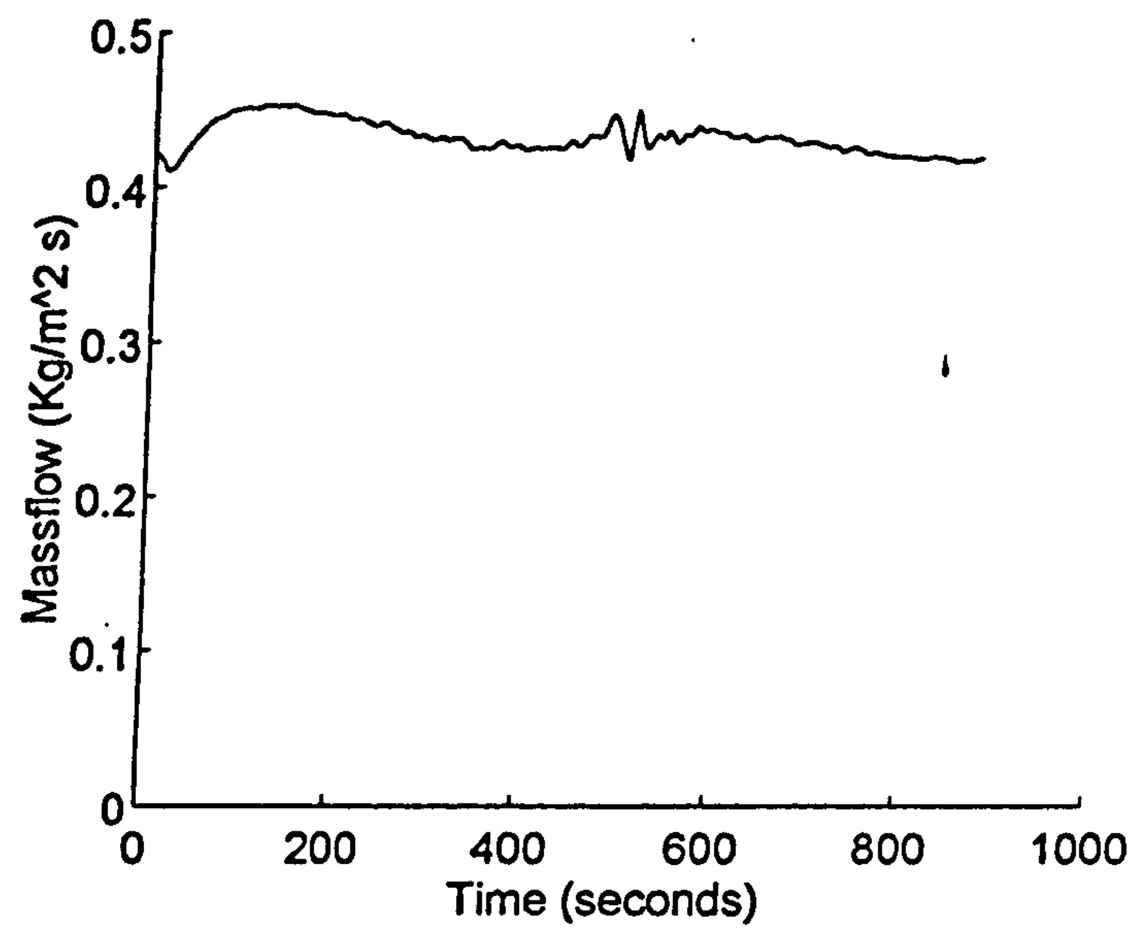
Massflow (Kg/m^2 s)
0.5
0.4
0.3
0.2
0.1
0
0
200
400
600
800
1000
Time (seconds)

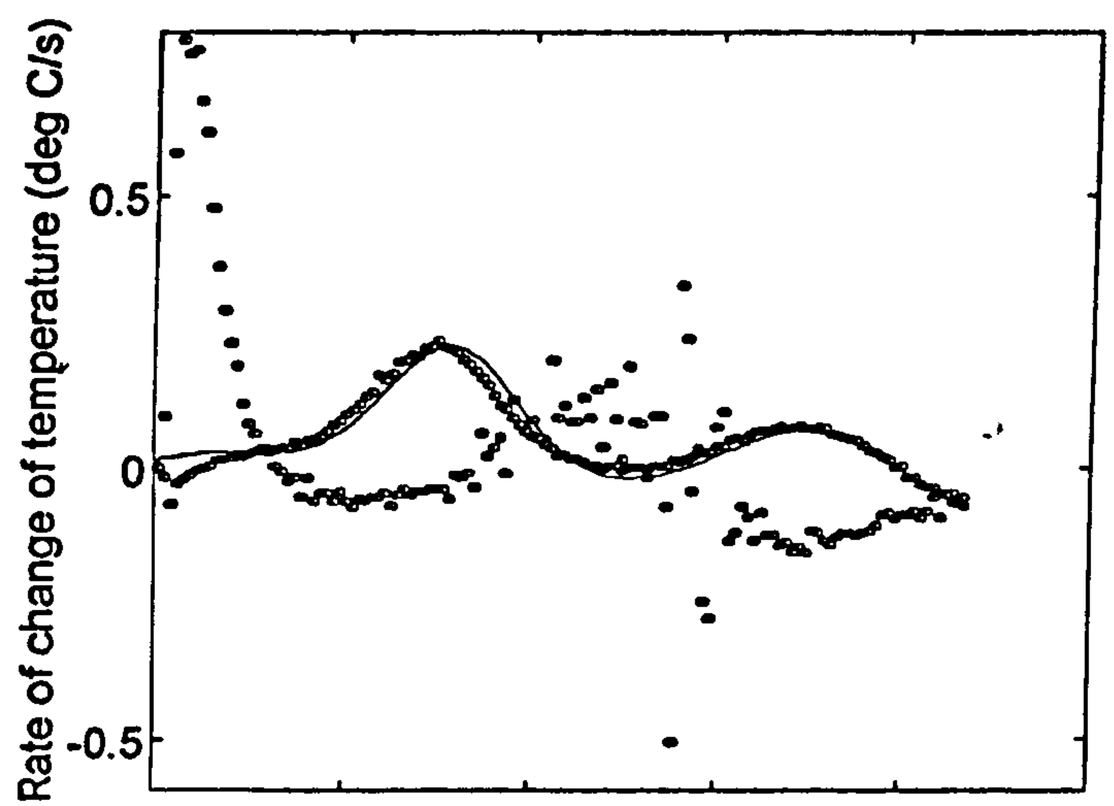
Rate of change of temperature (deg C/s)
0.5
0
-0.5
0
200
400
600
800
1000

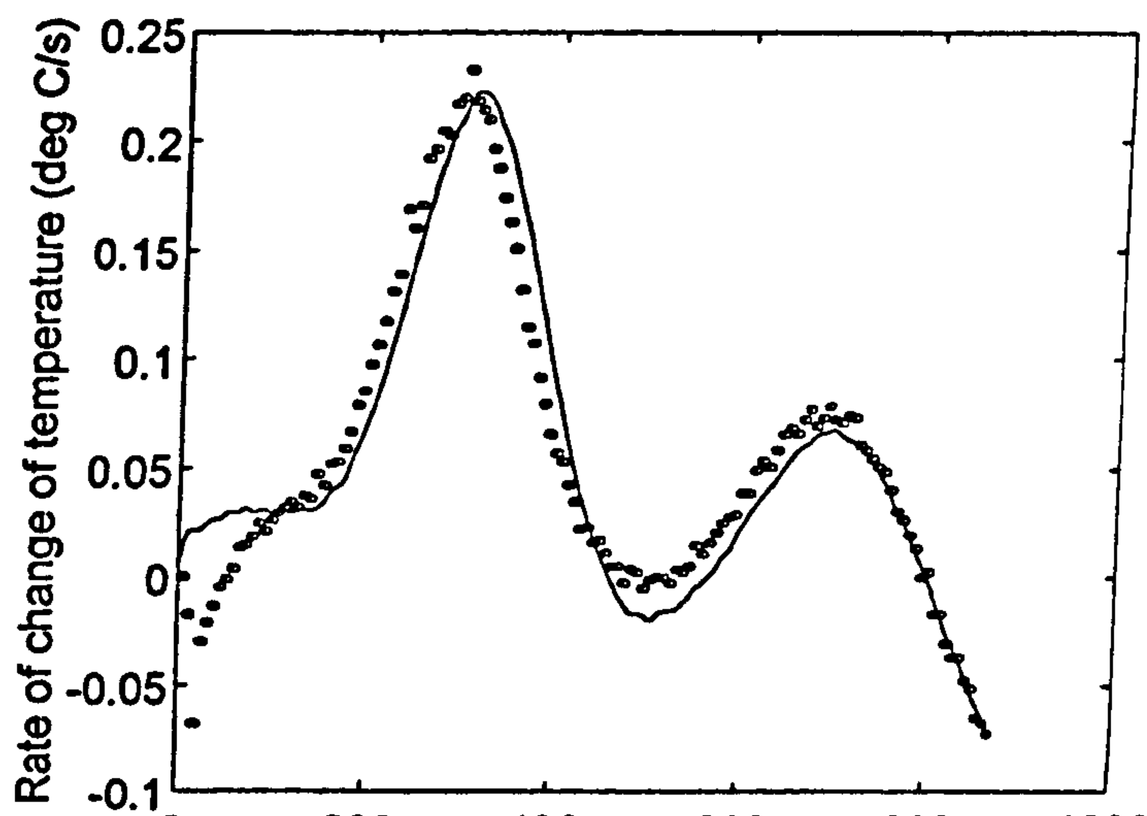
Rate of change of temperature (deg C/s)
0.25
0.2
0.15
0.1
0.05
0
-0.05
-0.1
0
200
400
600
800
1000

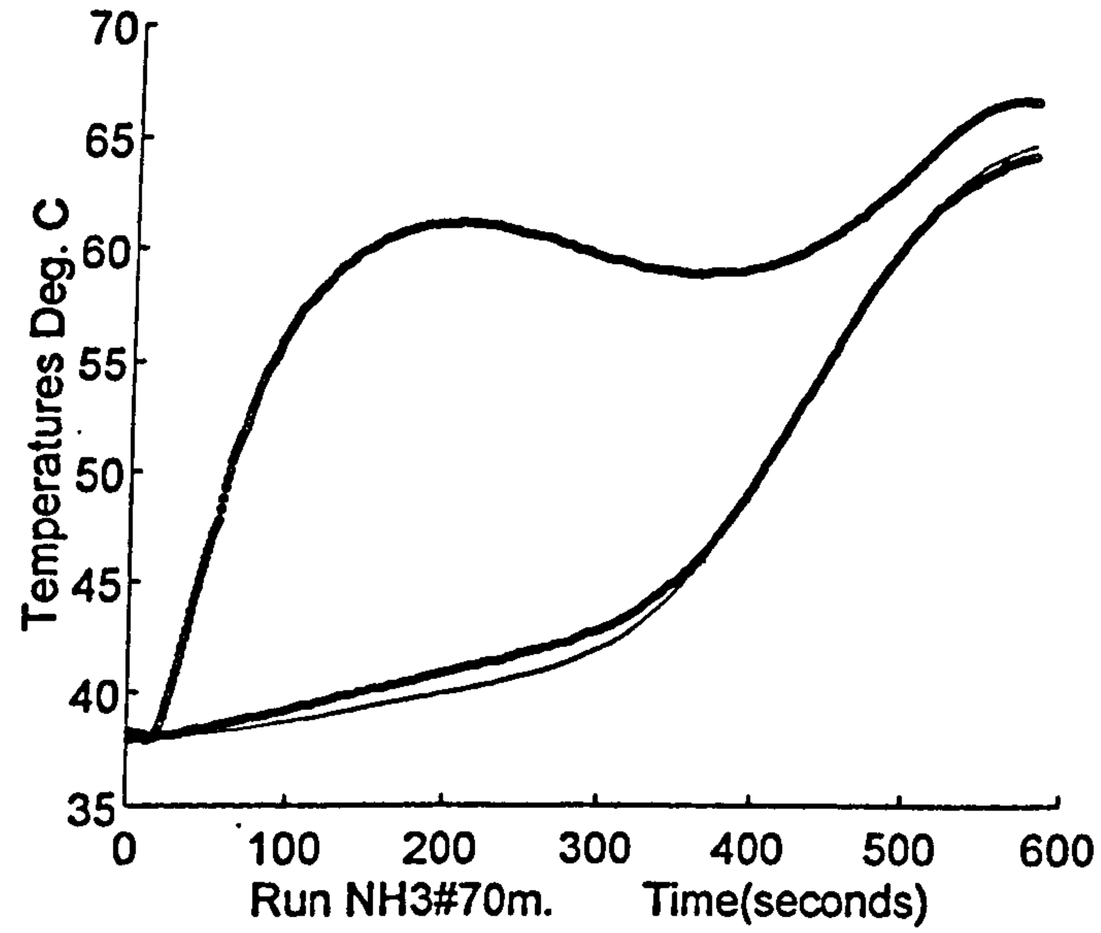
Temperatures Deg. C
70
65
60
55
50
45
40
35
0
100
200
300
400
500
600
Run NH3#70m. Time(seconds)

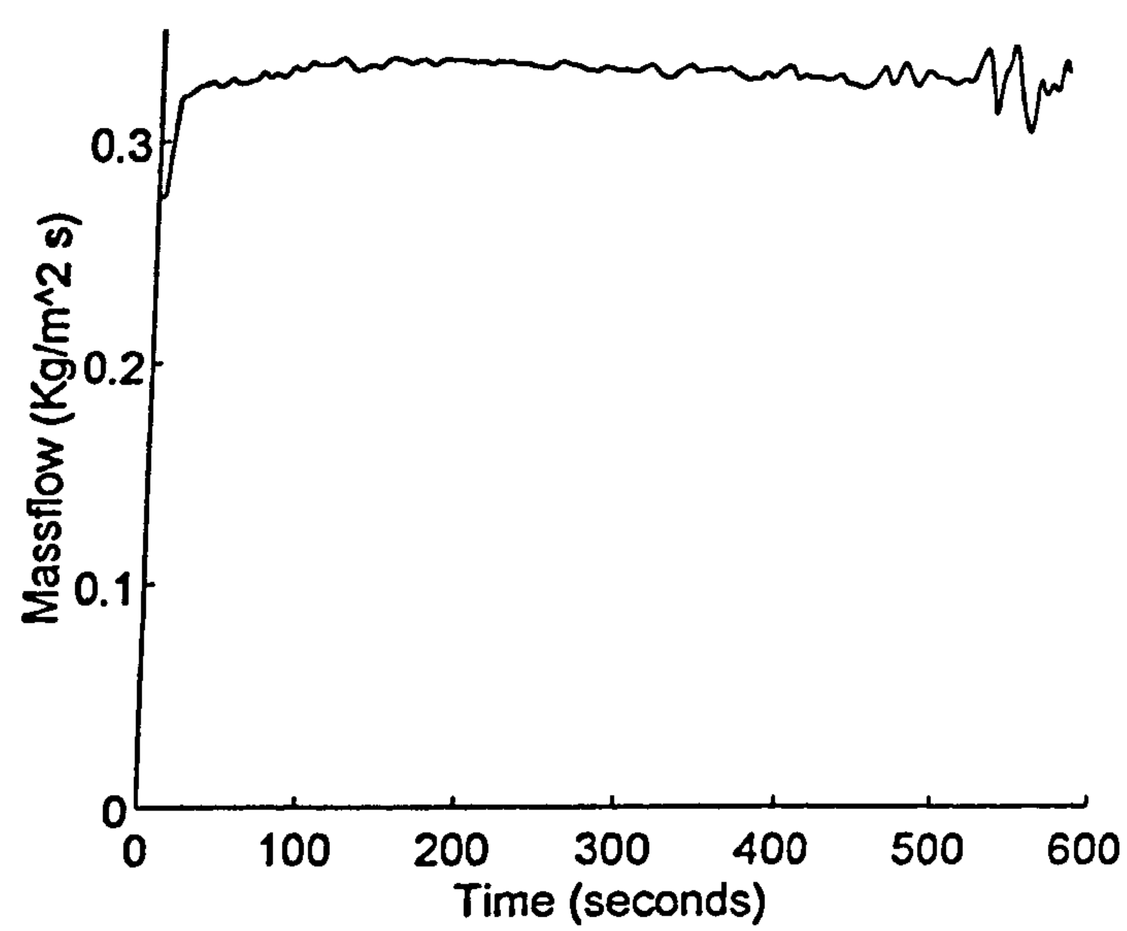
Massflow (Kg/m^2 s)
0.3
0.2
0.1
0
0
100
200
300
400
500
600
Time (seconds)

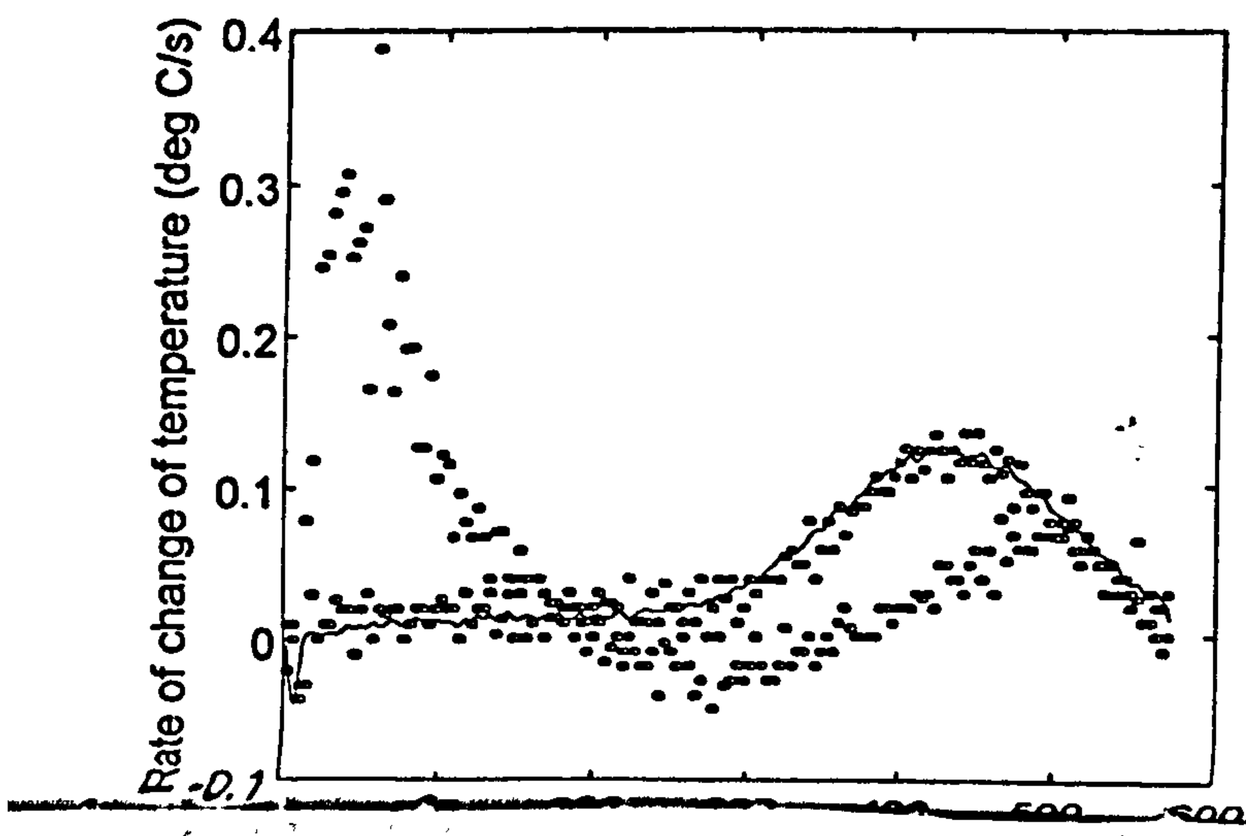
Rate of change of temperature (deg C/s)
0.4
0.3
0.2
0.1
0
-0.1

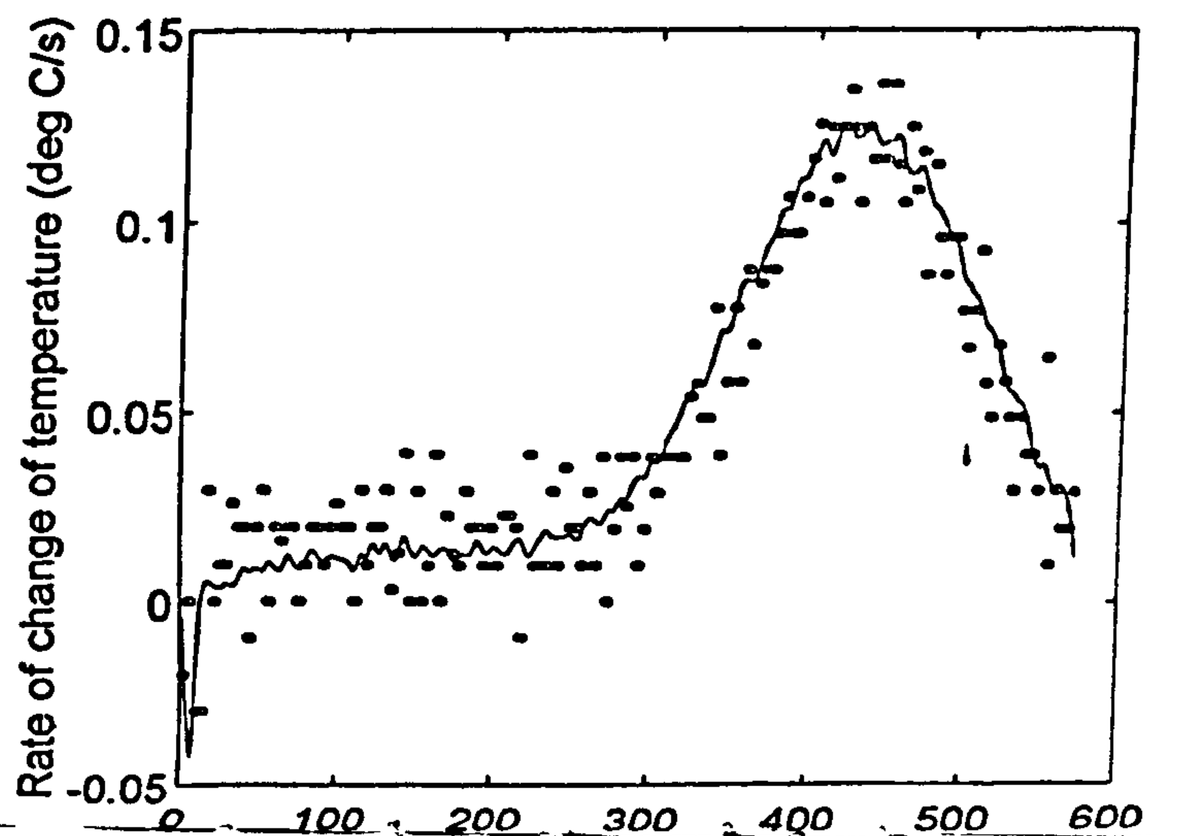
Rate of change of temperature (deg C/s)
0.15
0.1
0.05
0
-0.05
0
100
200
300
400
500
600

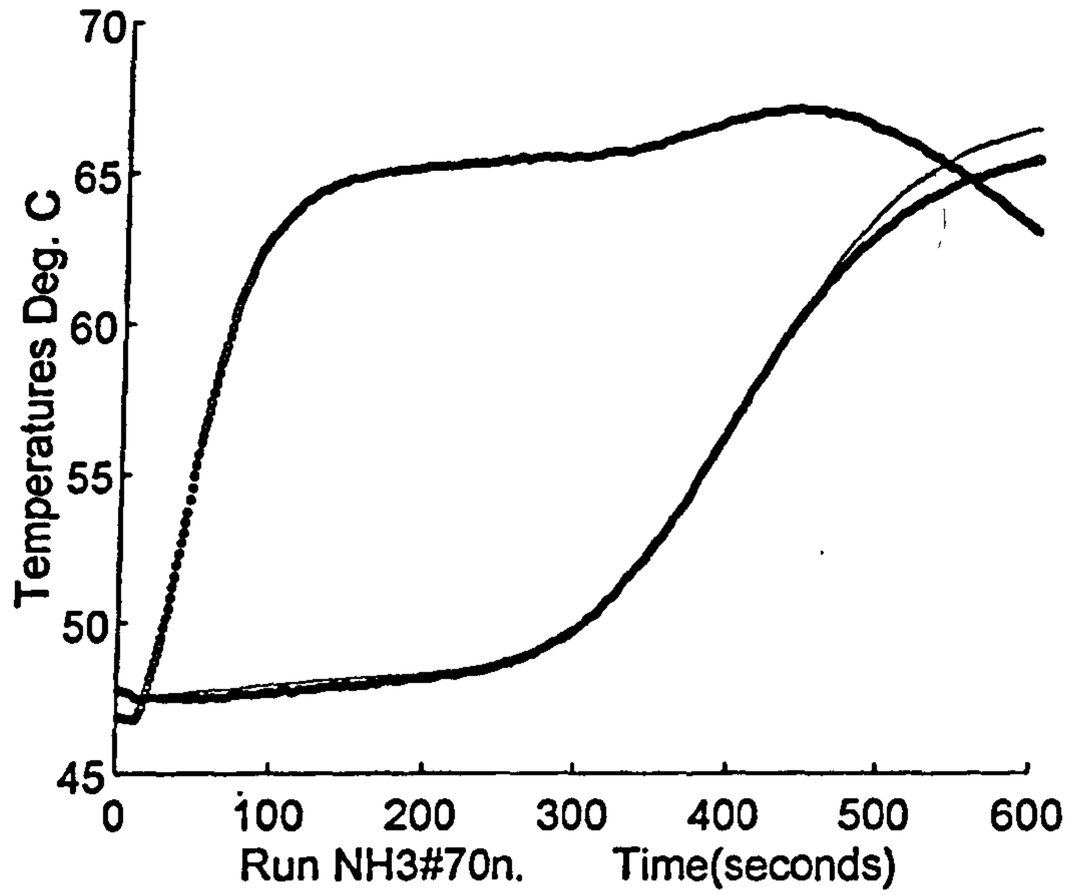
Temperatures Deg. C
70
65
60
55
50
45
0
100
200
300
400
500
600
Run NH3#70n. Time(seconds)

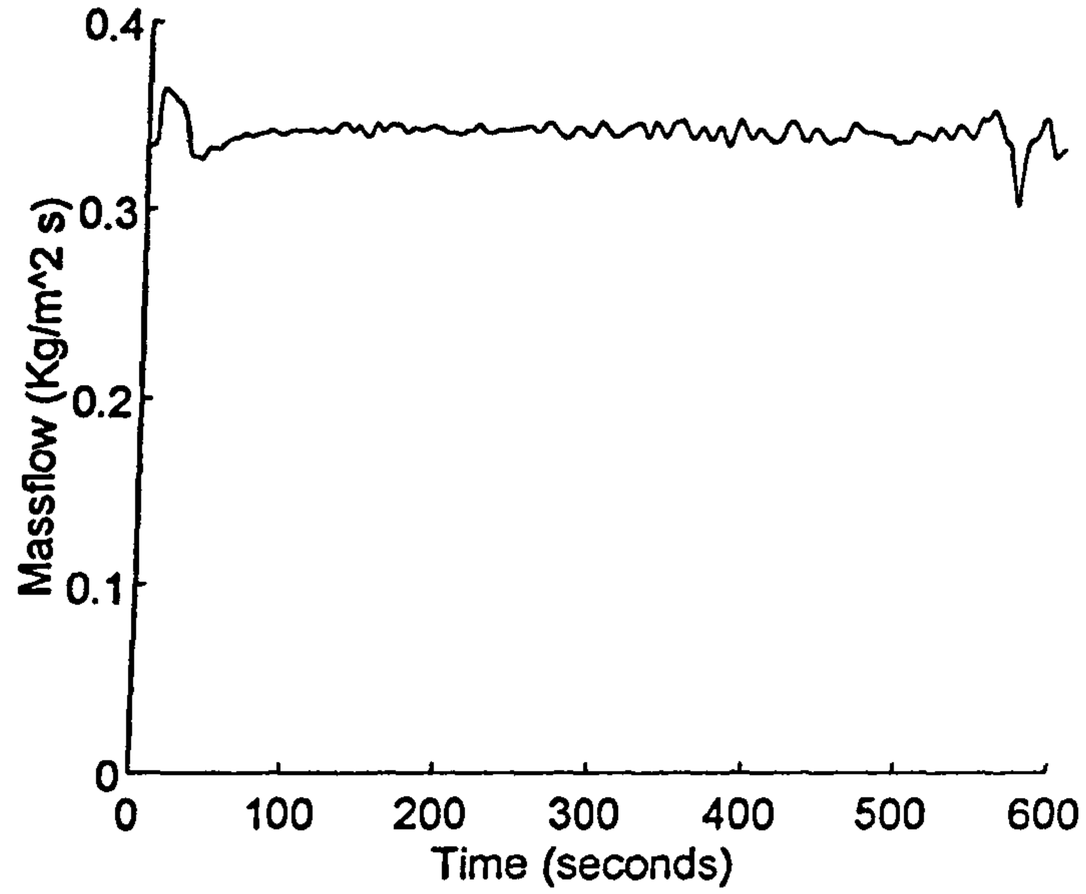
Massflow (Kg/m^2 s)
0.4
0.3
0.2
0.1
0
0
100
200
300
400
500
600
Time (seconds)

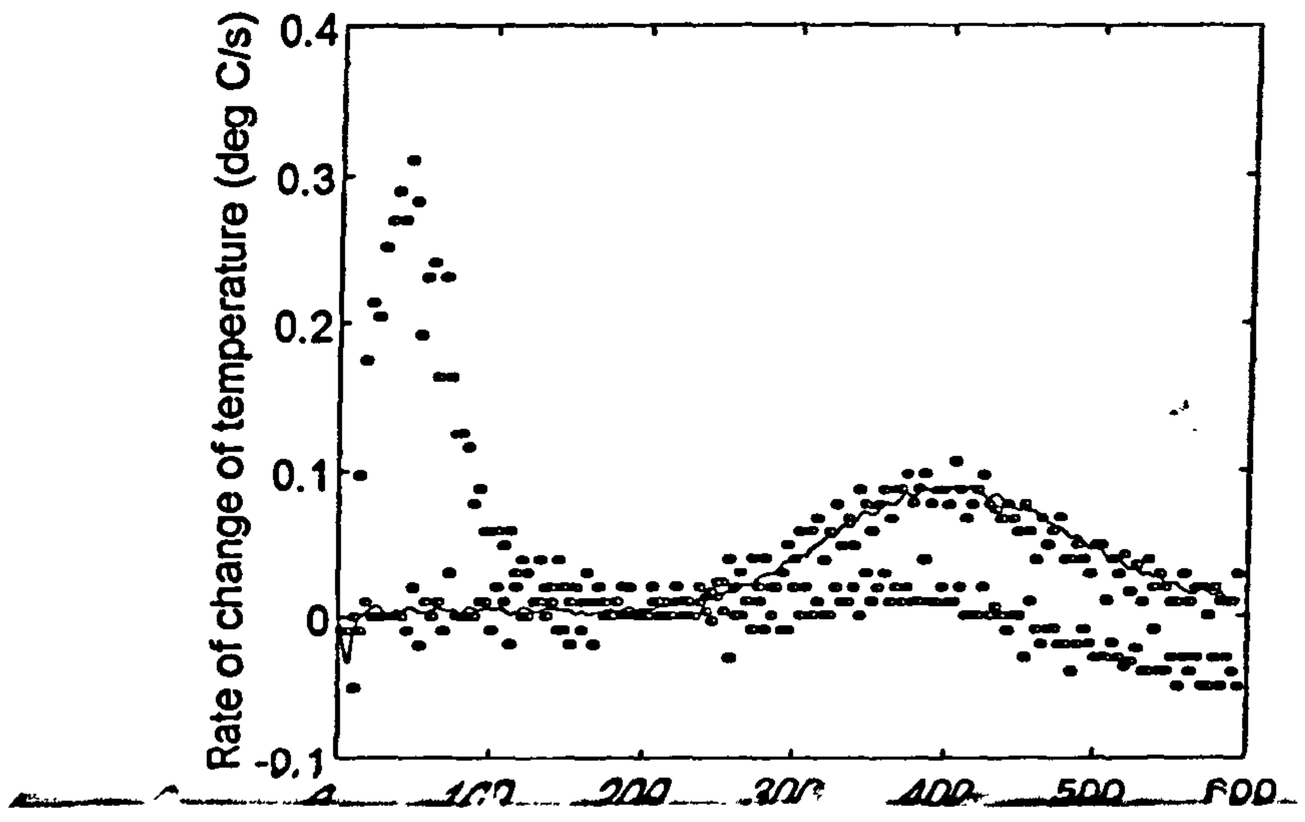
Rate of change of temperature (deg C/s)
0.4
0.3
0.2
0.1
0
-0.1
0
100
200
300
400
500
600

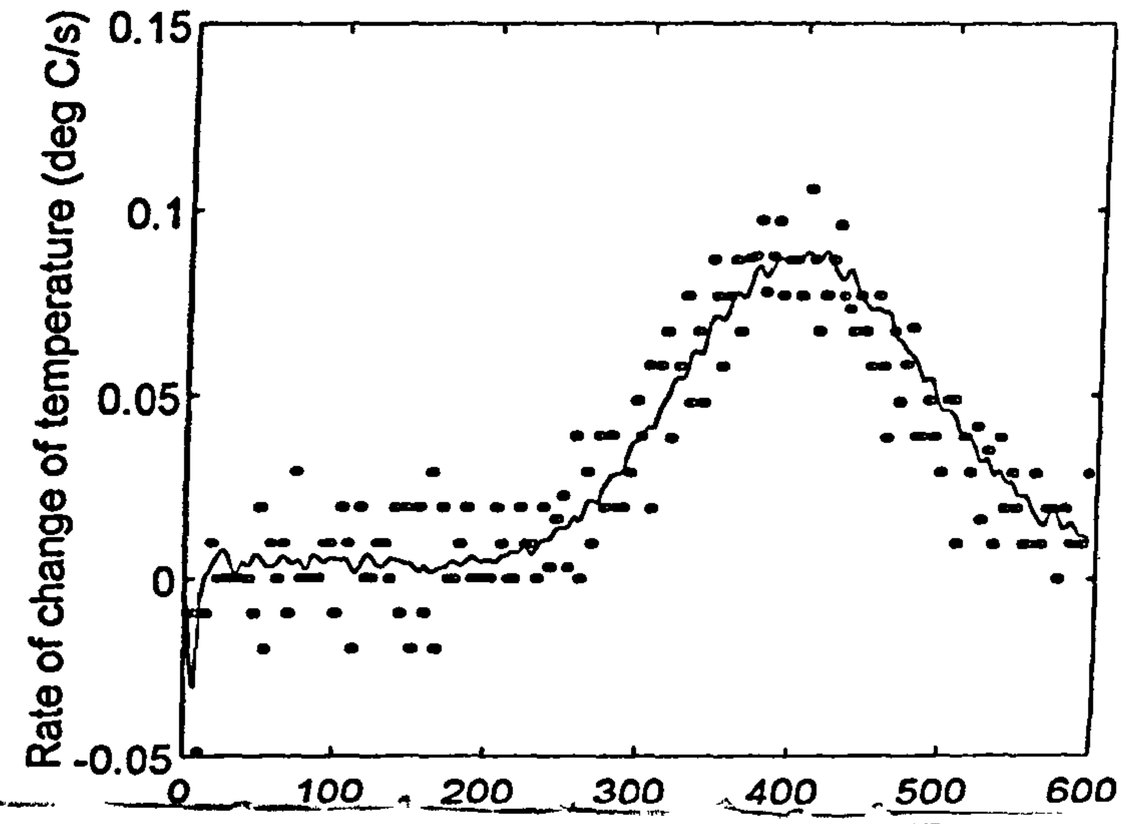
Rate of change of temperature (deg C/s)
0.15
0.1
0.05
0
-0.05
0
100
200
300
400
500
600

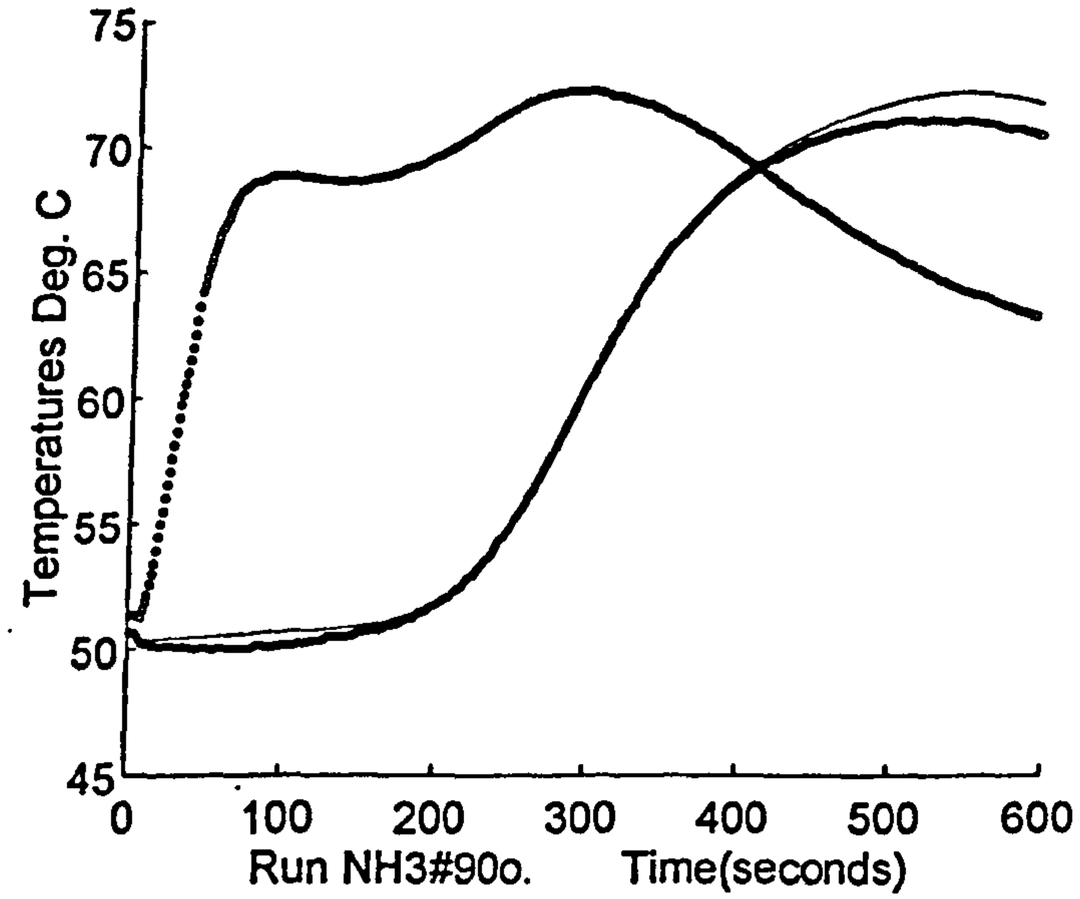
Temperatures Deg. C
75
70
65
60
55
50
45
0
100
200
300
400
500
600
Run NH3#90o. Time(seconds)

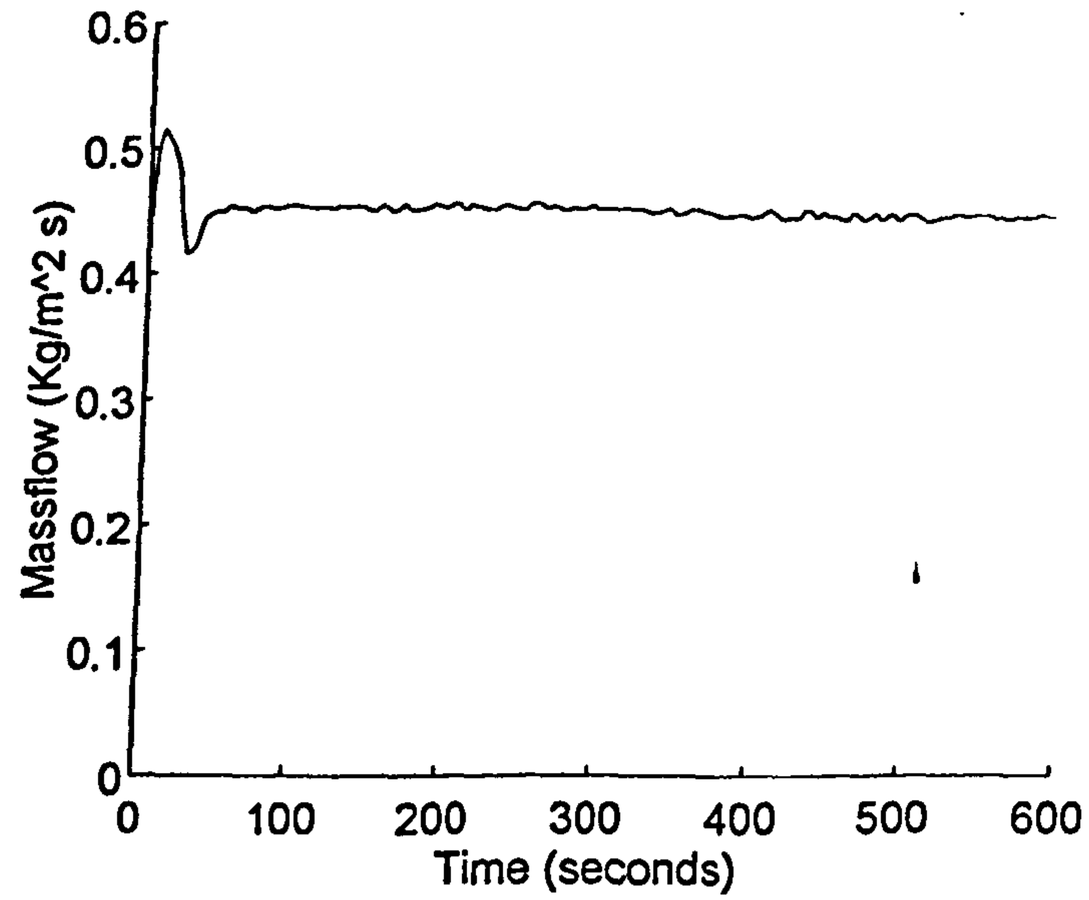
Massflow (Kg/m^2 s)
0.6
0.5
0.4
0.3
0.2
0.1
0
0
100
200
300
400
500
600
Time (seconds)

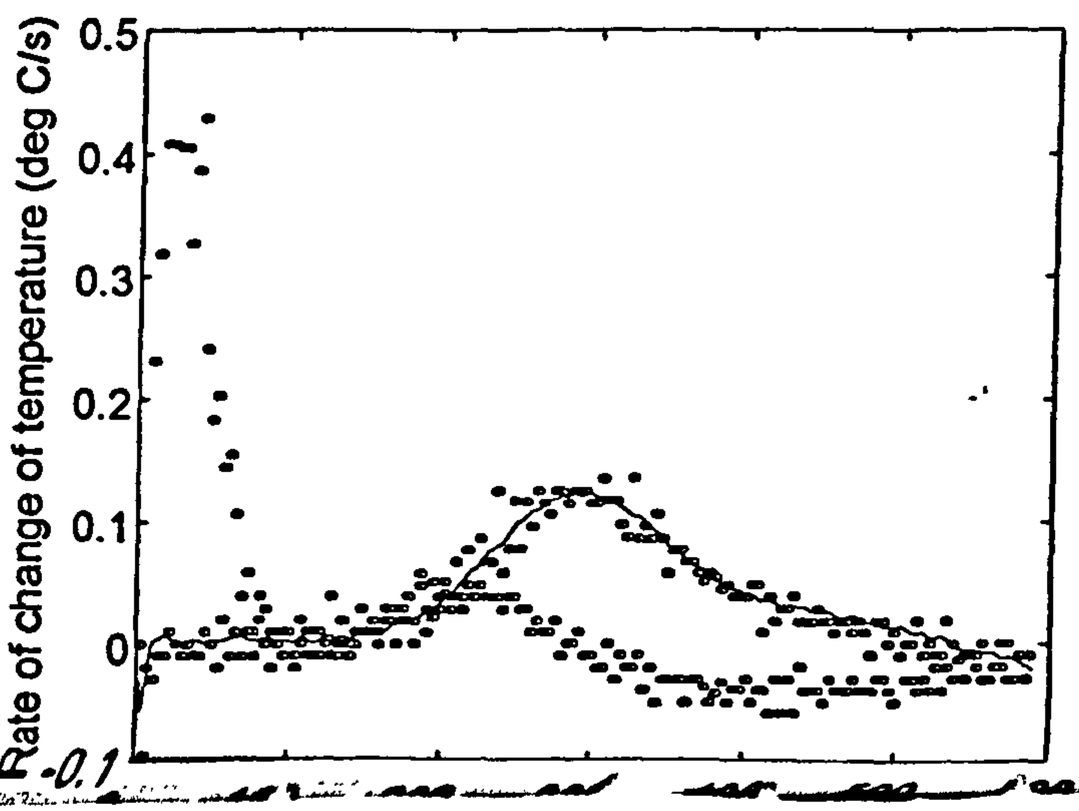
Rate of change of temperature (deg C/s)
0.5
0.4
0.3
0.2
0.1
0
-0.1

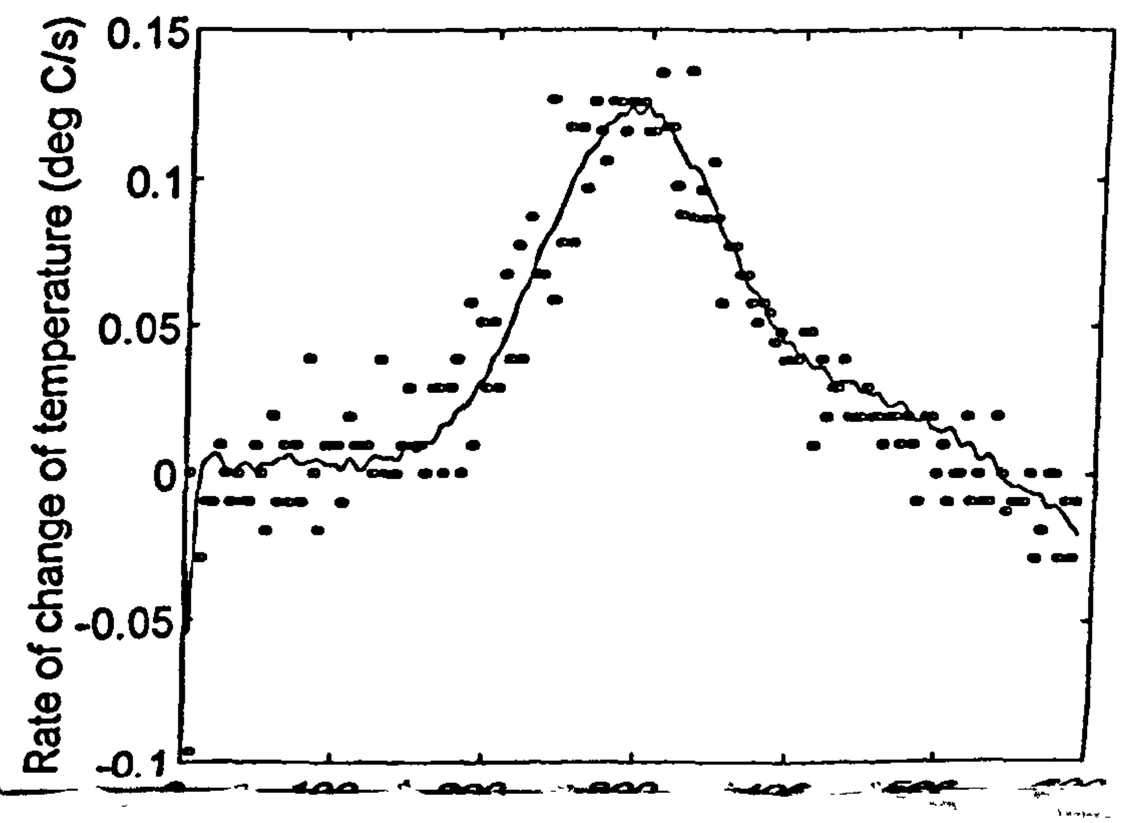
Rate of change of temperature (deg C/s)
0.15
0.1
0.05
0
-0.05
-0.1

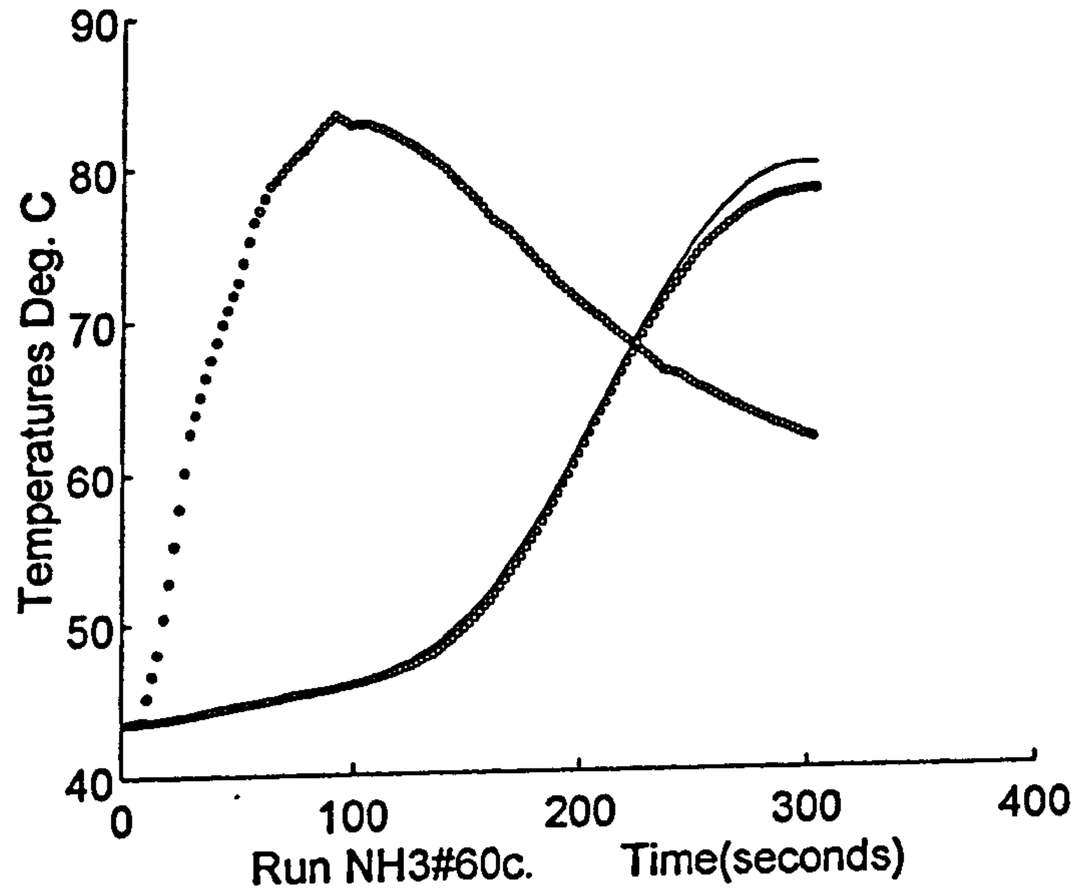
Temperatures Deg. C
90
80
70
60
50
40
0
100
200
300
400
Run NH3#60c.
Time(seconds)

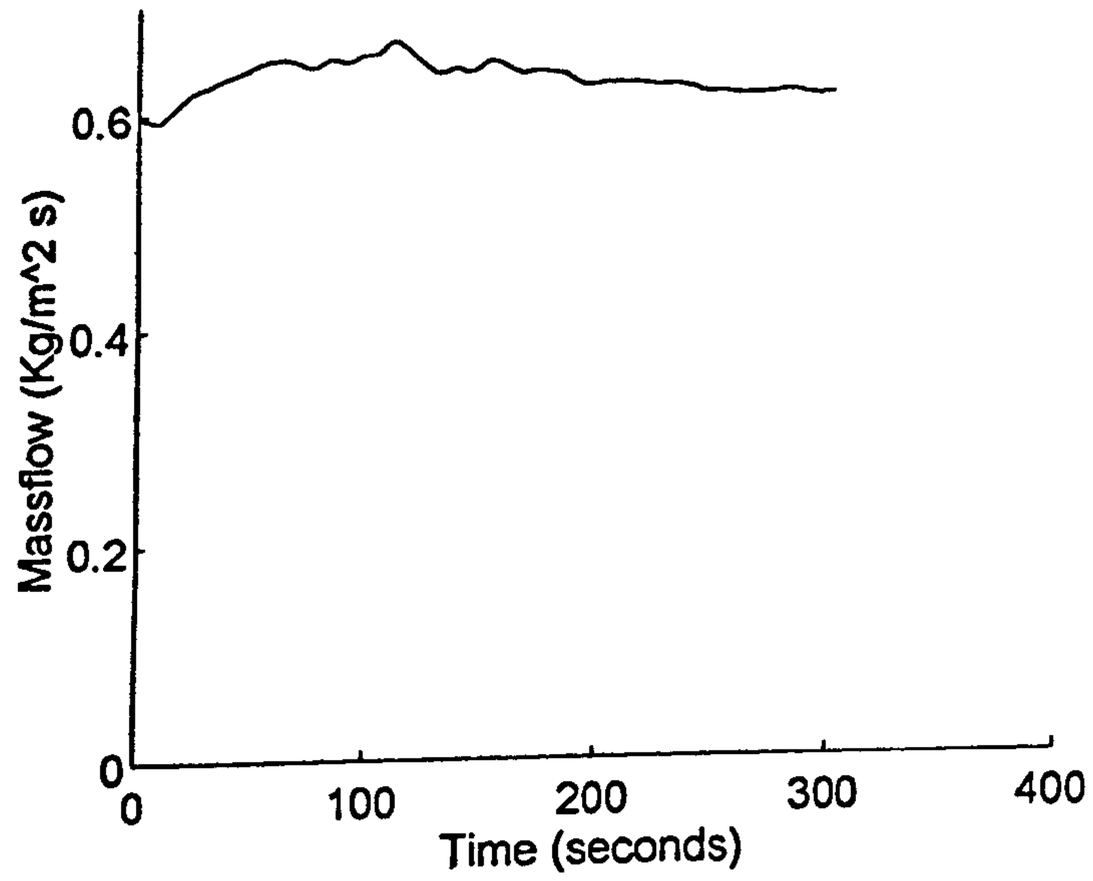
Massflow (Kg/m^2 s)
0.6
0.4
0.2
0
0
100
200
300
400
Time (seconds)

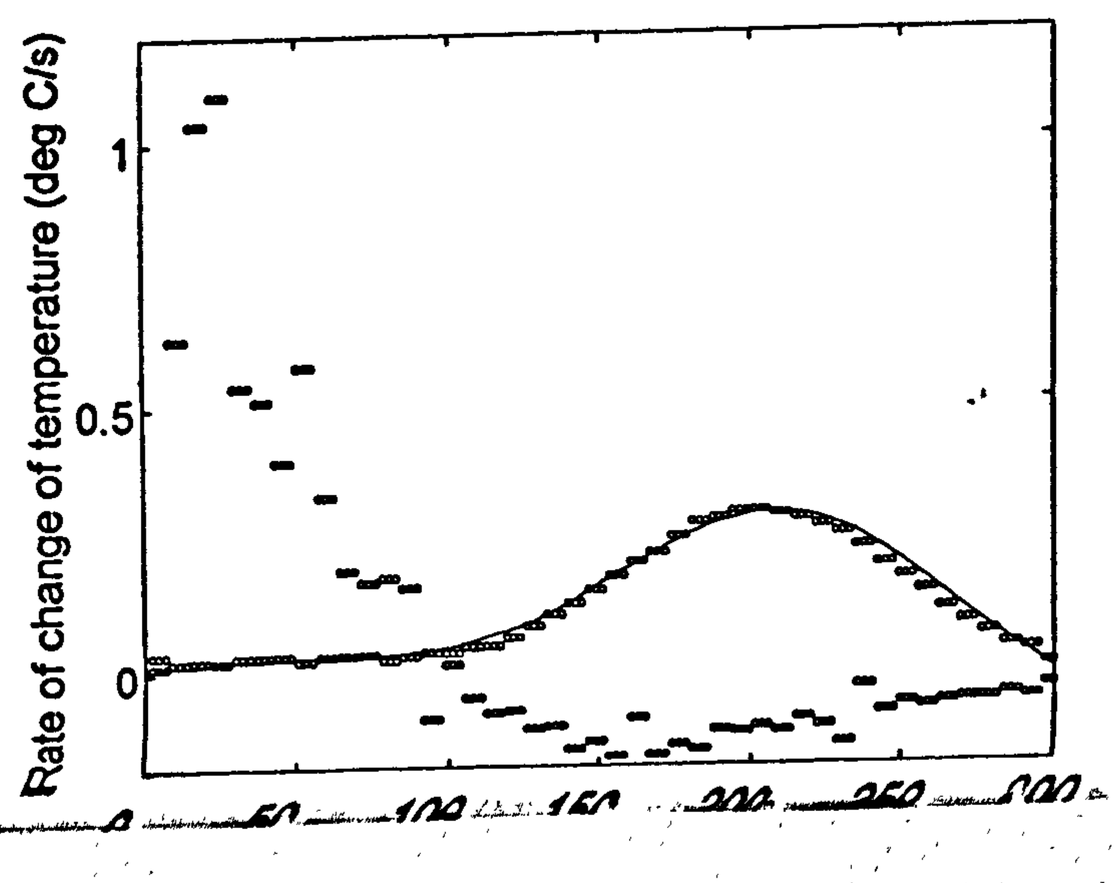
Rate of change of temperature (deg C/s)
1
0.5
0

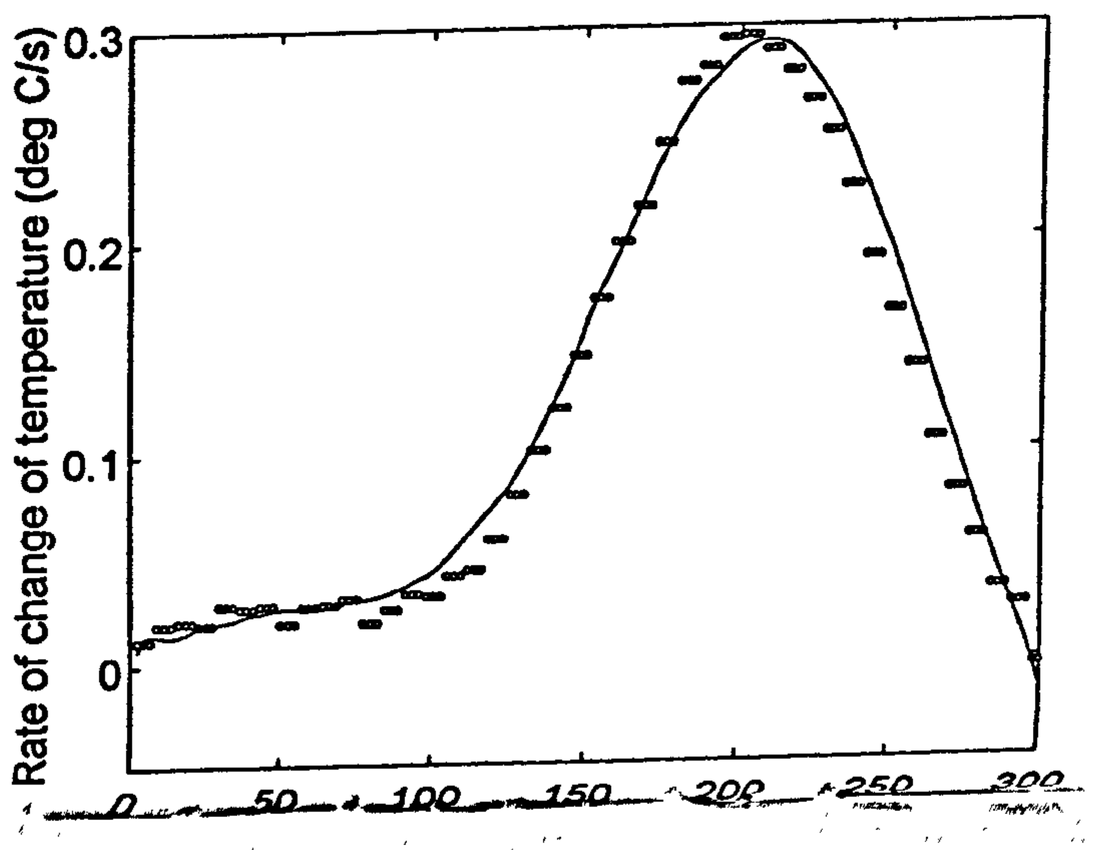
Rate of change of temperature (deg C/s)
0.3
0.2
0.1
0
0
50
100
150
200
250
300

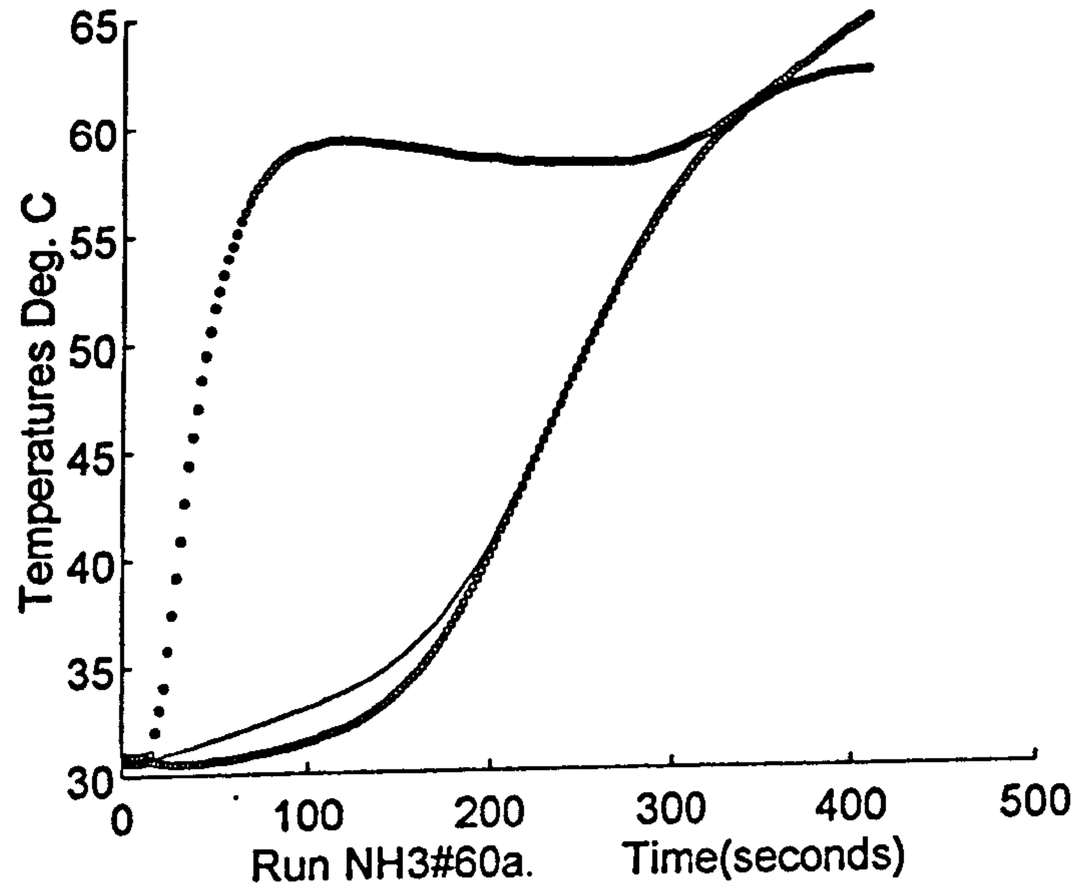
Temperatures Deg. C
65
60
55
50
45
40
35
30
0
100
200
300
400
500
Run NH3#60a.
Time(seconds)

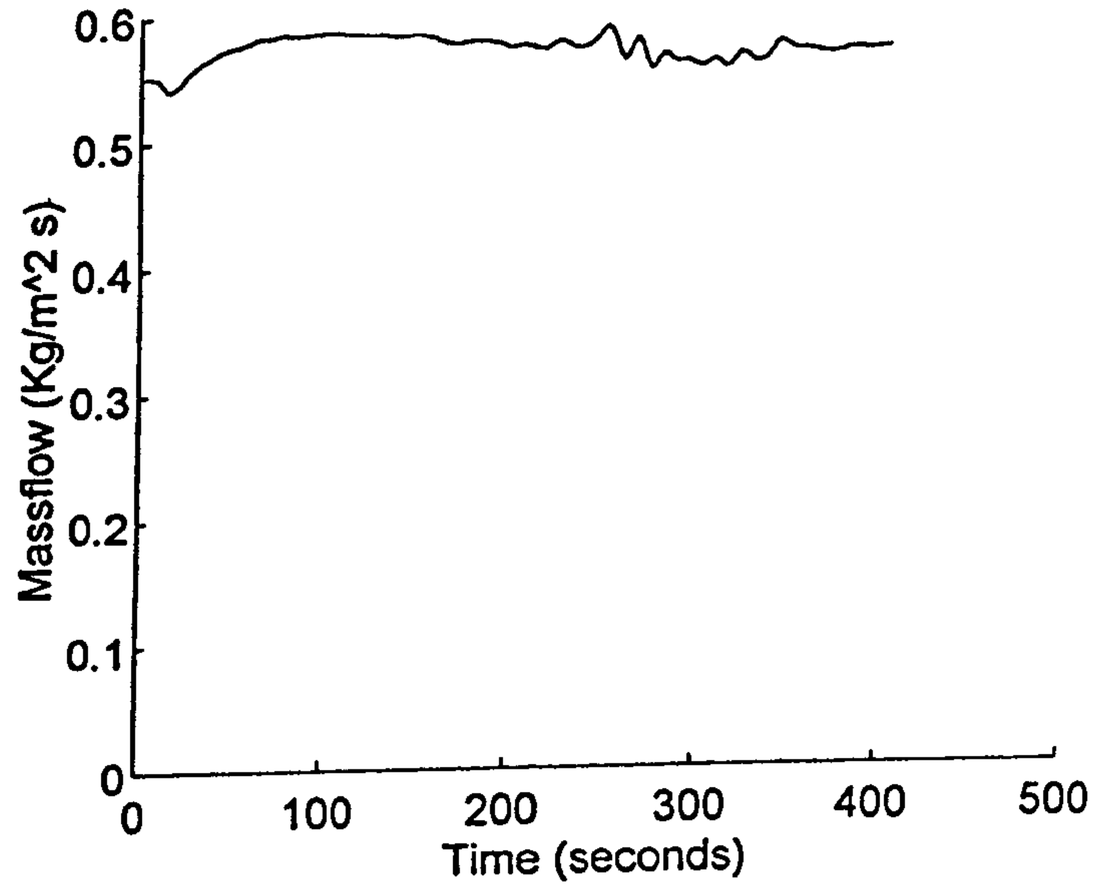
Massflow (Kg/m^2 s)
0.6
0.5
0.4
0.3
0.2
0.1
0
0
100
200
300
400
500
Time (seconds)

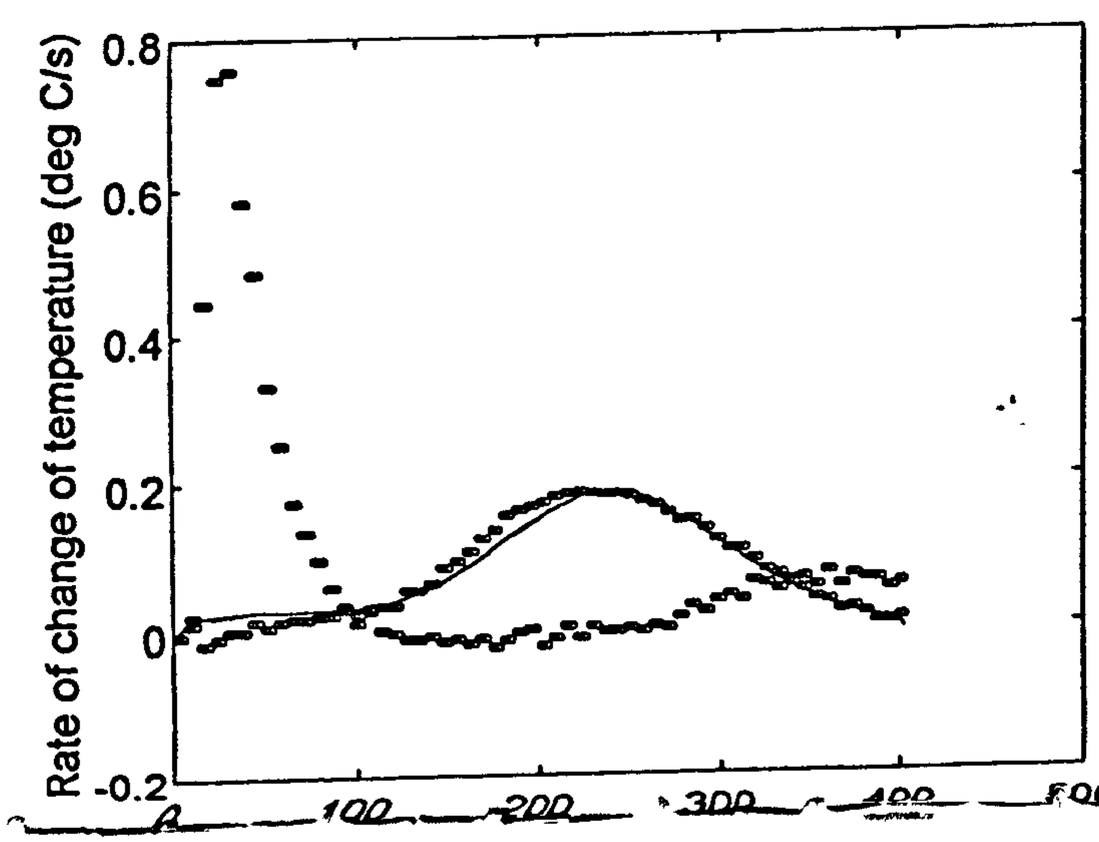
Rate of change of temperature (deg C/s)
0.8
0.6
0.4
0.2
0
-0.2
100
200
300
400
500

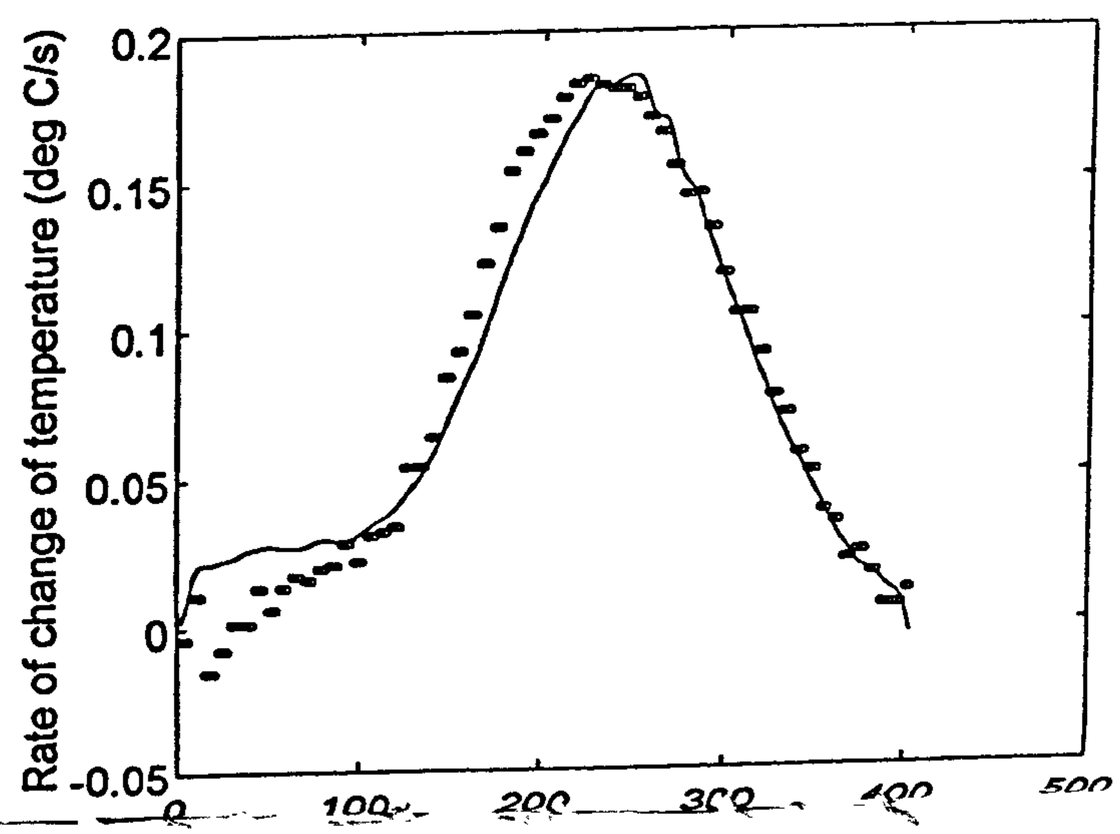
Rate of change of temperature (deg C/s)
0.2
0.15
0.1
0.05
0
-0.05
0
100
200
300
400
500

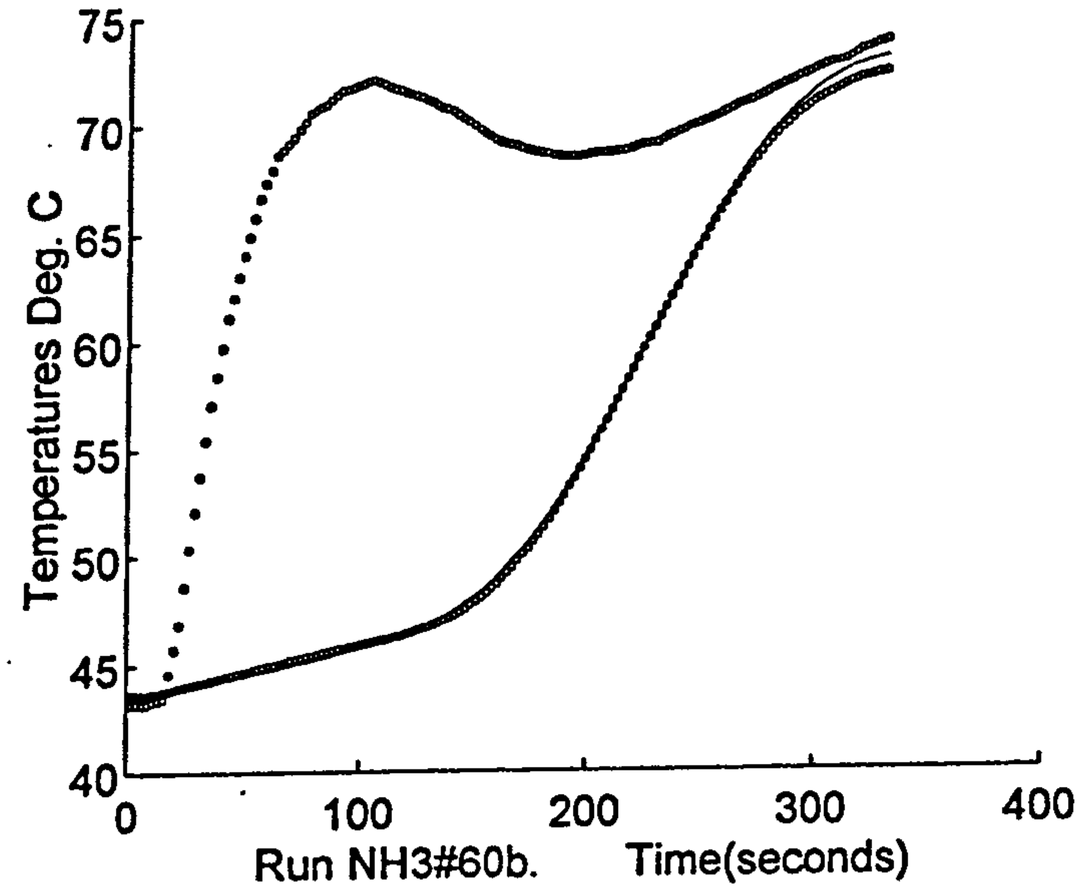
Temperatures Deg. C
75
70
65
60
55
50
45
40
0
100
200
300
400
Run NH3#60b.
Time(seconds)

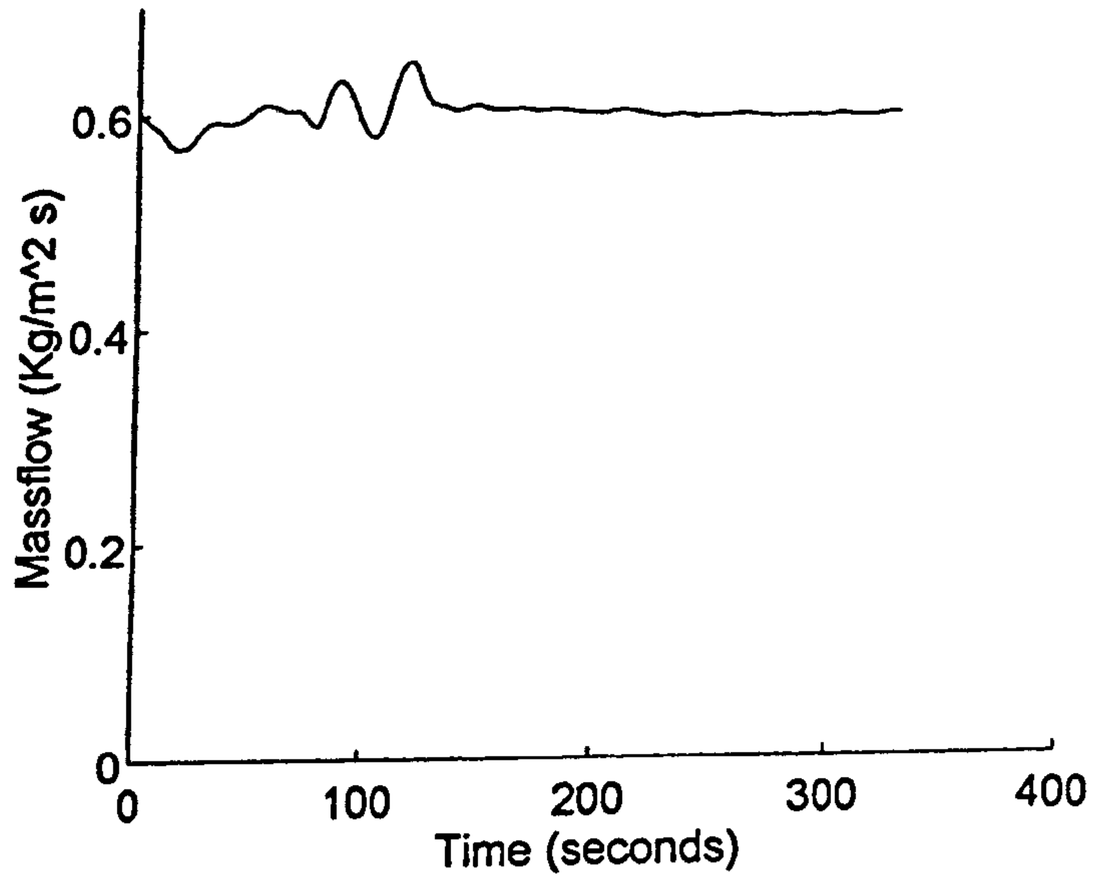
Massflow (Kg/m^2 s)
0.6
0.4
0.2
0
0
100
200
300
400
Time (seconds)

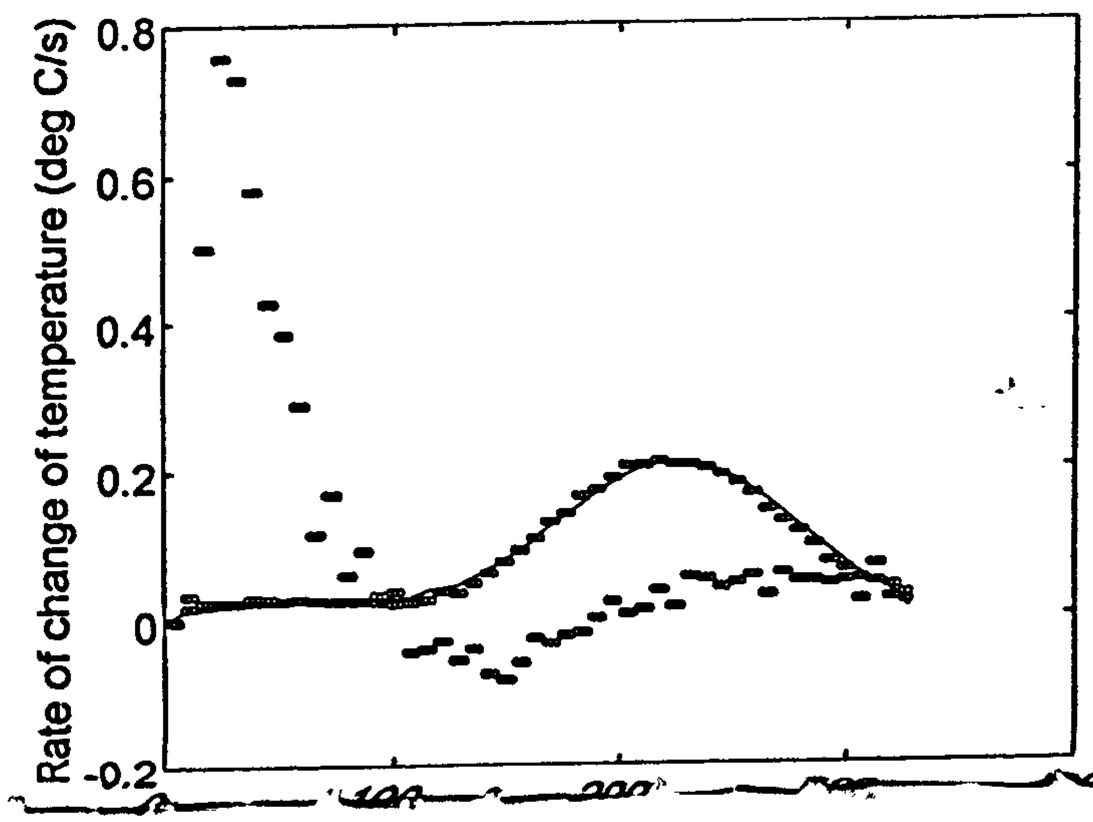
Rate of change of temperature (deg C/s)
0.8
0.6
0.4
0.2
0
-0.2

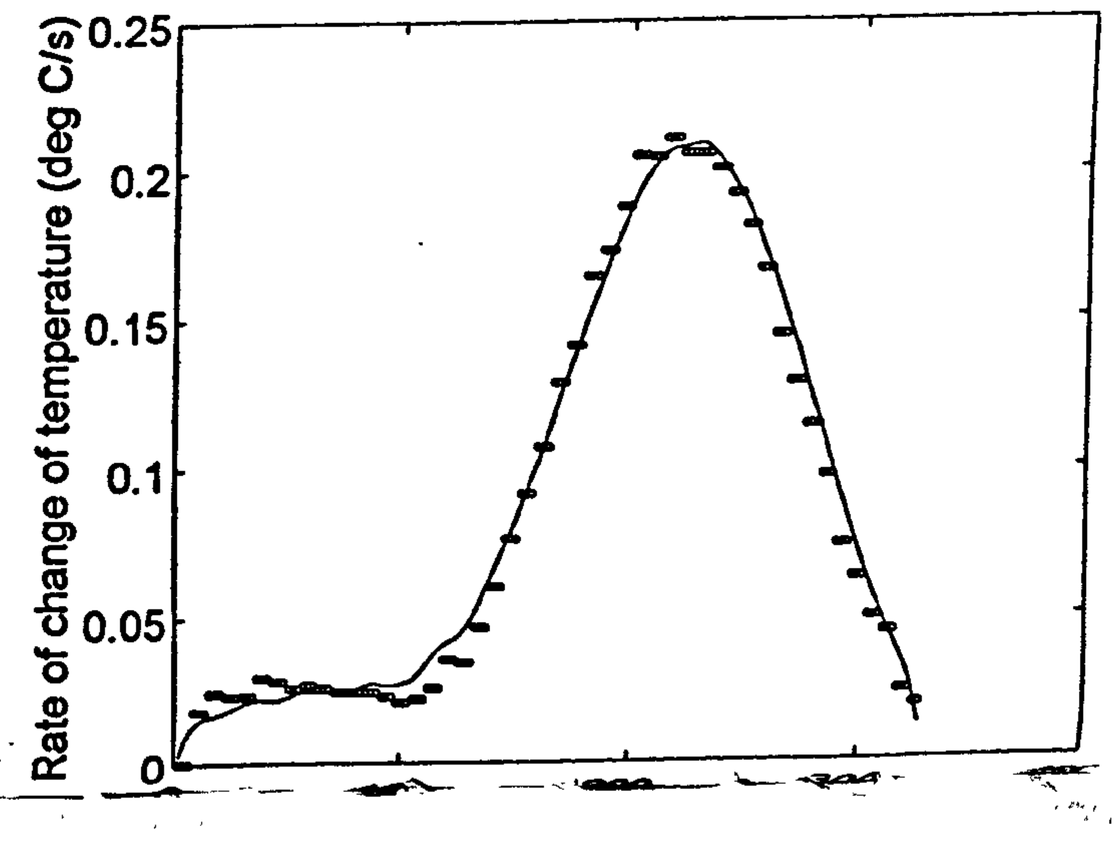
Rate of change of temperature (deg C/s)
0.25
0.2
0.15
0.1
0.05
0

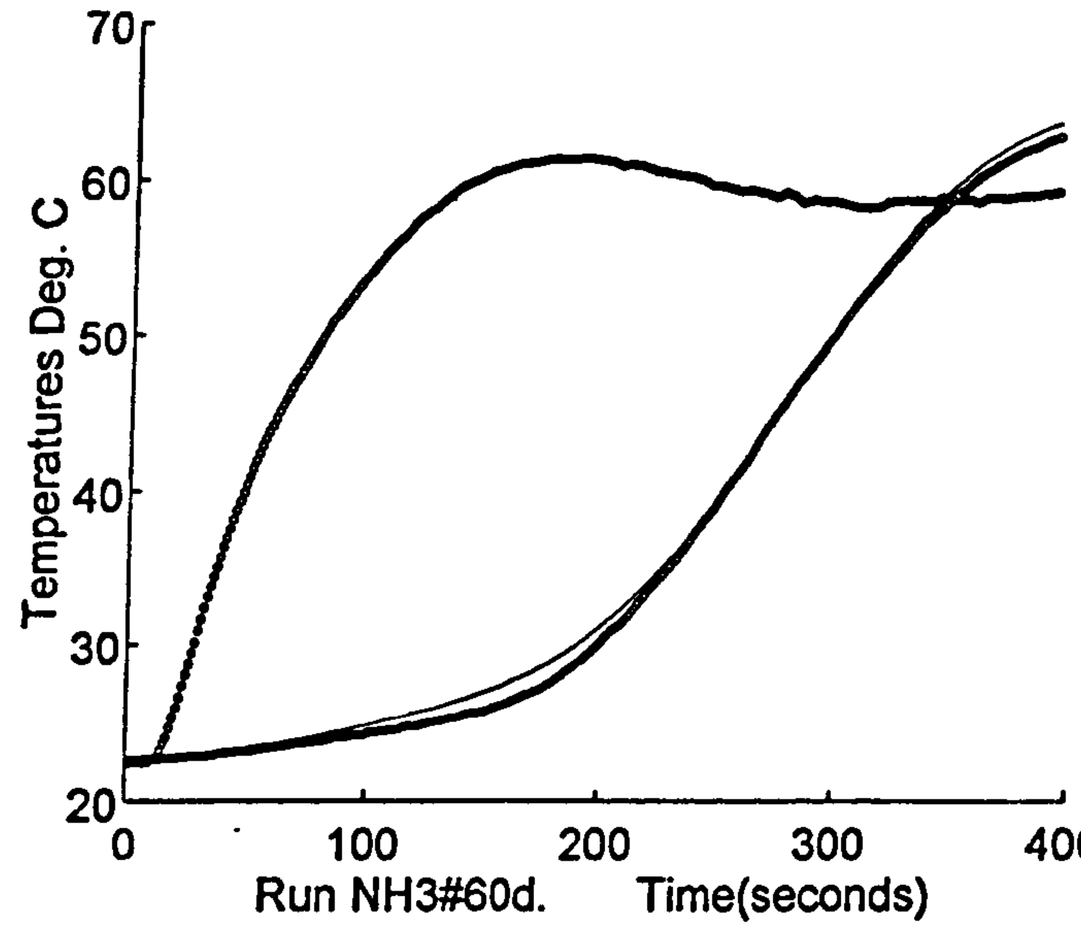
Temperatures Deg. C
70
60
50
40
30
20
0
100
200
300
400
Run NH3#60d. Time(seconds)

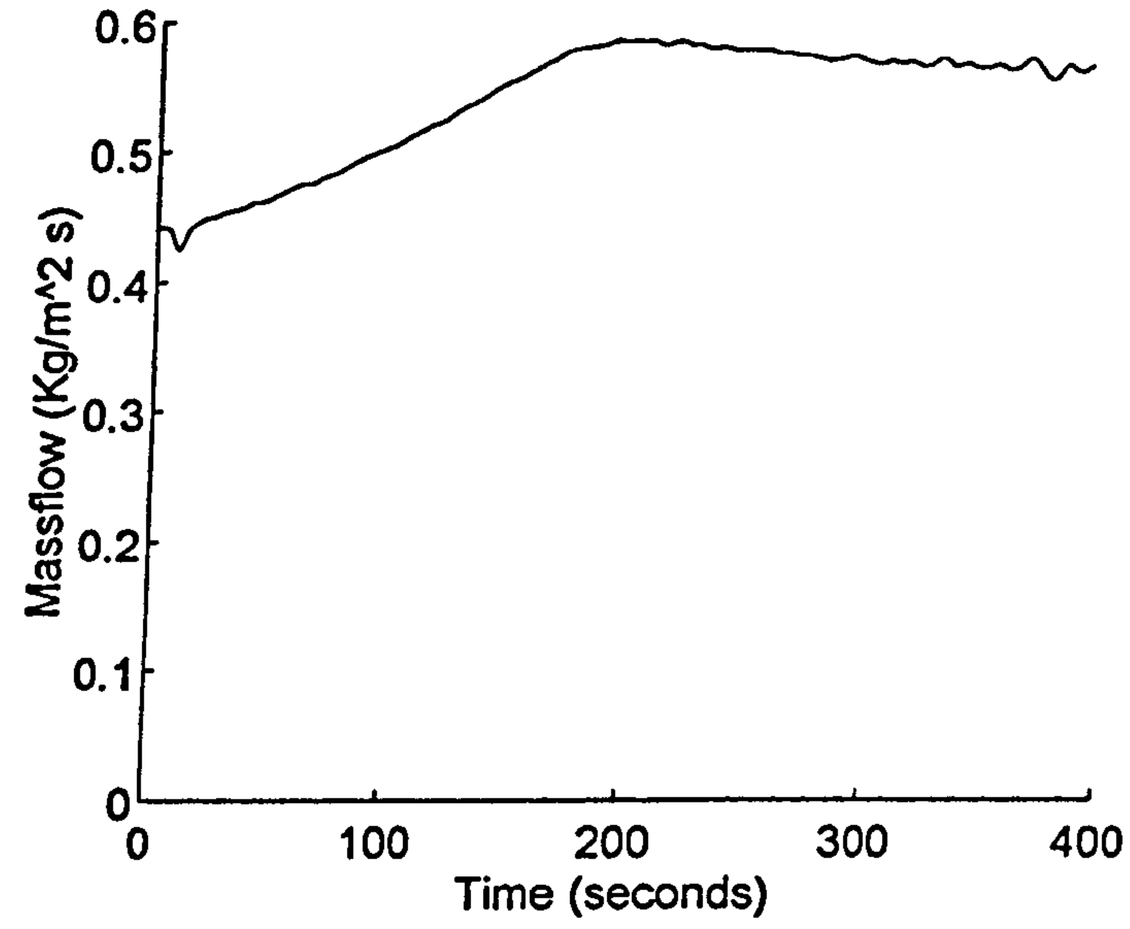
Massflow (Kg/m^2 s)
0.6
0.5
0.4
0.3
0.2
0.1
0
0
100
200
300
400
Time (seconds)

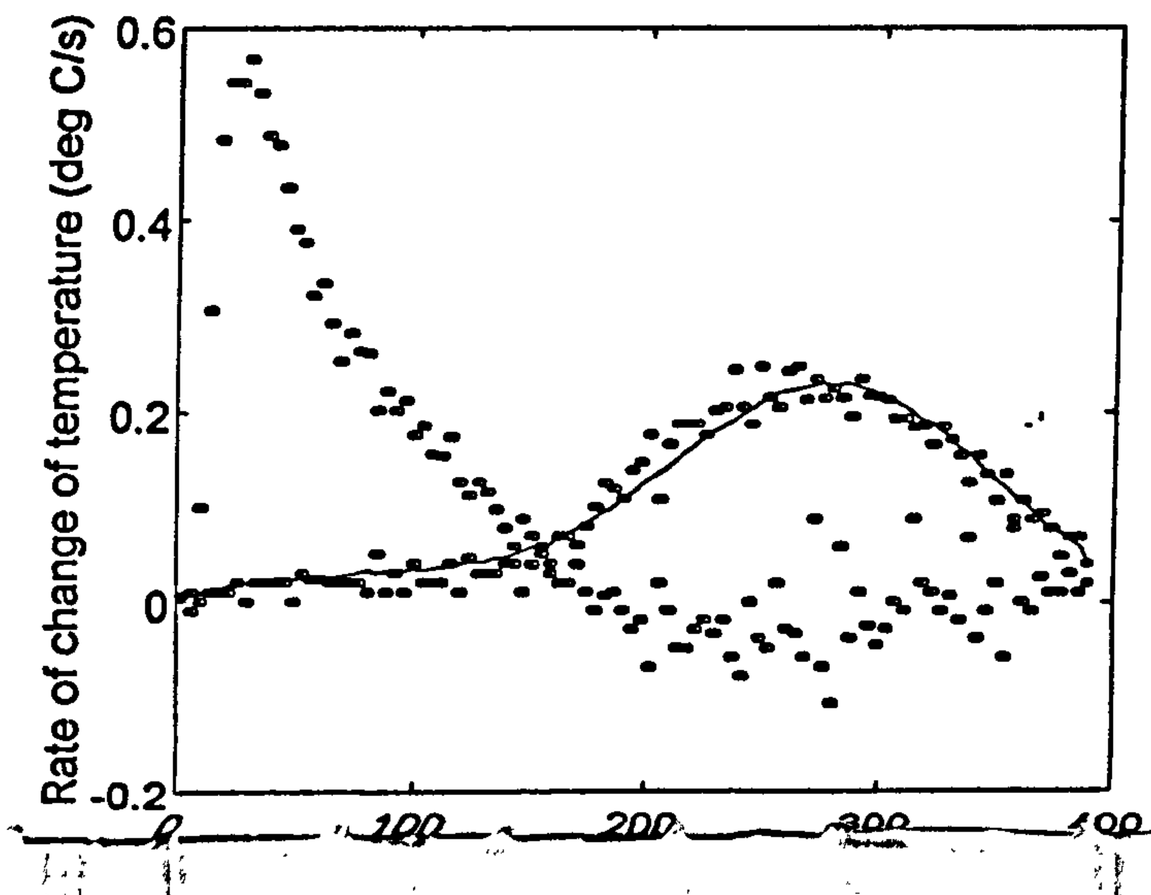
Rate of change of temperature (deg C/s)
0.6
0.4
0.2
0
-0.2
0
100
200
300
400

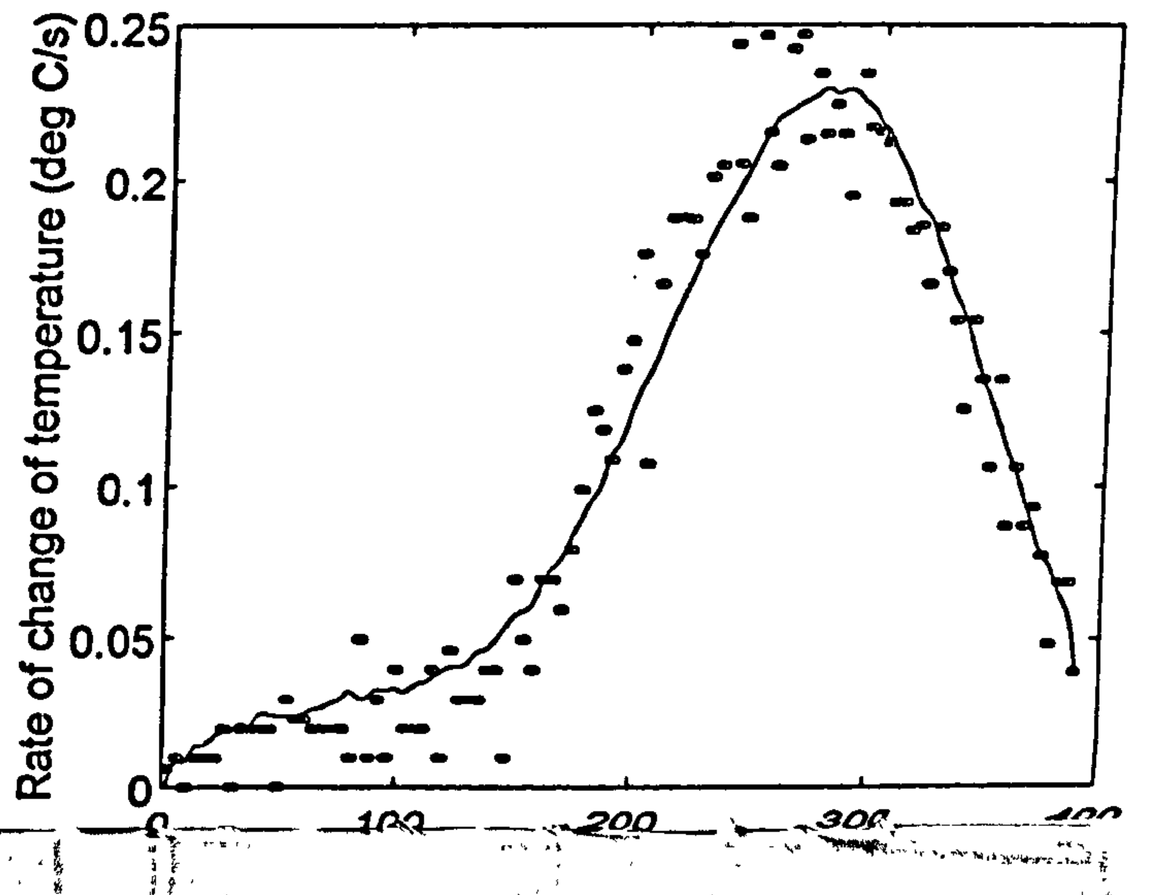
Rate of change of temperature (deg C/s)
0.25
0.2
0.15
0.1
0.05
0
0
100
200
300
400

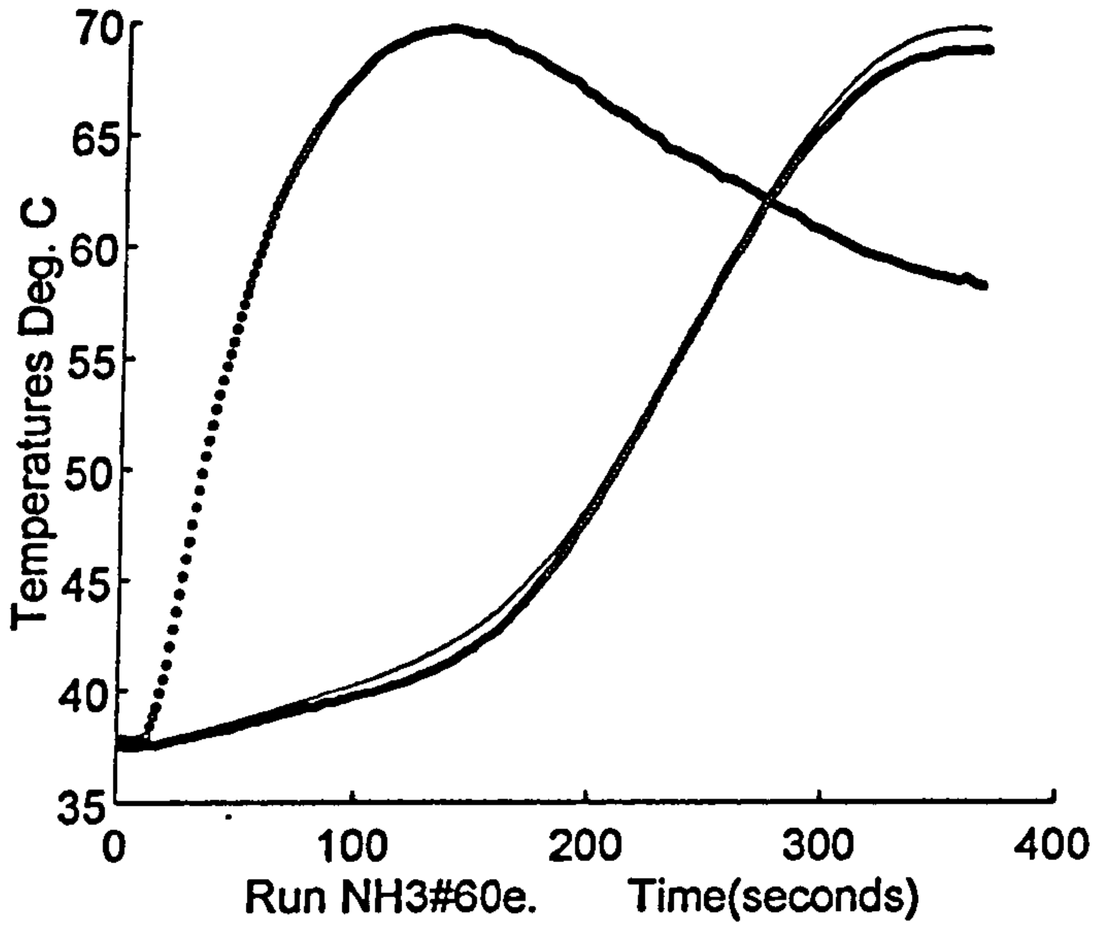
Temperatures Deg. C
70
65
60
55
50
45
40
35
0
100
200
300
400
Run NH3#60e.
Time(seconds)

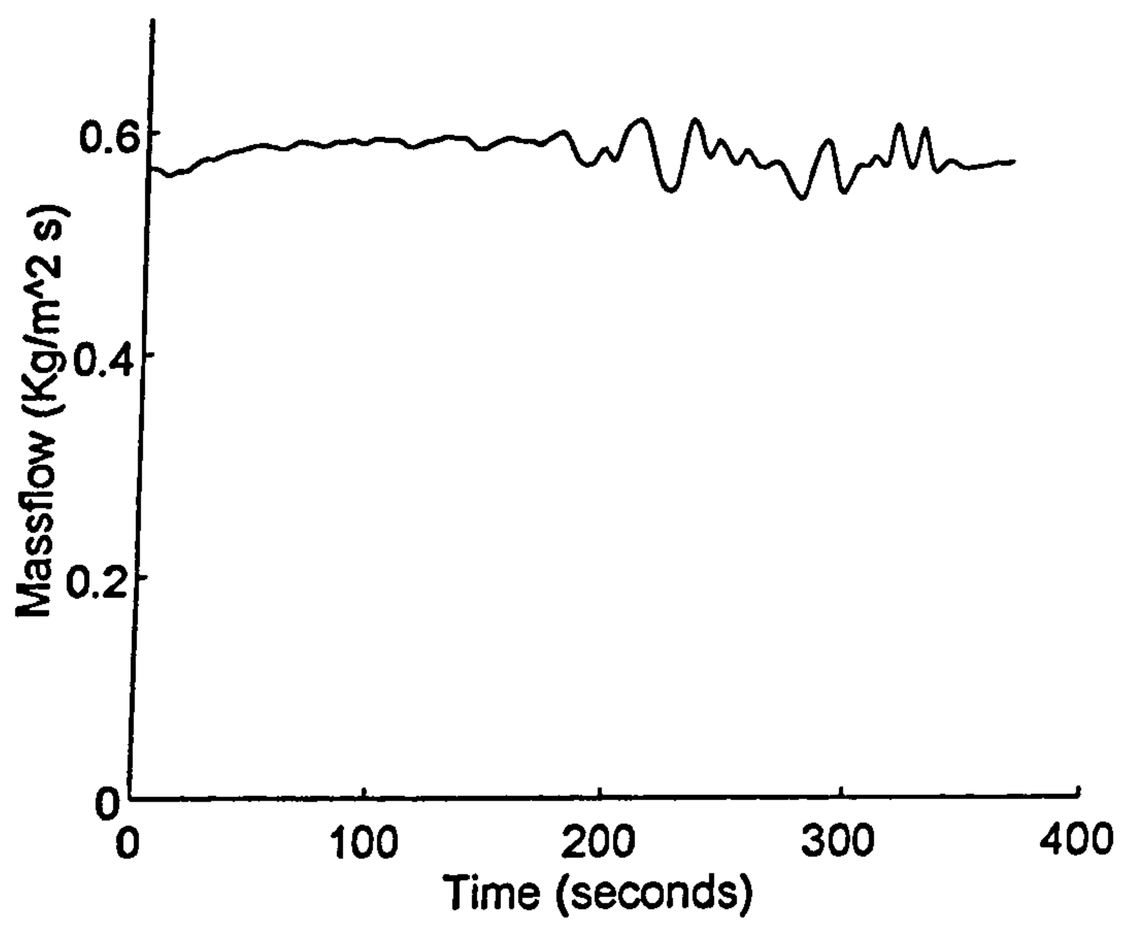
Massflow (Kg/m^2 s)
0.6
0.4
0.2
0
0
100
200
300
400
Time (seconds)

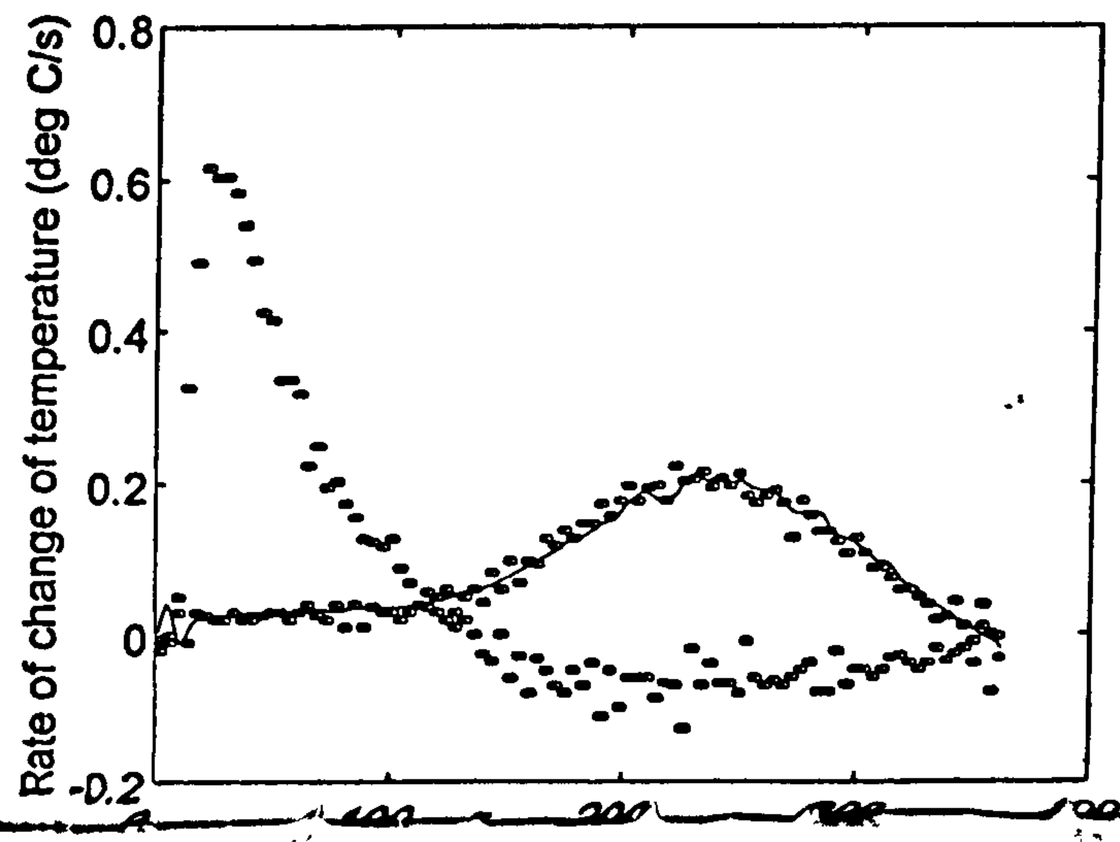
Rate of change of temperature (deg C/s)
0.8
0.6
0.4
0.2
0
-0.2

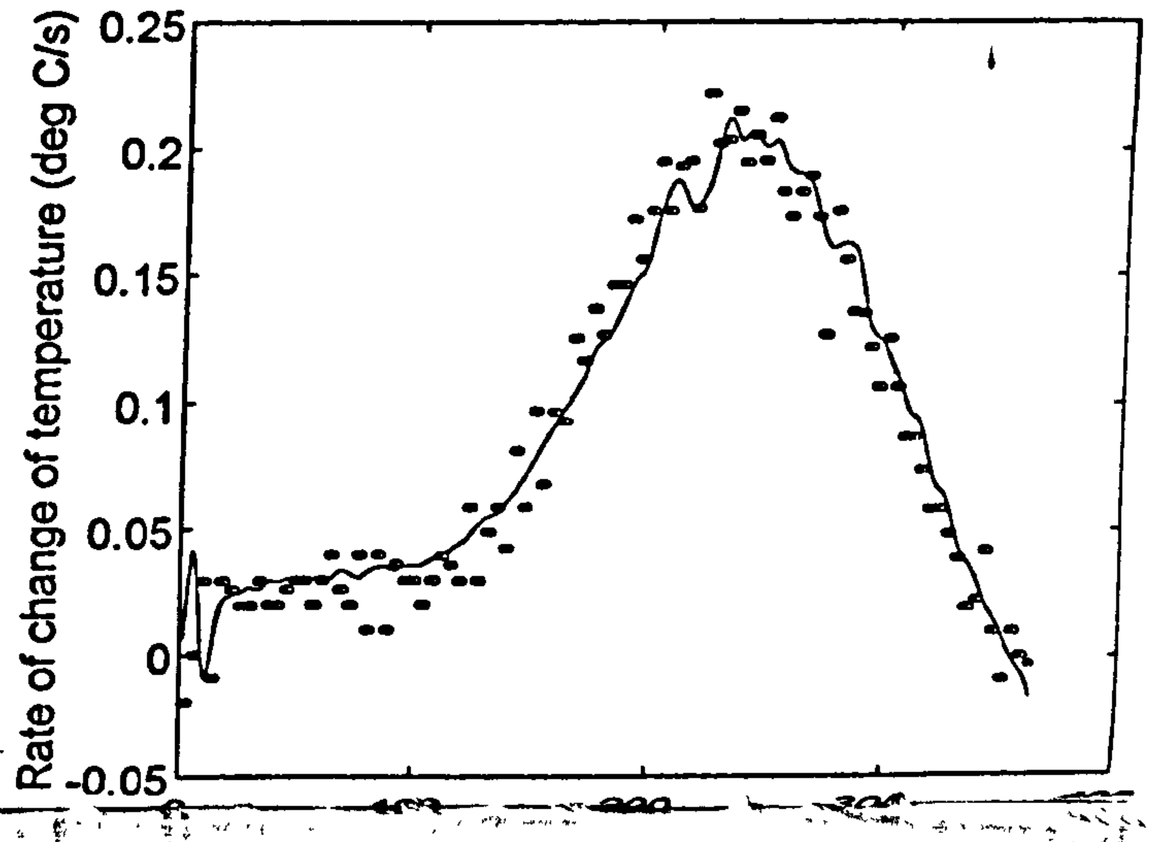
Rate of change of temperature (deg C/s)
0.25
0.2
0.15
0.1
0.05
0
-0.05

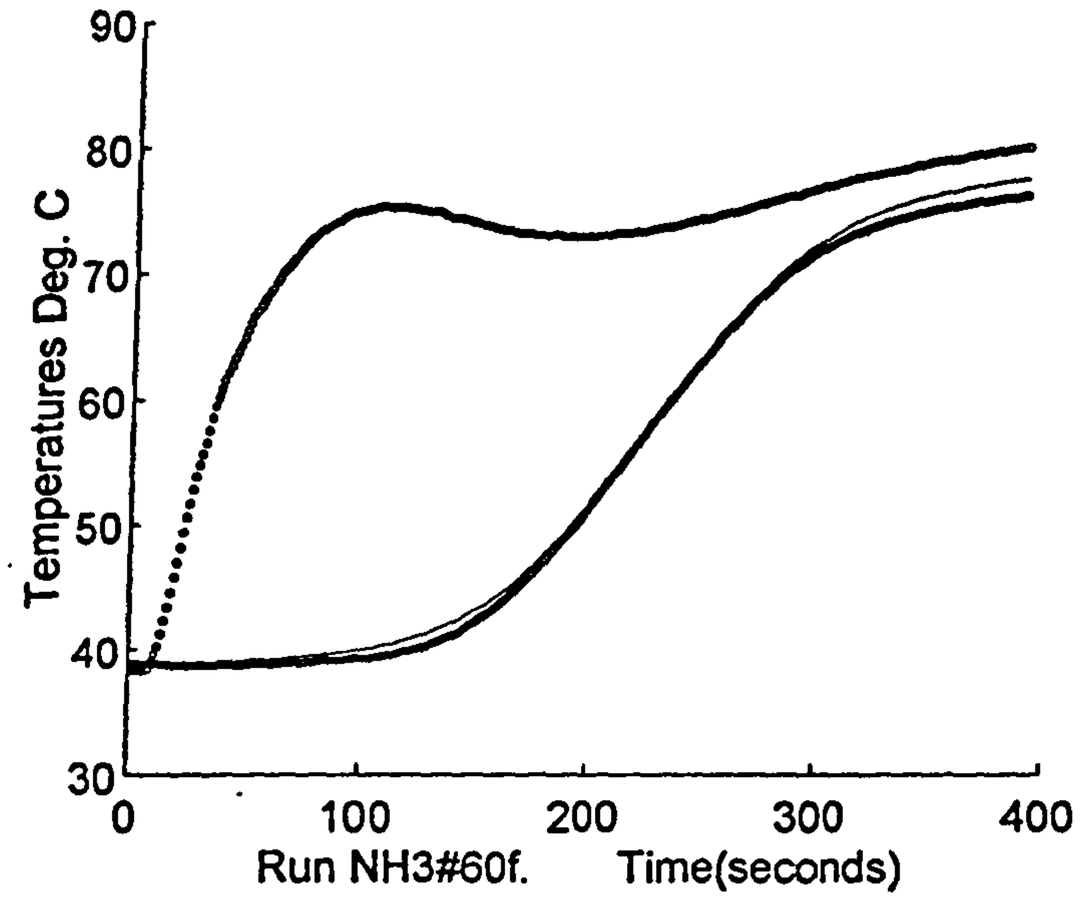
Temperatures Deg. C
90
80
70
60
50
40
30
0
100
200
300
400
Run NH3#60f. Time(seconds)

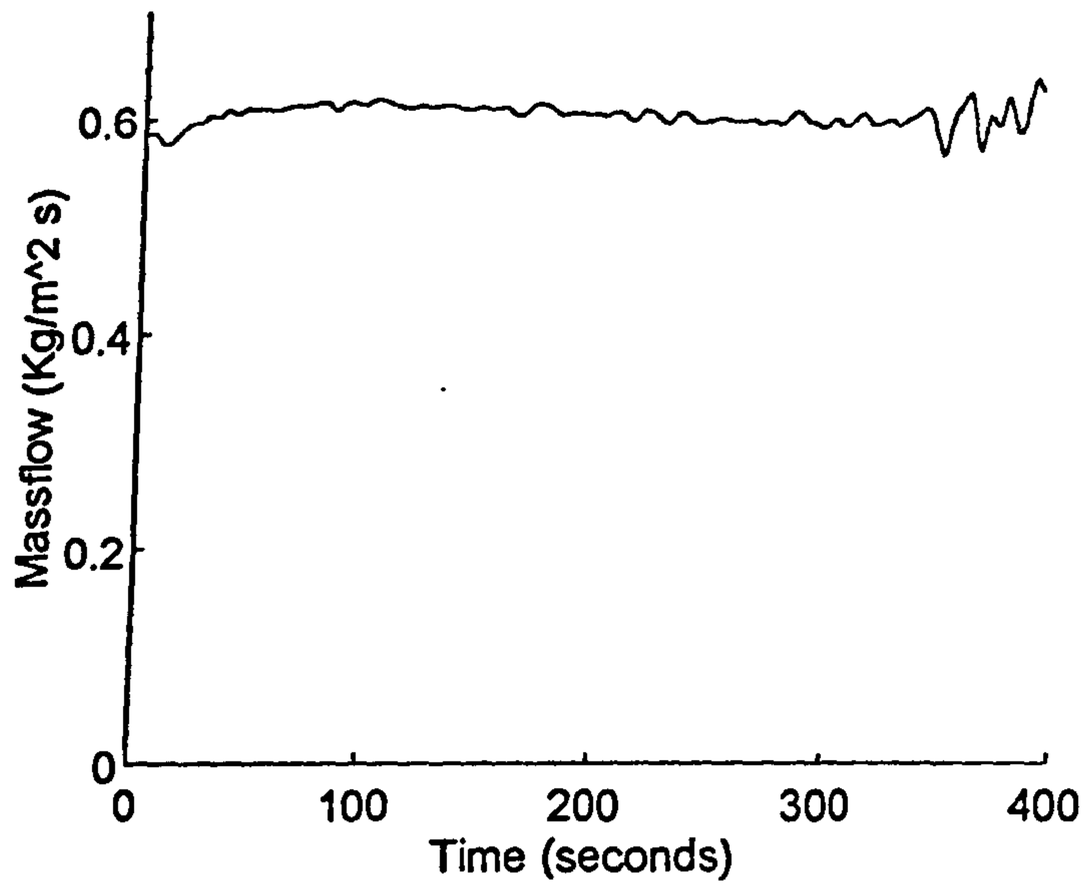
Massflow (Kg/m^2 s)
0.6
0.4
0.2
0
0
100
200
300
400
Time (seconds)

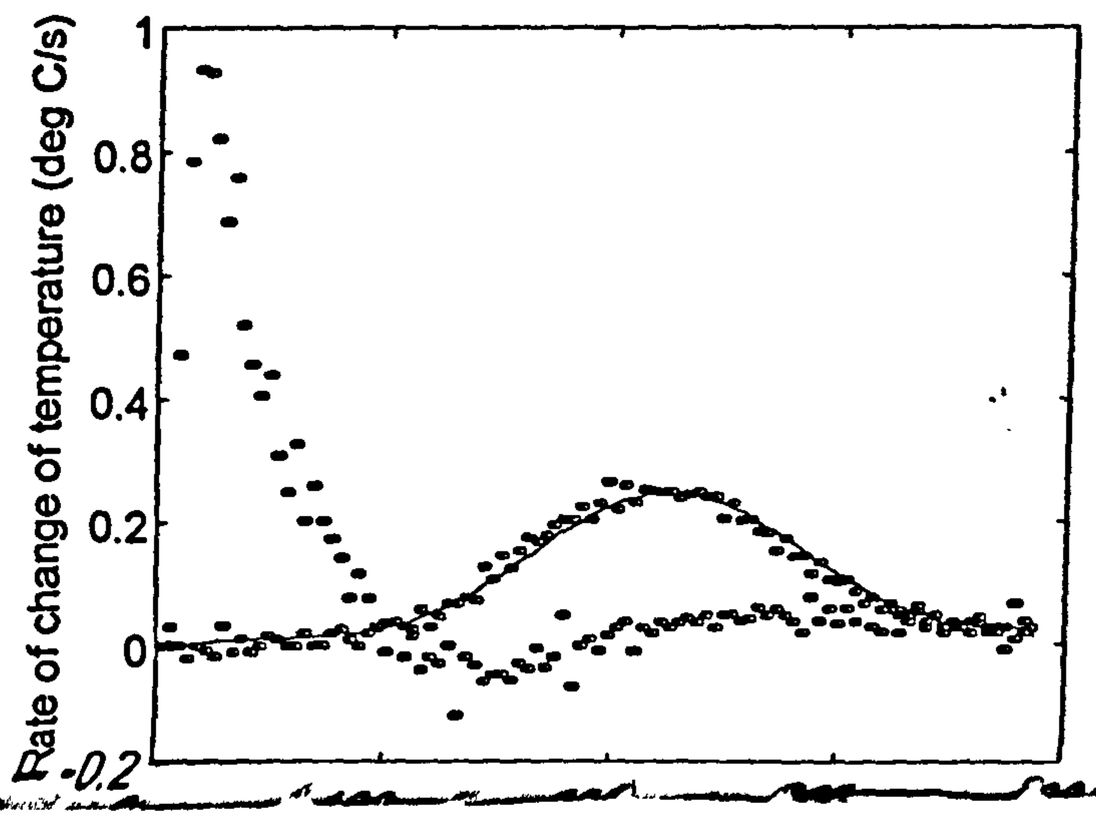
Rate of change of temperature (deg C/s)
1
0.8
0.6
0.4
0.2
0
-0.2

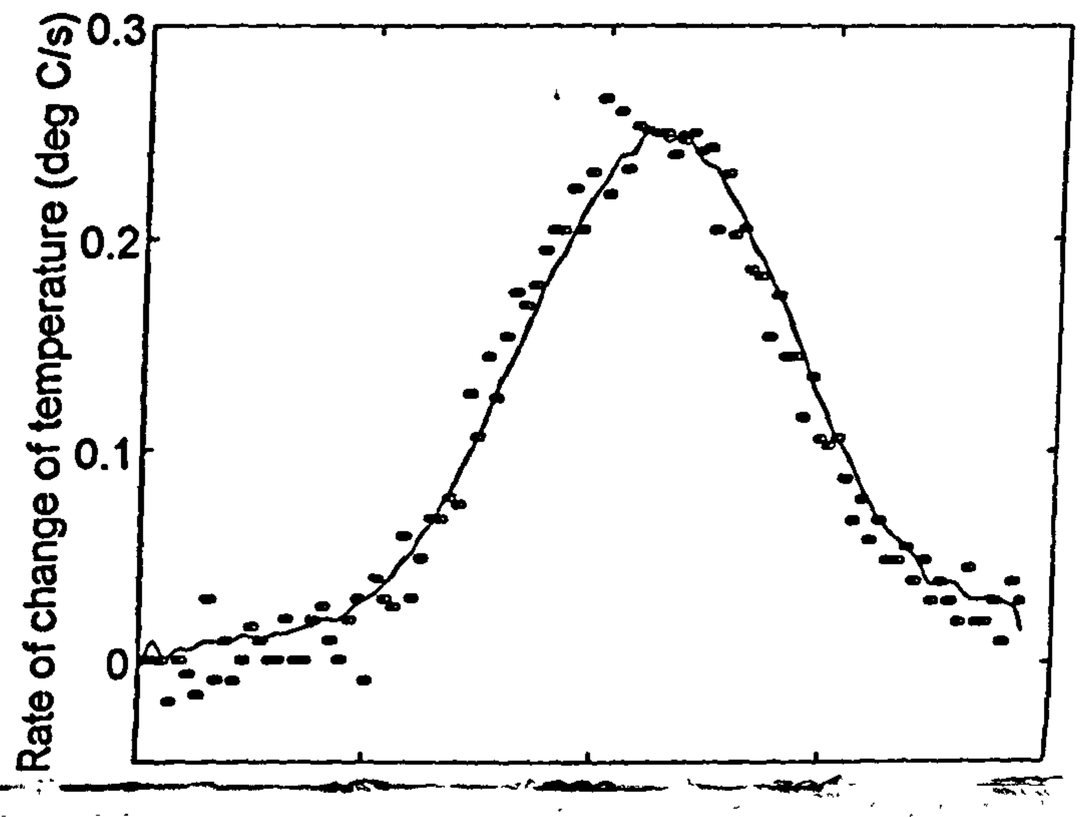
Rate of change of temperature (deg C/s)
0.3
0.2
0.1
0

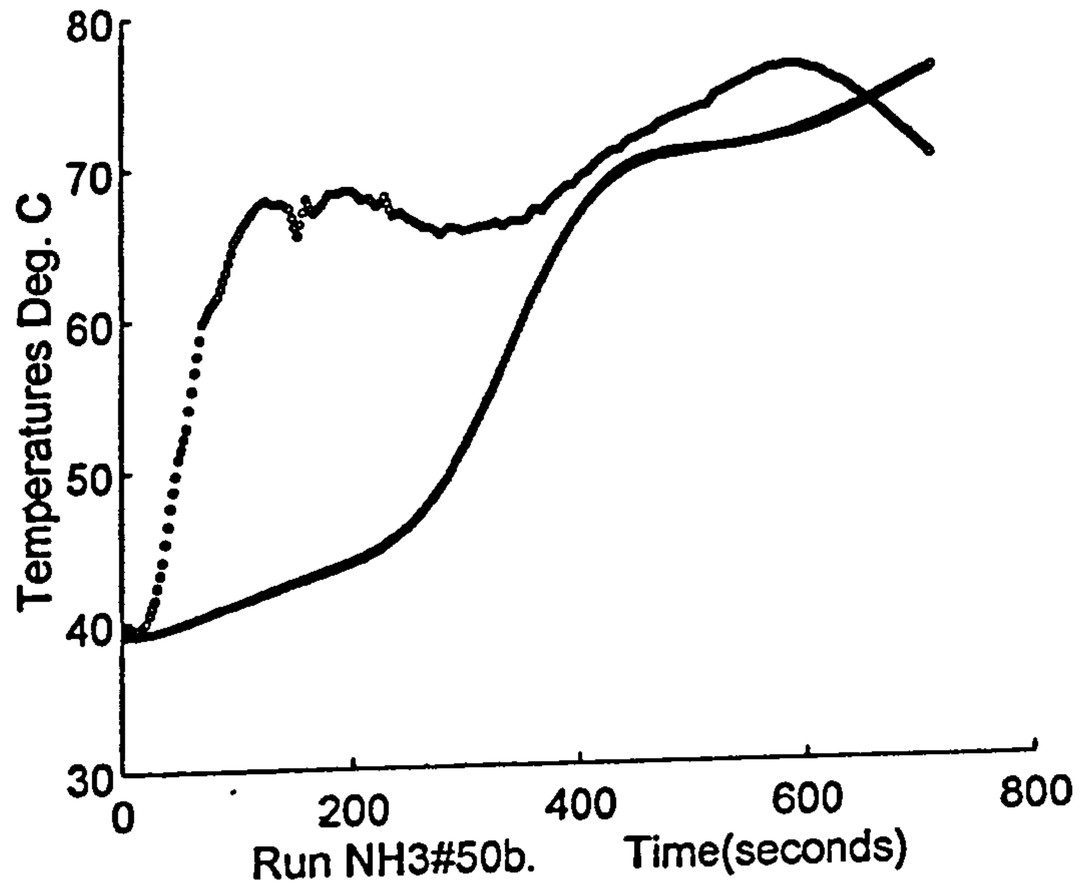
Temperatures Deg. C
80
70
60
50
40
30
0
200
400
600
800
Run NH3#50b.
Time(seconds)

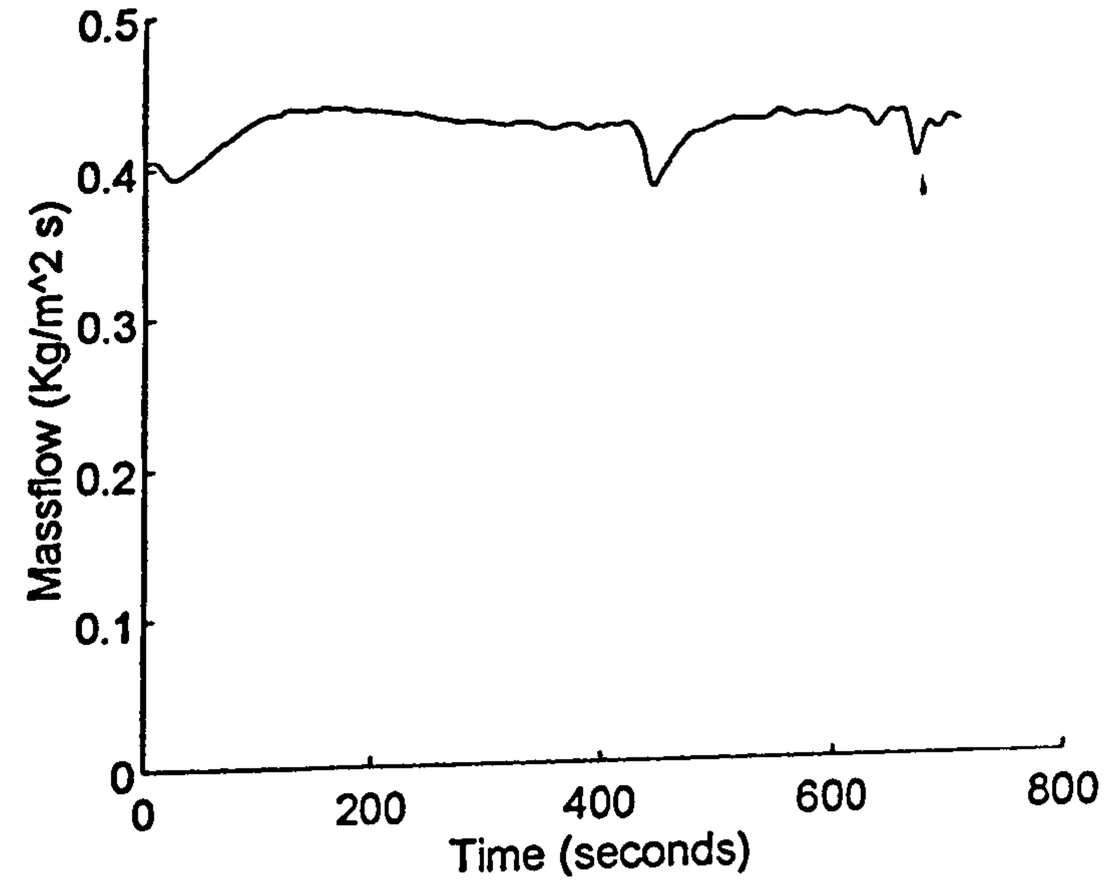
Massflow (Kg/m^2 s)
0.5
0.4
0.3
0.2
0.1
0
0
200
400
600
800
Time (seconds)

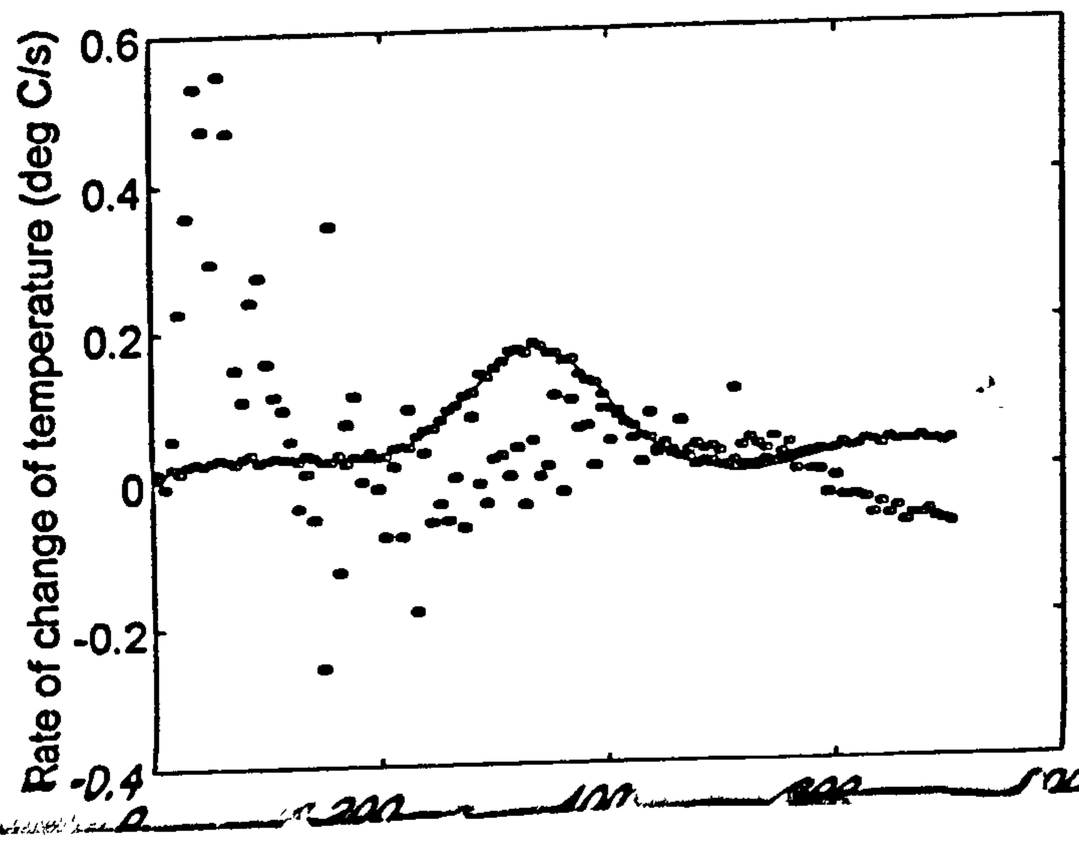
Rate of change of temperature (deg C/s)
0.6
0.4
0.2
0
-0.2
-0.4

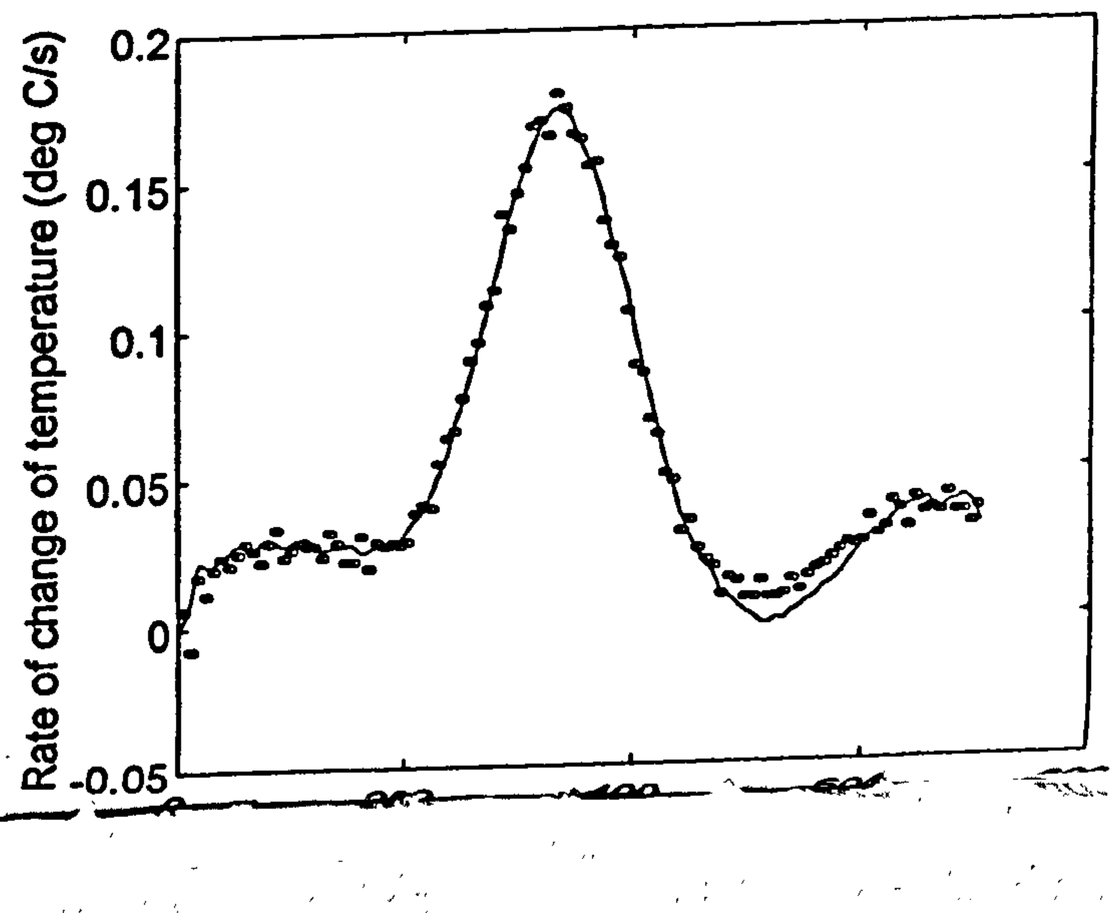
Rate of change of temperature (deg C/s)
0.2
0.15
0.1
0.05
0
-0.05

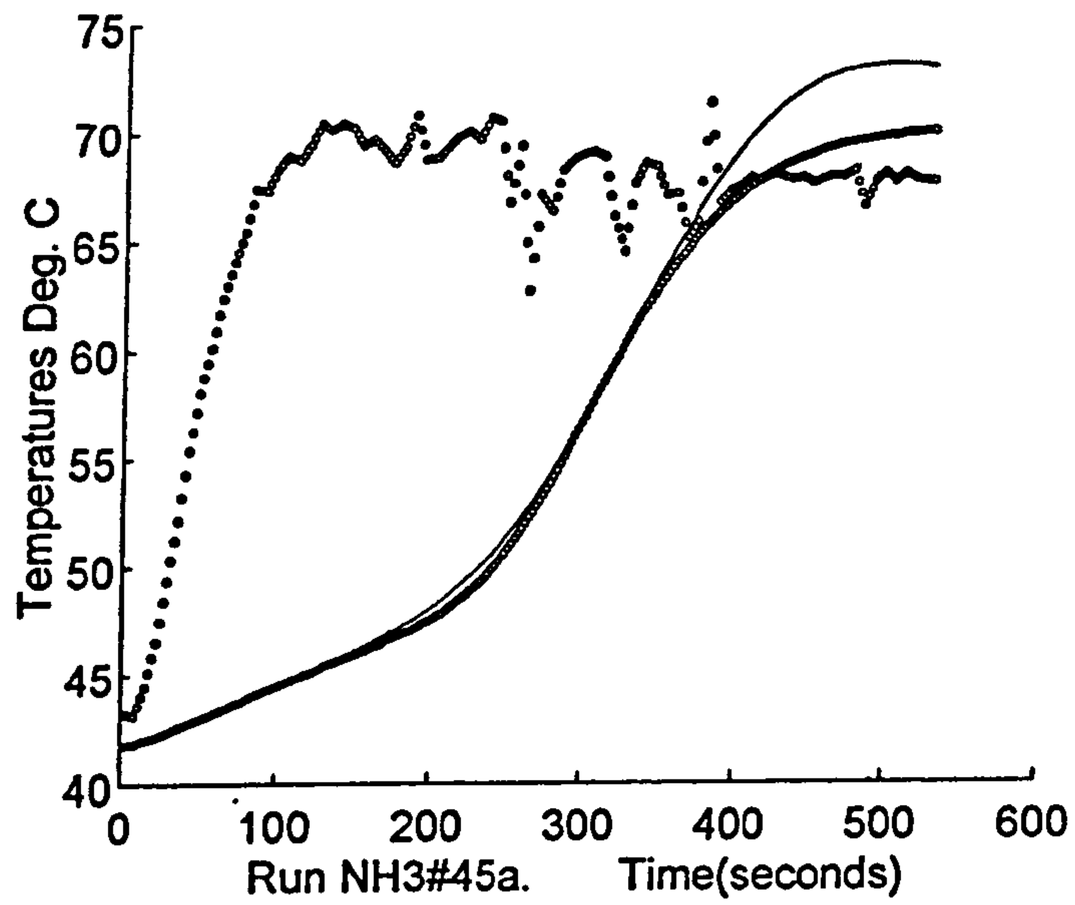
Temperatures Deg. C
75
70
65
60
55
50
45
40
0
100
200
300
400
500
600
Run NH3#45a. Time(seconds)

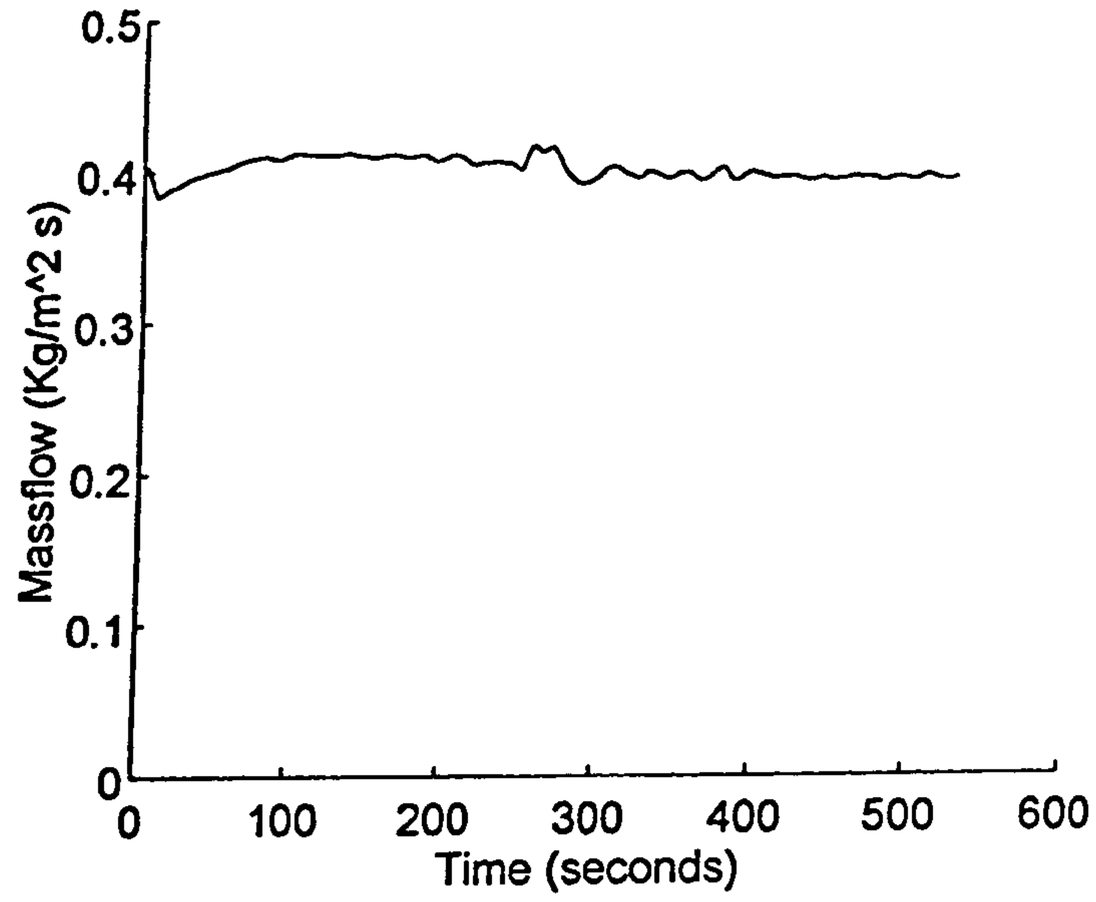
Massflow (Kg/m^2 s)
0.5
0.4
0.3
0.2
0.1
0
0
100
200
300
400
500
600
Time (seconds)

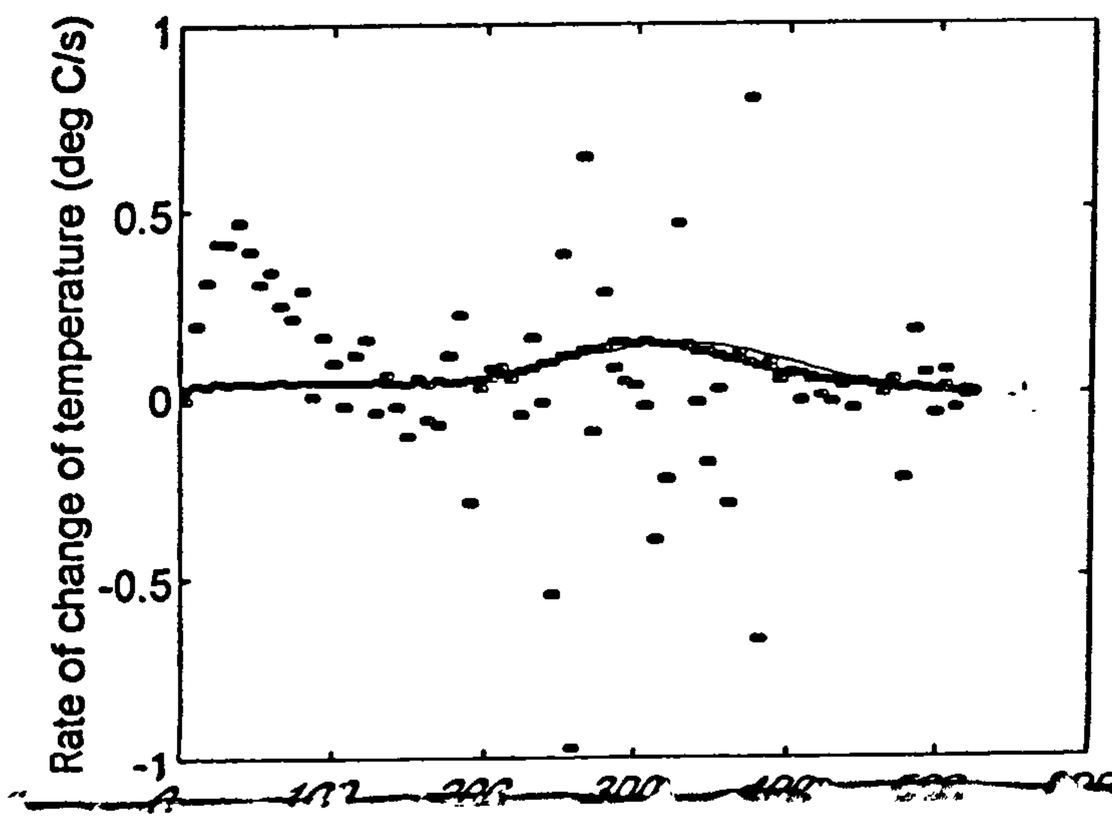
Rate of change of temperature (deg C/s)
1
0.5
0
-0.5
-1

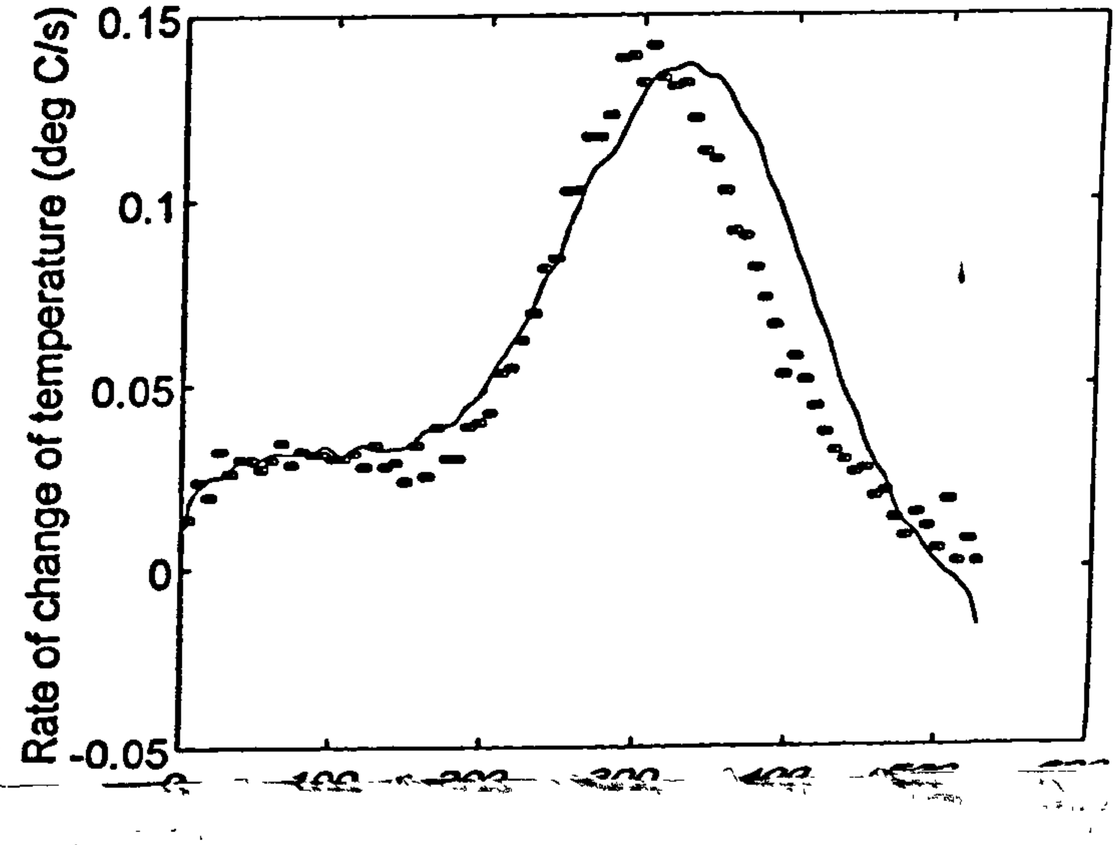
Rate of change of temperature (deg C/s)
0.15
0.1
0.05
0
-0.05

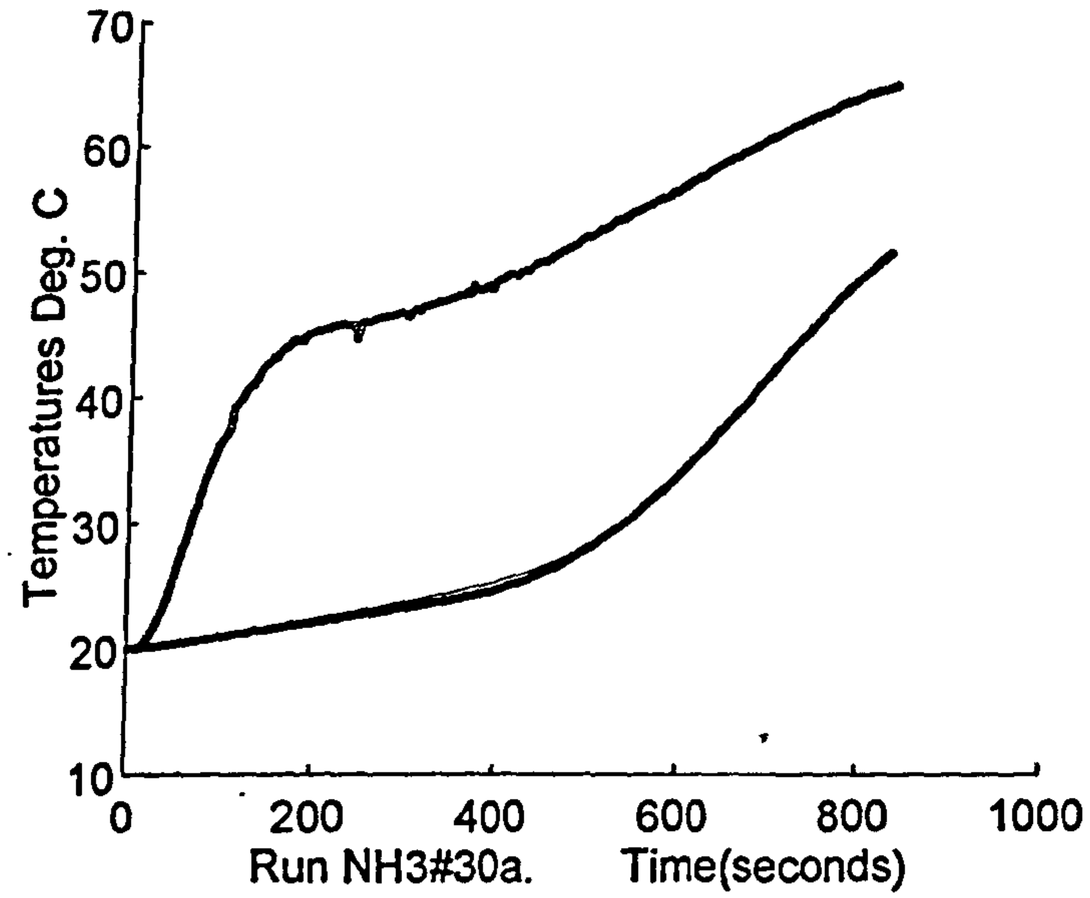
Temperatures Deg. C
70
60
50
40
30
20
10
0
200
400
600
800
1000
Run NH3#30a.
Time(seconds)

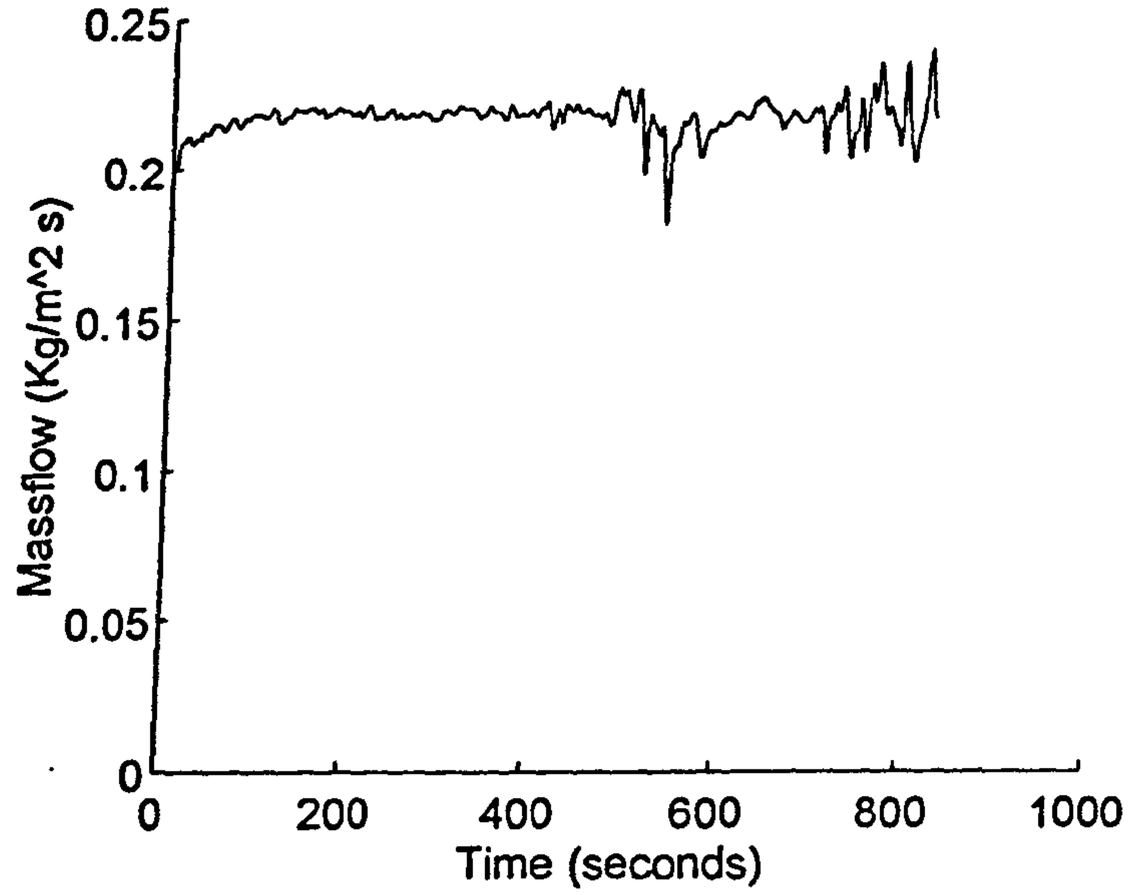
Massflow (Kg/m^2 s)
0.25
0.2
0.15
0.1
0.05
0
0
200
400
600
800
1000
Time (seconds)

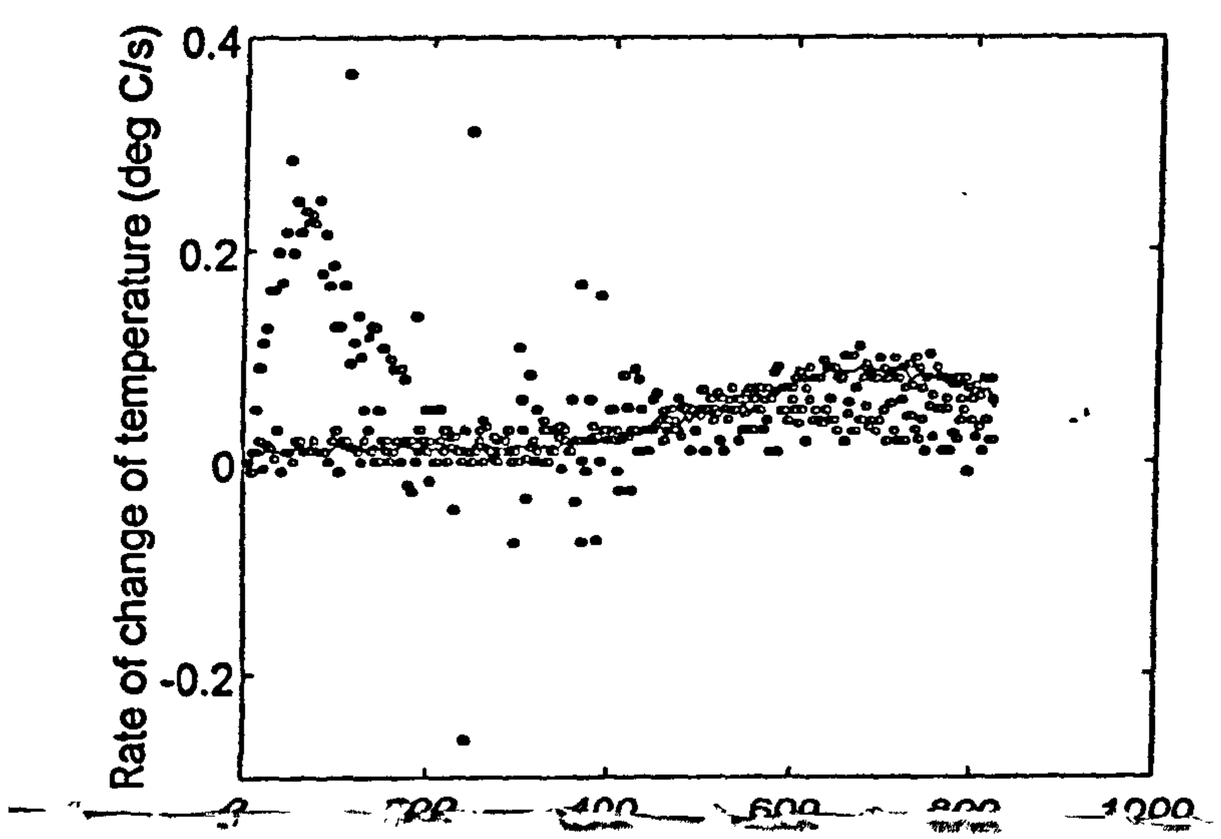
Rate of change of temperature (deg C/s)
0.4
0.2
0
-0.2
0
200
400
600
800
1000

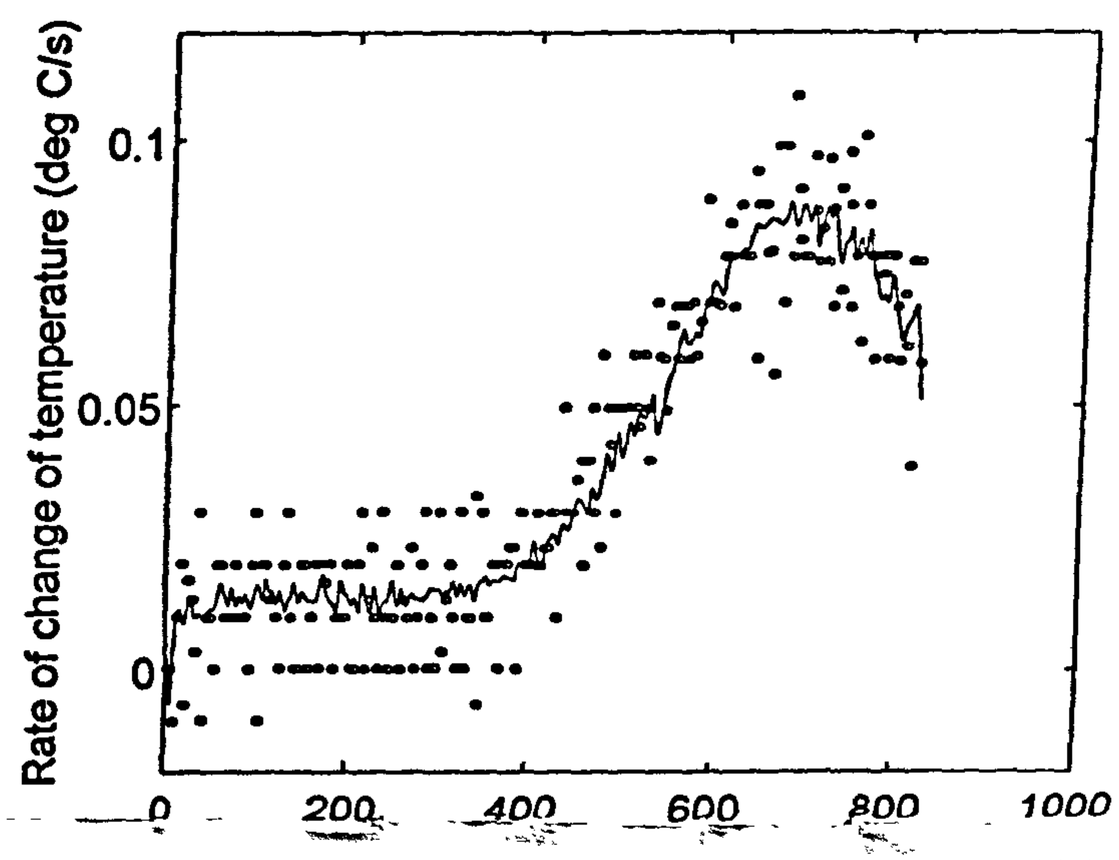
Rate of change of temperature (deg C/s)
0.1
0.05
0
0
200
400
600
800
1000

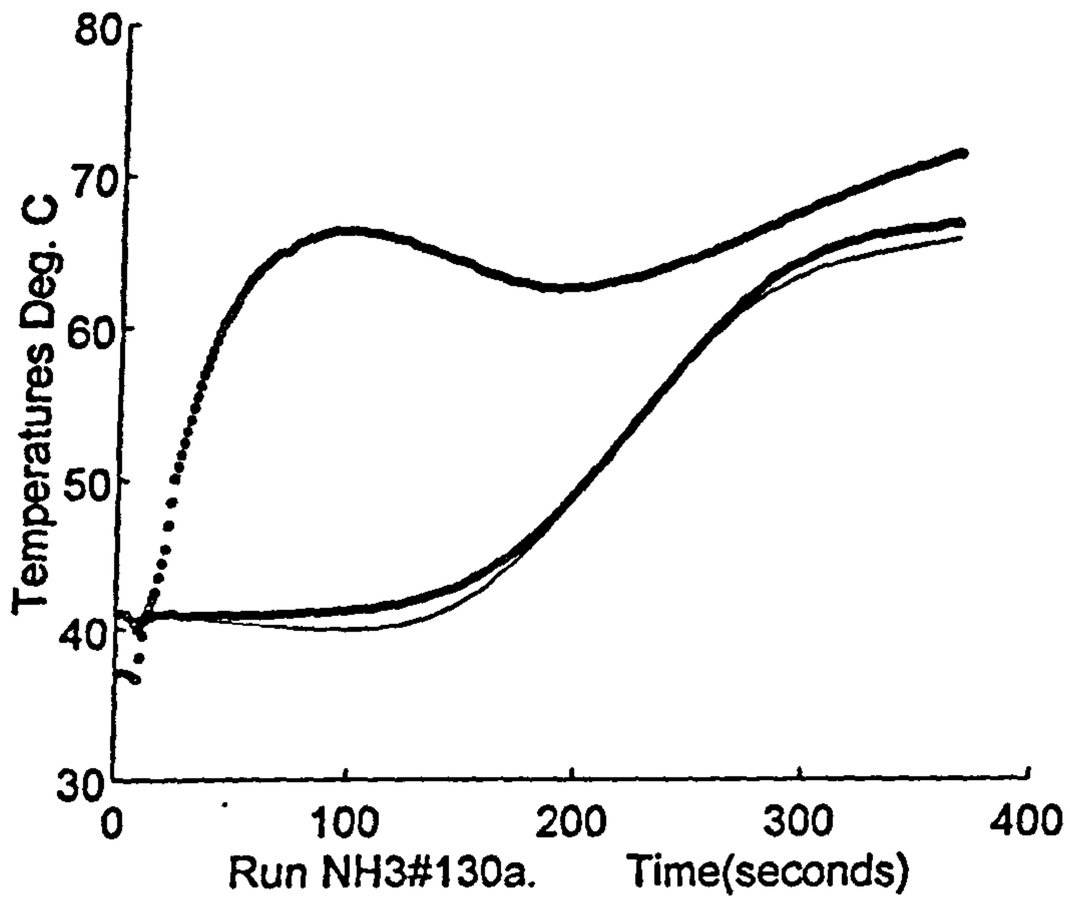
Temperatures Deg. C
80
70
60
50
40
30
0
100
200
300
400
Run NH3#130a.
Time(seconds)

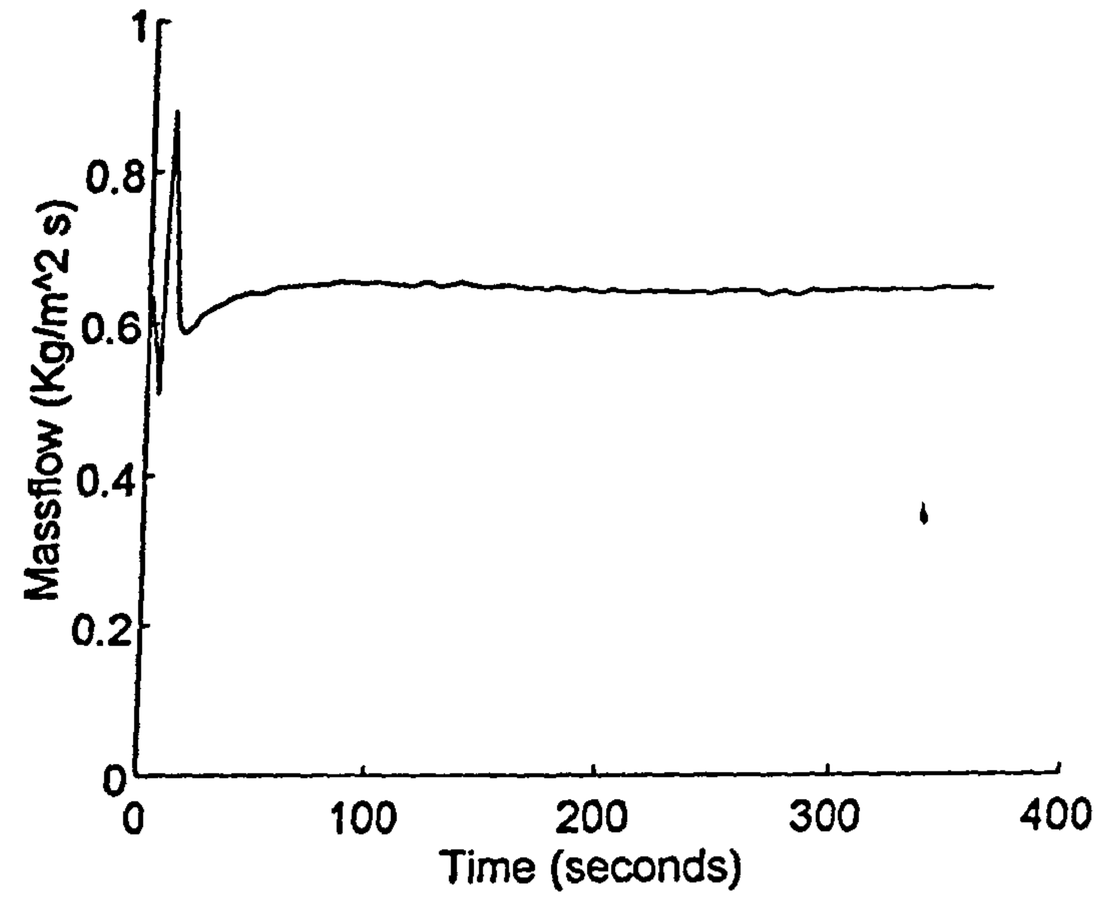
Massflow (Kg/m^2 s)
1
0.8
0.6
0.4
0.2
0
0
100
200
300
400
Time (seconds)

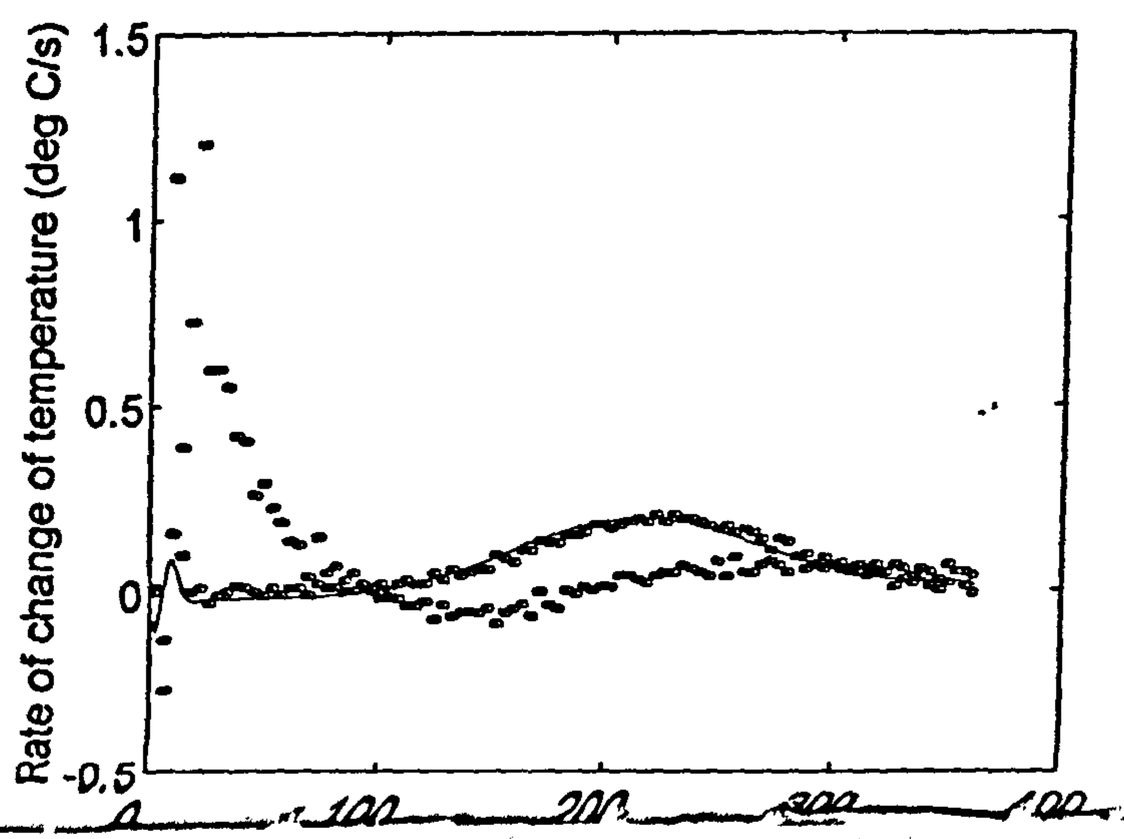
Rate of change of temperature (deg C/s)
1.5
1
0.5
0
-0.5

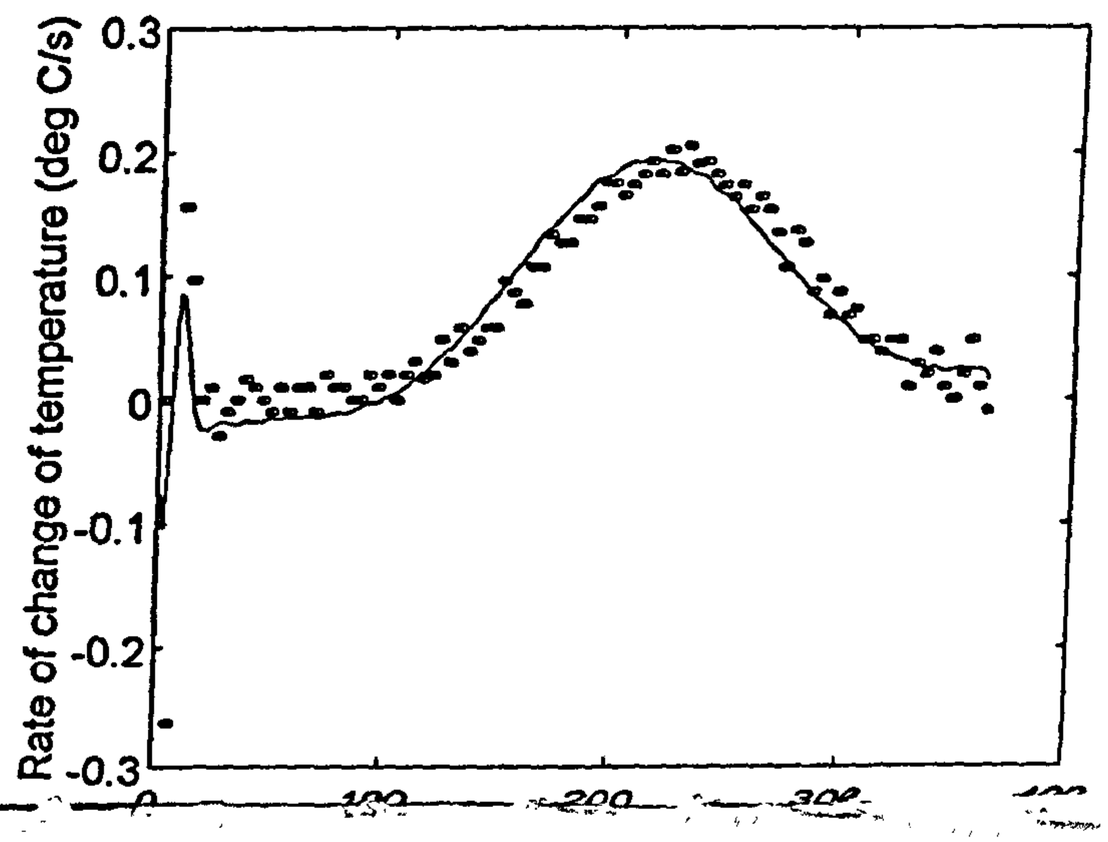
Rate of change of temperature (deg C/s)
0.3
0.2
0.1
0
-0.1
-0.2
-0.3

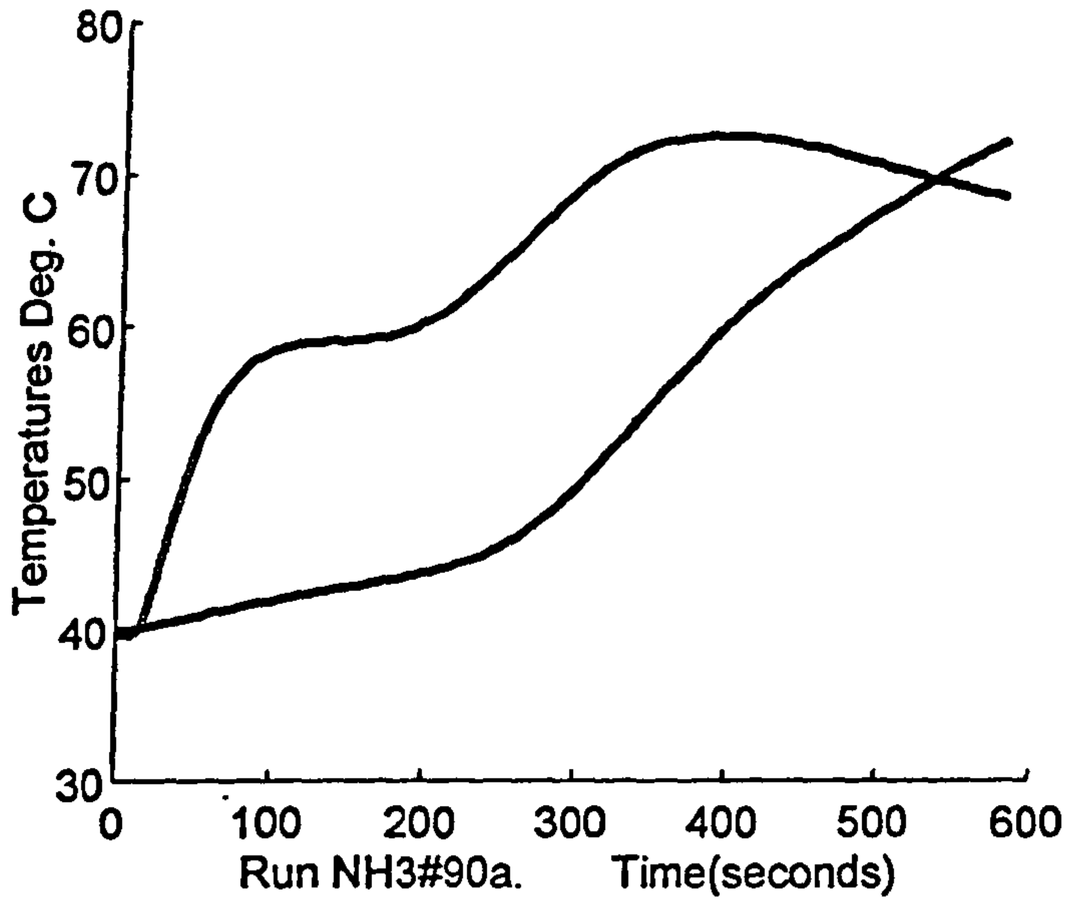
Temperatures Deg. C
80
70
60
50
40
30
0
100
200
300
400
500
600
Run NH3#90a. Time(seconds)

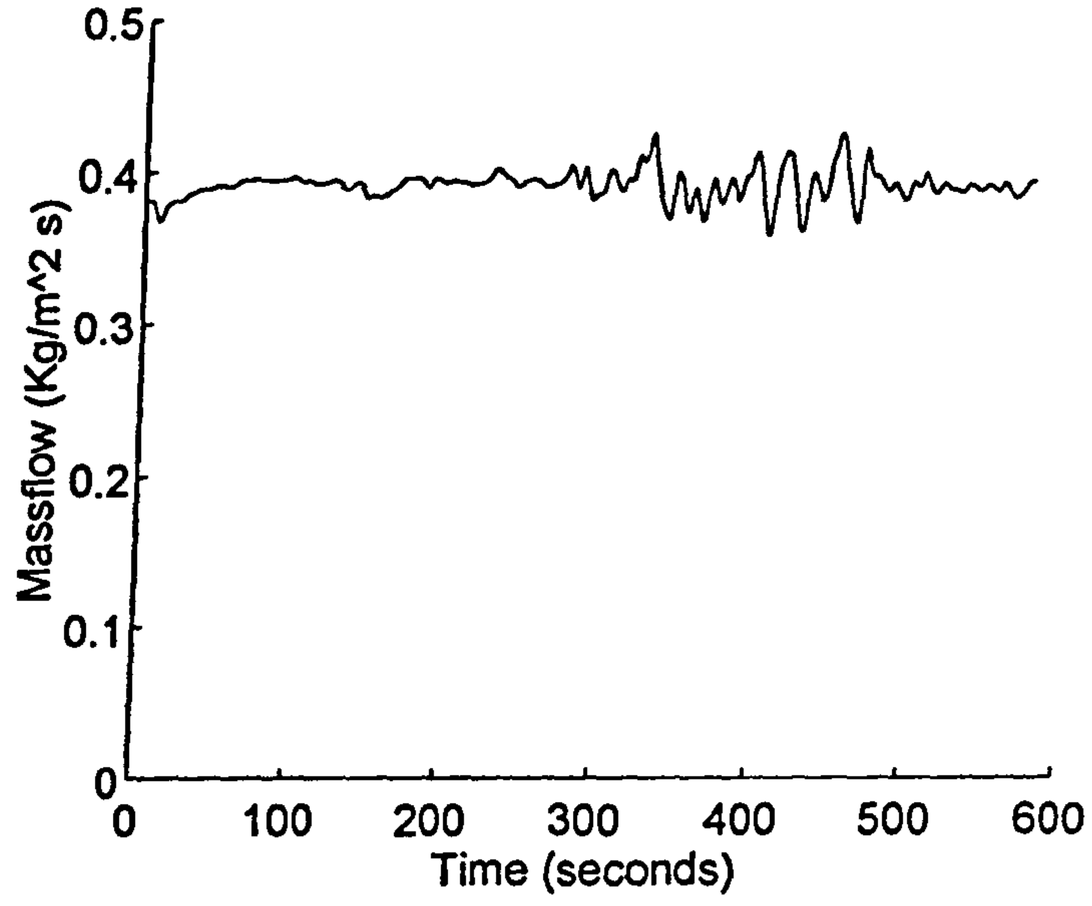
Massflow (Kg/m^2 s)
0.5
0.4
0.3
0.2
0.1
0
0
100
200
300
400
500
600
Time (seconds)

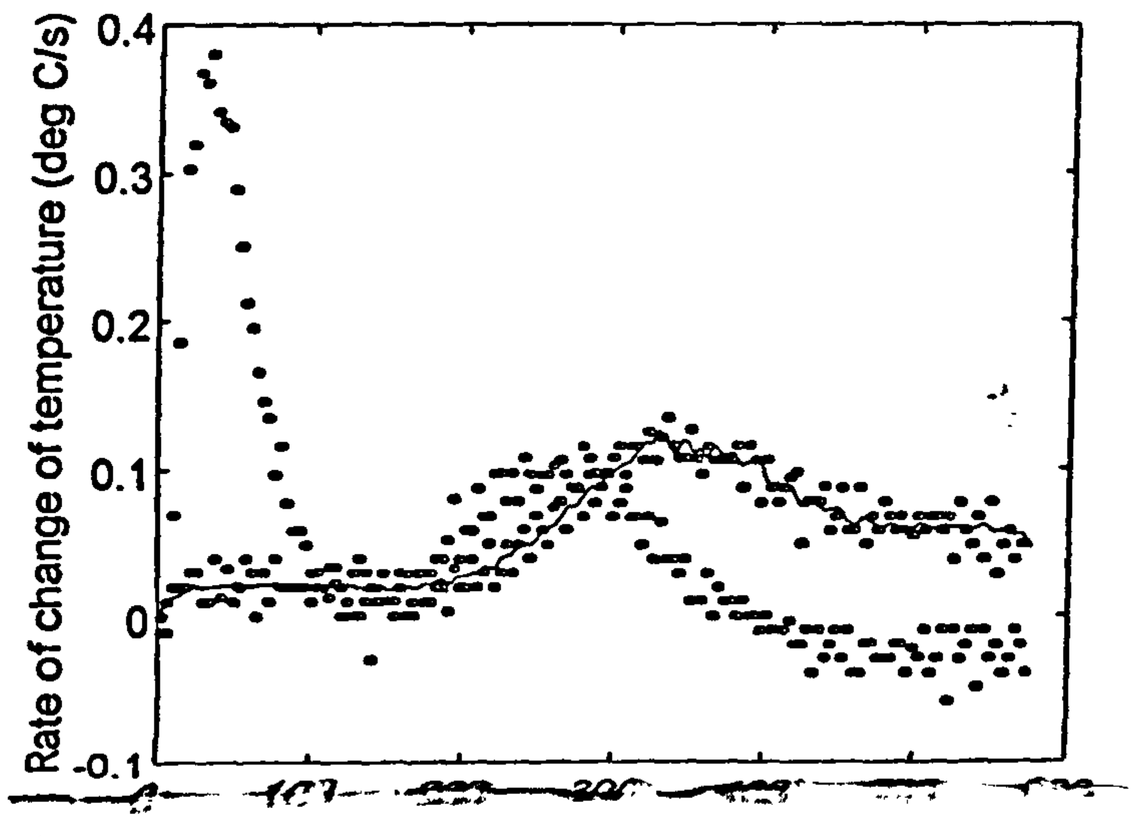
Rate of change of temperature (deg C/s)
0.4
0.3
0.2
0.1
0
-0.1

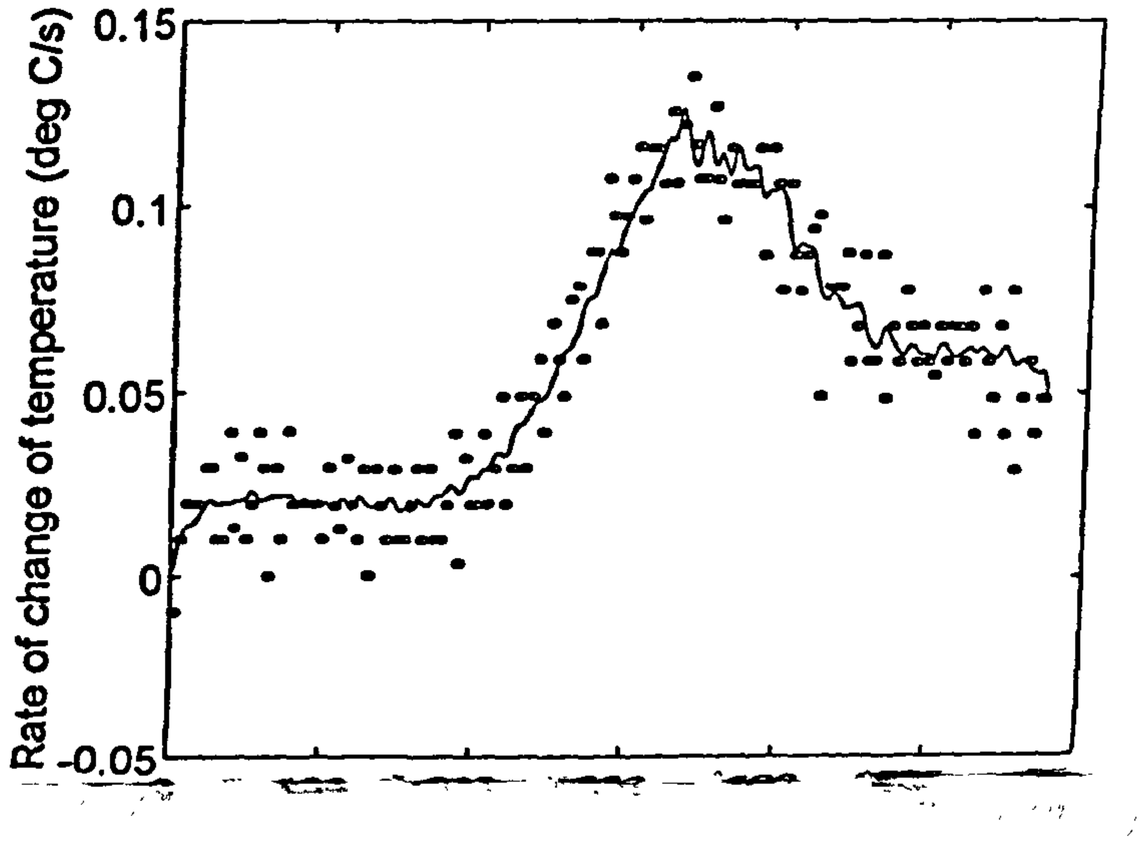
Rate of change of temperature (deg C/s)
0.15
0.1
0.05
0
-0.05

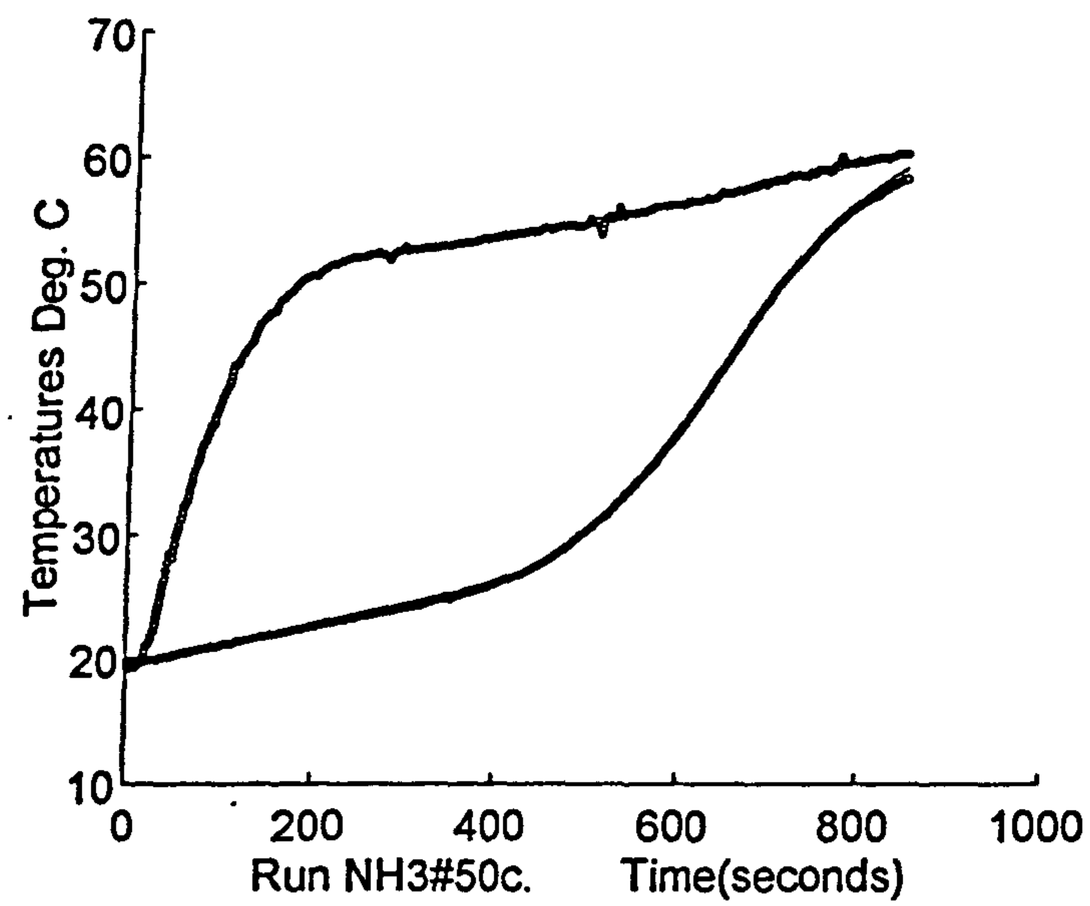
Temperatures Deg. C
70
60
50
40
30
20
10
0
200
400
600
800
1000
Run NH3#50c.
Time(seconds)

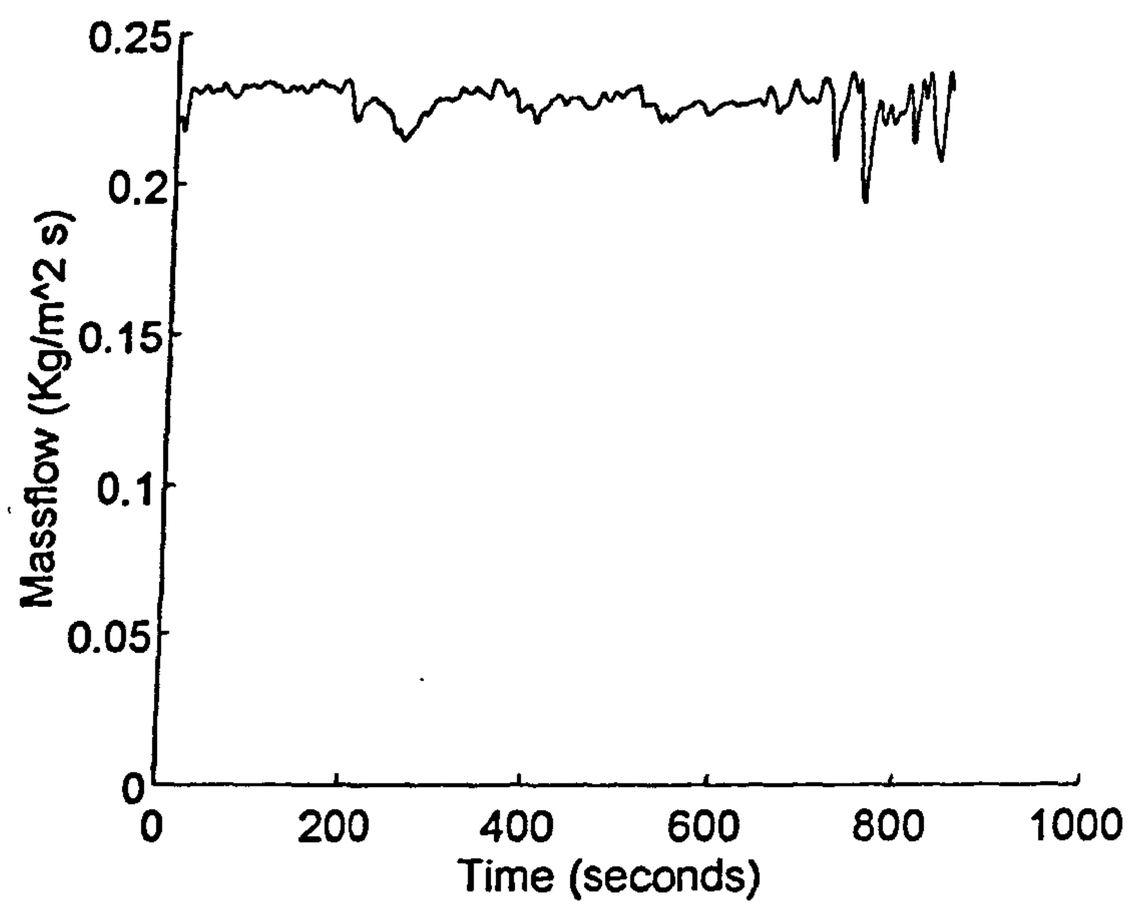
Massflow (Kg/m^2 s)
0.25
0.2
0.15
0.1
0.05
0
0
200
400
600
800
1000
Time (seconds)

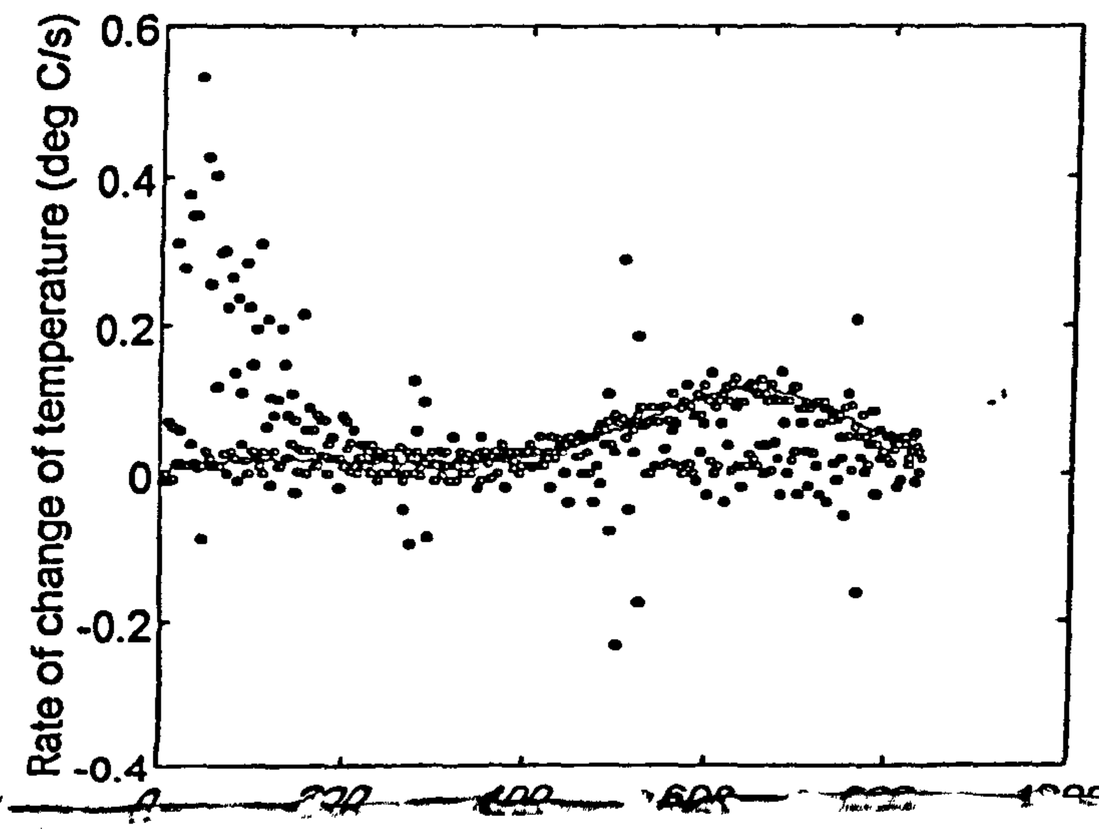
Rate of change of temperature (deg C/s)
0.6
0.4
0.2
0
-0.2
-0.4

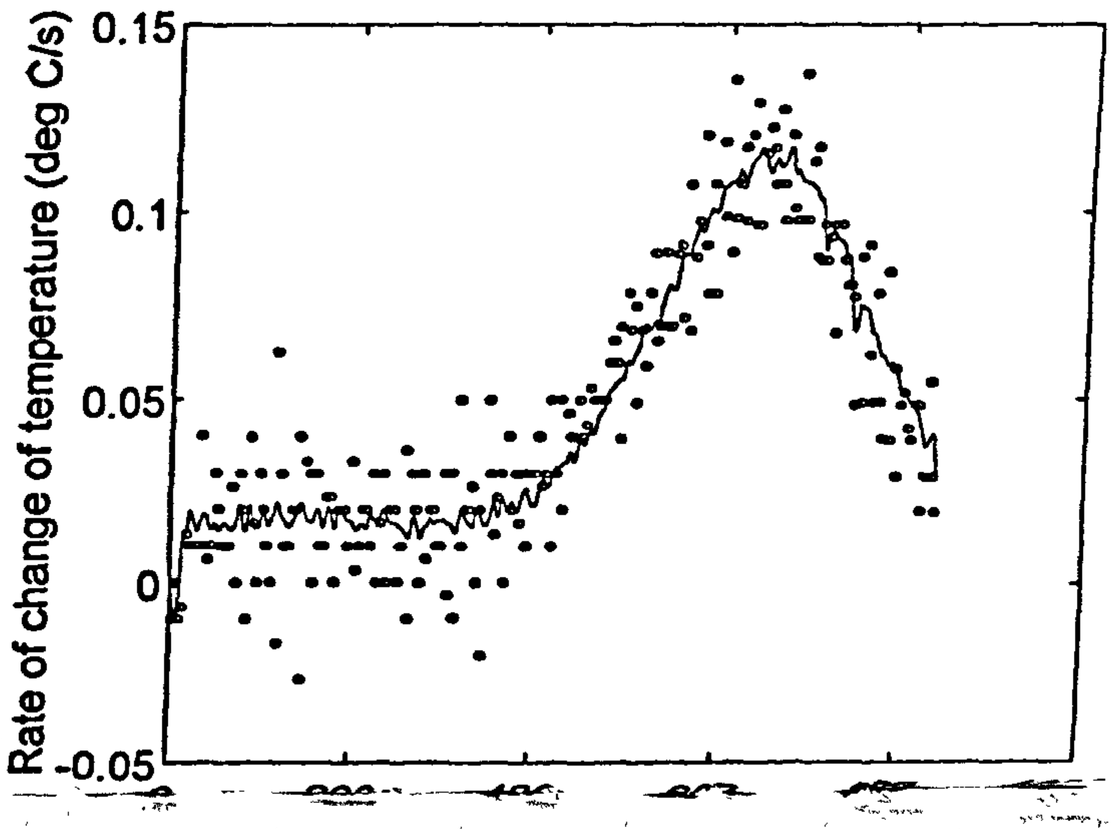
Rate of change of temperature (deg C/s)
0.15
0.1
0.05
0
-0.05

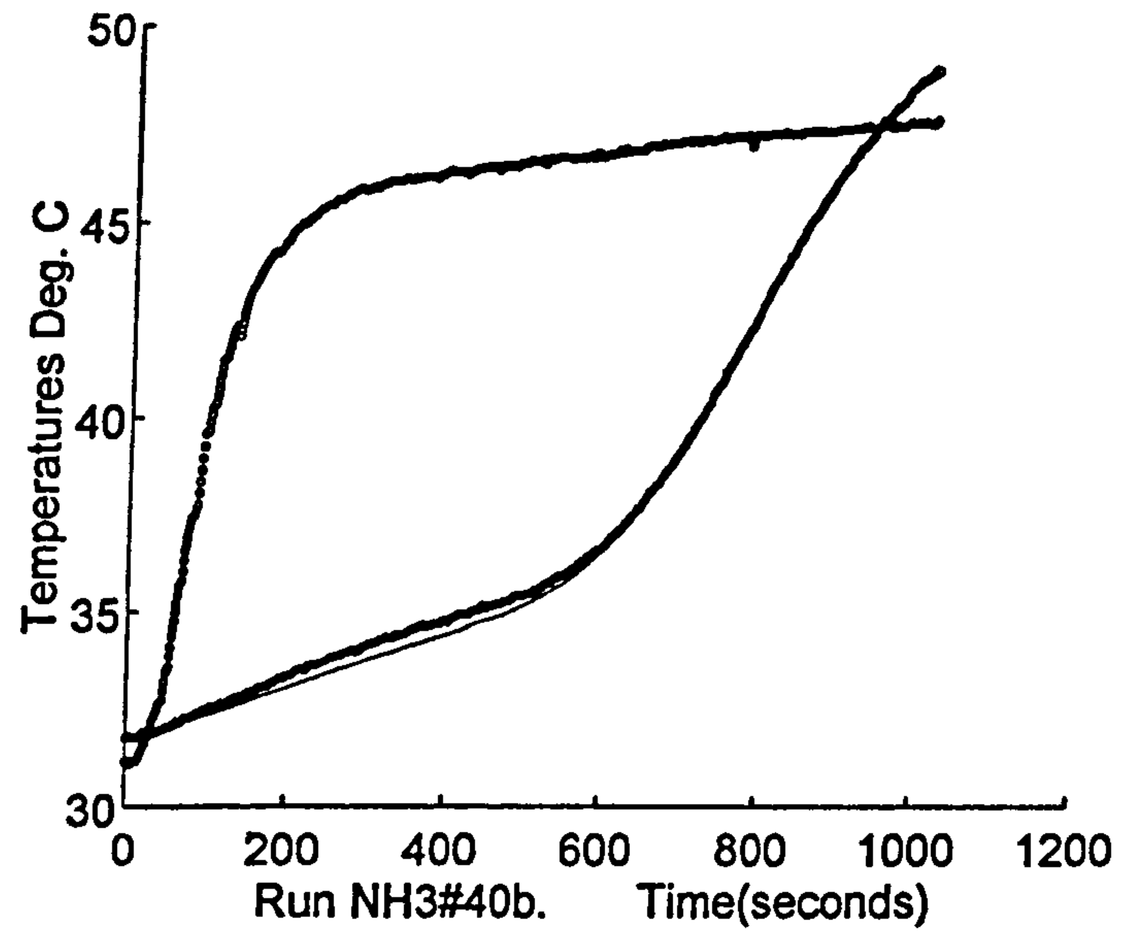
Temperatures Deg. C
50
45
40
35
30
0
200
400
600
800
1000
1200
Run NH3#40b. Time(seconds)

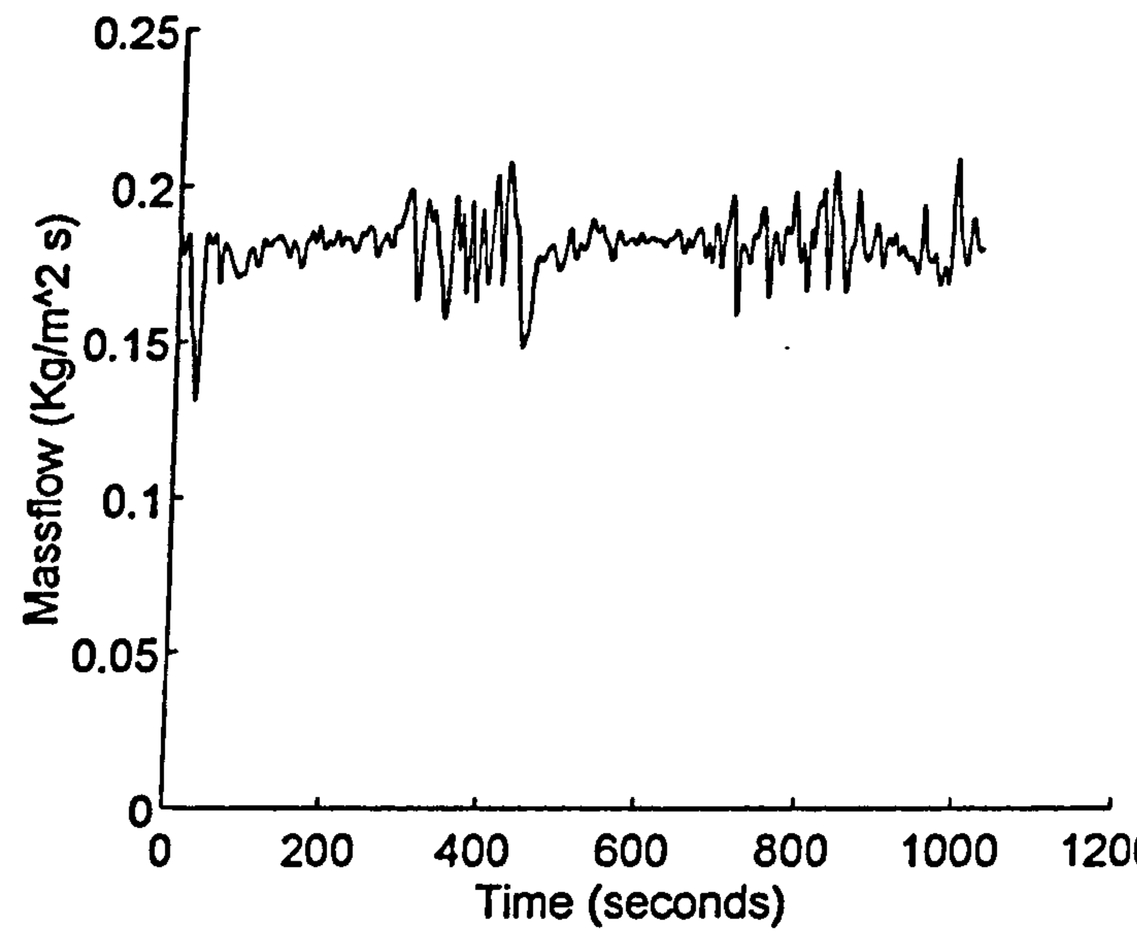
Massflow (Kg/m^2 s)
0.25
0.2
0.15
0.1
0.05
0
0
200
400
600
800
1000
1200
Time (seconds)

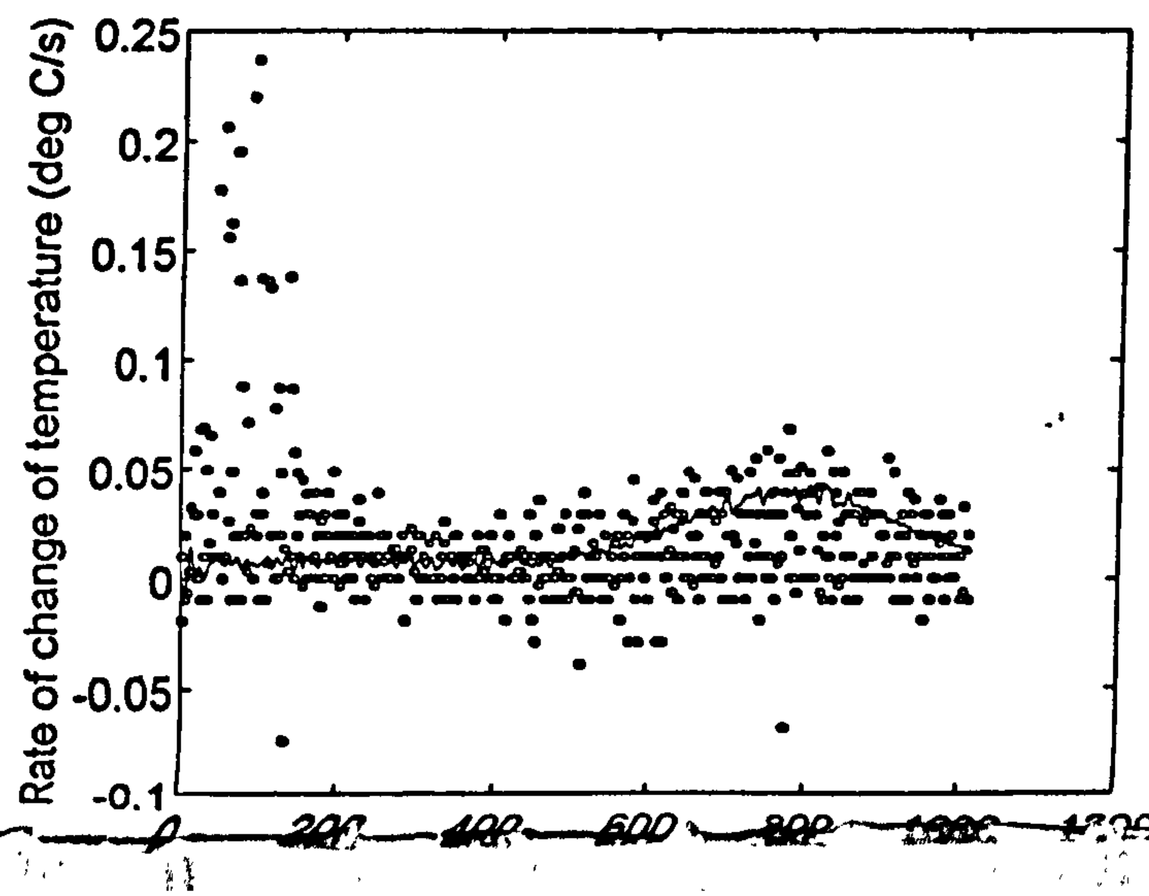
Rate of change of temperature (deg C/s)
0.25
0.2
0.15
0.1
0.05
0
-0.05
-0.1

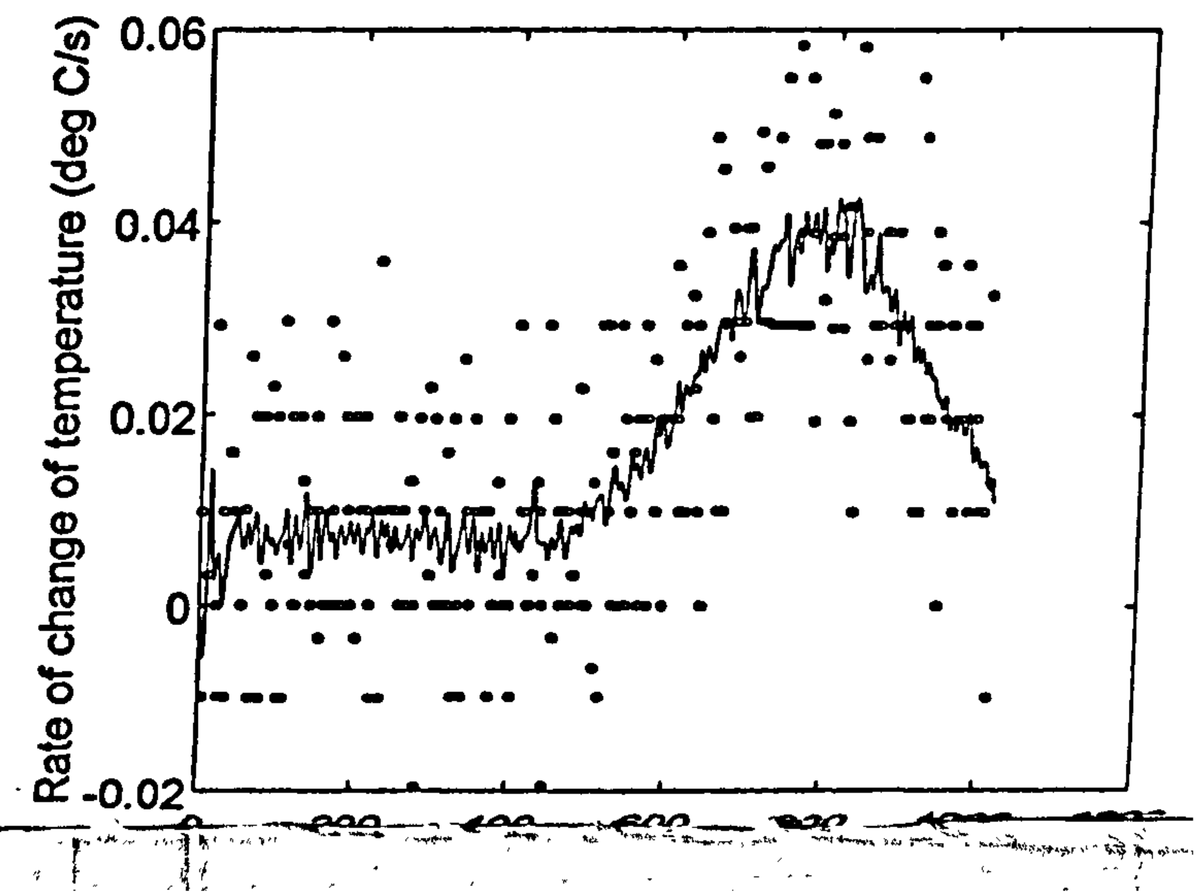
Rate of change of temperature (deg C/s)
0.06
0.04
0.02
0
-0.02

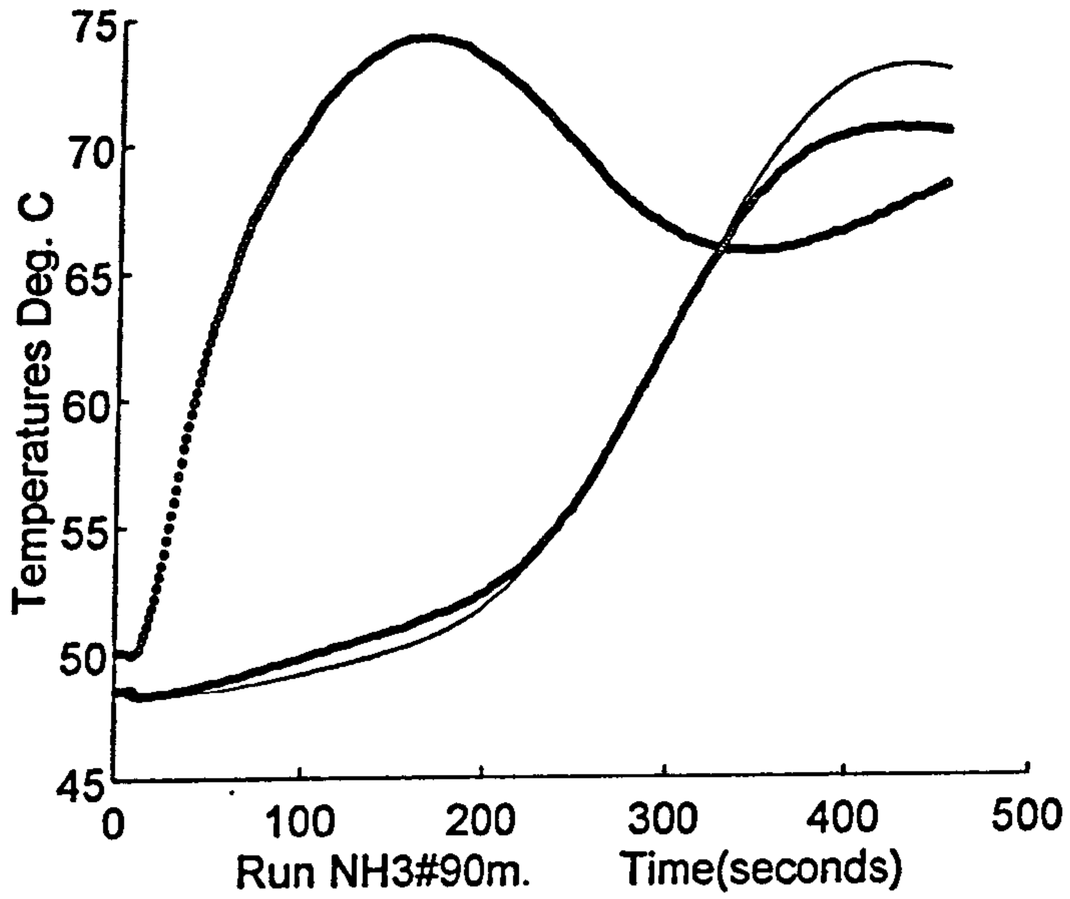
Temperatures Deg. C
75
70
65
60
55
50
45
0
100
200
300
400
500
Run NH3#90m.
Time(seconds)

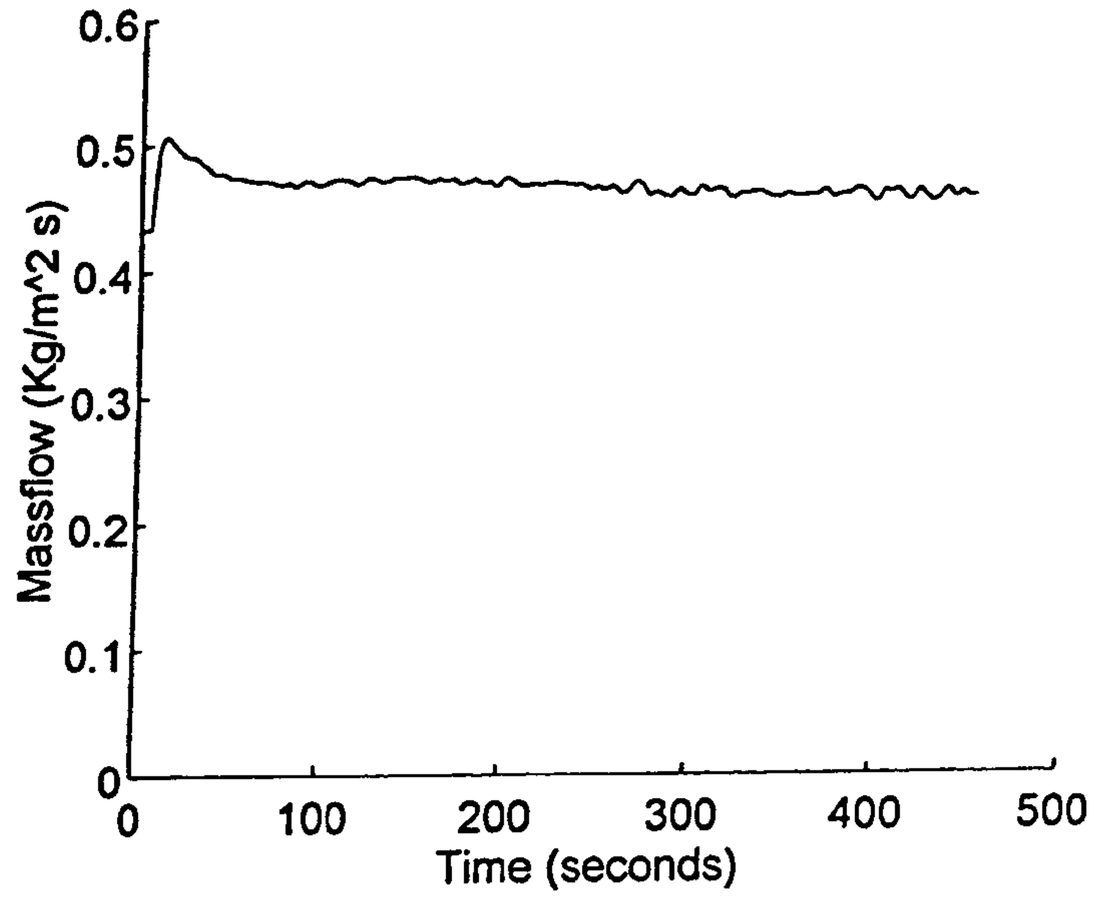
Massflow (Kg/m^2 s)
0.6
0.5
0.4
0.3
0.2
0.1
0
0
100
200
300
400
500
Time (seconds)

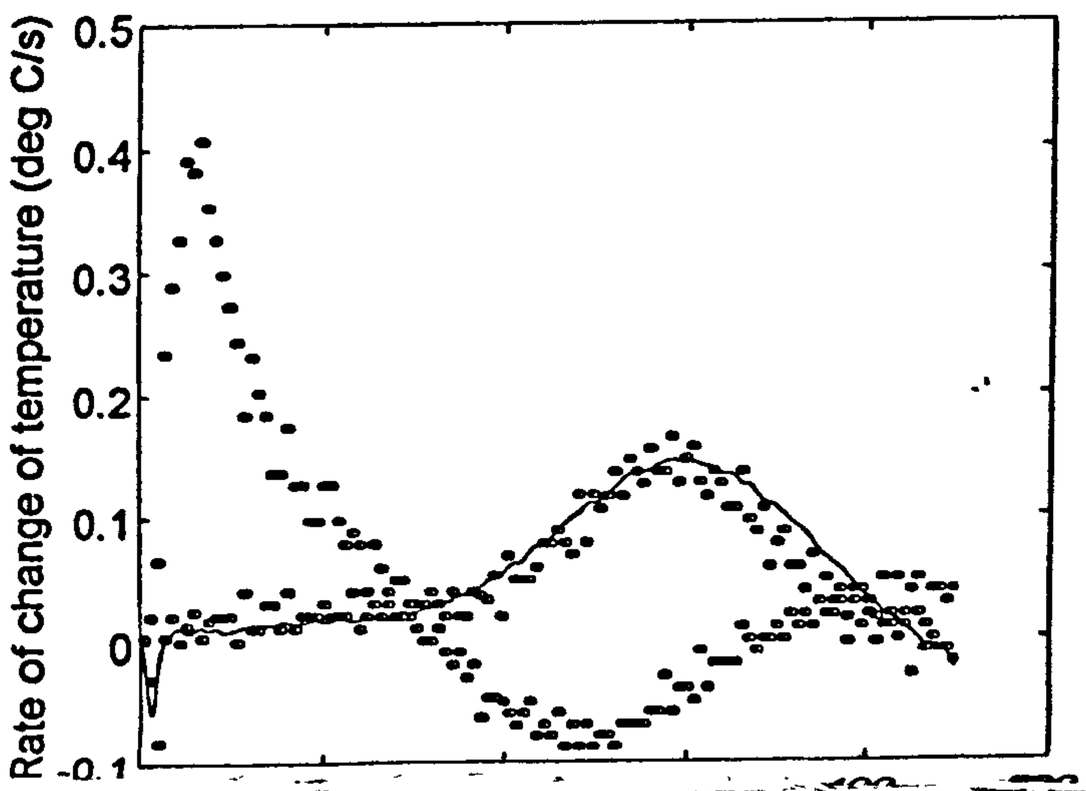
Rate of change of temperature (deg C/s)
0.5
0.4
0.3
0.2
0.1
0
-0.1

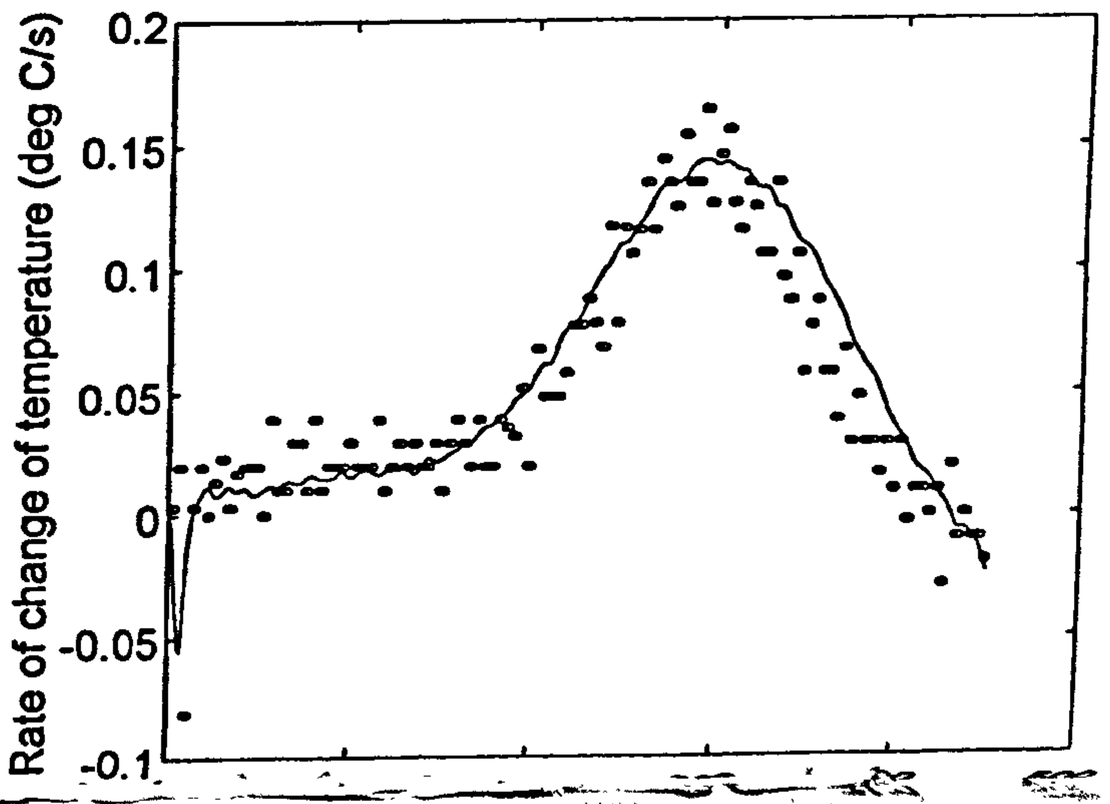
Rate of change of temperature (deg C/s)
0.2
0.15
0.1
0.05
0
-0.05
-0.1

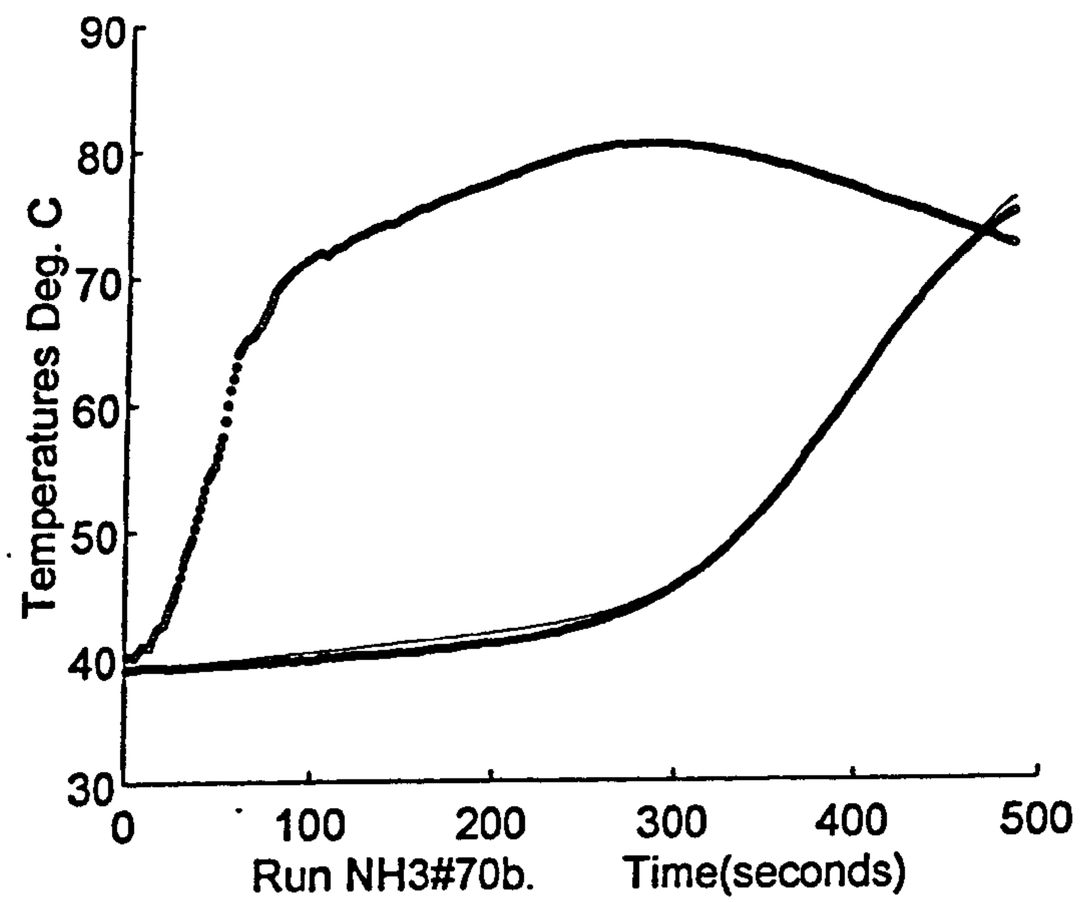
Temperatures Deg. C
90
80
70
60
50
40
30
0
100
200
300
400
500
Run NH3#70b.
Time(seconds)

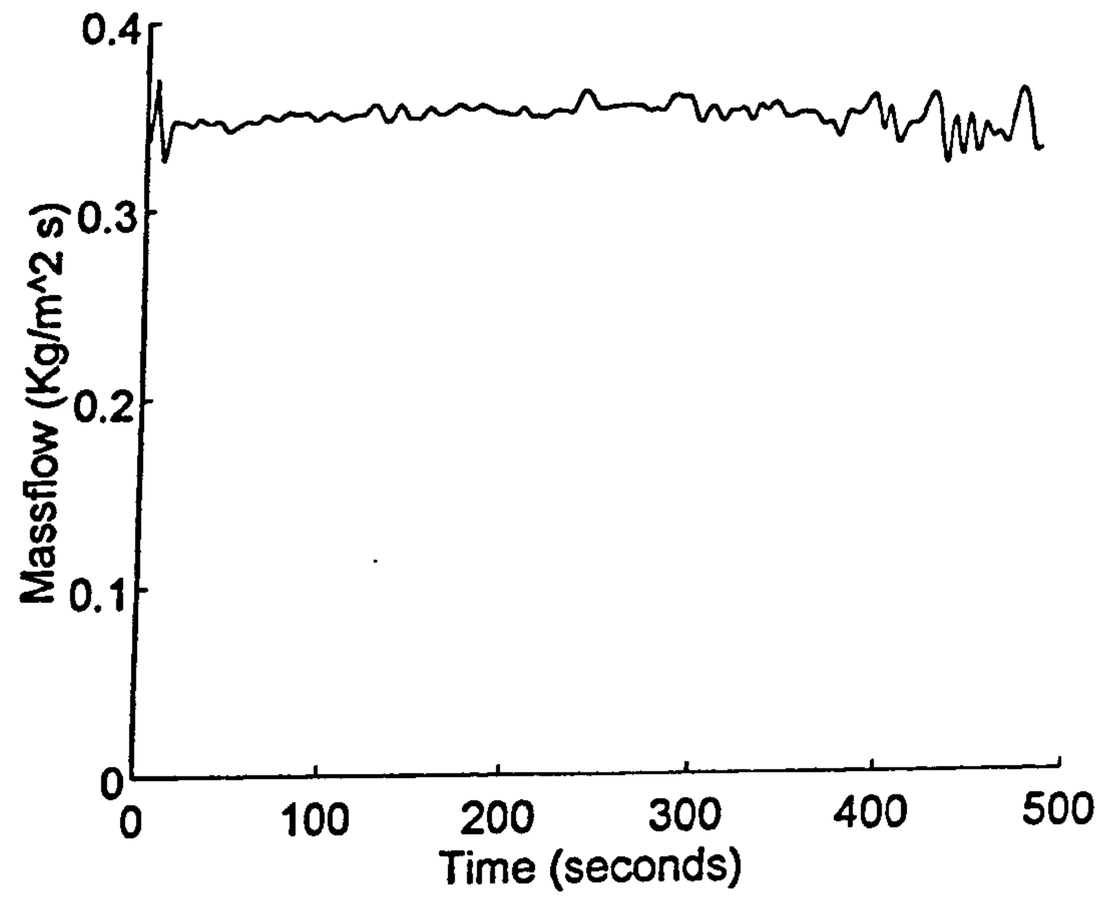
Massflow (Kg/m^2 s)
0.4
0.3
0.2
0.1
0
0
100
200
300
400
500
Time (seconds)

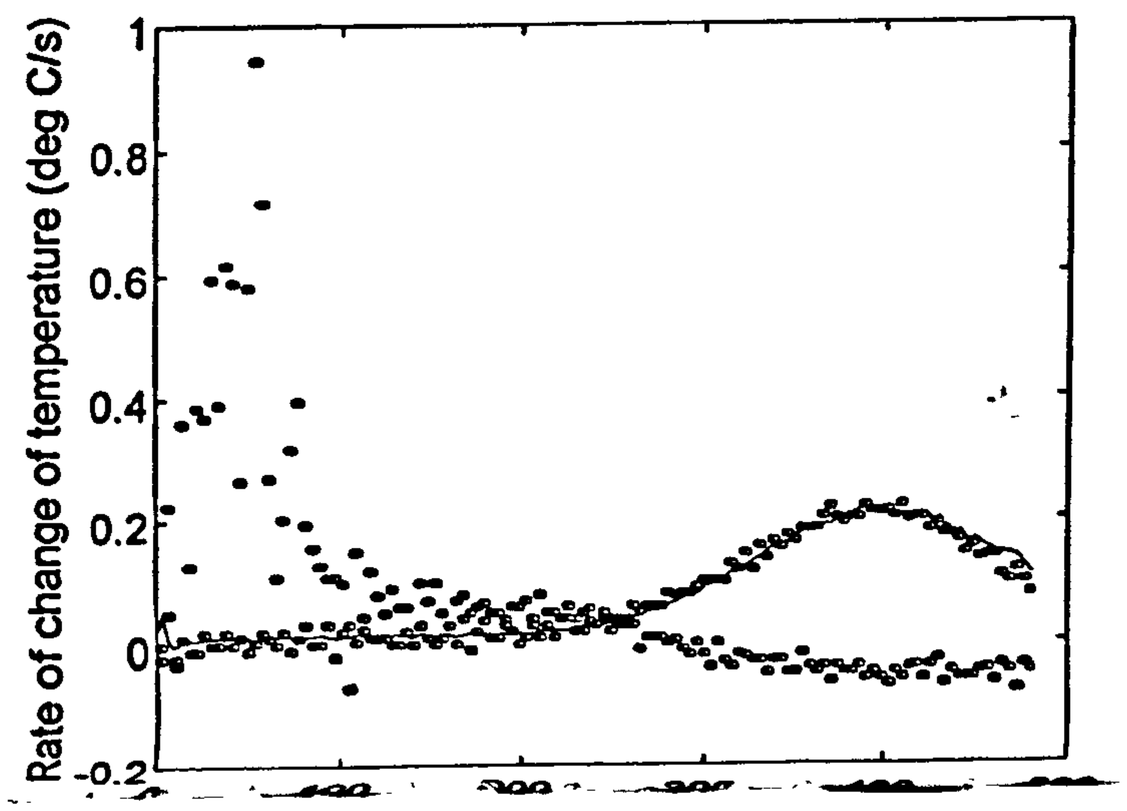
Rate of change of temperature (deg C/s)
1
0.8
0.6
0.4
0.2
0
-0.2

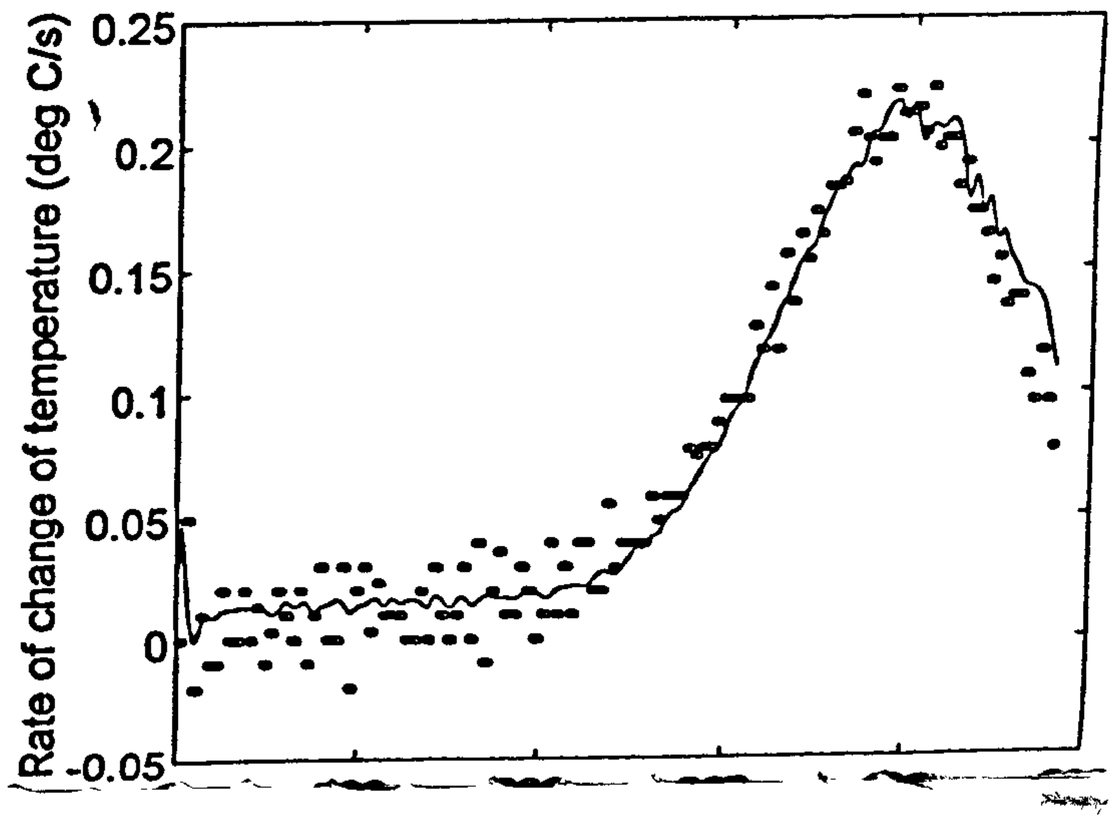
Rate of change of temperature (deg C/s)
0.25
0.2
0.15
0.1
0.05
0
-0.05

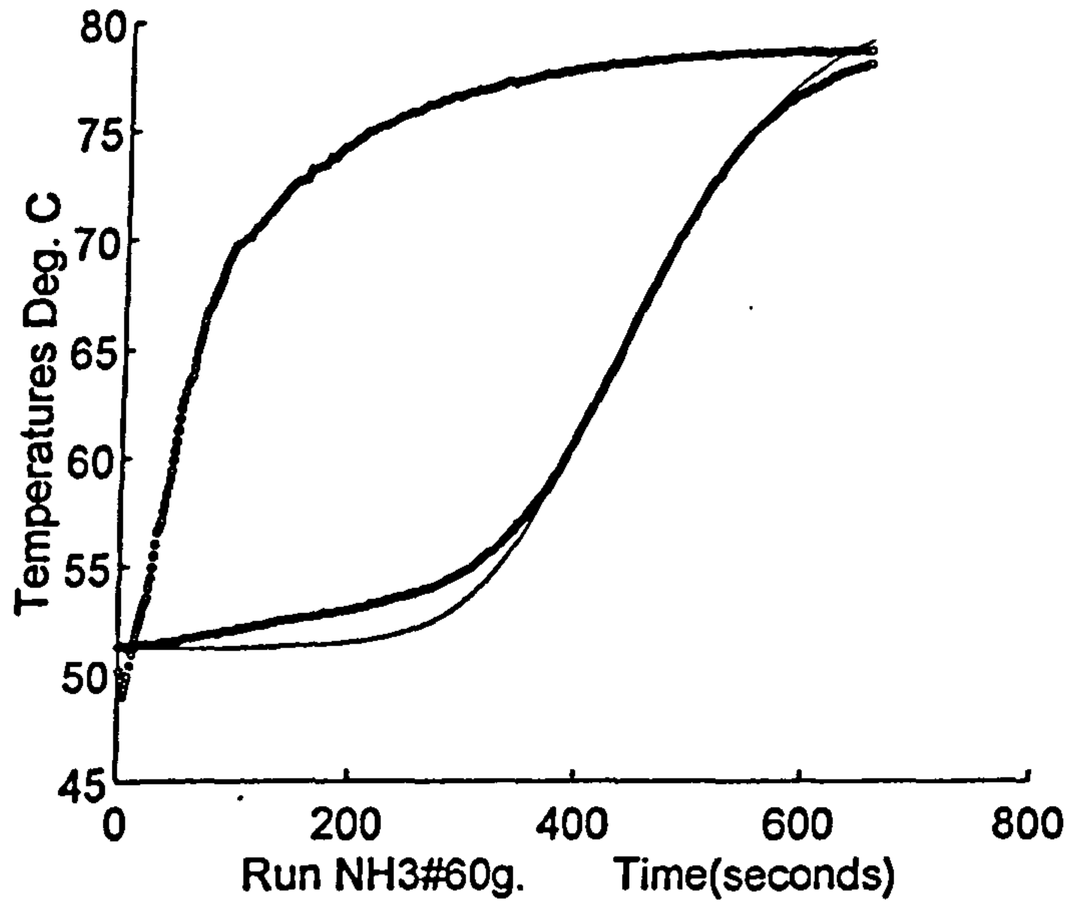
Temperatures Deg. C
80
75
70
65
60
55
50
45
0
200
400
600
800
Run NH3#60g. Time(seconds)

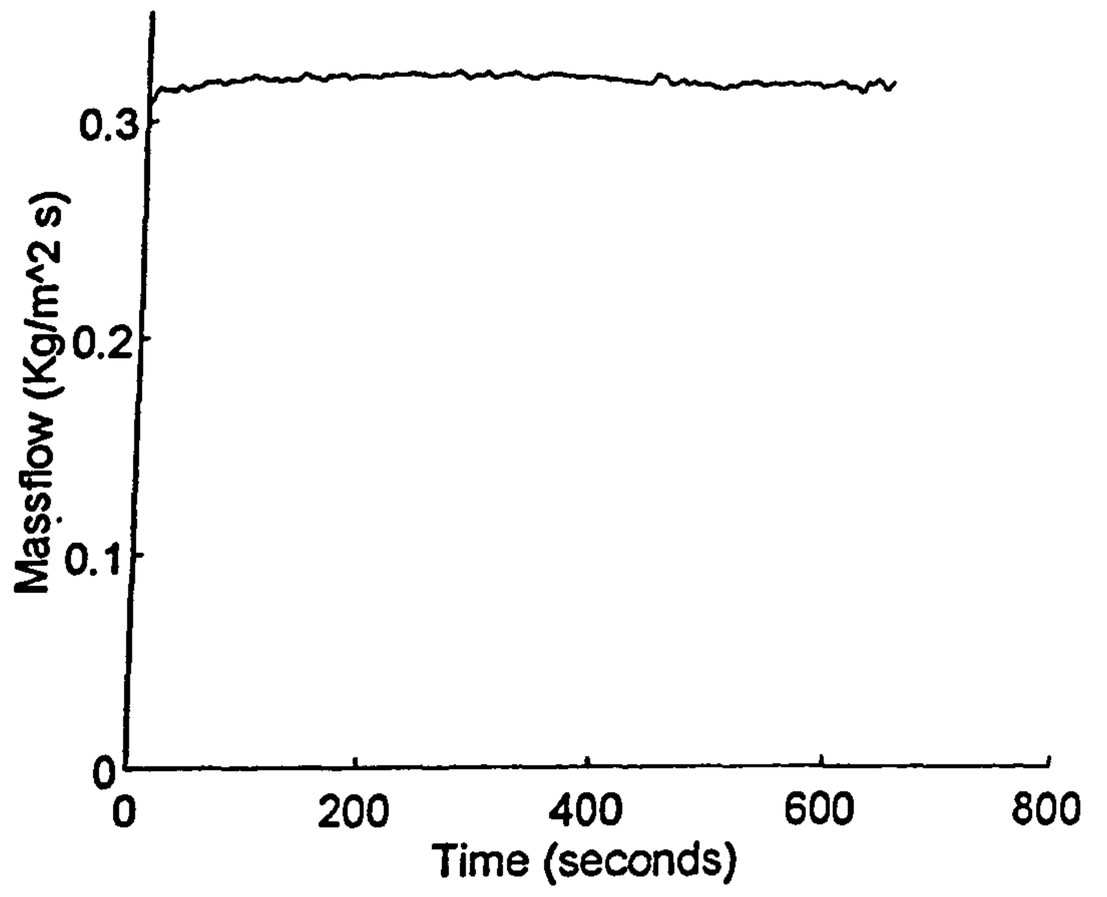
Massflow (Kg/m^2 s)
0.3
0.2
0.1
0
0
200
400
600
800
Time (seconds)

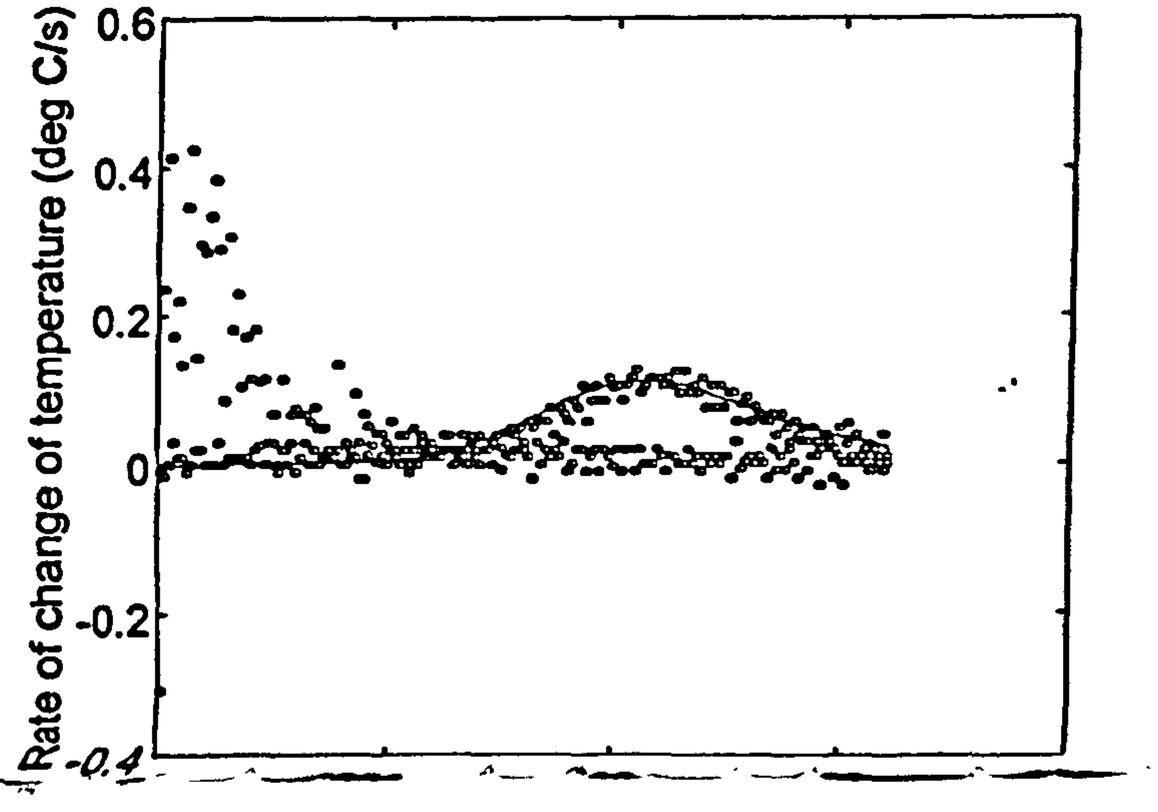
Rate of change of temperature (deg C/s)
0.6
0.4
0.2
0
-0.2
-0.4

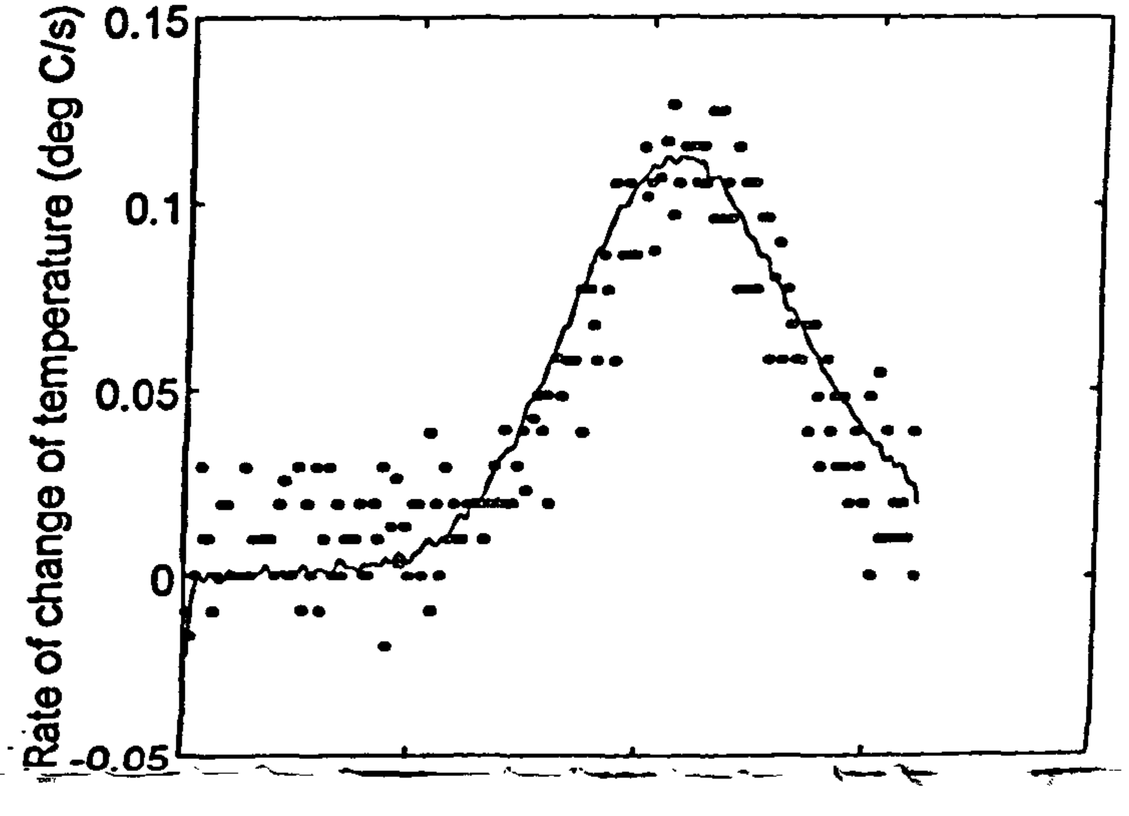
Rate of change of temperature (deg C/s)
0.15
0.1
0.05
0
-0.05

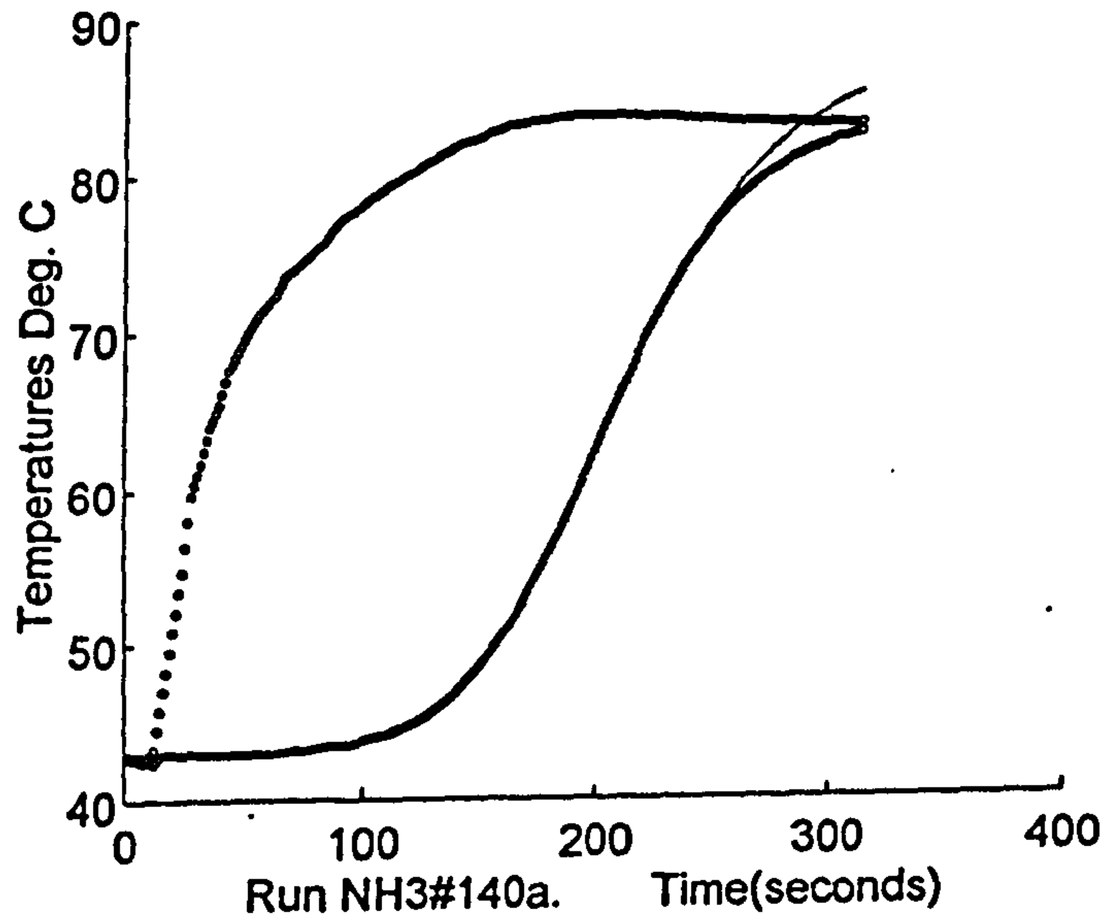
90
80
70
60
50
40
Temperatures Deg. C
0
100
200
300
400
Run NH3#140a.
Time(seconds)

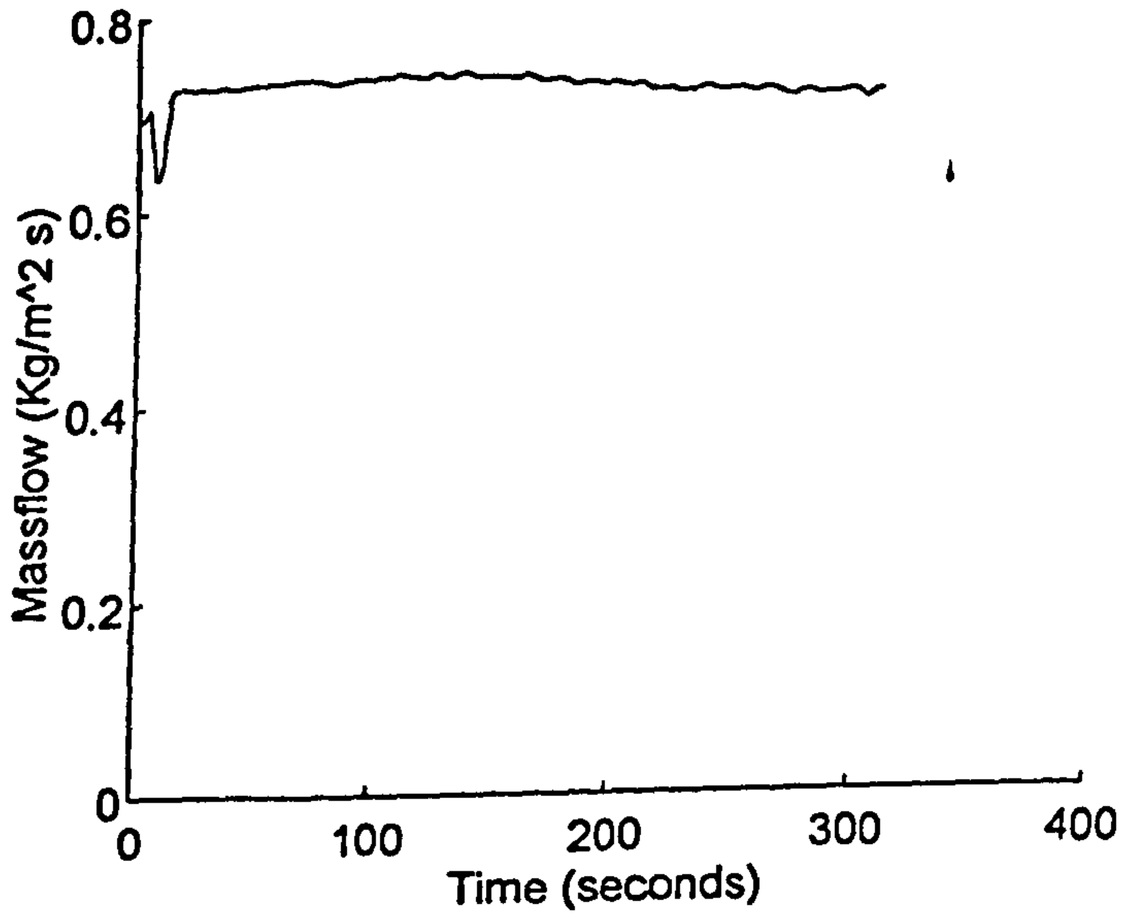
0.8
0.6
0.4
0.2
0
Massflow (Kg/m^2 s)
0
100
200
300
400
Time (seconds)

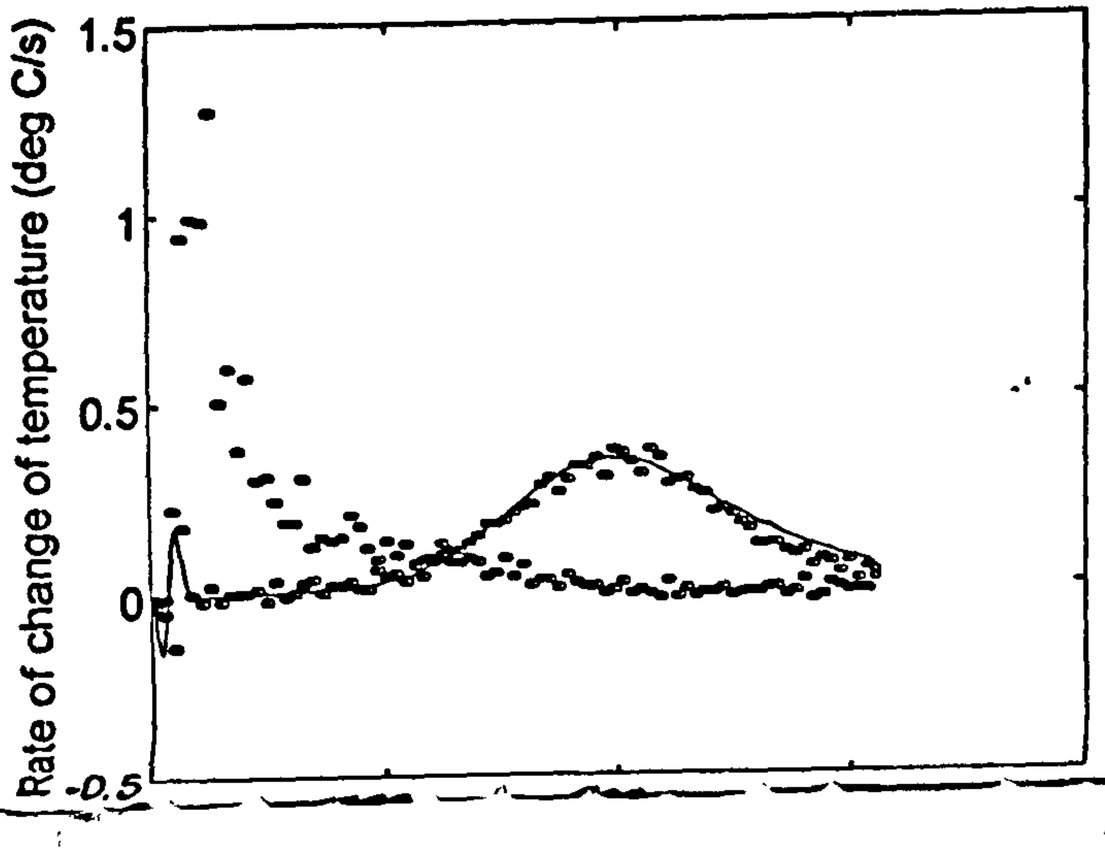
1.5
1
0.5
0
-0.5
Rate of change of temperature (deg C/s)

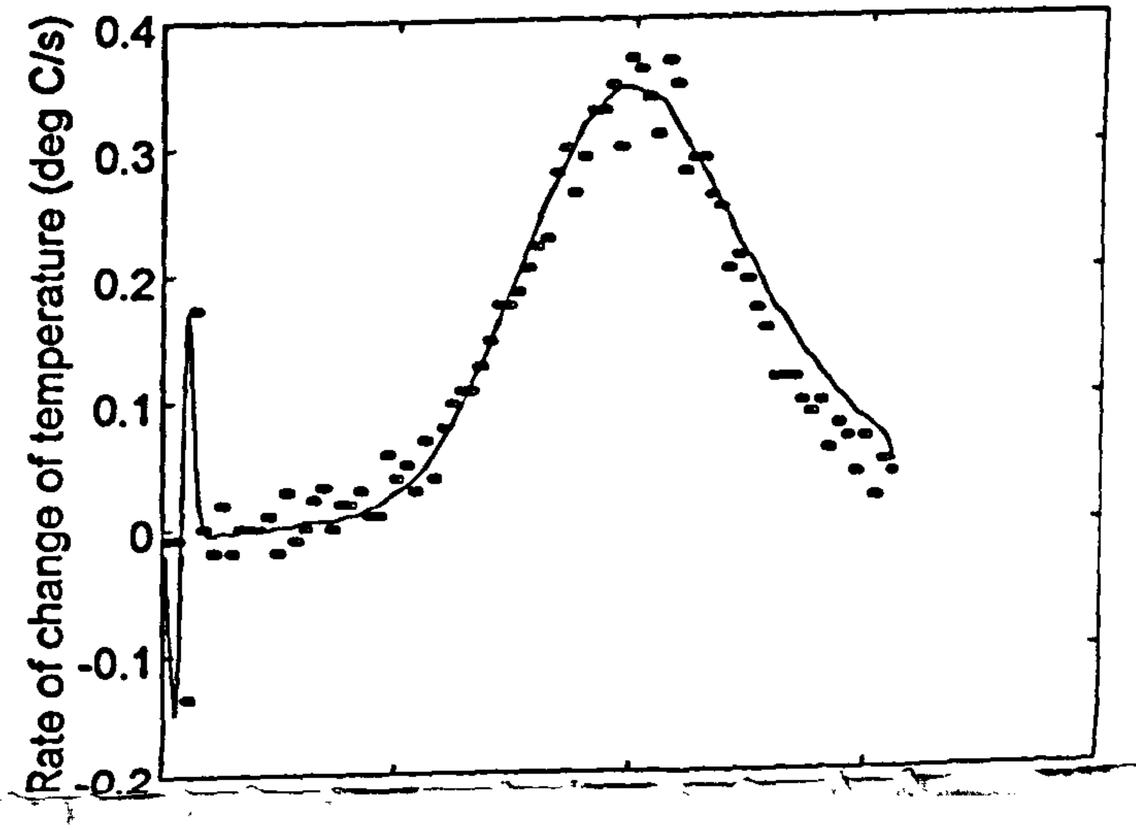
0.4
0.3
0.2
0.1
0
-0.1
-0.2
Rate of change of temperature (deg C/s)

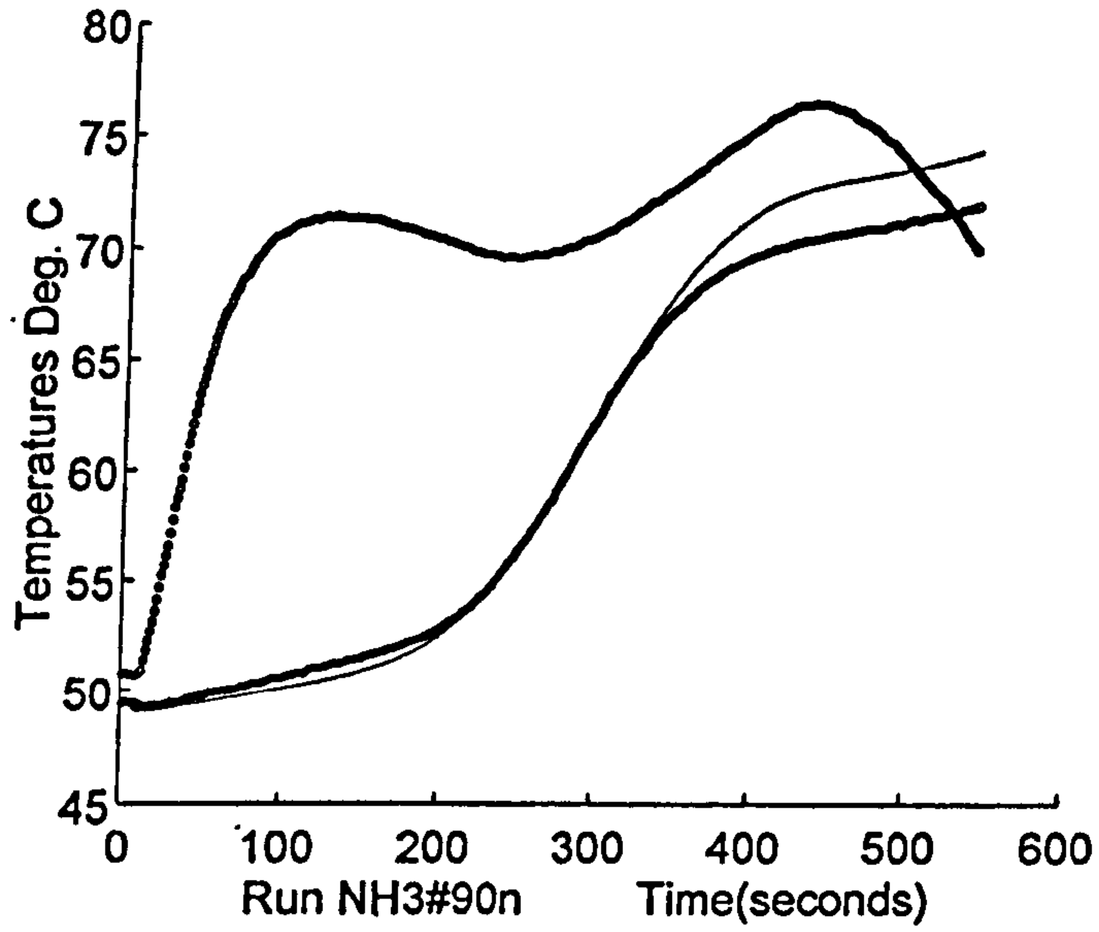
Temperatures Deg. C
80
75
70
65
60
55
50
45
0
100
200
300
400
500
600
Run NH3#90n
Time(seconds)

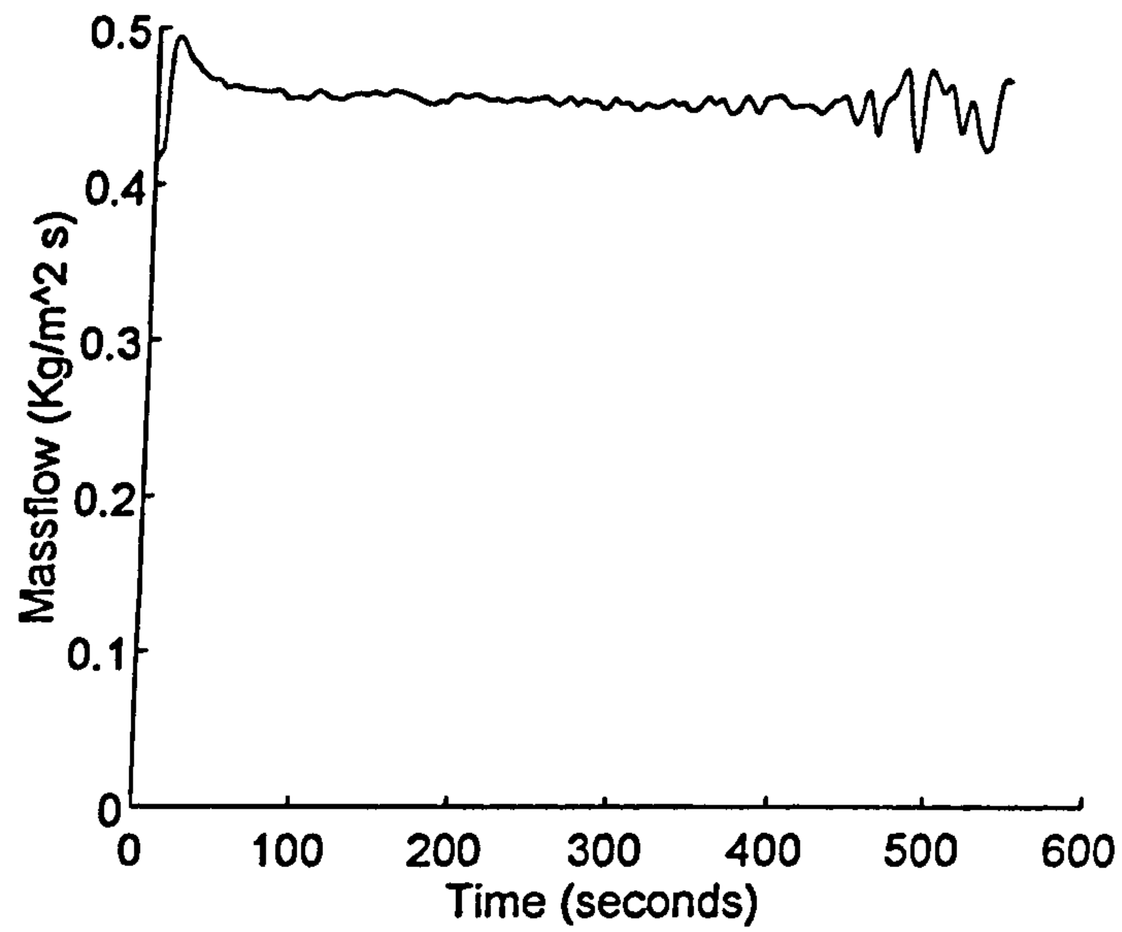
Massflow (Kg/m^2 s)
0.5
0.4
0.3
0.2
0.1
0
0
100
200
300
400
500
600
Time (seconds)

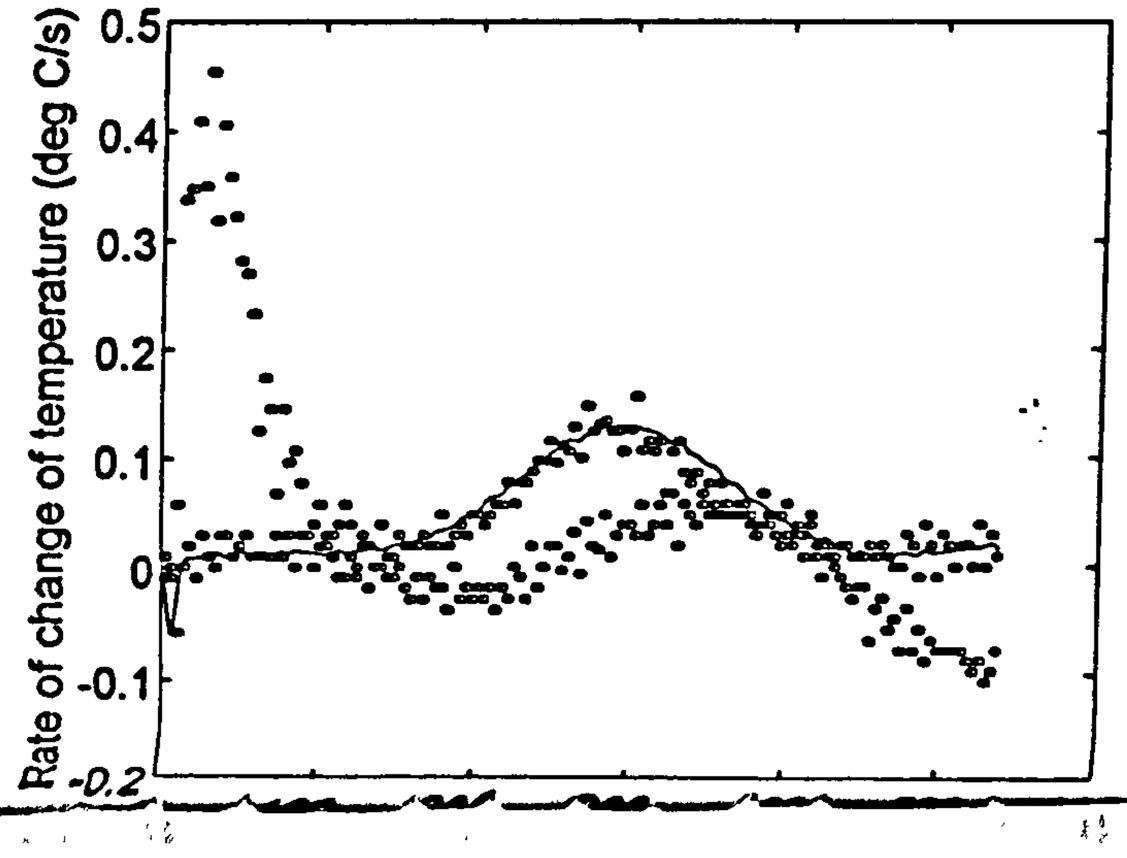
Rate of change of temperature (deg C/s)
0.5
0.4
0.3
0.2
0.1
0
-0.1
-0.2

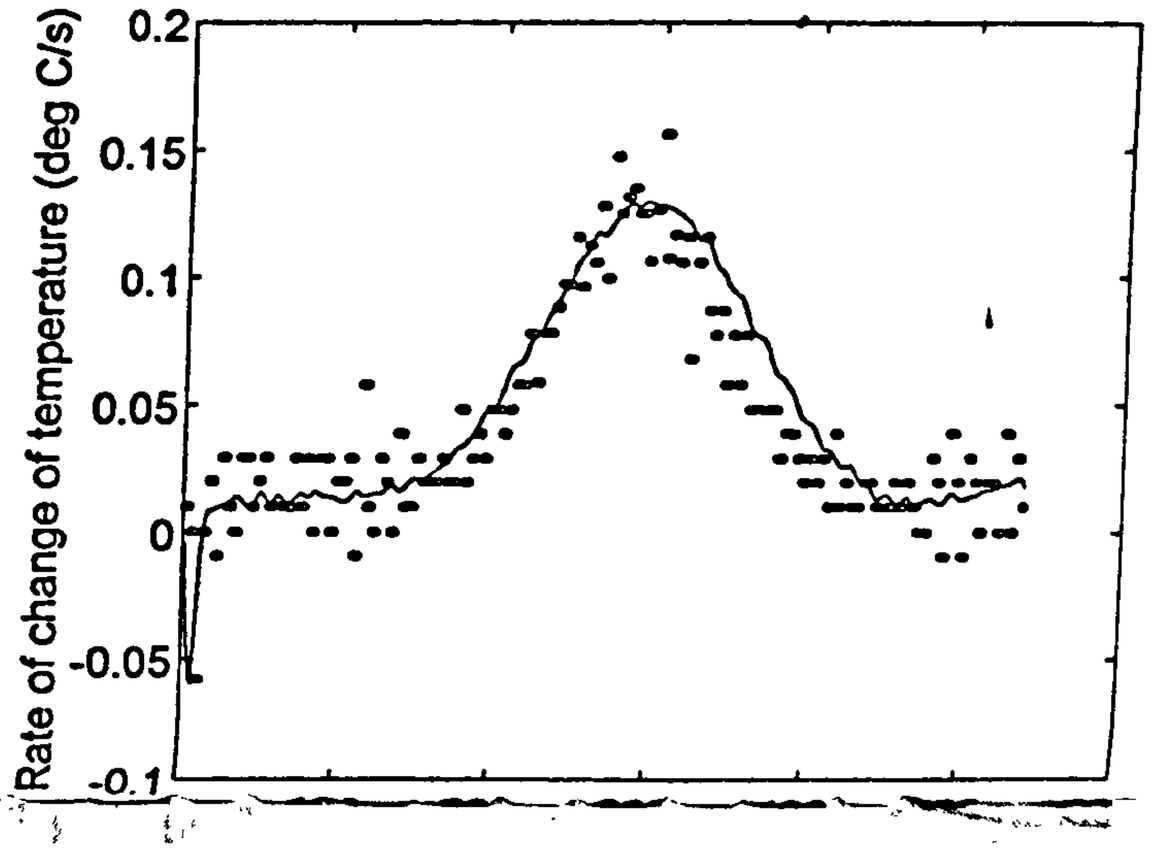
Rate of change of temperature (deg C/s)
0.2
0.15
0.1
0.05
0
-0.05
-0.1

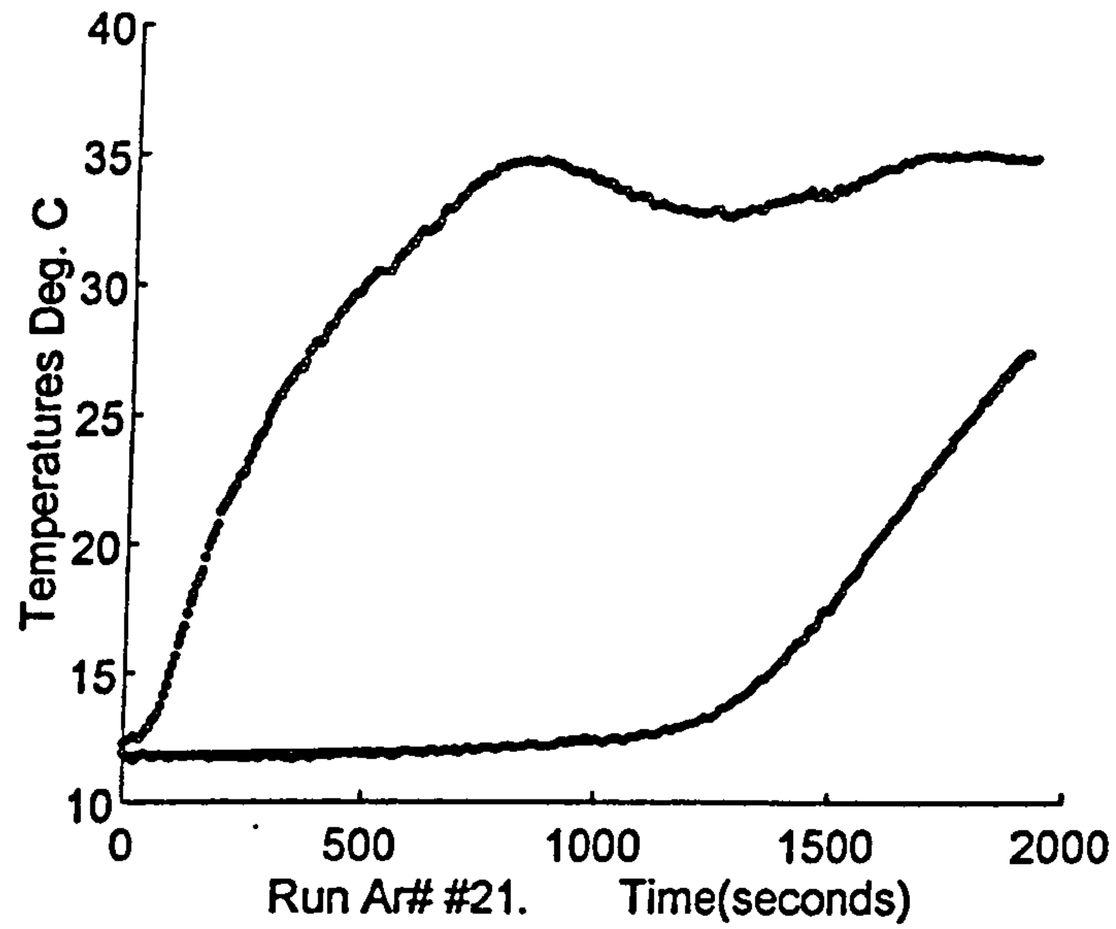
Temperatures Deg. C
40
35
30
25
20
15
10
0
500
1000
1500
2000
Run Ar# #21. Time(seconds)

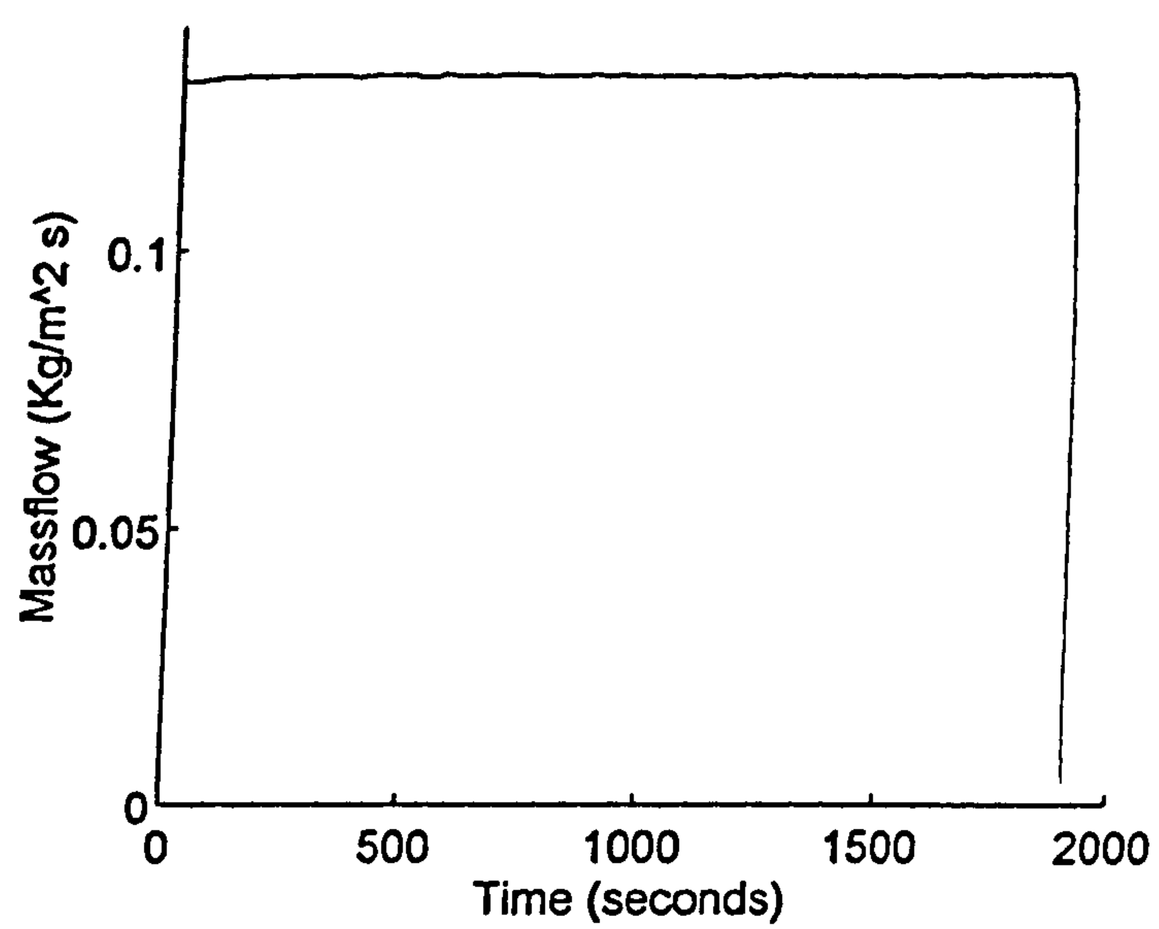
Massflow (Kg/m^2 s)
0.1
0.05
0
0
500
1000
1500
2000
Time (seconds)

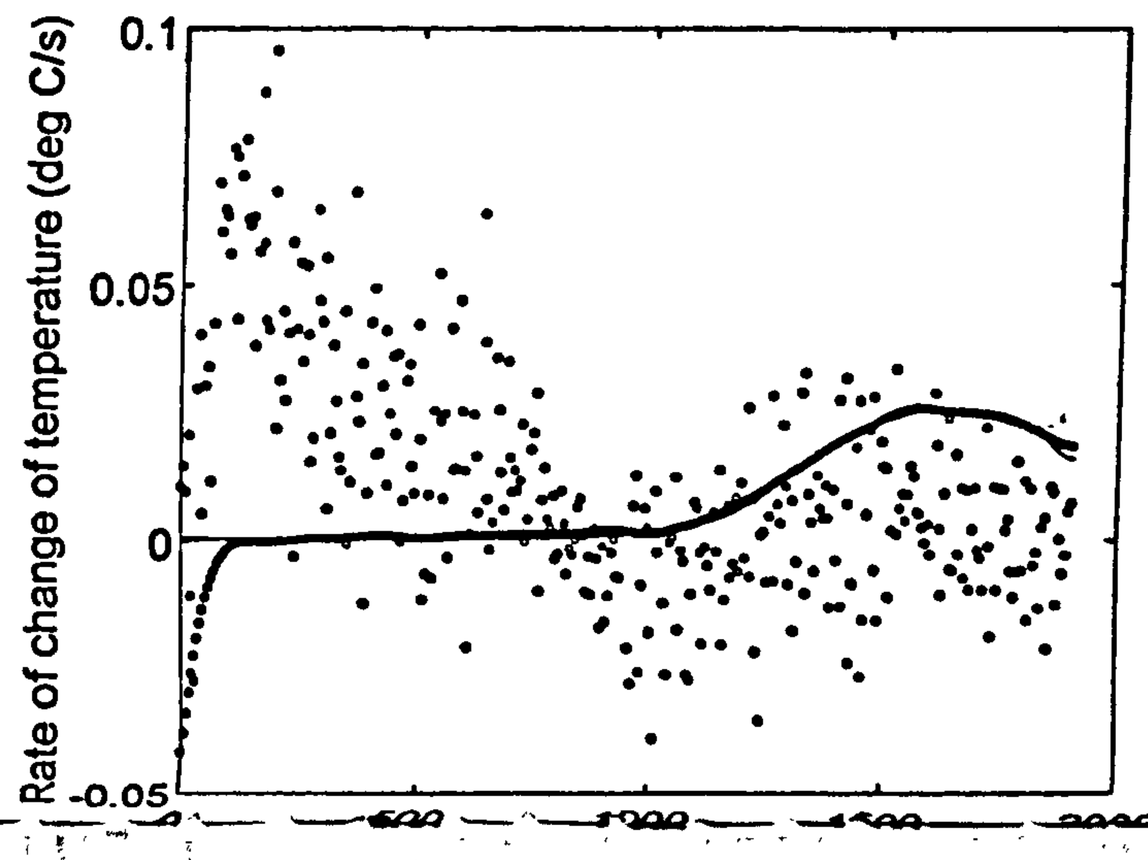
Rate of change of temperature (deg C/s)
0.1
0.05
0
-0.05

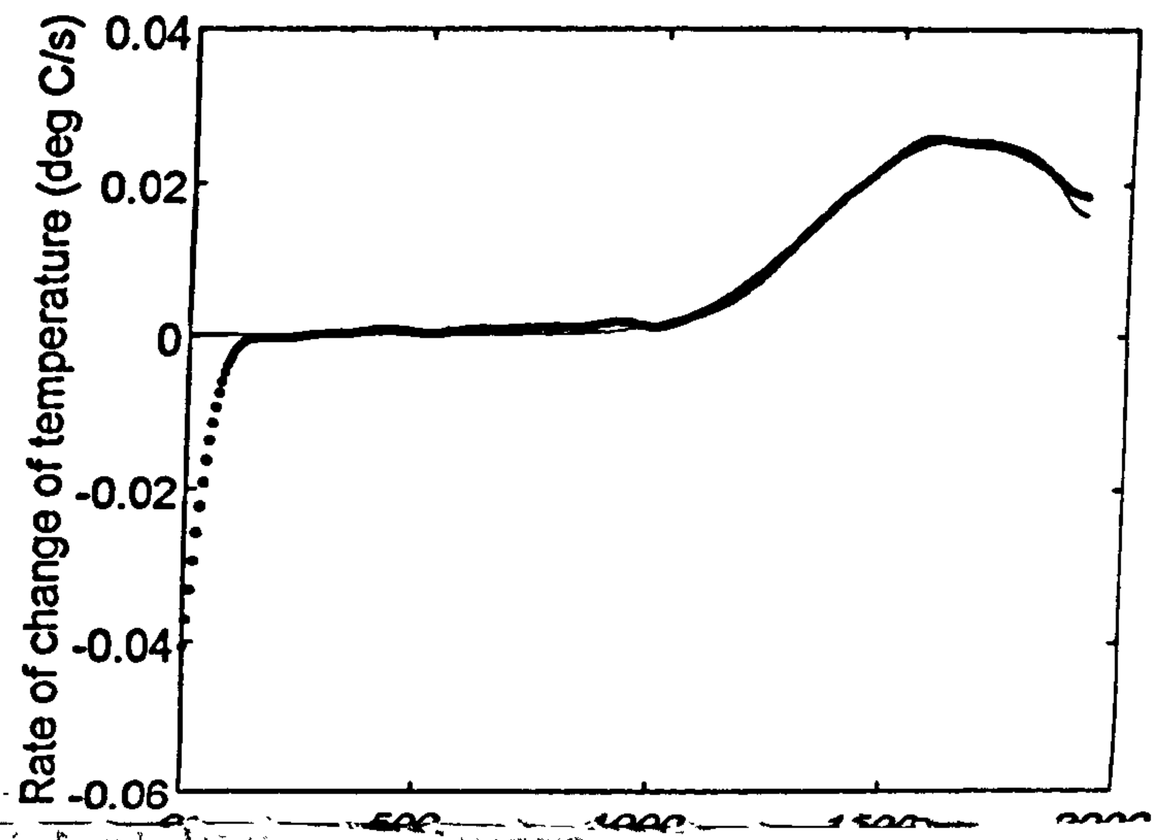
Rate of change of temperature (deg C/s)
0.04
0.02
0
-0.02
-0.04
-0.06

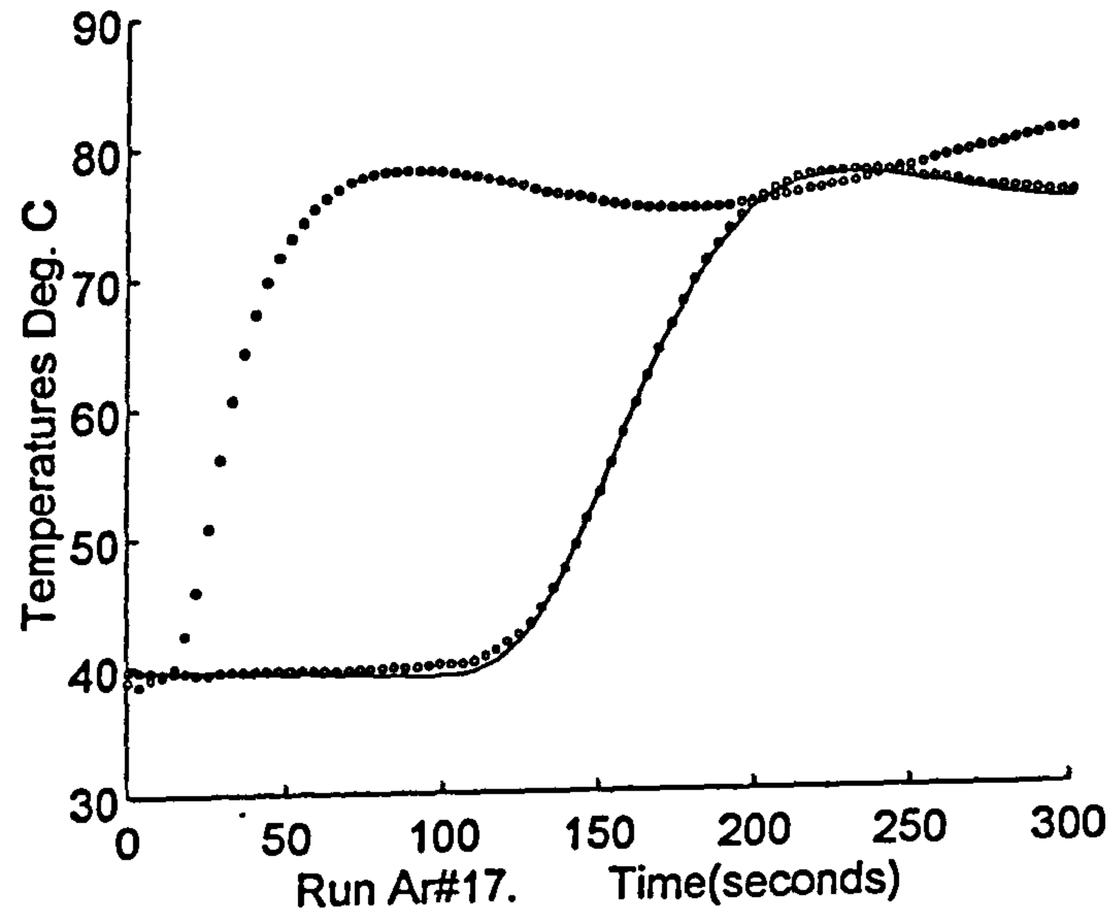
Temperatures Deg. C
90
80
70
60
50
40
30
0
50
100
150
200
250
300
Run Ar#17.
Time(seconds)

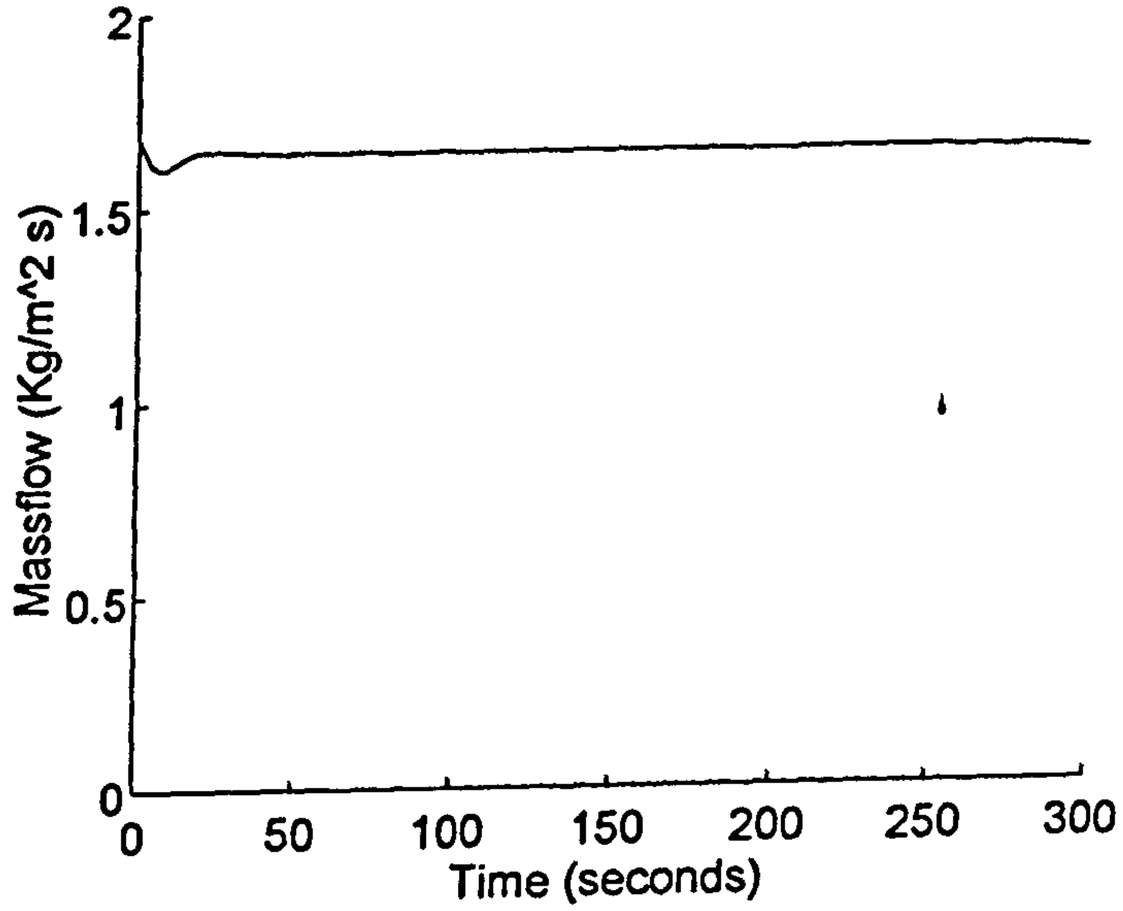
Massflow (Kg/m^2 s)
2
1.5
1
0.5
0
0
50
100
150
200
250
300
Time (seconds)

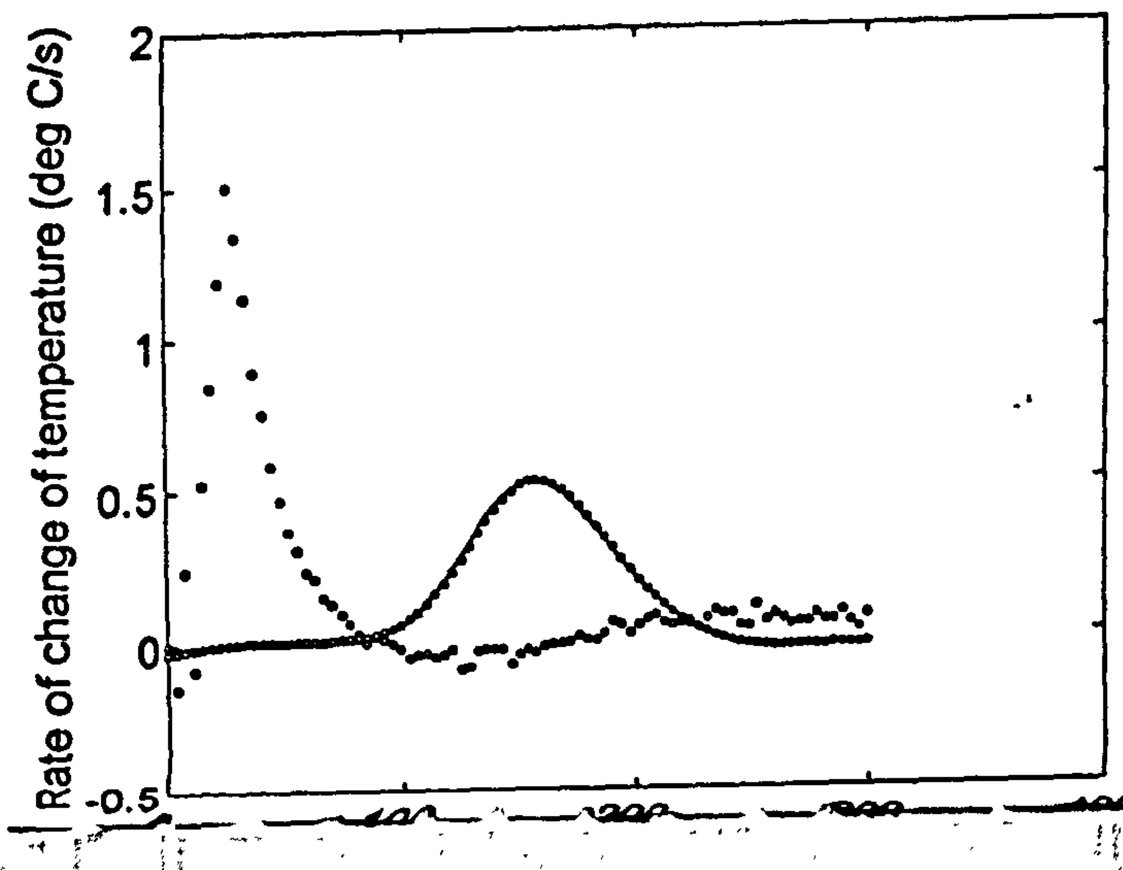
Rate of change of temperature (deg C/s)
2
1.5
1
0.5
0
-0.5

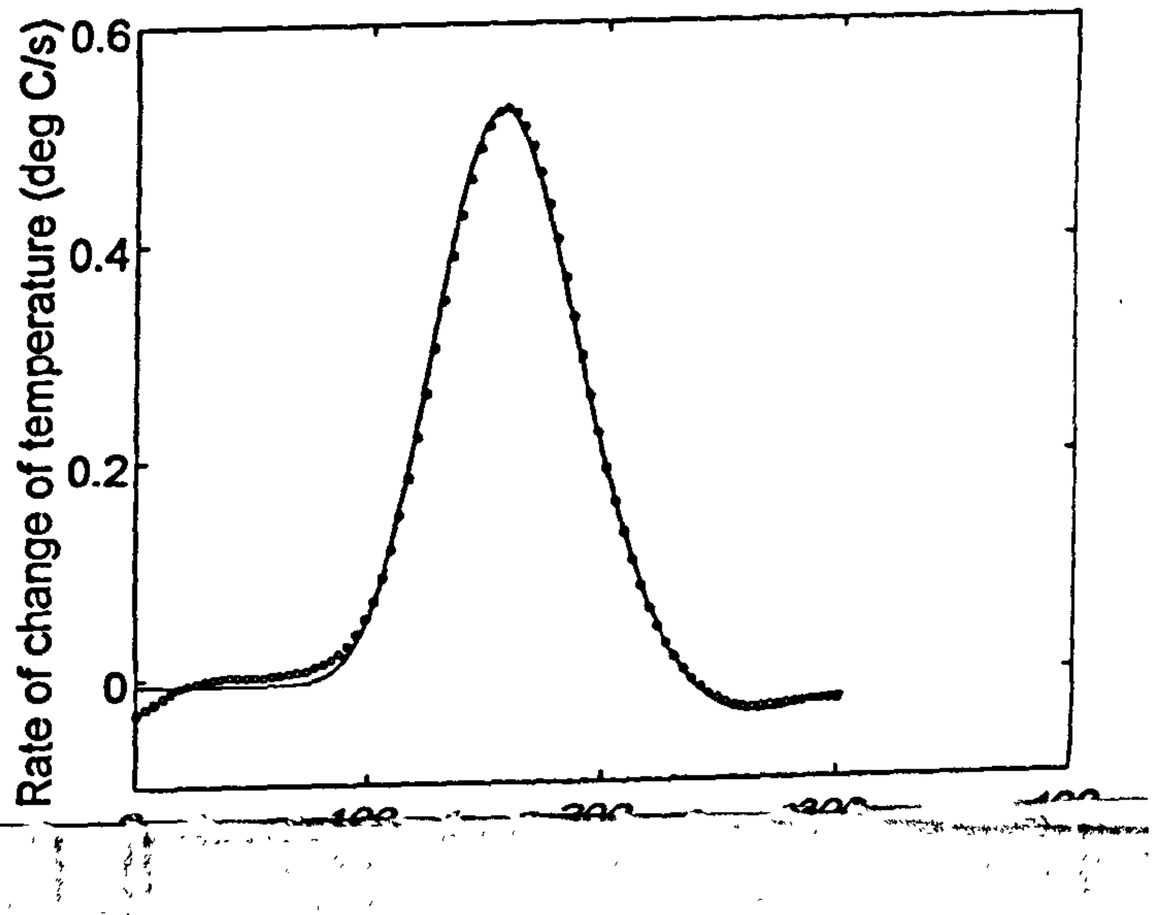
Rate of change of temperature (deg C/s)
0.6
0.4
0.2
0

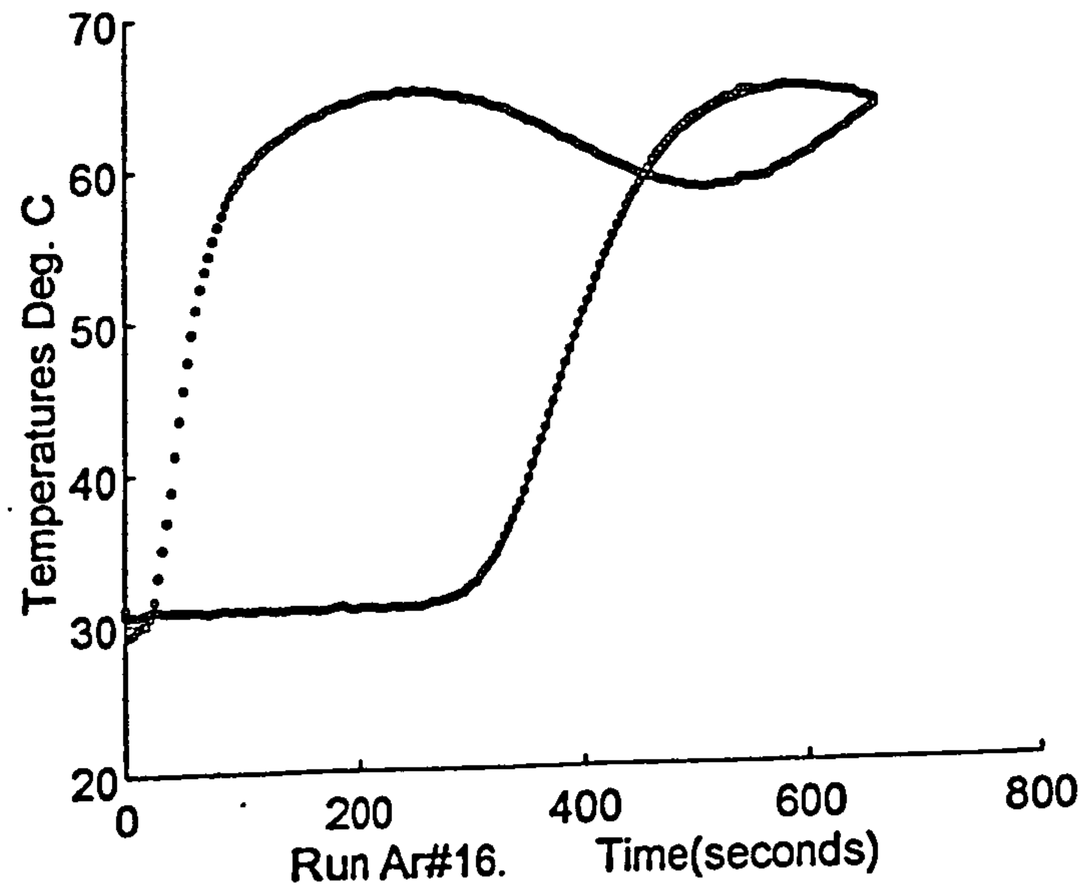
Temperatures Deg. C
70
60
50
40
30
20
0
200
400
600
800
Run Ar#16.
Time(seconds)

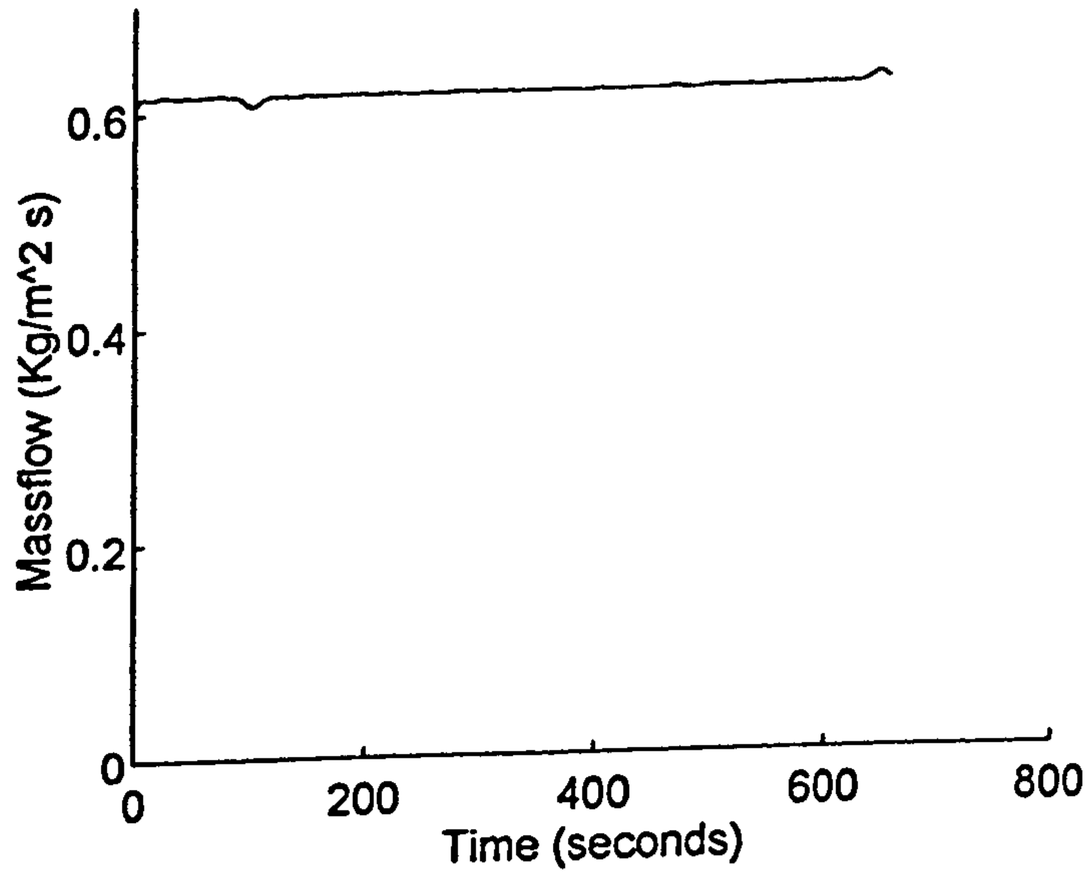
Massflow (Kg/m^2 s)
0.6
0.4
0.2
0
0
200
400
600
800
Time (seconds)

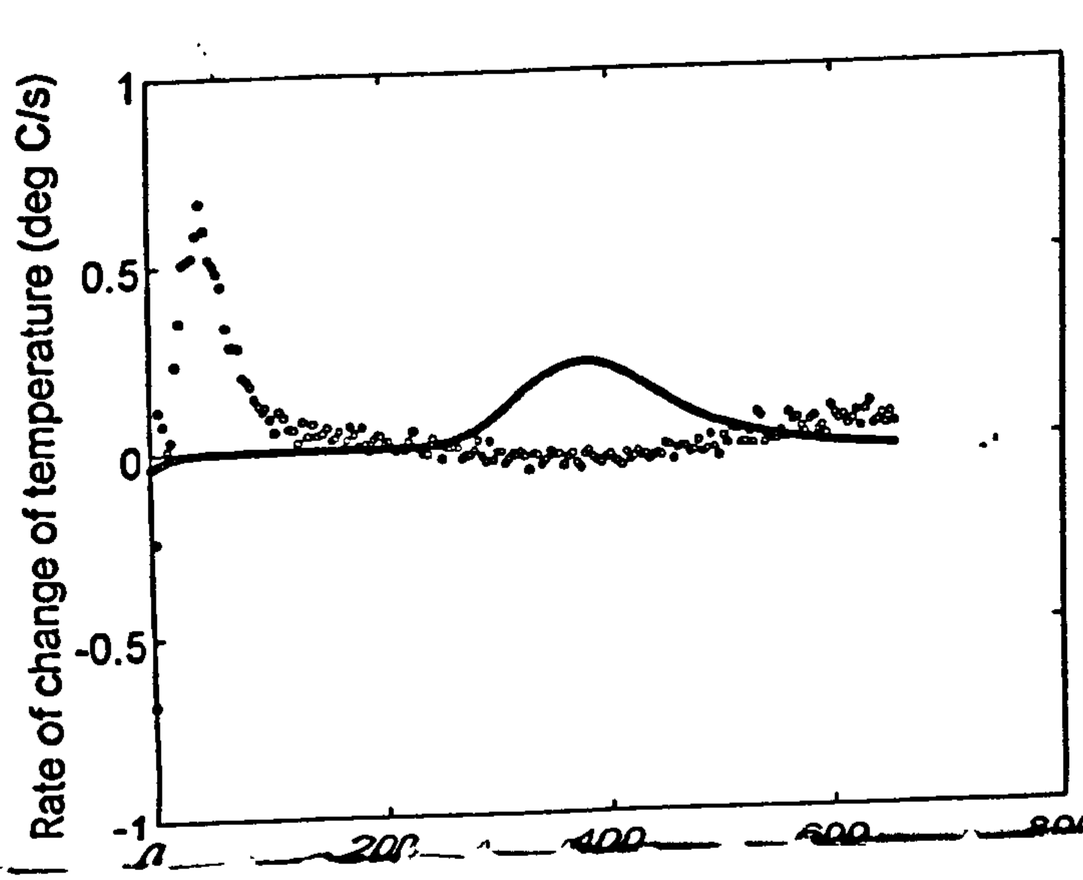
Rate of change of temperature (deg C/s)
1
0.5
0
-0.5
-1
0
200
400
600
800

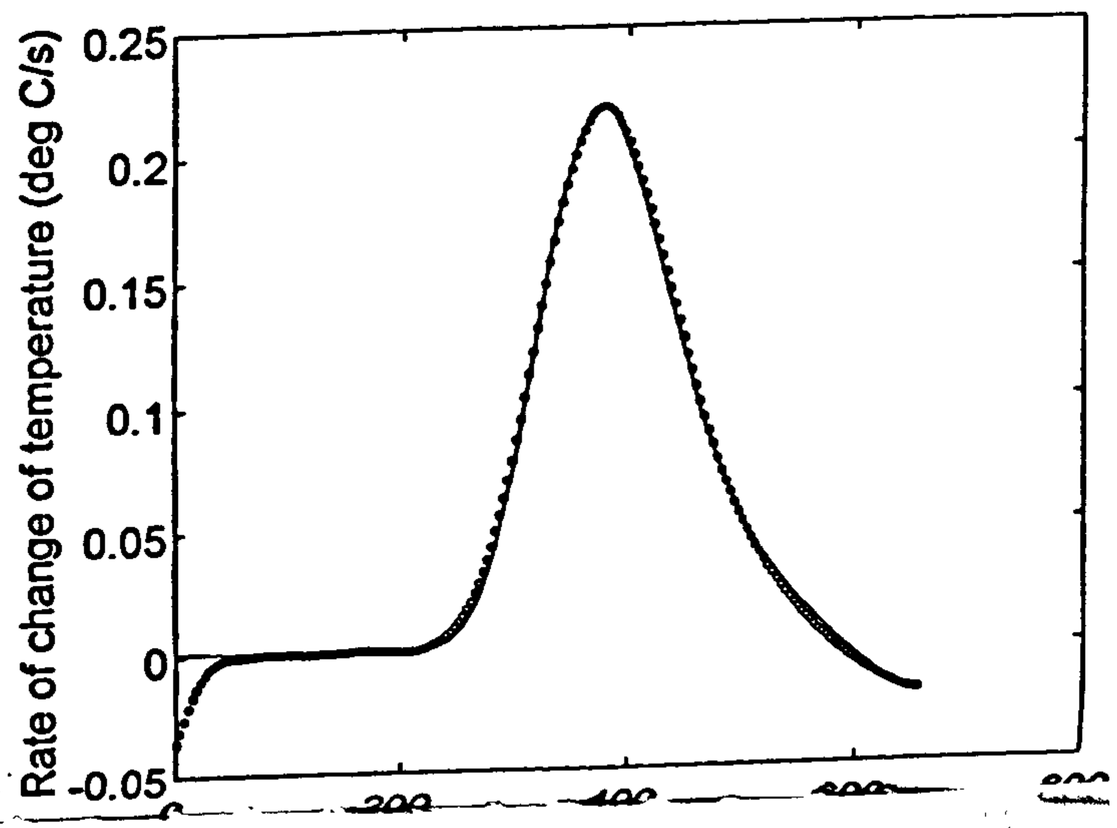
Rate of change of temperature (deg C/s)
0.25
0.2
0.15
0.1
0.05
0
-0.05

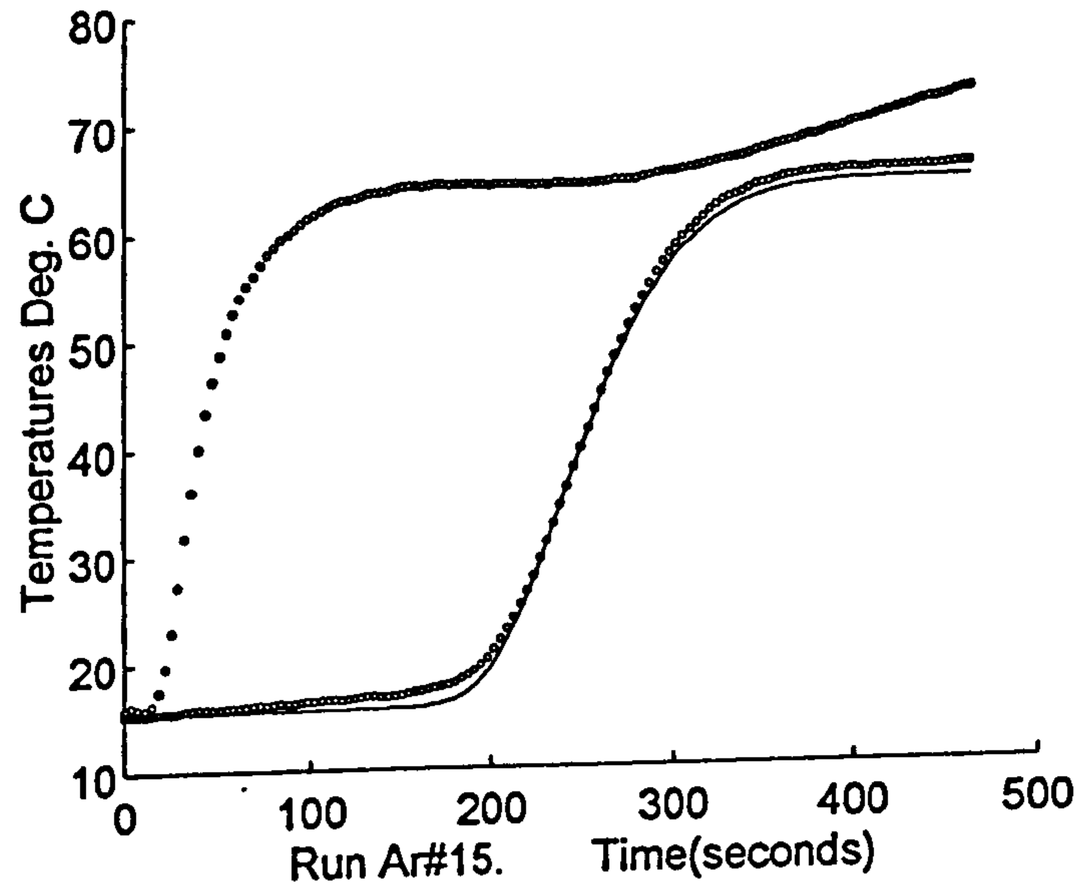
Temperatures Deg. C
80
70
60
50
40
30
20
10
0
100
200
300
400
500
Run Ar#15.
Time(seconds)

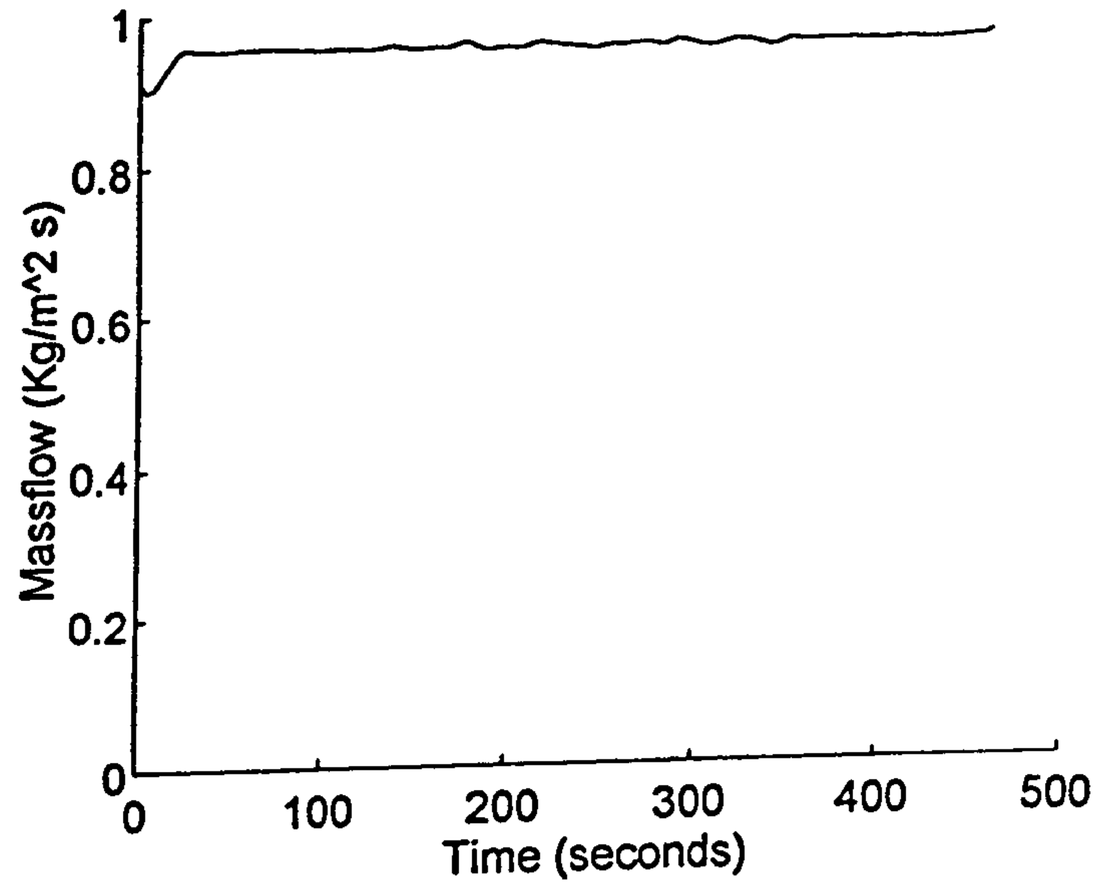
Massflow (Kg/m^2 s)
1
0.8
0.6
0.4
0.2
0
0
100
200
300
400
500
Time (seconds)

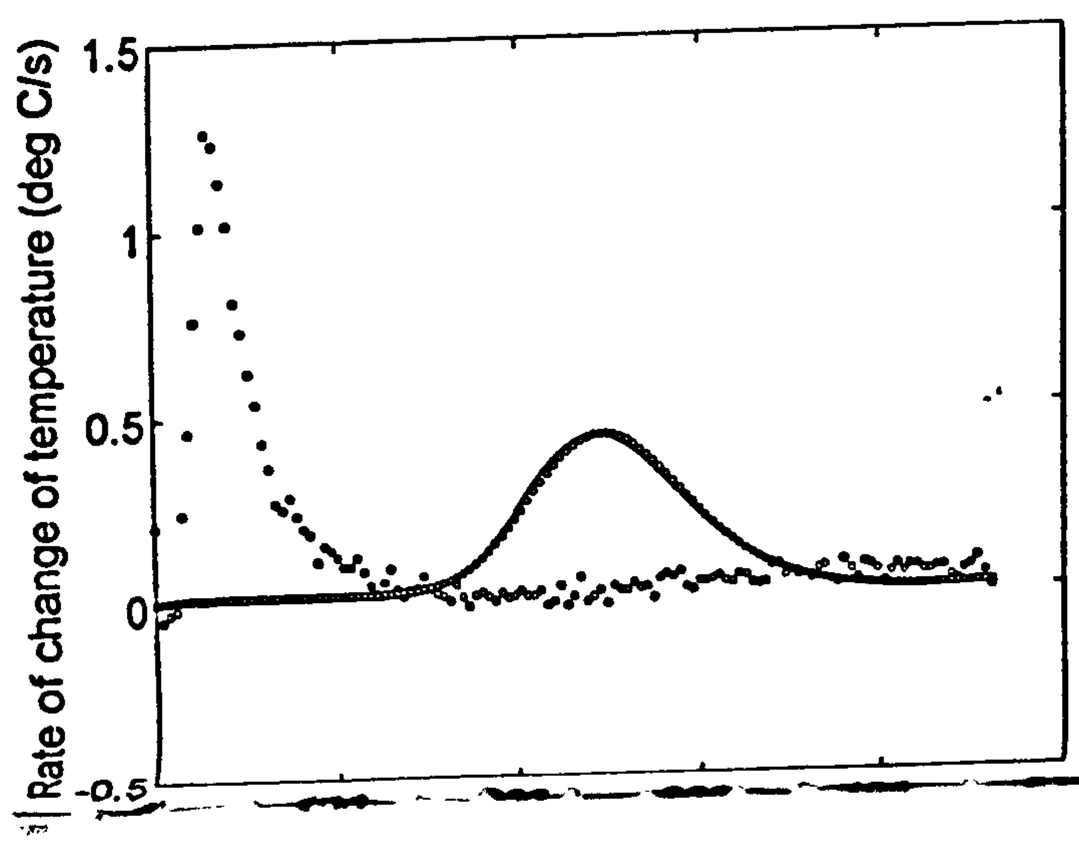
Rate of change of temperature (deg C/s)
1.5
1
0.5
0
-0.5

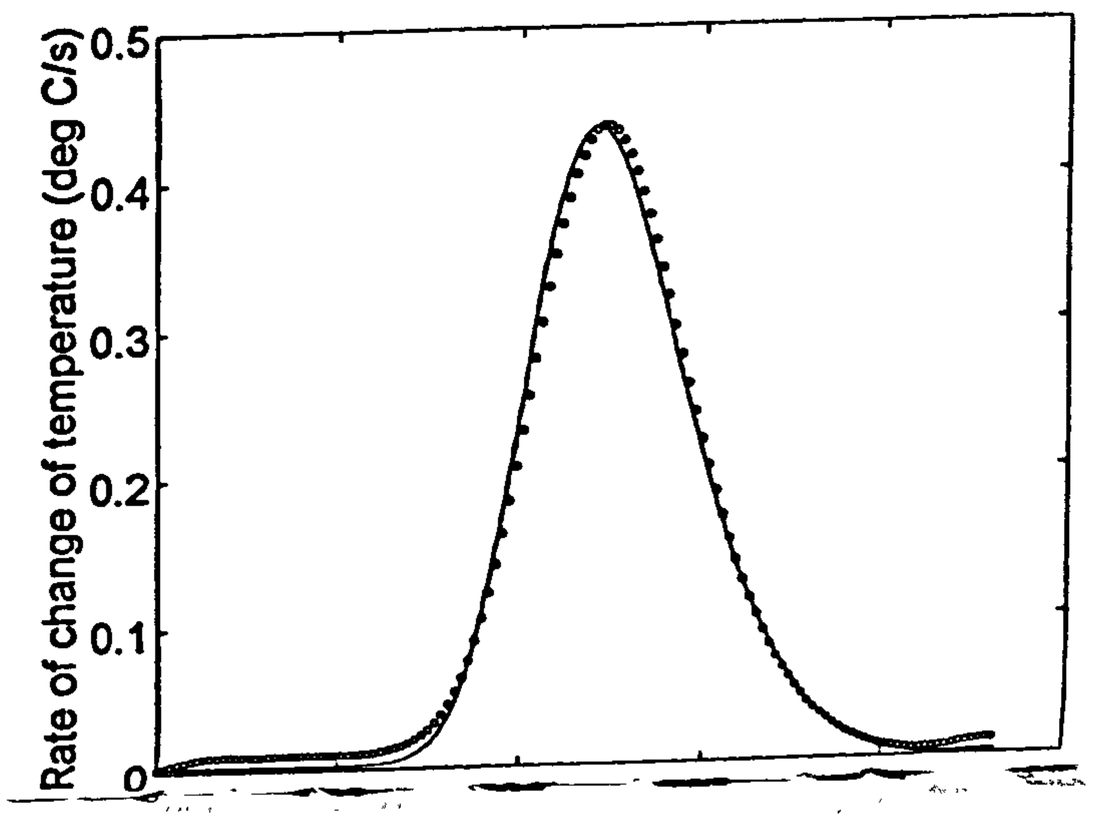
Rate of change of temperature (deg C/s)
0.5
0.4
0.3
0.2
0.1
0

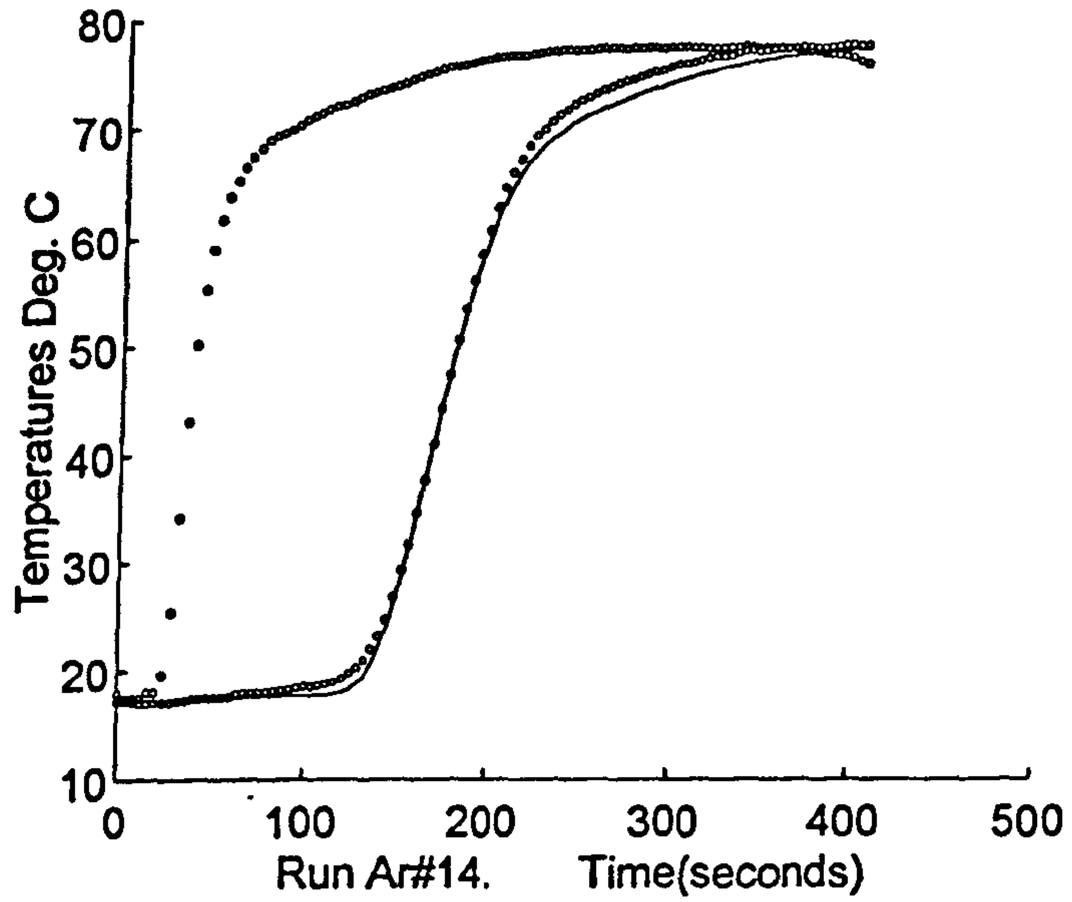
Temperatures Deg. C
80
70
60
50
40
30
20
10
0
100
200
300
400
500
Run Ar#14.
Time(seconds)

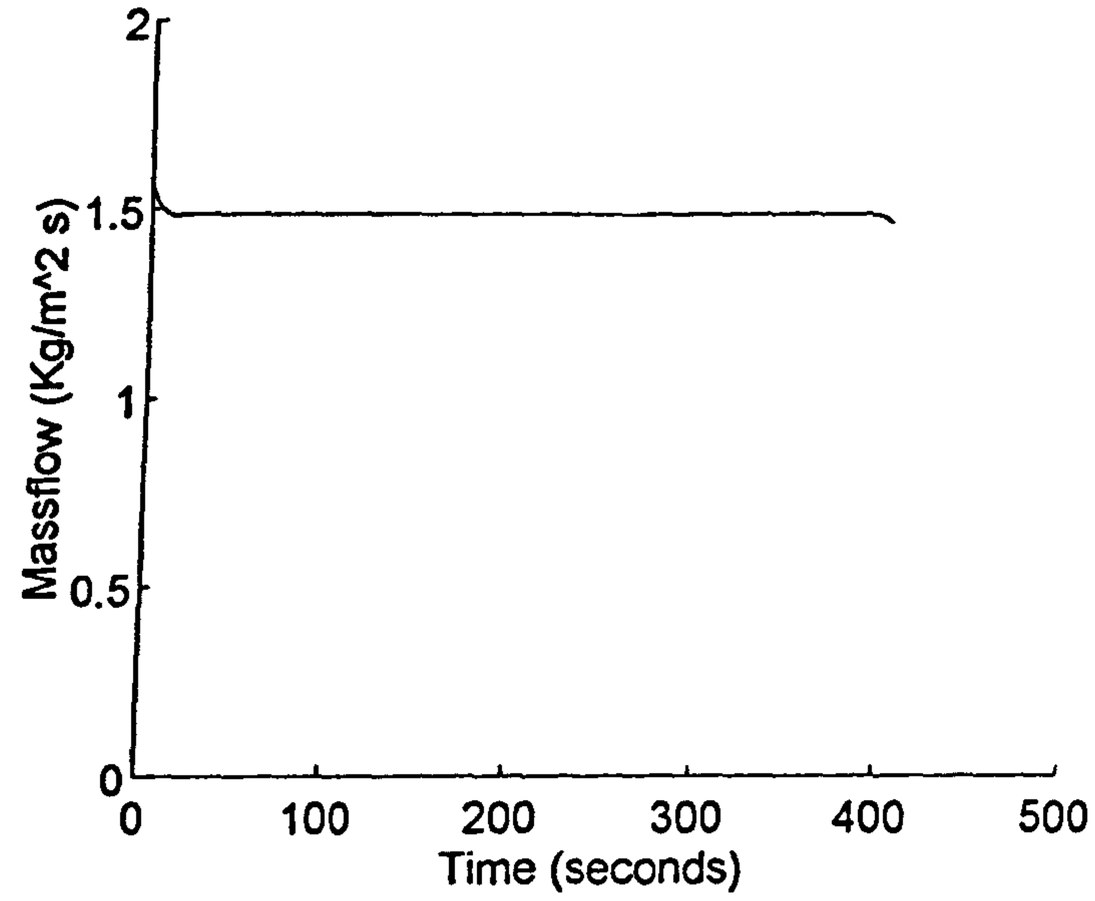
Massflow (Kg/m^2 s)
2
1.5
1
0.5
0
0
100
200
300
400
500
Time (seconds)

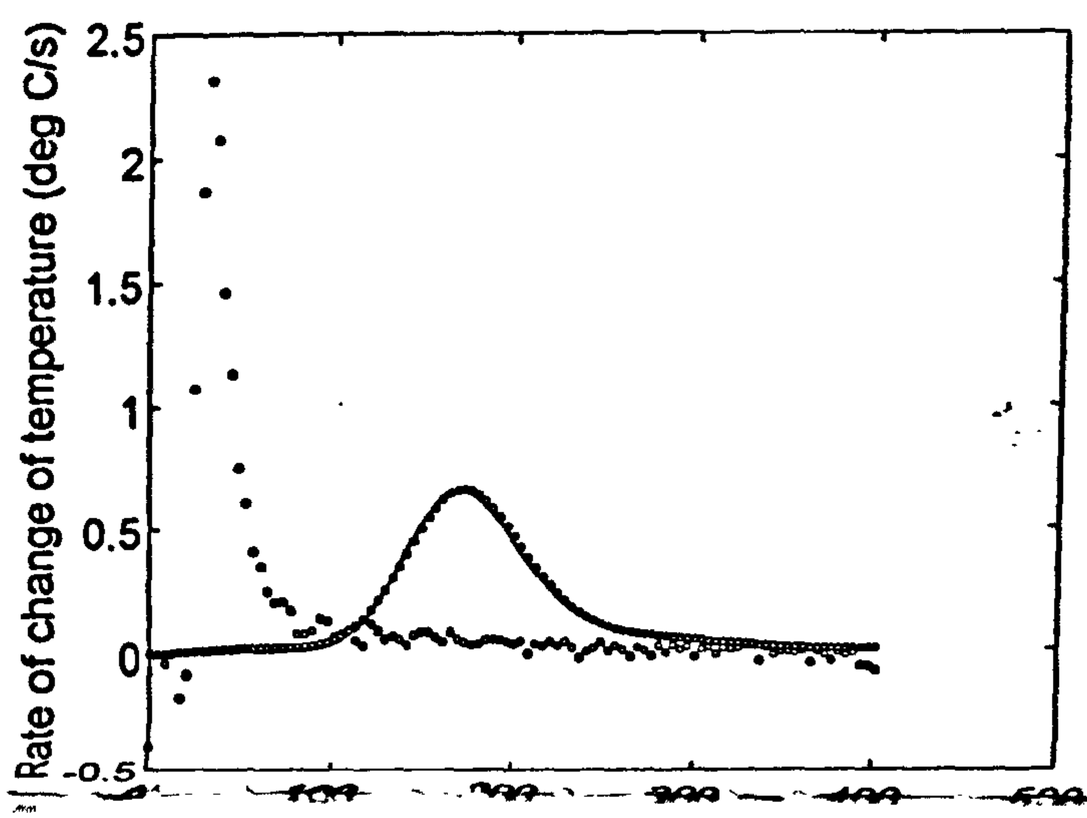
Rate of change of temperature (deg C/s)
2.5
2
1.5
1
0.5
0
-0.5

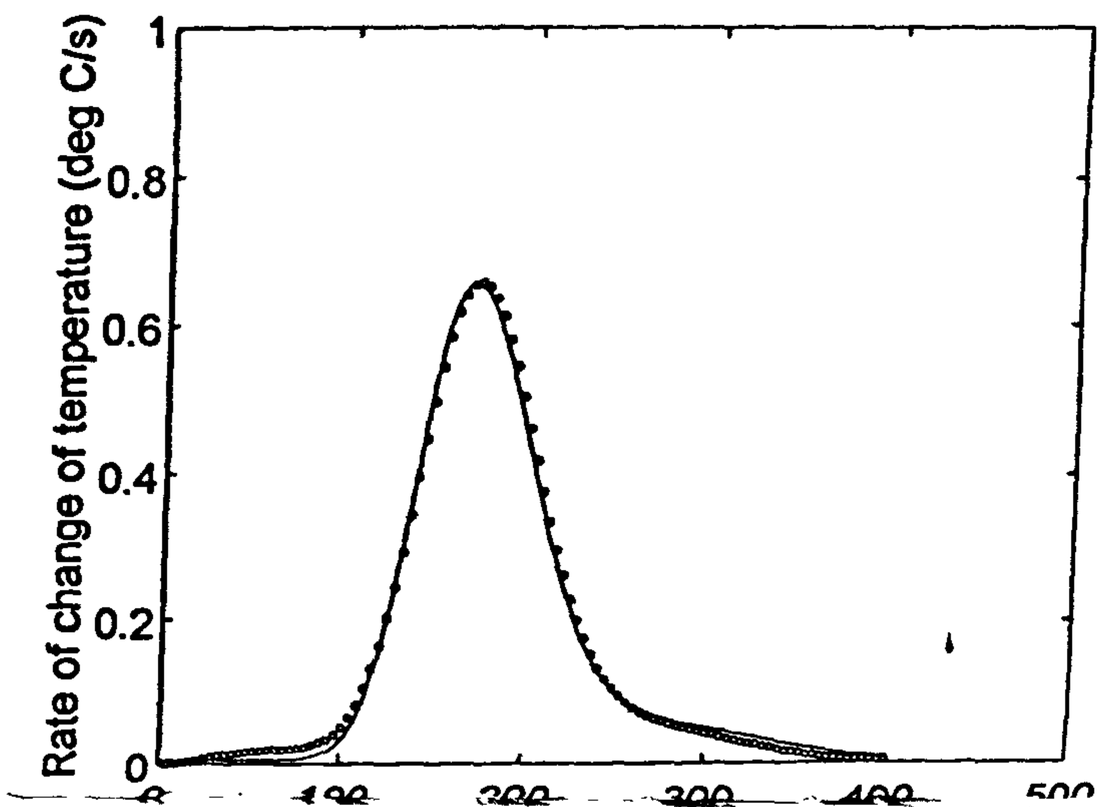
Rate of change of temperature (deg C/s)
1
0.8
0.6
0.4
0.2
0

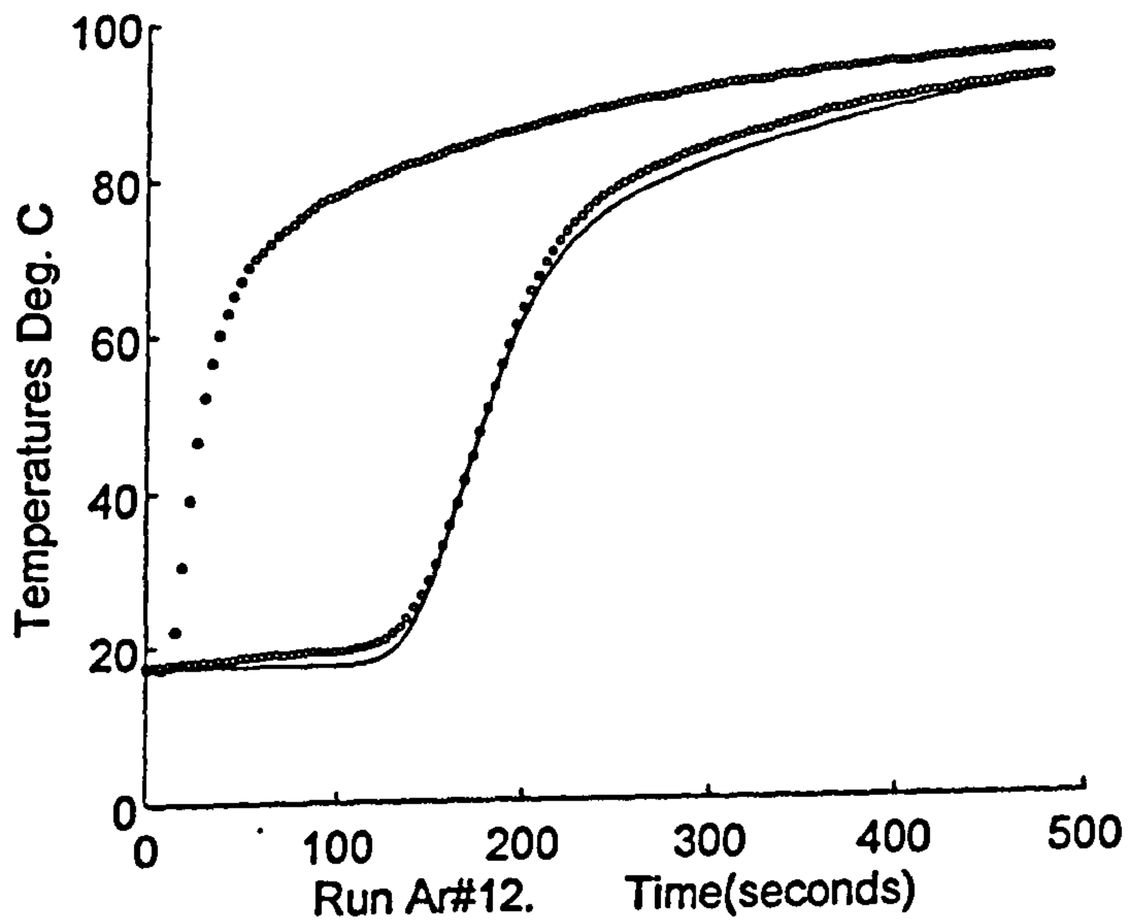
Temperatures Deg. C
100
80
60
40
20
0
0
100
200
300
400
500
Run Ar#12.
Time(seconds)

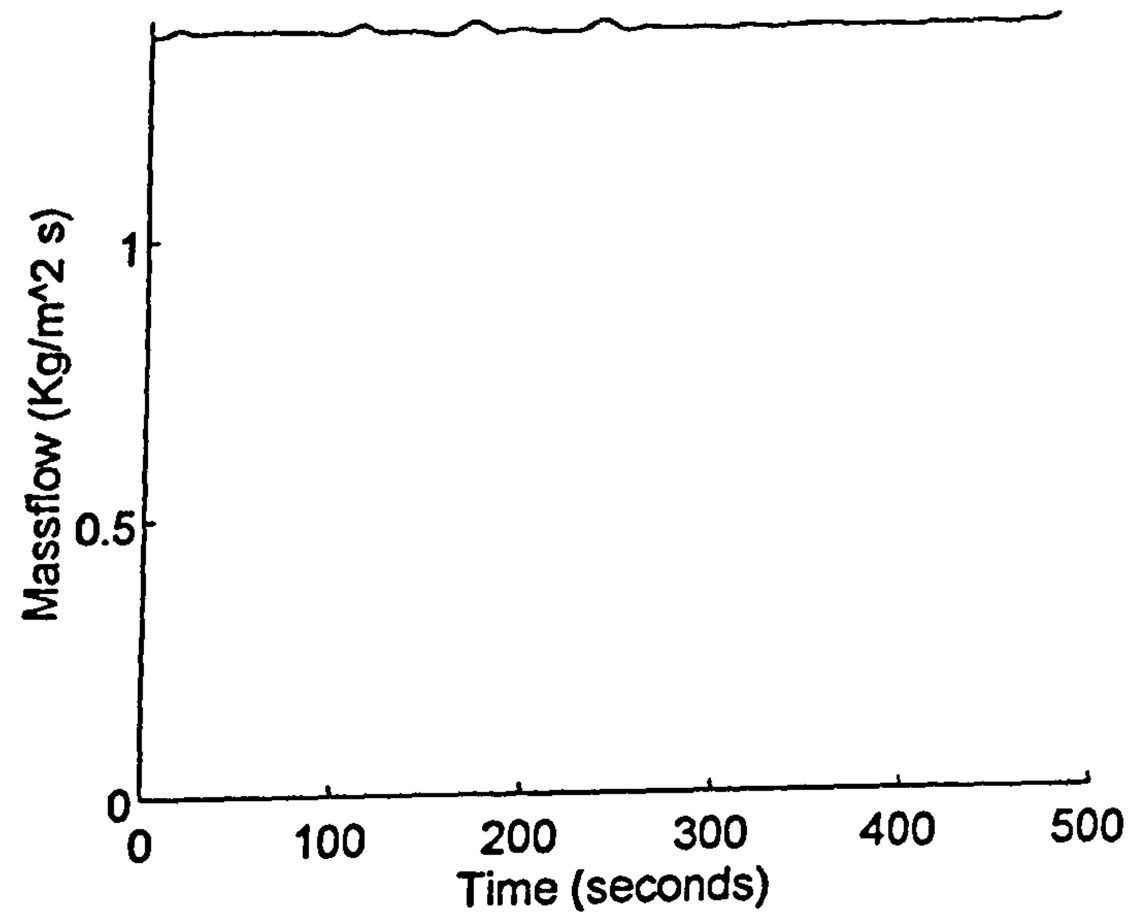
Massflow (Kg/m^2 s)
1
0.5
0
0
100
200
300
400
500
Time (seconds)

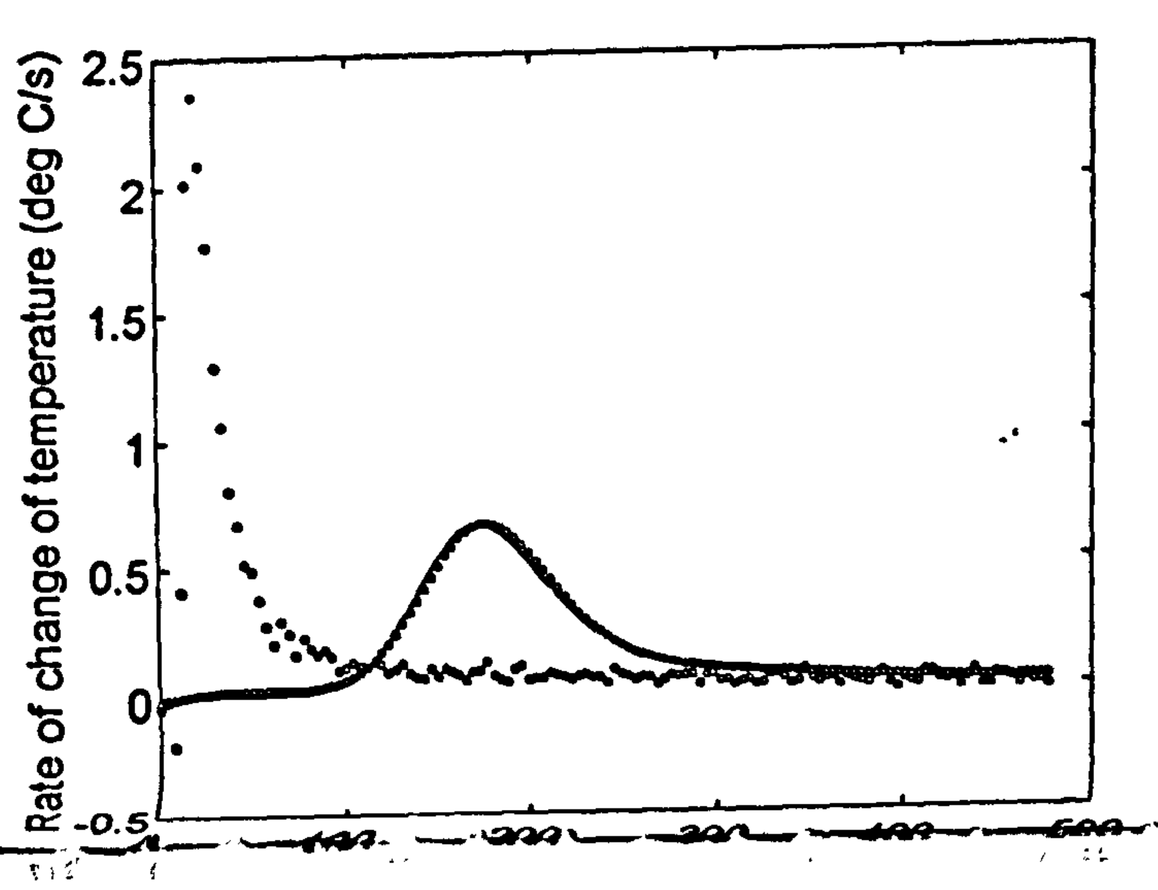
Rate of change of temperature (deg C/s)
2.5
2
1.5
1
0.5
0
-0.5

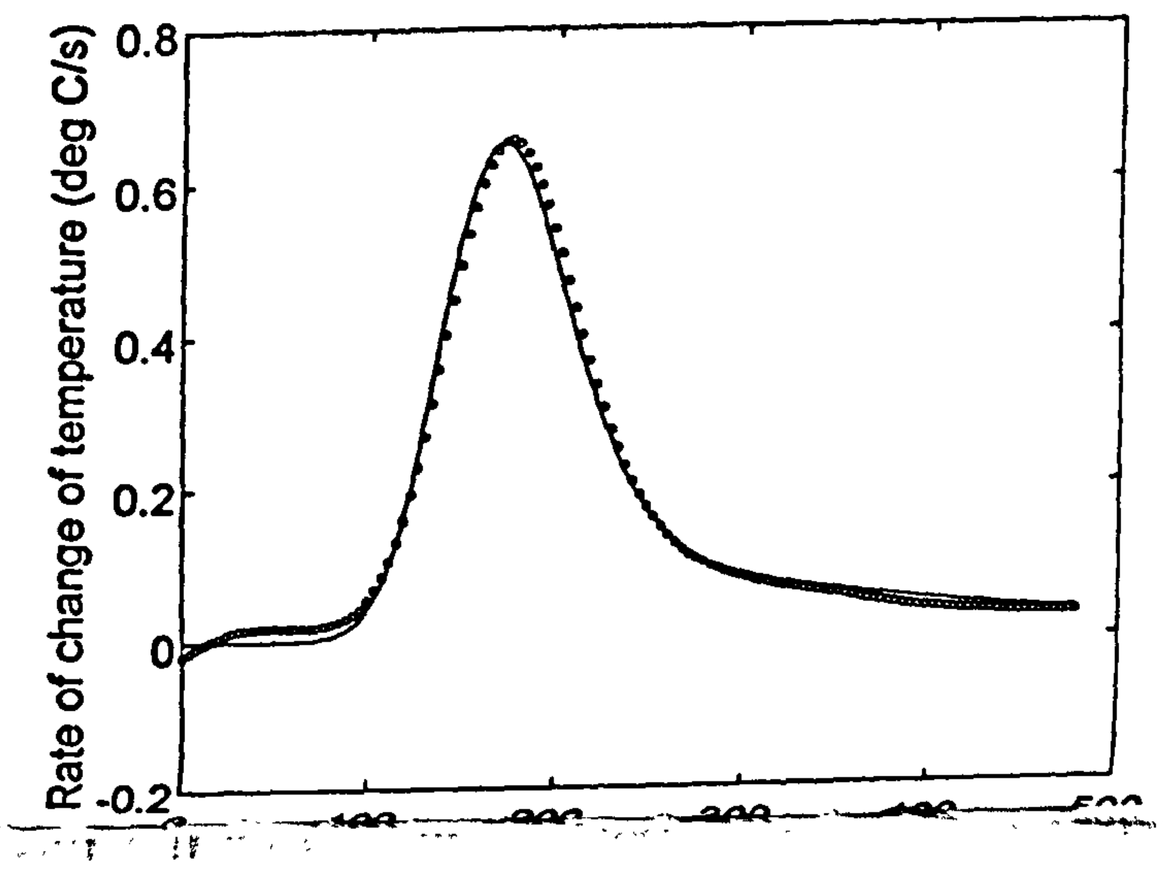
Rate of change of temperature (deg C/s)
0.8
0.6
0.4
0.2
0
-0.2

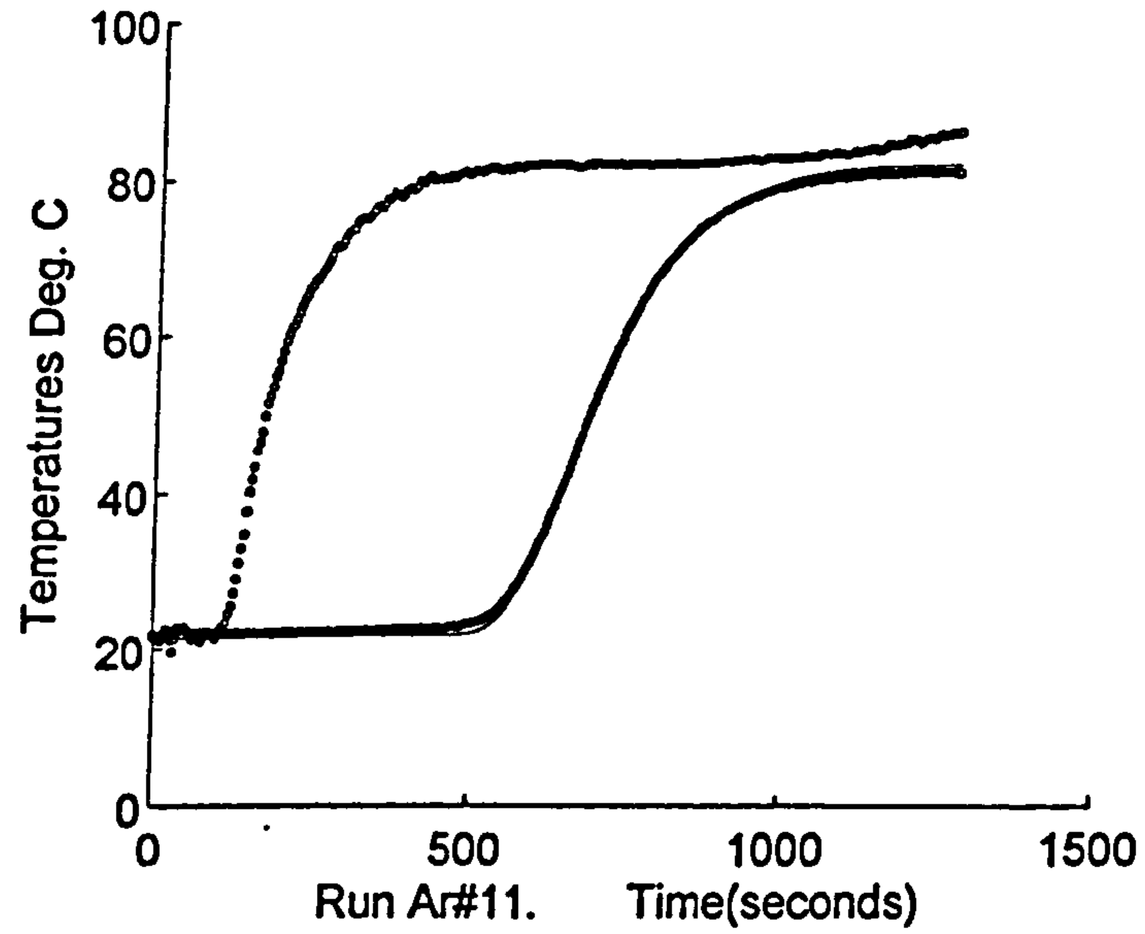
Temperatures Deg. C
100
80
60
40
20
0
0
500
1000
1500
Run Ar#11. Time(seconds)

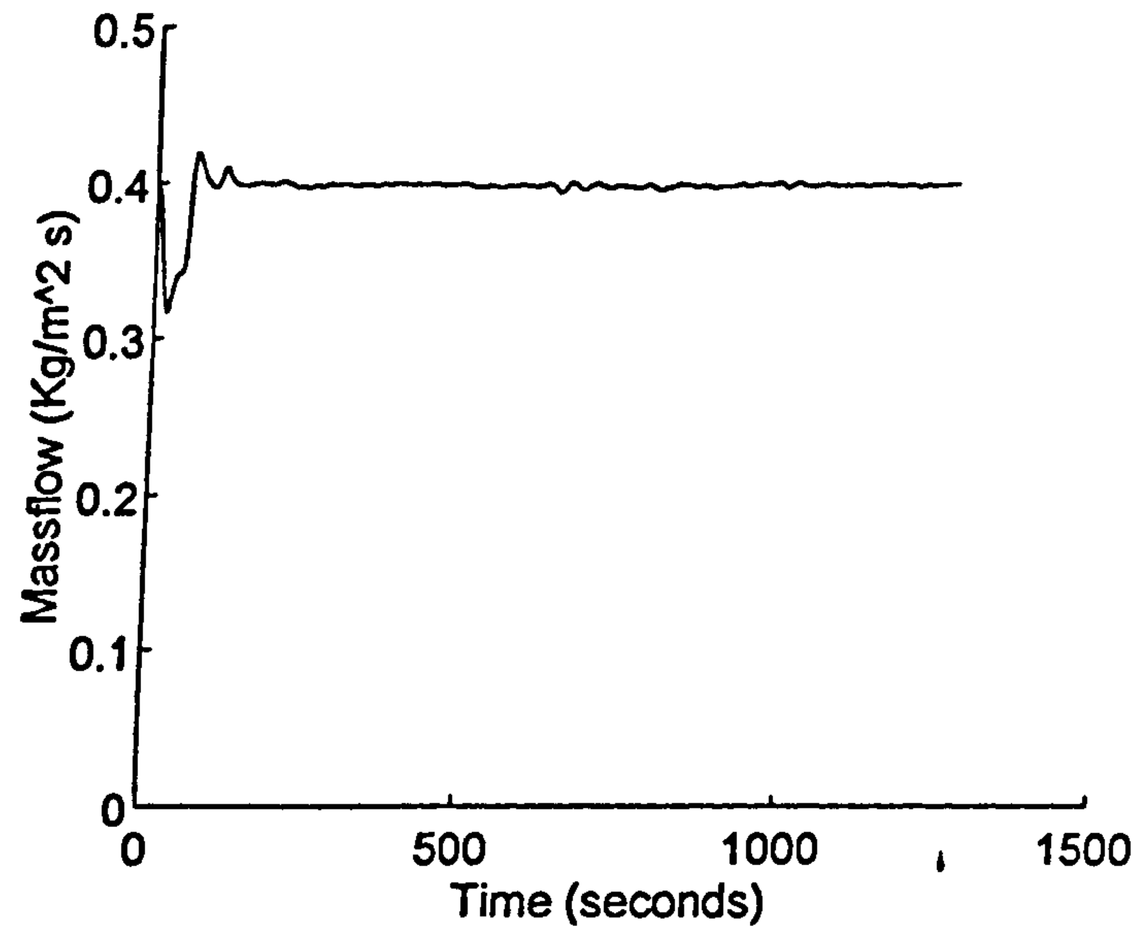
Massflow (Kg/m^2 s)
0.5
0.4
0.3
0.2
0.1
0
0
500
1000
1500
Time (seconds)

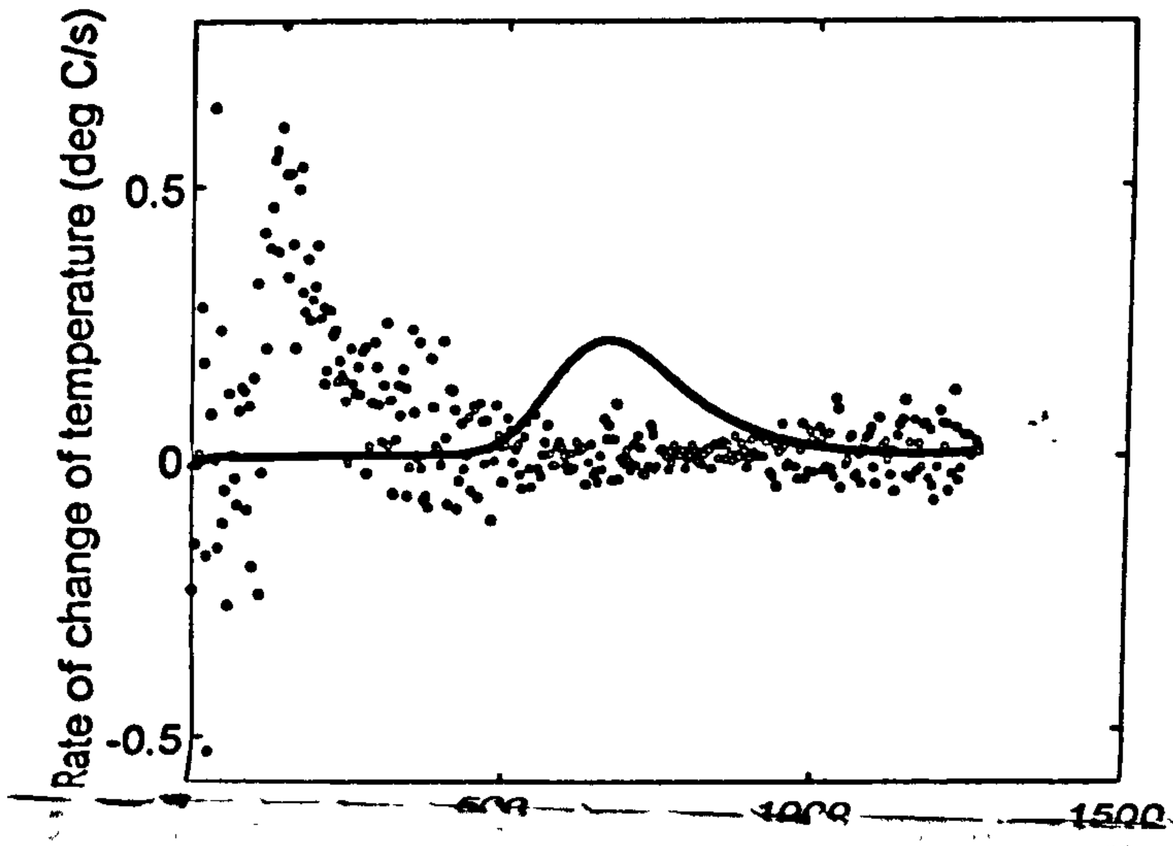
Rate of change of temperature (deg C/s)
0.5
0
-0.5
500
1000
1500

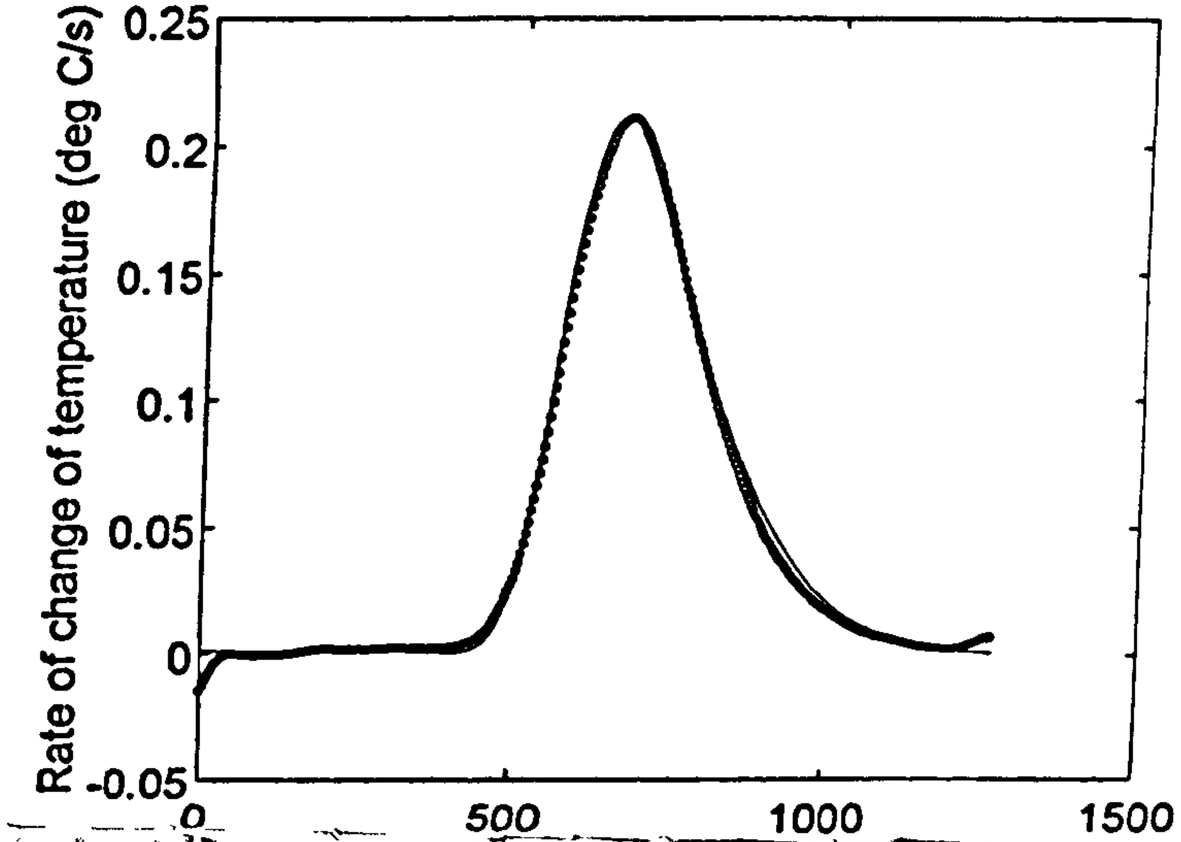
Rate of change of temperature (deg C/s)
0.25
0.2
0.15
0.1
0.05
0
-0.05
0
500
1000
1500

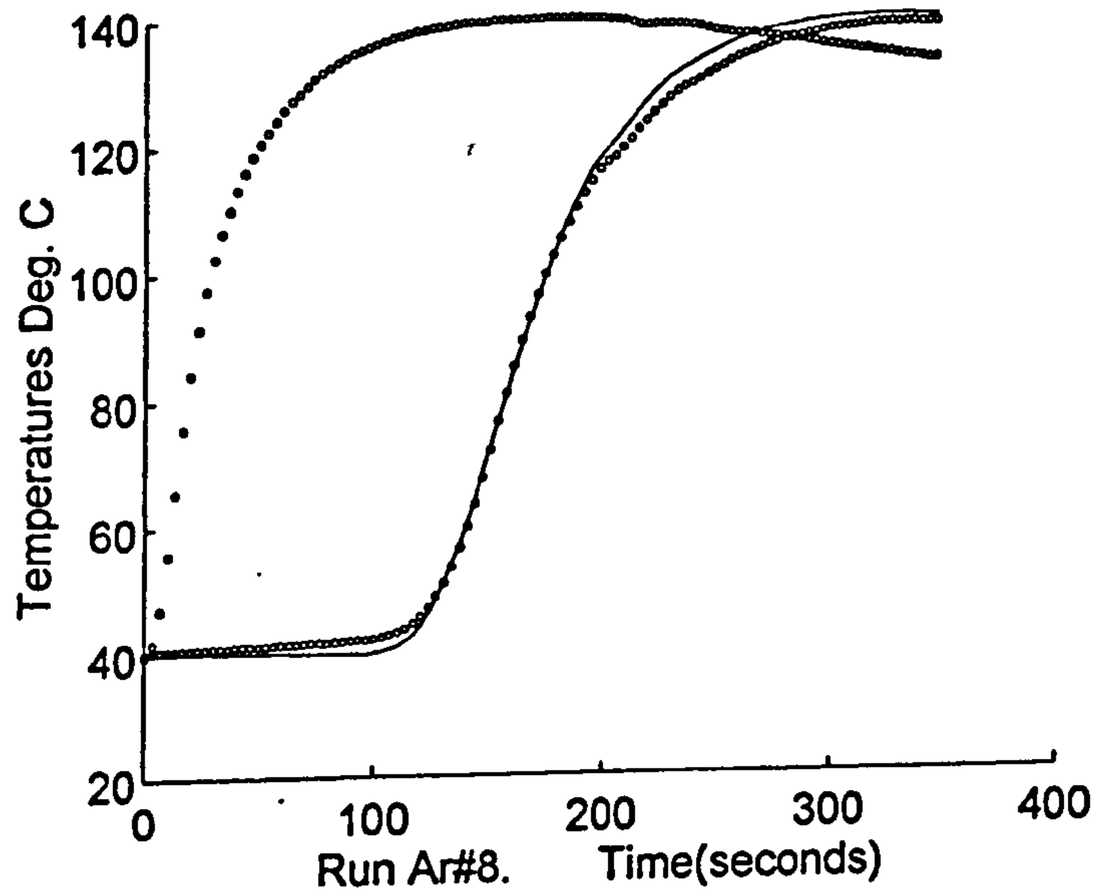
Temperatures Deg. C
140
120
100
80
60
40
20
0
100
200
300
400
Run Ar#8.
Time(seconds)

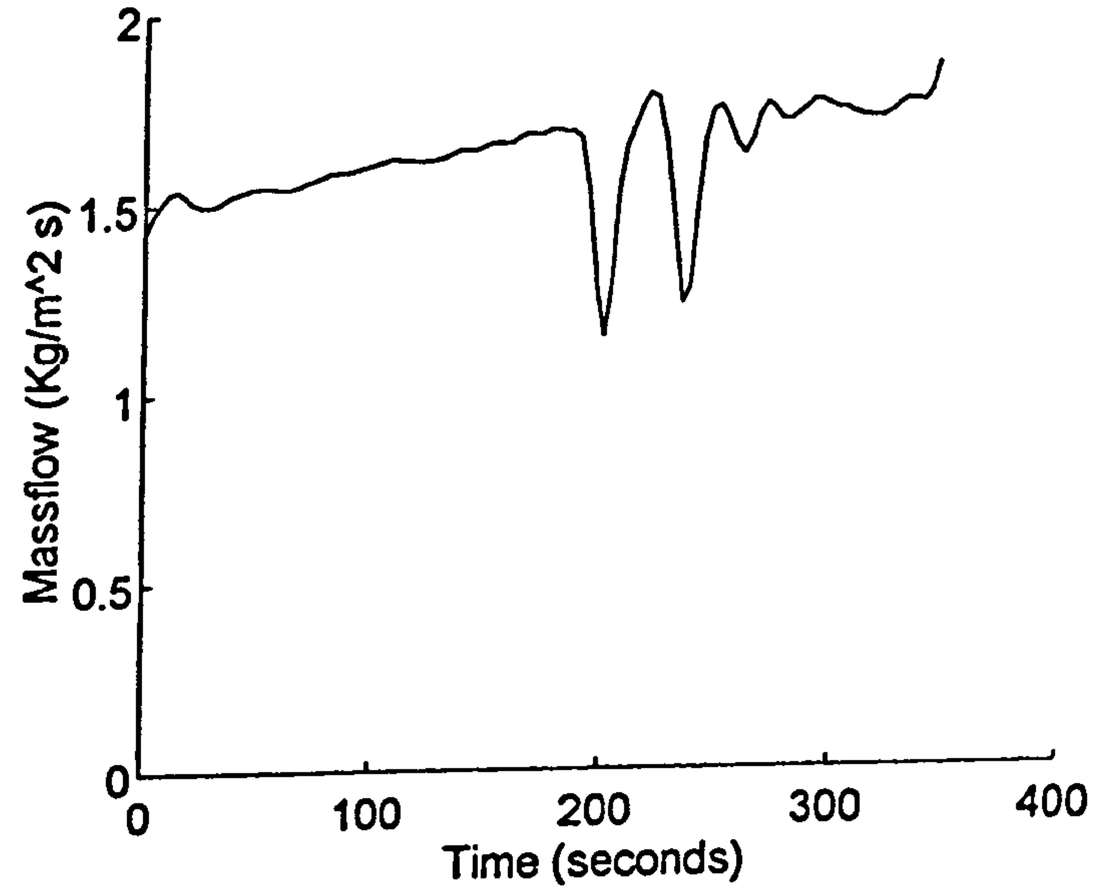
Massflow (Kg/m^2 s)
2
1.5
1
0.5
0
0
100
200
300
400
Time (seconds)

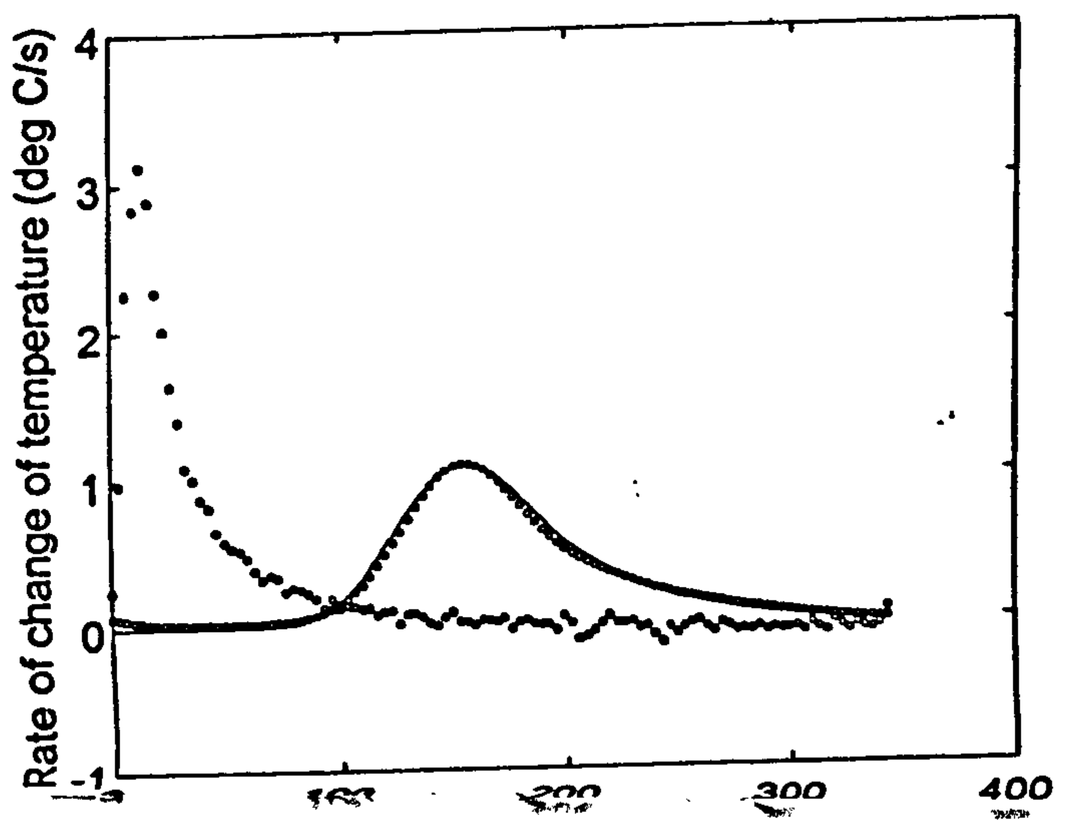
Rate of change of temperature (deg C/s)
4
3
2
1
0
-1
200
300
400

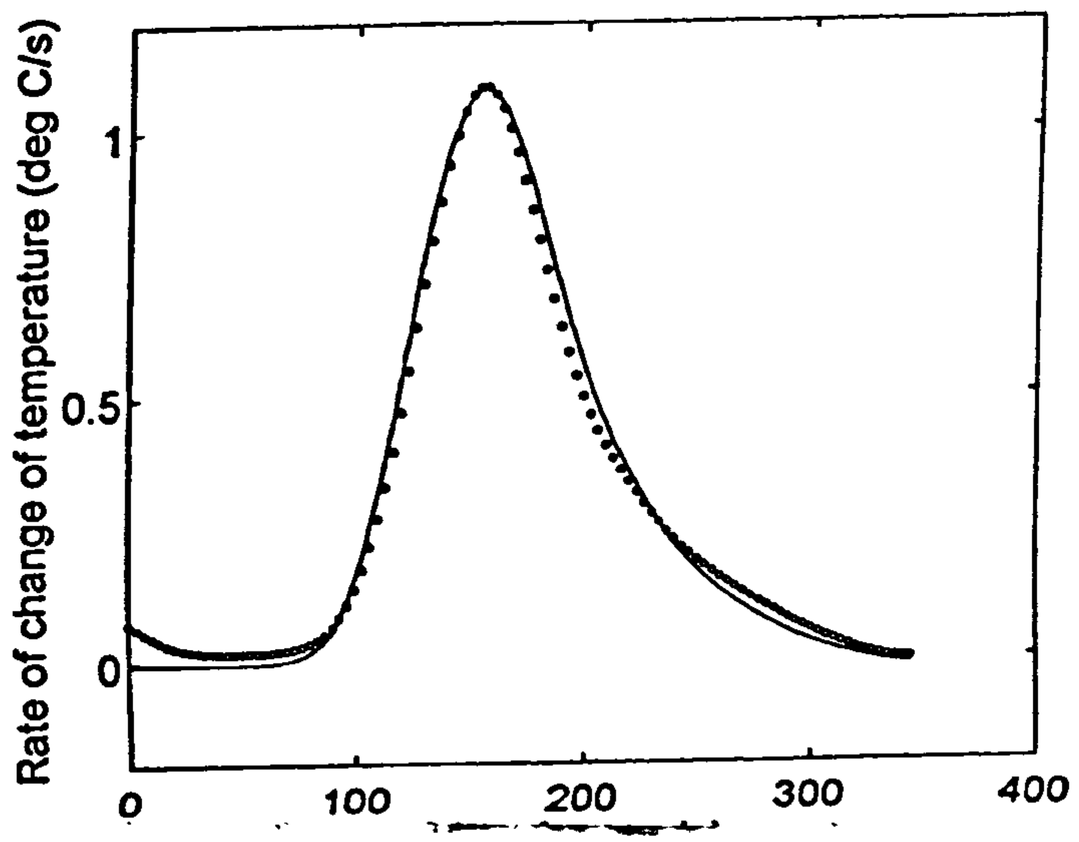
Rate of change of temperature (deg C/s)
1
0.5
0
0
100
200
300
400

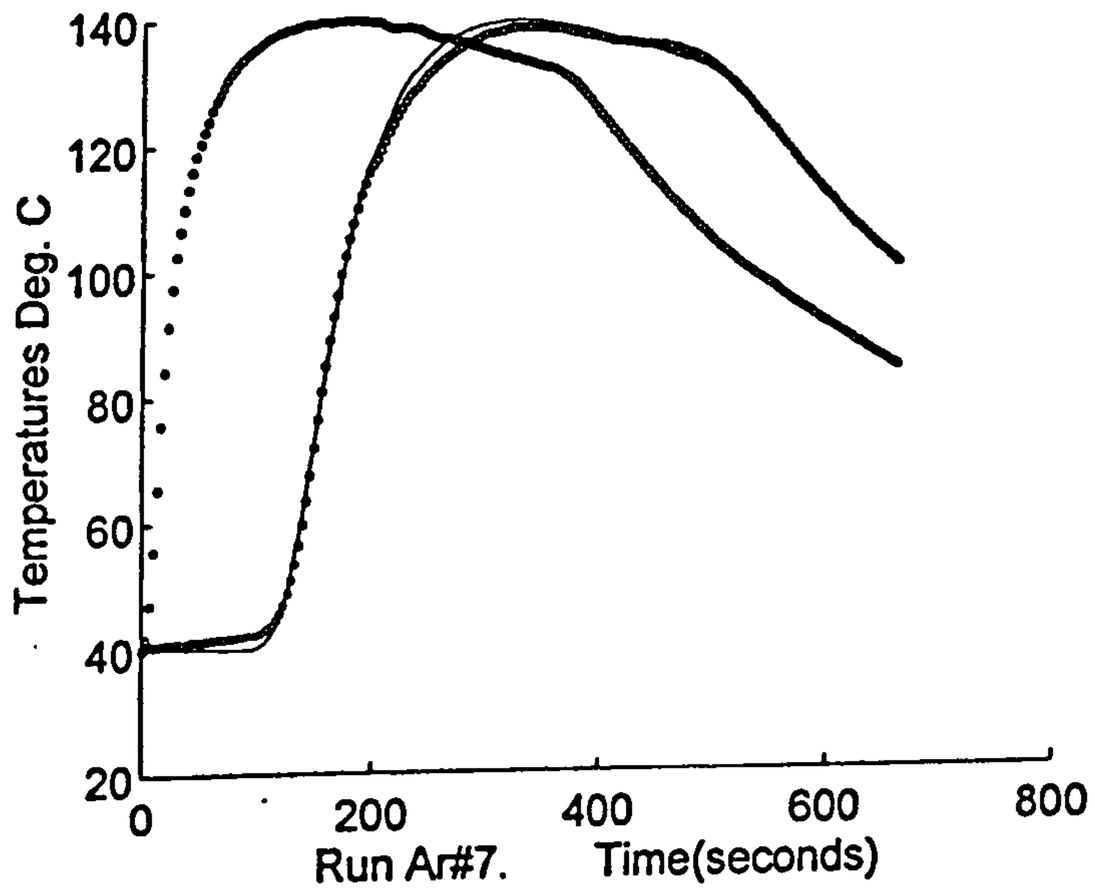
Temperatures Deg. C
140
120
100
80
60
40
20
0
200
400
600
800
Run Ar#7.
Time(seconds)

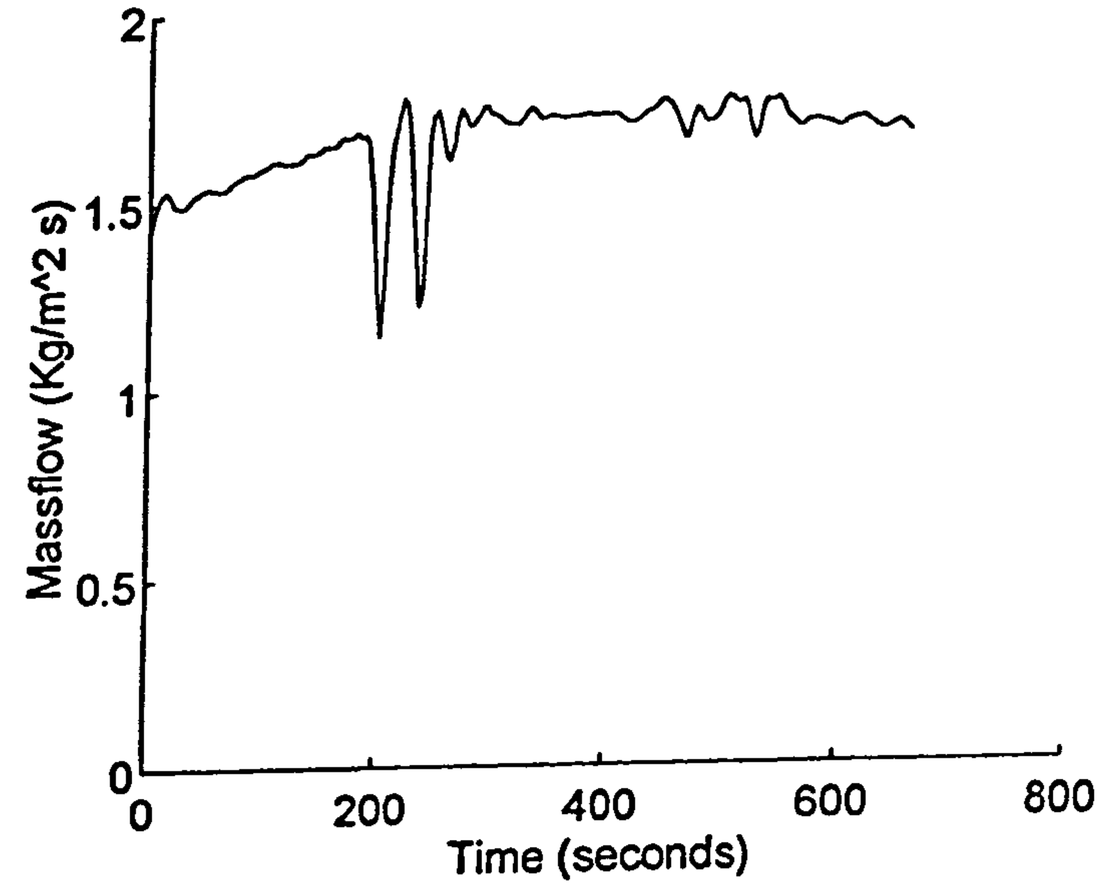
Massflow (Kg/m^2 s)
2
1.5
1
0.5
0
0
200
400
600
800
Time (seconds)

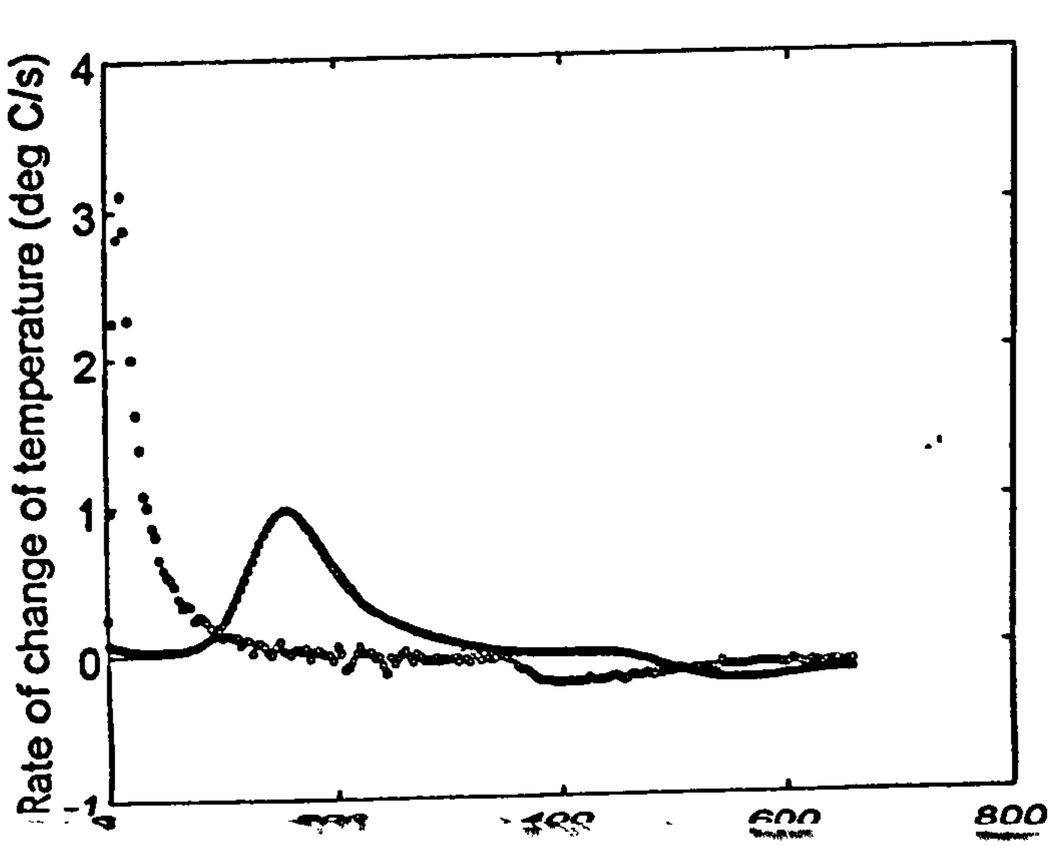
Rate of change of temperature (deg C/s)
4
3
2
1
0
-1
600
800

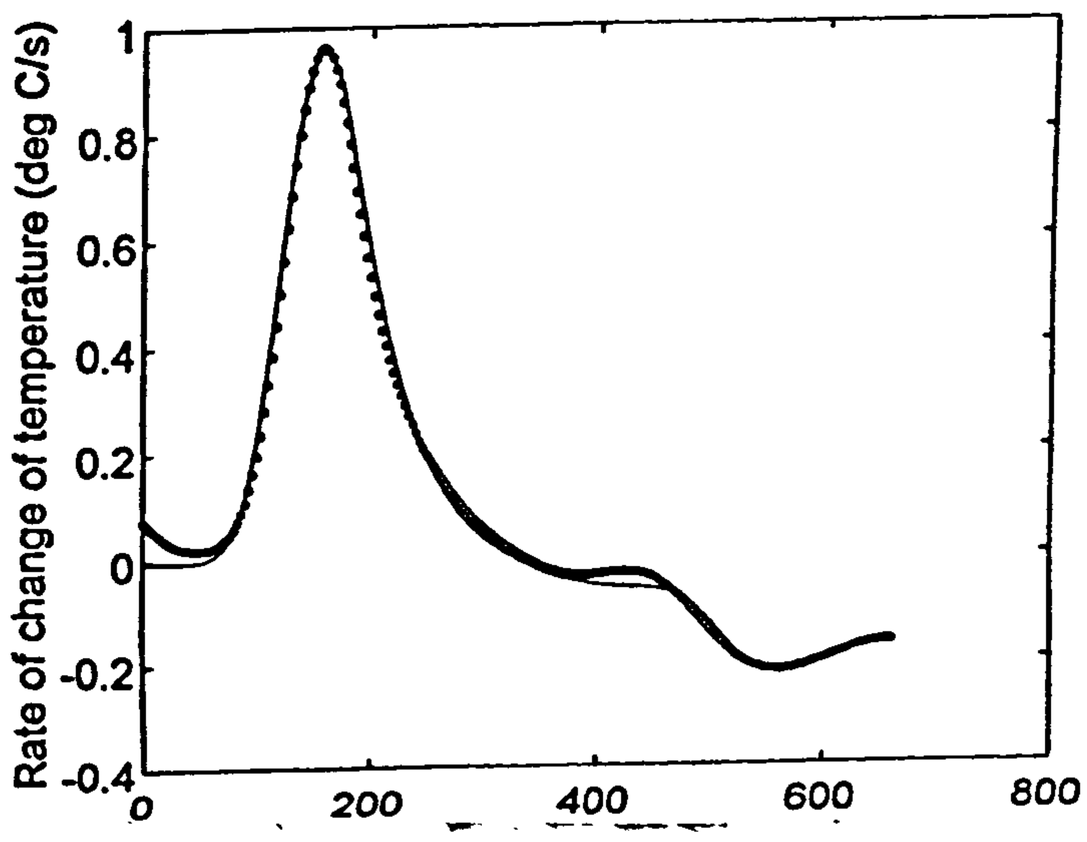
Rate of change of temperature (deg C/s)
1
0.8
0.6
0.4
0.2
0
-0.2
-0.4
0
200
400
600
800

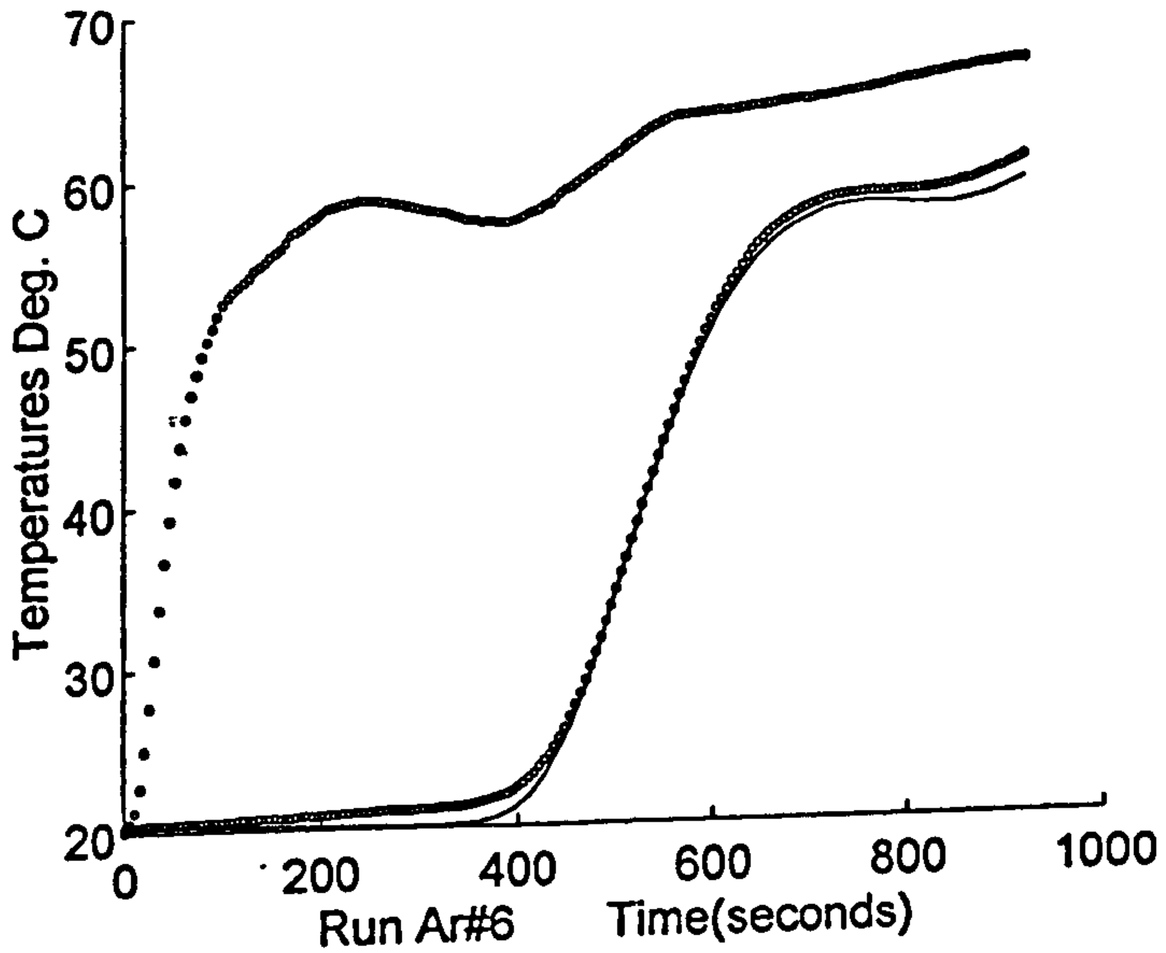
Temperatures Deg. C
70
60
50
40
30
20
0
200
400
600
800
1000
Run Ar#6
Time(seconds)

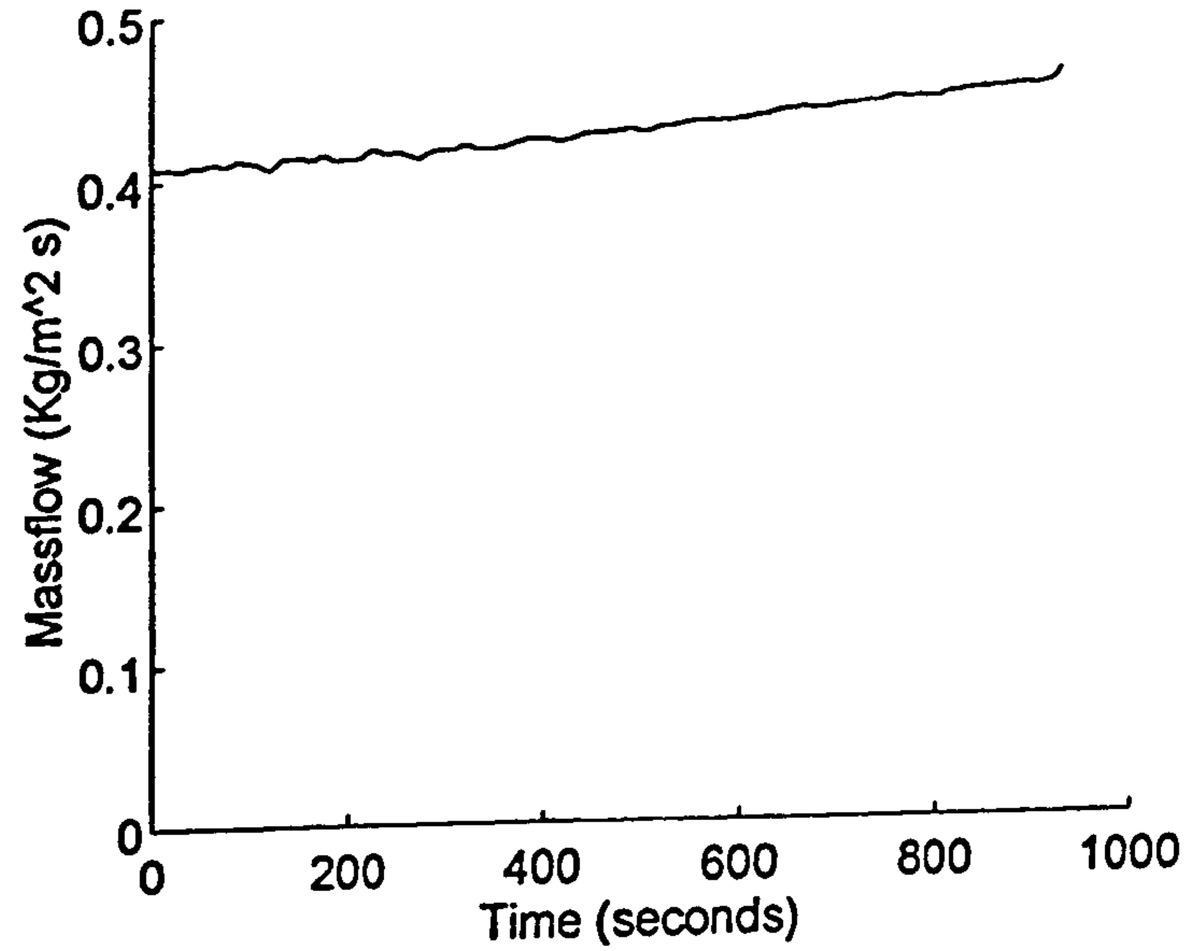
Massflow (Kg/m^2 s)
0.5
0.4
0.3
0.2
0.1
0
0
200
400
600
800
1000
Time (seconds)

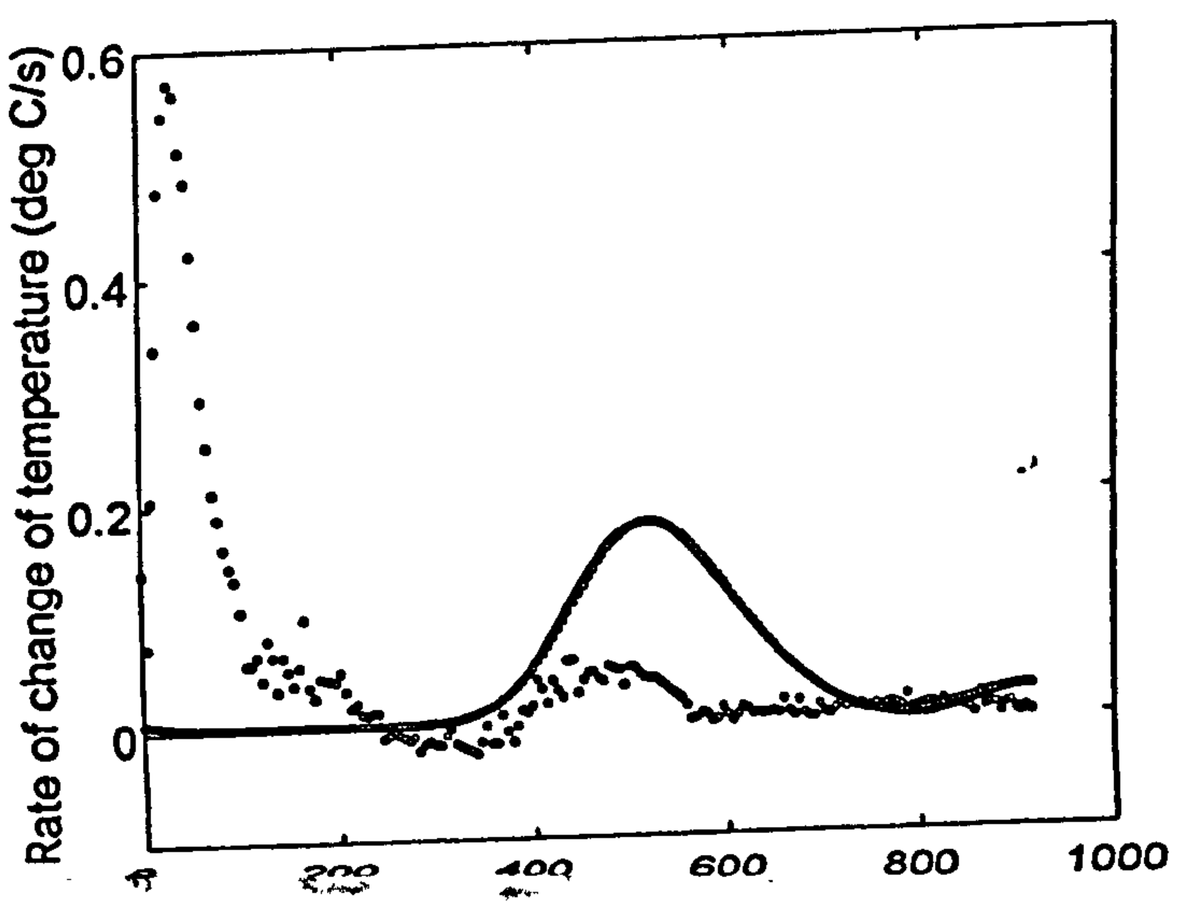
Rate of change of temperature (deg C/s)
0.6
0.4
0.2
0
200
400
600
800
1000

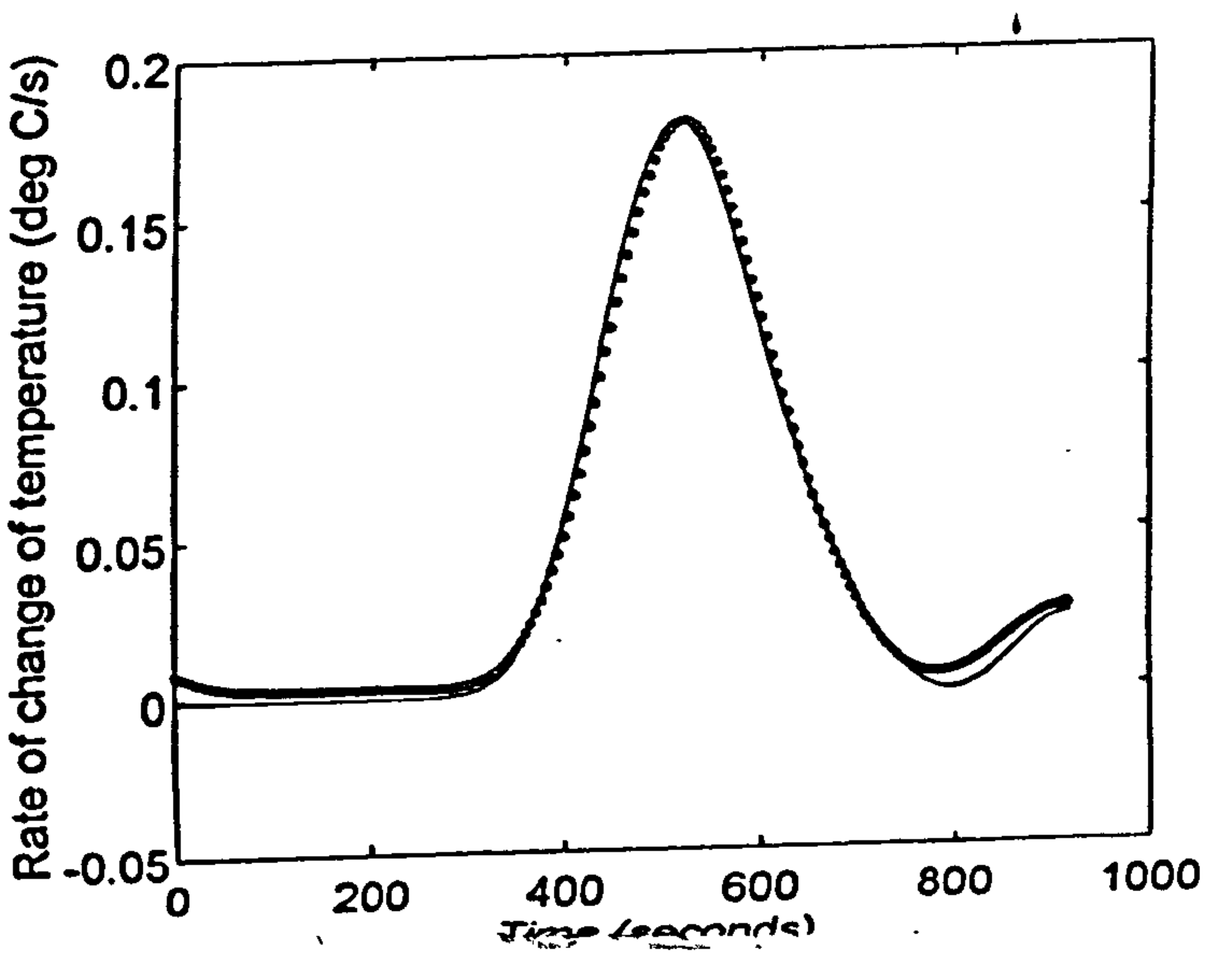
Rate of change of temperature (deg C/s)
0.2
0.15
0.1
0.05
0
-0.05
0
200
400
600
800
1000

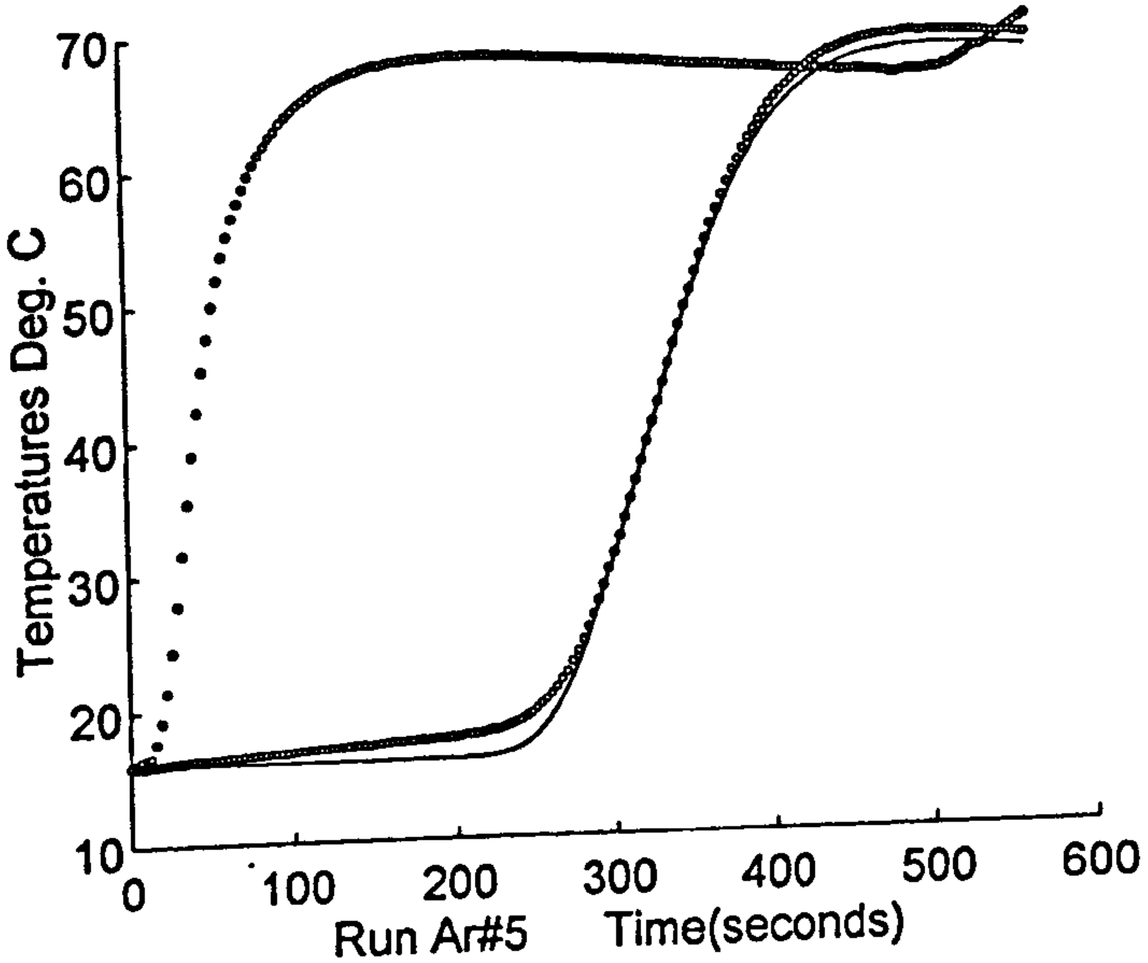
Temperatures Deg. C
70
60
50
40
30
20
10
0
100
200
300
400
500
600
Run Ar#5
Time(seconds)

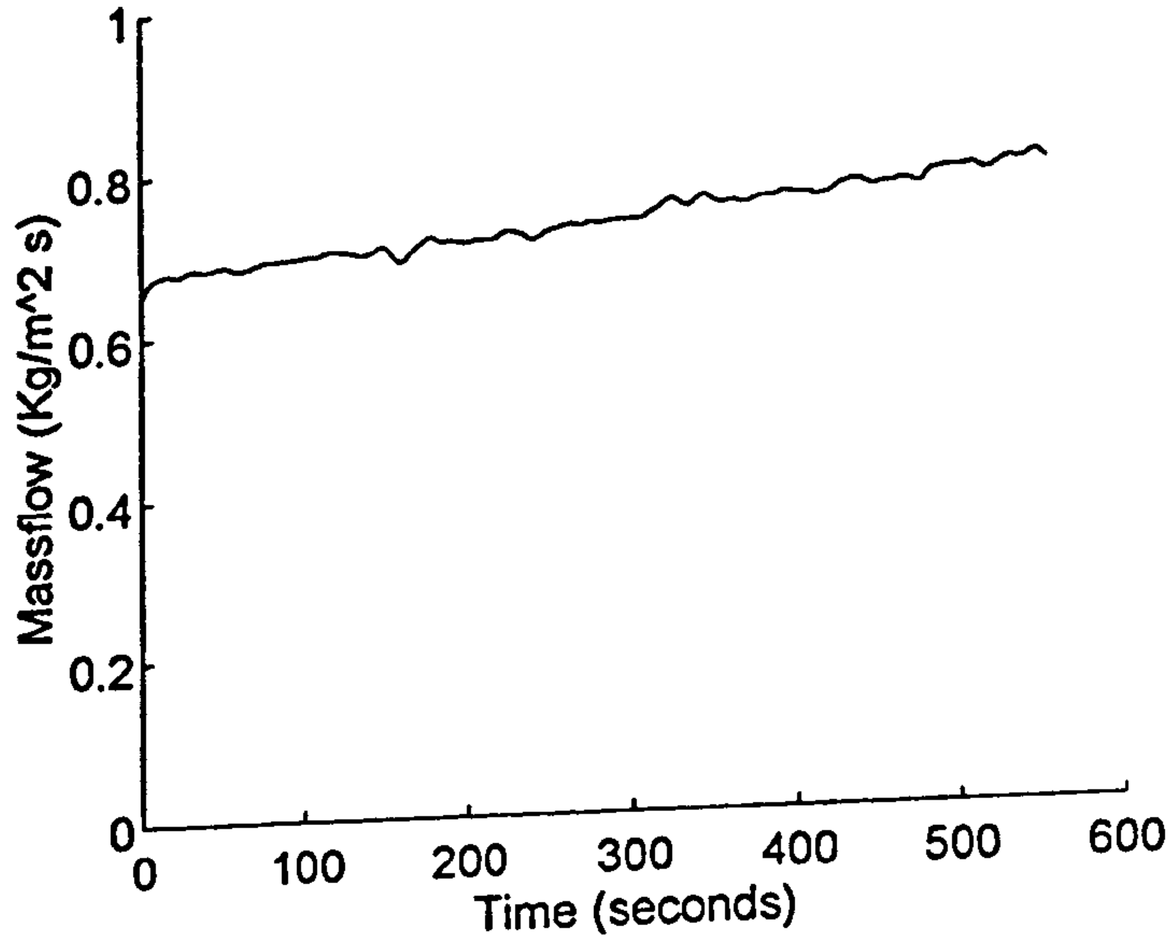
Massflow (Kg/m^2 s)
1
0.8
0.6
0.4
0.2
0
0
100
200
300
400
500
600
Time (seconds)

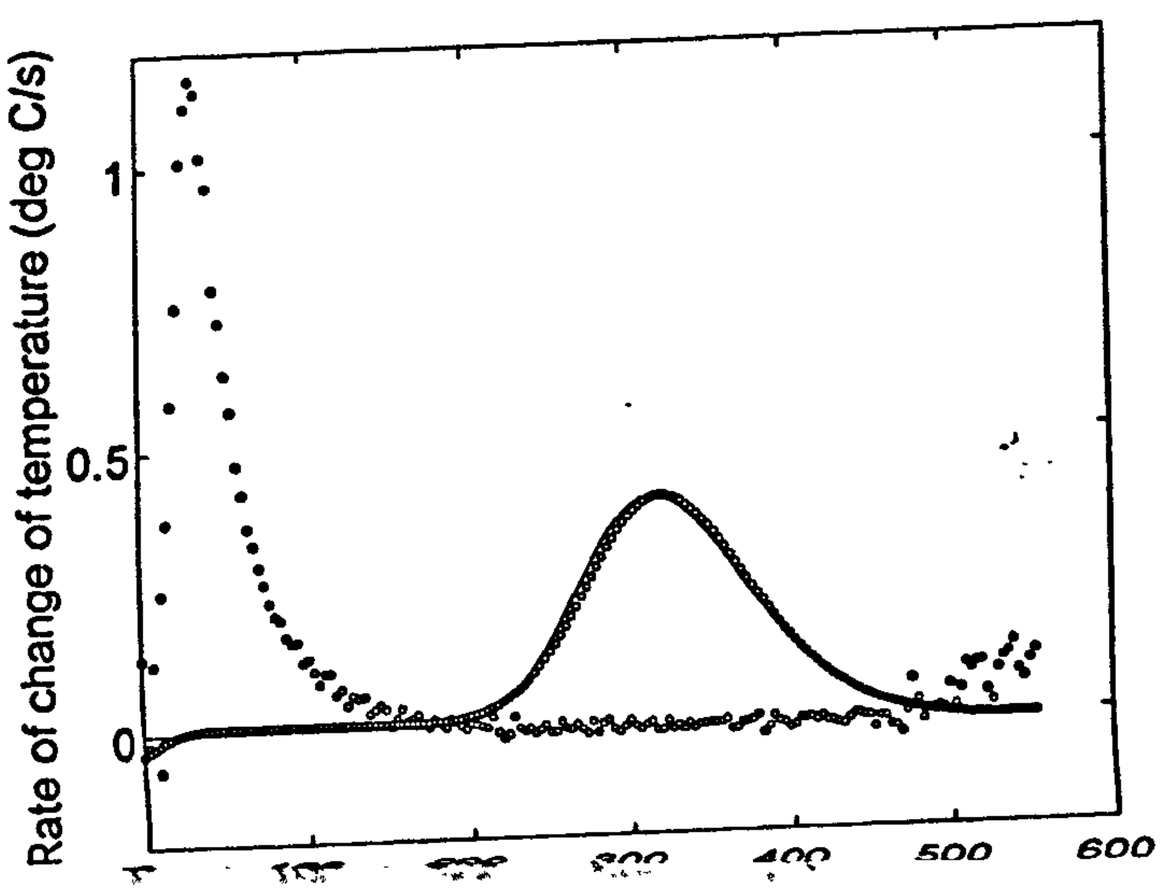
Rate of change of temperature (deg C/s)
1
0.5
0
400
500
600

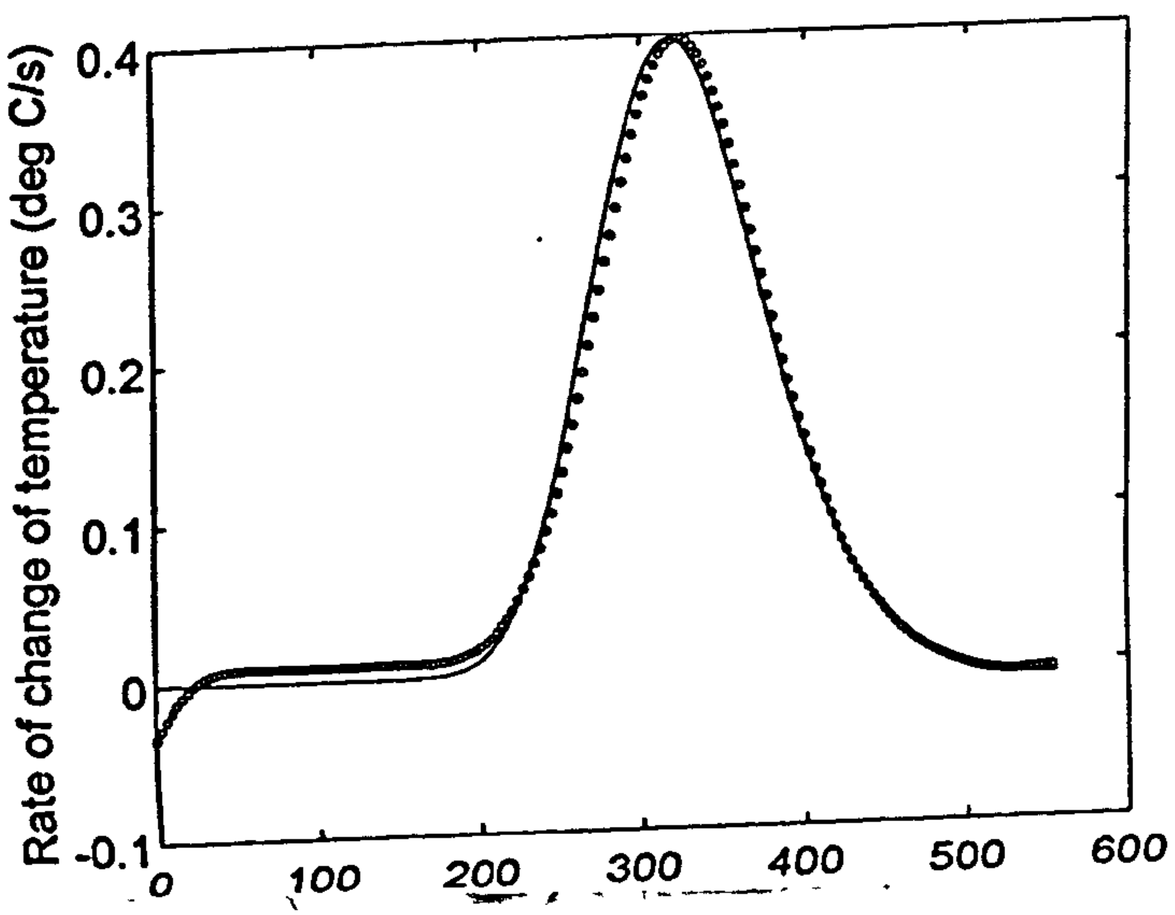
Rate of change of temperature (deg C/s)
0.4
0.3
0.2
0.1
0
-0.1
0
100
200
300
400
500
600

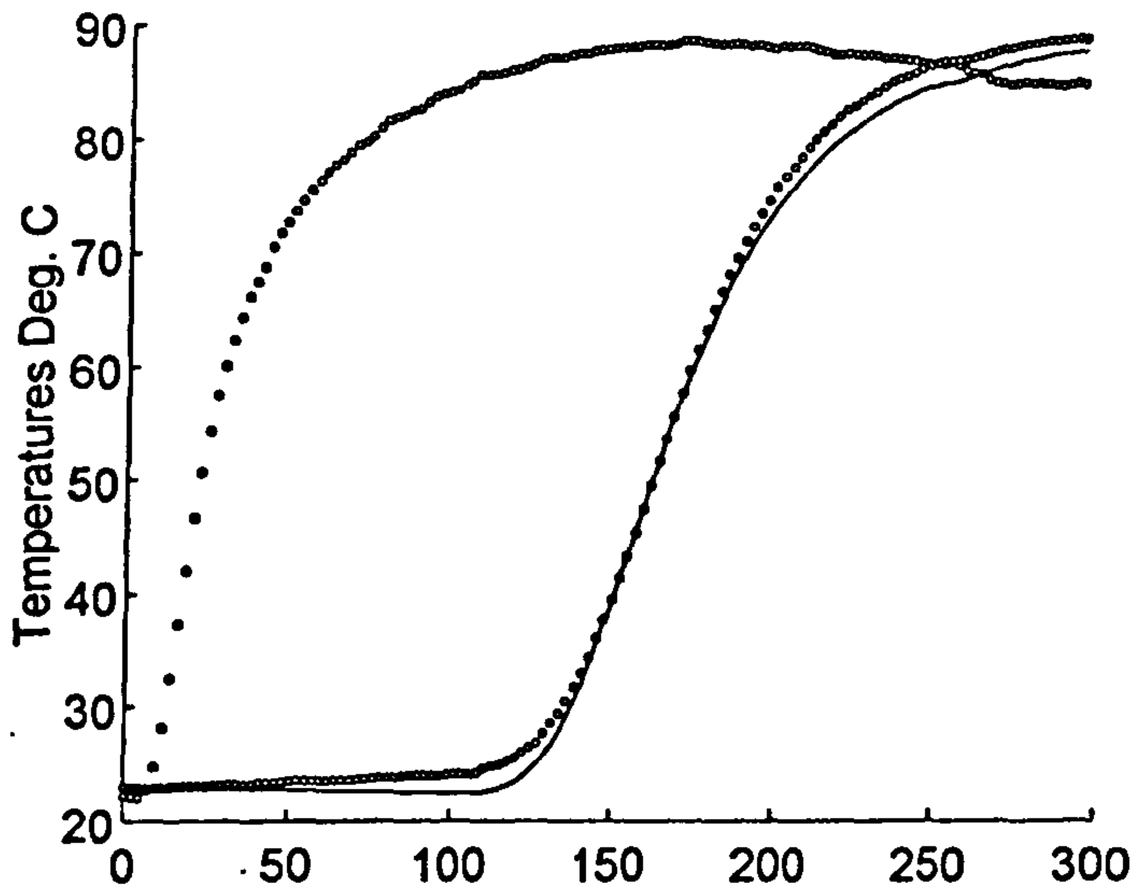

Run Ar#4 Time(seconds)

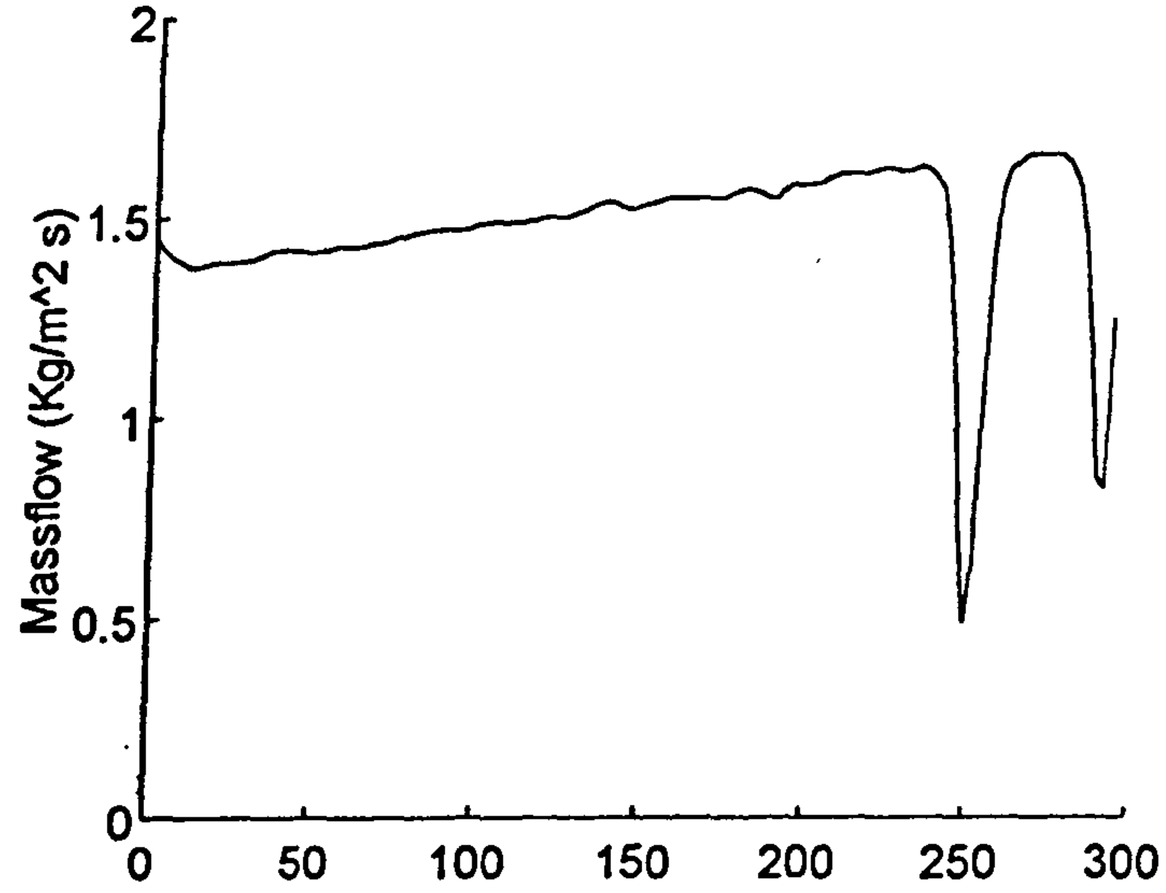

Time (seconds)